

The Pennsylvania State University

The Graduate School

**METALORGANIC CHEMICAL VAPOR DEPOSITION OF TWO-
DIMENSIONAL LAYERED CHALCOGENIDES**

A Dissertation in

Materials Science and Engineering

by

Xiaotian Zhang

© 2019 Xiaotian Zhang

Submitted in Partial Fulfillment
of the Requirements
for the Degree of

Doctor of Philosophy

August 2019

The dissertation of Xiaotian Zhang was reviewed and approved* by the following:

Joan M. Redwing
Professor of Materials Science and Engineering
Associate director of the Materials Research Institute
Director of the 2D Crystal Consortium – Materials Innovation Platform
Dissertation Advisor
Chair of Committee

Joshua A. Robinson
Associate professor of Materials Science and Engineering
Associate director of Center for Two-Dimensional and Layered Materials
Director of User Programs of the 2D Crystal Consortium – Materials
Innovation Platform

Thomas N. Jackson
Robert E. Kirby Chair Professor of Electrical Engineering

Susan B. Sinnott
Professor of Materials Science and Engineering and Chemistry
Head of the Department of Materials Science and Engineering

Suzanne E. Mohny
Professor of Materials Science and Engineering and Electrical Engineering
Chair of Intercollege Graduate Degree Program in Materials Science and
Engineering

*Signatures are on file in the Graduate School

ABSTRACT

Two dimensional (2D) materials have attracted wide interest because of their layered crystal structures and anisotropic properties which leads to potential new diversity of function in nanoelectronics, photonics, sensing, energy storage, and optoelectronics. Among them, the family of 2D layered chalcogenides (2DLCs) including transition metal dichalcogenides (TMDs) (in the form of MX_2 where $\text{M}=\text{Mo}, \text{W}$, etc. and $\text{X}=\text{S}, \text{Se}, \text{Te}$) and group IIIA metal chalcogenides (MCs) (typically in the form of MX and M_2X_3 where $\text{M}=\text{Ga}, \text{In}$ and $\text{X}=\text{S}, \text{Se}$) have been a focus of increasing interest due to their number of intriguing properties. Monolayer TMDs have exhibited unique optical and electrical properties such as indirect-to-direct band gap, spin valley polarization, interlayer exciton coupling, single photon emission. On the other hand, monolayer and few-layer MCs also demonstrate novel properties such as high carrier mobilities ($\sim 1000 \text{ cm}^2/\text{Vs}$) for $\gamma\text{-InSe}$ and ultrasensitive photoresponse as well as in-plane or/and out-of-plane ferroelectricity for $\alpha\text{-}$ and $\beta\text{-In}_2\text{Se}_3$. Therefore, the rapid development of device technologies based on 2DLCs causes increasing demand for synthesis of high-quality wafer-scale single crystal monolayer and few layer films.

Among techniques for thin film deposition, gas source chemical vapor deposition (CVD) /metalorganic CVD (MOCVD) is emerging as a promising method for wafer-scale growth of TMDs and related 2DLCs due to the ability to grow at high temperatures ($>700^\circ\text{C}$), moderate reactor pressures (10-700 Torr) and high chalcogen/metal gas phase ratios which are needed to achieve epitaxy and film stoichiometry. However, the effects of precursor chemistry on film properties have not been examined and methods to

achieve uniform, fully coalesced epitaxial monolayer TMD films are required. In addition, the growth of group III MCs by MOCVD is largely unexplored.

This dissertation focuses on a comprehensive study of gas source CVD/MOCVD growth of WSe_2 and In_2Se_3 which represent the TMDs and group IIIA MCs, respectively. In the MOCVD growth of WSe_2 , a defective graphene layer was found to form on the sapphire substrate simultaneously at high growth temperature and high Se:W ratio when using tungsten hexacarbonyl ($\text{W}(\text{CO})_6$) and dimethyl selenide ($(\text{CH}_3)_2\text{Se}$, DMSe) as precursors. The graphene layer alters the surface energy of the substrate reducing the lateral growth and coalescence of WSe_2 domains. By switching to hydrogen selenide (H_2Se) instead of DMSe, the defective graphene layer was eliminated and a multi-step diffusion-mediated process was developed for the epitaxial growth of coalesced monolayer WSe_2 films on c-plane sapphire. The multi-step process consists of an initial nucleation step which used a high $\text{W}(\text{CO})_6$ flow rate along with H_2Se at 800°C and 700 Torr to promote nucleation. The $\text{W}(\text{CO})_6$ was then switched out of the reactor and the sample was annealed in H_2Se to promote surface diffusion of tungsten-containing species to form oriented WSe_2 islands with uniform size and controlled density. The $\text{W}(\text{CO})_6$ was then switched back into the reactor at a lower flow rate to suppress further nucleation and laterally grow the WSe_2 islands to form a fully coalesced monolayer film in less than one hour. Reflection high energy electron diffraction (RHEED) and in-plane X-ray diffraction (XRD) measurements further confirm that the coalesced WSe_2 monolayer film is epitaxially oriented on sapphire as $[10\bar{1}0] \text{WSe}_2 \parallel [10\bar{1}0] \alpha\text{-Al}_2\text{O}_3$. High resolution annular dark field scanning transmission electron microscopy (ADF-STEM) and selected

area diffraction analysis of WSe₂ removed from the sapphire also indicate that the films are predominately single crystal with inversion domain boundaries (IDBs) that result from merging of 0° and 60° oriented domains. The process also provides fundamental insights into the 2D growth mechanism. The evolution of domain size and cluster density with annealing time follows a 2D ripening process, enabling an estimate of the tungsten-species surface diffusivity of 1.2×10^{-14} cm²/s. The lateral growth rate of domains was found to be relatively independent of substrate temperature over the range of 700-900 °C suggesting a mass transport limited process, however, the domain shape (triangular versus truncated triangular) varied with temperature over this same range due to local variations in the Se:W adatom ratio. The results provide an important step toward atomic level control of the epitaxial growth of WSe₂ monolayers in a scalable process that is suitable for large area device fabrication.

To pursue the scalable growth of “single crystal” TMDs, a defect-controlled approach for the nucleation and epitaxial growth of WSe₂ on hexagonal boron nitride (hBN) was investigated. The WSe₂ domains exhibit a preferred orientation of over 95% leading to a reduced density of IDBs upon coalescence. First-principles calculations and experimental studies as a function of growth conditions and substrate pre-treatment confirm that WSe₂ nucleation density and orientation are controlled by the hBN surface defect density rather than thermodynamic factors. Detailed TEM analysis provides support for the role of single-atom vacancies on the hBN surface which trap W atoms and break surface symmetry leading to a reduced formation energy for one orientation of WSe₂ domains. Through careful control of nucleation and extended lateral growth time,

fully coalesced WSe₂ monolayer films on hBN were achieved. Low temperature photoluminescence (PL) measurements and transport measurements of backgated field effect transistor (FET) devices fabricated on WSe₂/hBN films show improved optical and electrical properties compared to films grown on sapphire under similar conditions. These results reveal an important nucleation mechanism for epitaxial growth of van der Waals (vdW) heterostructures and demonstrate hBN as a superior substrate for single crystal transition metal dichalcogenide (TMD) films.

The final chapter of the dissertation demonstrates the initial attempts at low-temperature ($T < 450^{\circ}\text{C}$) MOCVD growth of WSe₂ for 2D materials and the properties of field effect transistors (FETs) fabricated using these layers. However, the FET mobility was found to be low ($\sim 0.01 \text{ cm}^2/\text{Vs}$) due to the nanocrystalline nature of the film obtained at low growth temperature. In comparison, the MOCVD growth of group IIIA MCs, β -In₂Se₃ thin films shows the potentials as an alternative low temperature material for 2D FETs. The growth of β -In₂Se₃ thin films on various substrates at 400°C using trimethylindium (TMIn) and H₂Se in a H₂ carrier gas was investigated. The β -In₂Se₃ films were identified by Raman spectroscopy and their epitaxial relationship with both sapphire and Si (111) substrates were confirmed by XRD technique. Top-gated thin film transistors (TFTs) fabricated on β -In₂Se₃ thin films exhibited higher mobility ($\sim 1 \text{ cm}^2/\text{Vs}$) and promising current on/off ratio. The results demonstrate the potential of group IIIA MCs for silicon BEOL-compatible process integration and extend the potential of 2D materials into low-temperature electronic, optoelectronic, and ferroelectric applications.

TABLE OF CONTENTS

LIST OF FIGURES	x
LIST OF TABLES	xix
ACKNOWLEDGEMENTS	xx
Chapter 1 Introduction	1
1.1 Why 2D Layered Chalcogenides?	1
1.2 Synthesis Development of 2D Layered Chalcogenides	3
1.3 Dissertation Outline and Published Work	5
1.4 References	9
Chapter 2 CVD System Setup and Characterization Techniques	20
2.1 Introduction	20
2.2 System Configuration	21
2.2.1 Gas panel	21
2.2.2 Reactor design	24
2.2.3 Reactor pressure	25
2.2.4 Vapor pressure and flow rate from a bubbler	26
2.3 Computational Modelling	27
2.4 Substrate Preparation	30
2.5 Etch-free Transfer of 2D TMD films	31
2.6 Characterization Techniques of 2D TMD films	34
2.6.1 Atomic force microscopy	34
2.6.2 Raman and photoluminescence spectroscopy	36
2.6.3 In-plane X-ray diffraction	38
2.6.4 Transmission electron microscopy	39
2.7 References	41
Chapter 3 Influence of Carbon and Precursor Consideration in the Growth of WSe ₂	46
3.1 Introduction	46
3.2 Experimental Details	48
3.2.1 MOCVD growth conditions	48
3.2.2 Post-growth characterization setup	49
3.3 Chalcogen Precursor: DMSe	50
3.3.1 Effect of Se:W ratio and high DMSe flow rate	50
3.3.2 Discovery of defective graphene layer	53
3.3.3 Origin of defective graphene layer	56
3.4 Chalcogen Precursor: H ₂ Se	58
3.4.1 Elimination of carbon	58
3.4.2 Fully coalesced WSe ₂ film	59
3.4.3 Toxicity and safety	62
3.5 Conclusions	62

3.6 References.....	64
Chapter 4 Diffusion-Controlled Epitaxial Growth of WSe ₂ on Sapphire.....	67
4.1 Introduction.....	67
4.2 Experimental Details	69
4.2.1 Gas source CVD growth conditions	69
4.2.2 Film characterization setup.....	70
4.3 Single-Step Growth	71
4.4 Multi-Step Growth.....	73
4.5 Nucleation.....	75
4.5.1 Initial nucleation clusters.....	75
4.5.2 Density of initial WSe ₂ islands.....	76
4.6 Ripening.....	78
4.6.1 Post-growth characterization	78
4.6.2 Ripening and surface diffusion.....	79
4.6.3 Derivation of surface diffusion coefficient.....	80
4.7 Lateral Growth.....	82
4.7.1 Coalesced monolayer film	82
4.7.2 Preferential orientation	84
4.7.3 Substrate temperature effect	86
4.8 Structural Characterization	89
4.8.1 RHEED	89
4.8.1.1 <i>In-plane lattice constant of WSe₂ layer</i>	89
4.8.1.2 <i>Reciprocal space structure of WSe₂ and its epitaxial relationship with sapphire</i>	90
4.8.2 In-plane XRD	92
4.8.3 High Resolution STEM	93
4.9 Conclusions.....	95
4.10 References.....	96
Chapter 5 Defect-Controlled Nucleation and Orientation of WSe ₂ on hBN	103
5.1 Introduction.....	103
5.2 Experimental Setup.....	106
5.2.1 Substrate preparation	106
5.2.2 WSe ₂ multi-step growth process	106
5.2.3 Plasma treatment	107
5.2.4 NH ₃ Annealing	107
5.2.5 Morphology characterization.....	107
5.2.6 TEM characterization	108
5.2.7 Photoluminescence measurement.....	108
5.2.8 Electrical measurement	109
5.2.9 First principles calculations	109
5.3 Preferential Domain Orientation.....	110
5.4 Defect-Controlled Nucleation.....	113

5.5 First-Principles Calculations.....	117
5.6 TEM Investigation	119
5.7 Controllable Nucleation via Defect Formation and Annealing	123
5.7.1 He plasma treatment	123
5.7.2 NH ₃ annealing	125
5.8 Coalesced Monolayer of WSe ₂ on hBN	129
5.8.1 Lateral growth of WSe ₂ domains	129
5.8.2 Epitaxial relationship between WSe ₂ and hBN	131
5.8.3 WSe ₂ /hBN vdW interface.....	132
5.9 Enhanced Optical and Transport Properties	133
5.9.1 Photoluminescence properties of coalesced WSe ₂	133
5.9.1.1 Room temperature PL and mappings.....	133
5.9.1.2 Low temperature PL.....	134
5.9.2 Transport properties of coalesced WSe ₂	138
5.10 Conclusions.....	142
5.11 References.....	144
Chapter 6 Low Temperature Growth of Layered Metal Chalcogenides via Metalorganic Chemical Vapor Deposition	156
6.1 Motivation.....	156
6.2 Low Temperature Growth of WSe ₂ Films	158
6.2.1 Growth condition.....	158
6.2.2 Device Fabrication.....	159
6.2.3 Film morphology	160
6.2.4 Device characterization	162
6.2.5 Summary.....	166
6.3 Epitaxial Growth of Layered β -In ₂ Se ₃ Thin Films	167
6.3.1 Introduction	167
6.3.2 Experimental setup	169
6.3.2.1 MOCVD growth conditions.....	169
6.3.2.2 Film characterization setup	169
6.3.3 Gas phase reaction.....	170
6.3.4 Temperature study	173
6.3.5 Se:In ratio study.....	174
6.3.6 Pulse growth	177
6.3.7 Substrate impact	179
6.3.8 Electrical characterization	182
6.3.9 Summary.....	183
6.4 References.....	184
Chapter 7 Summary and Future Work	191
7.1 References.....	196

LIST OF FIGURES

Figure 2-1. Schematic diagram of the gas panel of the CVD system	23
Figure 2-2. (a) Schematic plot of the cold-wall CVD reactor with inductive heater and (b) photo of the reactor when susceptor heated to 900 °C.....	25
Figure 2-3. (a) Schematic plot of the simplified CVD geometry and materials regarding the susceptor, growth chamber, and surrounding RF heating coils. (b)–(d) simulations of the cold-wall CVD reactor at 700 Torr and 500 sccm of H ₂ , where (b) and (c) show the gas streamlines and velocity profile and (d) shows the temperature profile for the susceptor and growth chamber. (e)–(g) Gas streamlines, gas velocity, and temperature profile at 100 Torr and 2000 sccm of H ₂	30
Figure 2-4. The schematic illustration of the etchant-free transfer method. (a) A 2D material film is grown on sapphire; (b) PMMA is Spin-coated on the film; (c) the film is scratched along the edge contours of the sapphire substrate using a blade; (d) The whole assembly is immersed into hot water (~80 °C) by a feeding angle ~ 45° for 5 to 10 minutes before the hydrophobic PMMA/2D film is delaminated from the sapphire substrate and floats on the water surface.....	33
Figure 2-5. Schematic representation of basic AFM modes: (a) Contact mode with tip-sample force as a feedback setpoint (F_{sp}); (b) Tapping or AC mode where the setpoint is oscillation amplitude (A_{sp}) or frequency (f_{sp}); (c) PeakForce Tapping mode where the tip is modulated at an off-resonance frequency and the feedback setpoint is the maximum force, or peak force, of each tapping cycle.....	35
Figure 2-6. (a) Bragg-Brentano measurement geometry. (b) and (c) In-plane measurement geometry from two perspectives. (Mikhail Chubarov, Penn State)	39
Figure 3-1. FESEM images of WSe ₂ domains grown on sapphire substrate using DMSe and W(CO) ₆ as precursors with Se:W ratios of (a) 800, (b) 1600, (c) 3200, (d) 4800. The (e) average domain size, (f) surface coverage and (g) domain thickness of the as-grown WSe ₂ at Se:W ratios from 800 to 8000.....	51
Figure 3-2. AFM images of WSe ₂ domains grown on sapphire substrate using DMSe and W(CO) ₆ as precursors with Se:W ratios of (a) 800, (b) 1600, (c) 3200, (d) 4800.	51

- Figure 3-3.** The (a) average domain size, (b) surface coverage and (c) domain thickness of the as-grown WSe₂ at Se:W ratios from 800 to 8000..... 52
- Figure 3-4.** (a) FESEM image of the WSe₂ sample grown at 800 °C with Se:W=3200 showing three regions: 1) sapphire surface; 2) WSe₂ triangular domains; 3) region of darker contrast between WSe₂ islands. (b) AFM image revealing a continuous layer ~1.5 nm thick and WSe₂ triangular domains ~6-9 nm thick on the sapphire surface. (c) AES spectra indicating the presence of Al and O in region 1, W, Se and C in region 2, and Al, O, and C in region 3. 54
- Figure 3-5.** Cross-sectional TEM image of WSe₂ sample grown using DMSe at 800 °C and Se:W=3200 revealing a carbon layer beneath the WSe₂. Some regions of the carbon layer exhibit a layered structure typical of defective graphene. 55
- Figure 3-6.** Cross-sectional TEM images of different regions on the WSe₂ sample grown using DMSe at 800 °C and Se:W=3200 showing different carbon layer thickness (a) ~1.2nm; (b) ~2.7nm; (c) ~5.5nm. 56
- Figure 3-7.** Sapphire surface after flowing only DMSe and H₂ at 800 °C under identical condition for WSe₂ growth: (a) FESEM image showing the presence of defective graphene domains; (b) Raman spectrum of sapphire surface showing G and 2D peaks associated with graphene and the family of D peaks indicating defects in the graphene. 57
- Figure 3-8.** Raman spectra of WSe₂ grown using (a) DMSe and (b) H₂Se at 800 °C and Se:W ratio of 3200. The insets are zoom-in regions showing the carbon D and G peaks in WSe₂ grown with DMSe but no carbon characteristic peaks in WSe₂ grown with H₂Se. 59
- Figure 3-9.** AFM images of WSe₂ grown using (a) DMSe and (b) H₂Se at 800 °C and Se:W ratio of 3200. 60
- Figure 3-10.** TEM image of the WSe₂ film grown using H₂Se at 800 °C and Se:W ratio of 3200, inset SAED pattern of the yellow circle showing two hexagonal diffraction patterns with 30° misorientation indicating epitaxial growth of WSe₂ on sapphire..... 61
- Figure 4-1.** FESEM image of WSe₂ domains grown at W(CO)₆ flow rate of 3.0×10^{-4} sccm, H₂Se flow rate of 7 sccm, 800 °C substrate temperature, and growth time of 90 min. 73
- Figure 4-2.** (a) Schematic diagram of the multi-step process showing variation in W(CO)₆ flow rate that was used to control nucleation, ripening and lateral growth. AFM images of WSe₂ grown on sapphire substrate (surface steps

- aligned horizontally) after **(b)** nucleation stage (inset shows the 5 times magnification of the surface, scale bar: 50 nm), **(c)** ripening stage, and **(d)** lateral growth stage..... 74
- Figure 4-3.** High-resolution XPS spectra of Se 3d and W 4f for samples (top) after the lateral growth to form a coalesced WSe₂ film and (bottom) immediately after the nucleation step when nanoscale clusters are present on the surface..... 76
- Figure 4-4.** **(a)** AFM images of WSe₂ grown on sapphire substrate under varied nucleation times of 30 sec, 1 min, and, 2 min, and ripening time of 10 min. **(b)** Sample surface coverage as a function of nucleation time. **(c)** WSe₂ domain density as a function of nucleation time showing an $\sim 12/(\mu\text{m}^2 \cdot \text{min})$ nucleation rate..... 77
- Figure 4-5.** **(a)** AFM images of WSe₂ grown on sapphire substrate under 30 sec nucleation time and varied ripening time for 7.5, 15, and 30 min. **(b)** WSe₂ domain size as a function of ripening time and cubic root of ripening time (inset). **(c)** Cluster density as a function of ripening time and reciprocal of ripening time (inset). **(d)** Substrate surface coverage as a function of ripening time. 78
- Figure 4-6.** **(a)** Schematic plot showing the method to estimate diffusivity. The average distance between clusters $L_{av} = \sqrt{(1/N)}$, where N is the cluster density. Assume the size of the cluster is small to be neglected, the estimated mean cluster displacement $L_D \approx 1/2L_{av}$. **(b)** The reciprocal of cluster density as a function of ripening time showing a linear relationship in the first 10 min with a slope of $2 \times 10^{-3} \mu\text{m}^2/\text{min}$, from which the diffusivity can be derived as $1.2 \times 10^{-14} \text{ cm}^2/\text{s}$ 81
- Figure 4-7.** **(a)** SEM images of WSe₂ grown on sapphire substrate under 30 sec nucleation time, 15 min ripening time and varied lateral growth time for 5 min, 20 min, 30 min, and 45 min. **(b)** WSe₂ monolayer domain size and surface coverage as a function of lateral growth time and bilayer surface coverage as a function of lateral growth time. A fully coalesced monolayer WSe₂ film is achieved in ~ 45 min lateral growth. **(c)** Orientation histogram from 10 min and 20 min samples confirms that WSe₂ domain edges are primarily oriented at 0° and 60° with respect to steps on sapphire. **(d)** Schematic illustrating 0° and 60° oriented WSe₂ domains on sapphire (0001) surface..... 83
- Figure 4-8.** **(a)** Raman spectrum of coalesced monolayer WSe₂ film. **(b)** PL spectra of different regions on monolayer WSe₂ film showing the optical band gap energy varies 1.60-1.64 eV. **(c)** 5 $\mu\text{m} \times 5 \mu\text{m}$ Raman intensity map at

- 310 cm^{-1} showing most of region across the film is monolayer. **(d)** 5 $\mu\text{m} \times 5 \mu\text{m}$ PL peak position map illustrating the uniformity of PL spectra across the film..... 85
- Figure 4-9.** **(a)** SEM images of WSe₂ grown on sapphire substrate under 30 sec of nucleation, 15 min of ripening, and 10 min of lateral growth at varied substrate temperatures of 600 °C, 700 °C, 800 °C, and 900 °C. H₂Se flow rate was held constant at 7 sccm and Se:W ratio was ~26000 during the lateral growth stage. Inset SEM images show the shape of the WSe₂ domains. **(b)** WSe₂ domain size and domain density as a function of substrate temperature. **(c)** Schematic diagram showing the variation of WSe₂ domain shape under different surface Se:W ratios. **(d)** SEM image of WSe₂ grown under 30 sec of nucleation, 15 min of ripening, and 10 min of lateral growth at substrate temperature of 900 °C. H₂Se flow rate was increased to 10 sccm and Se:W ratio was ~37000 during the lateral growth stage. Inset SEM image shows the shape of WSe₂ domain..... 87
- Figure 4-10.** RHEED patterns of WSe₂ collected from 20 keV incident electrons scattered from two azimuthal angles about 30° apart, **(a)** $\phi = 239.0^\circ$ and **(b)** $\phi = 269.6^\circ$. **(c)** Integrated intensity from the yellow dashed box plotted in parallel momentum transfer k_{\parallel} direction in (a). **(d)** Integrated intensity from the yellow dashed box plotted in parallel momentum transfer k_{\parallel} direction in (b)..... 90
- Figure 4-11.** **(a)** Experimentally constructed RHEED 2D reciprocal space structure of WSe₂ plotted as the intensity (k_{\parallel}) vs. 360° azimuthal directions from 100 RHEED patterns recorded when the sample was rotated azimuthally with a 1.8° step size from 0° to 180° in 100 steps. **(b)** Theoretical simulation of 2D reciprocal space structure of WSe₂ looking along the out-of-plane [0001] direction which matches the experimental result in (a), showing $[10\bar{1}0]$ WSe₂ \parallel $[10\bar{1}0]$ α -Al₂O₃. 91
- Figure 4-12.** **(a)** θ -2 θ X-ray diffractogram recorded at $\phi=30^\circ$ showing reflections which correspond to $(11\bar{2}0)$ of WSe₂ and α -Al₂O₃. **(b)** ϕ -scan recorded at $2\theta = 37.91^\circ$ showing $[11\bar{2}0]$ WSe₂ \parallel $[11\bar{2}0]$ α -Al₂O₃. 92
- Figure 4-13.** **(a)** Low-magnification TEM image of coalesced WSe₂ showing single layer structure and sequent layers and the corresponding SAED pattern (inset). **(b)** Atomic resolution HAADF-STEM image showing the existence of anti-phase grain boundaries in the film. **(c)** Higher resolution HAADF-STEM image showing 4|8 rings attributed to the coalescence of 0° and 60° WSe₂ domains. 94
- Figure 5-1.** **(a)** AFM image of epitaxial WSe₂ domains on hBN. **(b)** Orientation histogram of 0° and 180° oriented WSe₂ domains on hBN. **(c)** ADF-STEM

image of region with two types of merging domains. **(d)** HAADF-STEM image (top) and corresponding inverse FFT image (bottom) of region A in (c) showing no grain boundary formed between two domains with same orientation. **(e)** HAADF-STEM image (top) and corresponding inverse FFT image (bottom) of region B in (c) showing inversion domain boundary formed between two domains with 0° and 180° orientation. 112

Figure 5-2. HAADF-STEM image of WSe₂ on BN, the anti-phase grain boundary between the 0° and 60° domains contains 4|8 rings highlighted in the image. It is noted that a slight sample tilt and high contrast are applied in the imaging condition to blur the information of underlying BN and the corresponding Moiré patterns between WSe₂ and BN, which help identify the WSe₂ lattice. ... 113

Figure 5-3. **(a)** SEM images of WSe₂ grown on hBN (left) and sapphire (right) respectively under varied nucleation time of 30 s, 1 min, and 2 min and same 10 min ripening and growth time. Scale bar: 1 μm . **(b)** Domain density histogram versus nucleation time showing the nucleation on hBN is not controlled by the amount of precursors on the surface. 115

Figure 5-4. Color-marked SEM images of WSe₂ grown on hBN with a preferred orientation shown in Figure 2a. Scale bar: 1 μm 115

Figure 5-5. WSe₂ grown on pristine hBN surface under 30 s nucleation and 10 min ripening showing a non-uniform distribution of WSe₂ domains. 116

Figure 5-6. **(a)** Equilibrium defect concentration for a point defect with formation energies between 1.5 and 2 eV, as a function of temperature: a defect needs to have a formation energy in this range to achieve concentrations on the order of μm^{-2} at 800 $^\circ\text{C}$. **(b)** Defect formation energy for N and B vacancies under N-rich and N-poor conditions, considering bare vacancies (solid) and hydrogen-passivated ones (dashed). The orange energy range marks the calculated WSe₂ bandgap aligned with that of hBN. 119

Figure 5-7. **(a)** Top and side view of the relaxed DFT structure of a W interstitial atom (red) sandwiched between pristine WSe₂ and a boron vacancy in hBN. **(b)** HRTEM images of monolayer to multilayer pristine hBN at 80 kV with a monochromated electron source; the intrinsic vacancies in BN is mostly V_N on the surface, which is also shown at the other side of the step edge. **(c)** HAADF-STEM image of a single W atom trapped at hBN surface after seeding process (30 s of W(CO)₆ flow at 800 $^\circ\text{C}$), the overlay on the plot is the corresponding imaging intensity near the single W atom. **(d)** HAADF-STEM image of a brighter imaged defect indicating the glue W atom between WSe₂ and the underlying BN (red, top right). The WSe₂ domain also has inevitably formed defects such as V_{Se} and V_{Se_2} (green, bottom right). **(e)** The migration barrier of a W adatom on a WSe₂ surface between the ground state

at the (Metal) site and the metastable state at the (Hollow) site is 0.4 eV from a nudged elastic band calculation.	122
Figure 5-8. SEM images from left to right showing WSe ₂ grown on pristine hBN, hBN treated by 1 s He plasma at 50 W, and hBN treated by 15 s He plasma at 50W respectively.	124
Figure 5-9. HAADF-STEM image of W and Se atoms trapped at hBN surface after growth process (with 5 s He plasma treated BN substrate), the overlay plots are the corresponding imaging intensity near the single W (blue) and Se (orange) atoms; respectively.	124
Figure 5-10. WSe ₂ grown on 5 s He plasma treated hBN surface under 30 s nucleation and 10 min ripening showing that the distribution of WSe ₂ domains on hBN becomes more uniform.	125
Figure 5-11. SEM images from left to right showing WSe ₂ grown on hBN annealed in NH ₃ at 1100 °C for 30 min, hBN first treated by 1 s He plasma at 50 W then annealed in NH ₃ at 1100 °C for 30 min, and hBN first treated by 5 s He plasma at 50W then annealed in NH ₃ at 1100 °C for 30 min respectively...	127
Figure 5-12. (a) Measured percentage of major domain orientation of WSe ₂ domains grown on hBN surfaces under different treatment. (b) Measured nucleation density of WSe ₂ domains grown on hBN surfaces under different treatment.	127
Figure 5-13. Room temperature PL spectrum of WSe ₂ / hBN sample annealed in NH ₃ at 1100 °C for 30 min in the region where emission from N antisite defects is expected.	128
Figure 5-14. (a) WSe ₂ monolayer domain area on hBN as a function of lateral growth time. The slope shows a linear growth rate of $7.5 \times 10^3 \text{ nm}^2/\text{min}$. (b) WSe ₂ monolayer coverage on hBN as a function of lateral growth time. The slope shows a linear growth rate of 0.58 %/min. (c) SEM image of coalesced monolayer WSe ₂ film on hBN. (d) AFM images of WSe ₂ grown on NH ₃ annealed hBN surfaces under 30 s nucleation time, 10 min ripening time and varied lateral growth time for 15, 30, and 60 min. The results show the increasing WSe ₂ domain size with lateral growth time without any additional nucleation.....	130
Figure 5-15. (a) Atomic resolution HAADF-STEM image showing the Moiré pattern of WSe ₂ on hBN. (b) SAED pattern showing the epitaxial relationship between WSe ₂ and hBN. (c) Schematic illustrating 3×3 WSe ₂ unit cells on 4×4 hBN.....	131

- Figure 5-16. (a)** Cross-sectional HRTEM image of the WSe₂ film on hBN showing a clear WSe₂ and hBN interface. **(b)** Intensity profile of the red dot line in (e) showing the interlayer spacing of hBN-hBN, hBN-WSe₂, and WSe₂-WSe₂ are 0.33 nm, 0.49 nm, and 0.67 nm respectively. 133
- Figure 5-17. (a)** PL spectra showing an over 50 × enhancement in intensity for WSe₂/hBN compared to WSe₂/sapphire. **(b)** 5 μm × 5 μm PL maps of coalesced WSe₂/hBN showing a uniform PL peak position at 1.65 eV (top) compared to varied peak positions ranging from 1.58-1.64 eV for coalesced WSe₂/sapphire (bottom)..... 134
- Figure 5-18. (a)-(b)** Temperature-dependent PL spectra of WSe₂/hBN and WSe₂/sapphire under 488 nm laser excitation, respectively. The measured temperature ranges for both samples are from 80 K to 300 K. **(c)-(d)** Plots of fitted PL emission peak energy of WSe₂/hBN and WSe₂/sapphire versus temperature, respectively. 137
- Figure 5-19.** Deconvoluted PL spectra of WSe₂/hBN and WSe₂/sapphire at 80 K. The deconvoluted spectra were acquired by performing multipeak Lorentzian fitting using three peak components: neutral exciton (X⁰), trion (X⁻) and defect-bound exciton (X^B). 138
- Figure 5-20.** Electrical FET characterization of transferred WSe₂ and transferred WSe₂/hBN on SiO₂/p⁺⁺ Si. Schematic showing a back gated WSe₂ FETs (a) directly on 100 nm SiO₂ and (d) on 10 nm hBN on 100 nm SiO₂ on p⁺⁺ Si with Ni contacts. (b,e) Drain current (I_{DS}) versus back gate voltage (V_{BG}) at various drain voltages (V_{DS}) with step of 0.2 V and (c,f) I_{DS} versus V_{DS} at various V_{BG} with step of 2.5 V for WSe₂ on SiO₂ and on hBN/SiO₂, respectively. 140
- Figure 5-21.** Mobility extraction for WSe₂ on SiO₂ and hBN/SiO₂. (a,b) The field effect mobility (μ_{FE}) versus V_{BG} at V_{DS} = 1.8 V and V_{DS} = -1.8 V for WSe₂ on SiO₂ and on hBN/SiO₂, respectively. The mobility is derived from the peak transconductance method where $\mu_{FE} = \frac{\partial I_{DS}}{\partial V_{GS}} \frac{L_{CH}}{C_G W V_{DS}}$. For WSe₂ on SiO₂, the mobility (μ_{FE} ≈ 0.2 cm²/V-s) is extracted from the reverse sweep direction (negative to positive V_{BG}) since interface trap discharging obscures the forward sweep characteristics. For WSe₂ on hBN/SiO₂, the large contact resistance causes the extracted μ_{FE} to decrease when V_{BG} < -43 V. Hence, the peak mobility of 4.2 cm²/V-s is contact limited, underestimating the true hole mobility of the material. 141
- Figure 6-1. (a)** SEM image of continuous WSe₂ thin film on SiO₂/Si substrate. **(b)** Raman spectrum of ~3 nm WSe₂ thin film. **(c)** AFM image of 3 nm thick WSe₂ thin film. **(d)** WSe₂ film thickness as function of growth time. 161

- Figure 6-2.** (a) Cross-section and (b) optical microscopic image of a double gate WSe₂ TFT. (c) Array of WSe₂ TFTs. 163
- Figure 6-3.** I_D-V_{DS} characteristics of WSe₂ TFTs using as-grown film. (a) Top gate TFT with 6 nm thick channel and (b) bottom gate TFT with 3 nm thick channel. 163
- Figure 6-4.** (a) I_D-V_{DS} and (b) I_D-V_G characteristics of WSe₂ TFTs using 3 nm thick RIE thinned film. 164
- Figure 6-5.** (a) Total resistance extracted from I_D-V_{DS} characteristics of TFTs with RIE etched 3 nm thick WSe₂ channel for different channel length (with channel width fixed at 200 μm) and gate voltage (V_{DS} = 0.4 V). (b) Contact resistance and sheet resistance of channel for V_G = -10 V and -20 V. 166
- Figure 6-6.** In-Se phase diagram. 172
- Figure 6-7.** Significant coating on the reactor wall after a few runs at high pressure and low gas velocity due to the strong gas phase reaction between precursors. 172
- Figure 6-8.** FESEM images (left) and Raman spectra (right) of β-In₂Se₃ films grown on c-plane sapphire at (a) 350 °C; (b) 400 °C; (c) 450 °C; (d) 500 °C. The flow rate for TMIn is 7.7×10⁻² sccm; for H₂Se is 7 sccm. 174
- Figure 6-9.** AFM images of β-In₂Se₃ films grown at different H₂Se flow rate (a) 2 sccm and (b) 4 sccm with a pulse flow of TMIn flow rate at 1.5×10⁻² sccm every 30 s on/off for 30 min at 400 °C. (c) φ-scan recorded at 2θ = 37.91° of sample in (b) showing [11 $\bar{2}$ 0] β-In₂Se₃ || [11 $\bar{2}$ 0] α-Al₂O₃. (d) Cross-sectional TEM image of β-In₂Se₃ sample in (b) showing layered structure of the film and clean interface with sapphire substrate. EDS spectra of (e) In and (f) Se in corresponding region in (d) showing a Se:In ratio of 3:2. 176
- Figure 6-10.** AFM images of β-In₂Se₃ films grown at different H₂Se flow rate (a) 2 sccm and (b) 4 sccm with a pulse flow of TMIn flow rate at 1.5×10⁻² sccm every 30 s on/off for 30 min at 400 °C. (c) φ-scan recorded at 2θ = 37.91° of sample in (b) showing [11 $\bar{2}$ 0] β-In₂Se₃ || [11 $\bar{2}$ 0] α-Al₂O₃. (d) Cross-sectional TEM image of β-In₂Se₃ sample in (b) showing clear layered structure of the film and clean interface with sapphire substrate. EDS spectra of (e) In and (f) Se in corresponding region in (d) showing a Se:In ratio of 3:2. 179
- Figure 6-11.** (a) FESEM image and (b) AFM image of β-In₂Se₃ film grown on Si (111) substrate. (c) Raman spectrum of β-In₂Se₃ film grown on Si (111) confirming the only existence of β phase. (d) θ-2θ X-ray diffractogram showing the β-In₂Se₃ film is epitaxial with Si (111) in c-axis. Pole figures of

(e) β - In_2Se_3 film along (1 0 10) and (f) Si substrate along (2 0 2) showing the in-plane epitaxy between film and substrate.	181
Figure 6-12. (a) FESEM image and (b) Raman spectrum of γ - In_2Se_3 film grown on 300 nm amorphous SiO_2/Si substrate.	181
Figure 6-13. (a) schematic of top gate beta-phase In_2Se_3 thin film transistors (TFTs), (b) $\log(I_D)$ - V_{GS} for $V_{DS} = 1$ and 8V, (c) I_D - V_{DS} characteristics for V_{GS} from 0 to 8V (step: 1V), (d) linear (I_D) - V_{GS} with linear field effect mobility for $V_{DS} = 1$ V ($W:L = 200 \mu\text{m}: 5 \mu\text{m}$).	183

LIST OF TABLES

Table 6-1. Melting temperatures and bulk bandgap energies of selected layered chalcogenides.....	158
---	-----

ACKNOWLEDGEMENTS

Back to year 2010 when I first stepped onto the land of the United States and started my college life at Penn State, I never expected that I would fall in love with this small town named *State College* and stay there for the whole nine years through my Bachelor to Ph.D. life. I always believe in science and trust it as the way to understand, explain, and explore the world. Becoming a scientist is a significant part of my lifetime dream and I really appreciate my advisor Joan Redwing who accepted me into the group even when I was only a senior undergraduate and started my journey in science ever since then. I would like to thank her not just for her guidance and support in research, but most importantly, for her mentorship in which freedom, logic, and courage accompany my path towards the truth. I always received the maximum degree of freedom from her for my own ideas as well as enough support and encouragement as a push towards the right direction. I really enjoy this style and revere her altitude in both research and life.

I would also like to extend my gratitude to my committee members, Prof. Joshua Robinson, Prof. Thomas Jackson, and Prof. Susan Sinnott for their support in both experimental and theoretical aspects. In particular, I would like to point out my gratitude for all the knowledge of 2D materials from Prof. Joshua Robinson and numerous but very useful ideas and knowledge from Prof. Thomas Jackson. I would also like to express my appreciation to all my great lab mates from the research group (Dr. Tanushree Choudhury, Dr. Mikhail Chubarov, Anushka Bansal, Azimkhan Kozhakhmetov, Dr. Zakaria Al Balushi, Dr. Sarah Eichfeld, and more) for their help and support in both mental and physical way and Fu Zhang for his fantastic work in film transfer and

microscopy. I never forget to acknowledge the financial support from the Dow Chemical Company and the National Science Foundation through EFRI 2-DARE Grant EFRI-1433378 and through the Penn State 2D Crystal Consortium – Materials Innovation Platform (2DCC-MIP) under NSF cooperative agreement DMR-1539916.

In the end, I want to say *thank you* to my parents Jiao Zhang and Aihua Yuan. They never show up in any of my work or contribution, but it is really them who make me stand as who I am.

The achievement stayed in the past, but the discovery leads to the future.

Chapter 1

Introduction

1.1 Why 2D Layered Chalcogenides?

Since the discovery of graphene, 2-dimensional layered chalcogenides (2DLCs) including transition metal dichalcogenides (TMDs) and recent group IIIA-VA metal chalcogenides (MCs) have been intensively studied due to their intriguing and novel electronic, and optoelectronic properties such as direct-to-indirect bandgap transition,¹ large exciton binding energies,^{2,3} interlayer exciton coupling,⁴⁻⁶ spin-valley polarization,⁷ and single photon emission^{8,9}. This opens up the possibility of using monolayer and multilayer 2DLCs for next generation electronics, photonics, optoelectronics,^{10,11} valleytronics,^{12,13} and quantum communication.¹⁴

The lack of dangling bonds on the surface of 2DLCs make the monolayers stable against the environment influence and preserve the properties of crystals. Furthermore, the significant reduction in film thickness down to few-atom size leads to strong anisotropic features and quantum confinement in the monolayers.^{15,16} This brings out new physical properties such as large exciton binding energy, which is crucial to optoelectronic applications including such as sensitive photodetectors and optical devices where narrow spectrum is highly desired.¹⁷ In addition, the recent observation of single photon emitters with narrow linewidth and long lifetime in TMDs such as WSe₂¹⁸ and MoSe₂¹⁹ enables their further studies in quantum optics and potential applications in quantum communication and nanosensors. Like other single photon emitters, the defects/impurities

and the strain in the films are likely the cause of the single photon emission in TMDs.²⁰ Considering the large surface area and atomically thin structures, TMDs have the advantage in defect and strain engineering, which offers a controllable way to intentionally introduce single quantum emissions in TMDs.

Another unique aspect in monolayer 2DLCs is the lack of inversion symmetry in monolayer structure. This leads to a spin-orbit driven splitting of the valence band where charge carriers in TMDs exhibit a “valley” degree of freedom.^{21–23} The two valleys can be optically or/and magnetically controlled using circularly polarized light due to valley Hall effect and valley Zeeman effect.^{17,24} Together with a large spin-orbit interaction and strong light-matter interactions, this opens up the new exploration of valley physics and possibilities for valley-based electronics (also called as “valleytronics”).¹⁷ Moreover, the strong spin-orbit coupling from the transition metal elements gives rise to an effective interaction between the valley pseudospin and the spin, making possible the interplay between these two degrees of freedom, and allowing spin manipulations via the valley phenomena.^{25,26}

Benefitting from the van der Waals (vdW) bonding out of plane, heterostructures of various 2DLCs are also possible, without conventional limitations such as lattice mismatch and symmetric alignment. The vdW heterostructure includes the stackings of multiple monolayers of 2DLCs as well as vertical stackings of monolayers at a twist angle, where new physics such as interlayer exciton coupling^{4–6} and unconventional superconductivity^{27,28} have been explored. Considering further possibility of tuning the properties such as introducing strain and electrostatic gating, monolayer 2DLCs hold great

potential both as a platform for fundamental physics and future nanoscale device applications.

1.2 Synthesis Development of 2D Layered Chalcogenides

In the early stage of studies, most of monolayer and few-layer 2DLCs were obtained from mechanical or chemical exfoliation from single crystal bulk crystals. However, the limited efficiency as well as the lack of both scalability and thickness control hamper the rapid development of device technologies based on 2DLCs and their heterostructures, which presents increasing demand for synthesis of wafer-scale high quality single crystal monolayer and few layer films. The discovery of powder vapor transport (PVT) (also referred to as powder source chemical vapor deposition (CVD)) in 2DLCs offers the way to prepare large single crystal TMD domains due to the straightforward equipment requirements and high chalcogen gas phase concentrations resulting from evaporation, and therefore it has been widely used in more recent research.^{29–31} However, due to the limited controllability of source supply during the process, PVT of 2DLCs often have difficulty in achieving uniform films across large substrate areas as well as the growth of heterostructures.

Due to these limitations, additional efforts have focused on other methods such as gas source CVD/metalorganic CVD (MOCVD) and molecular beam epitaxy (MBE), where precursors are located outside the reaction chamber and their flow rates can be precisely and independently controlled. Epitaxial 2DLC films have been grown on CaF_2 , GaAs, epitaxial graphene and sapphire substrates by molecular beam epitaxy (MBE)^{32–39} but

domain sizes are typically smaller than films grown by PVT or CVD. As a result, recent efforts have focused on the development of gas source CVD methods such as metalorganic CVD (MOCVD) for 2DLCs which offers process flexibility and scalability.^{40,41}

Initial studies before the discovery of graphene already demonstrated the CVD and MOCVD growth of layered TMD films such as MoS₂ and WSe₂, hundreds of nanometers thick, using a variety of metal precursors (W(CO)₆, Mo(CO)₆, MoCl₅, WCl₆, etc.) and chalcogen sources (H₂S, HSC(CH₃)₃, diethyl selenide, etc.).^{42–46} Lubricant and catalytic applications were mostly considered in these studies and precise control of film thickness and film crystallinity was not the focus. After the concept of 2D materials, efforts have focused on adapting these to prepare large area, coalesced polycrystalline TMD monolayer and few-layer films on a variety of substrates.^{40,47–50}

The crystallinity is one major concern in 2DLCs and can significantly impact the properties. To reduce the prevalence of random orientations and high-angle grain boundaries, epitaxial growth of TMD and MC domains or films has been investigated on various single crystal substrates such as epitaxial graphene,^{41,51–53} hexagonal boron nitride (hBN),^{54,55} Au (111),³¹ GaSe,⁵⁶ and c-plane sapphire.⁵⁷ However, even oriented domains can be obtained by selecting the right substrates, inversion domain boundaries (IDBs) (also referred to as mirror twin grain boundaries) were still observed in these films resulting from a merging of a mixture of 0° and 180° oriented domains.^{53,55,58,59} IDBs have been predicted and experimentally demonstrated to exhibit metallic character and consequently can serve as conducting channels within the monolayer that negatively impact both electrical and optical properties.^{60–63} In addition, non-uniformities in the optical and transport properties of these TMD films arise from steps and surface dangling bonds at the interface between

the 2D film and 3D substrate.^{58,64,65} All of these factors negatively impact the properties of coalesced monolayer films and also promote undesirable multilayer growth. In this case, additional effort has been focused on single preferred orientation of 2DLCs and recent first-principles calculations proposed that the orientation selectivity can originate from defects on the hBN surface that act as nucleation sites and break the nearly degenerate 0/180° domain orientations.⁶⁶

1.3 Dissertation Outline and Published Work

This dissertation focuses on a comprehensive study of gas source CVD/MOCVD growth of 2DLCs. There are two main discussions: Chapter 3-5 includes the discussion high-temperature growth of monolayer WSe₂ towards single crystal; Chapter 6 discusses the growth of WSe₂ and epitaxial growth of β -In₂Se₃ at low temperature. The outline of each chapter and published work are listed as follow:

Chapter 2 presents detailed setup of the gas source chemical vapor deposition system and discusses results from computational fluid dynamic modelling in terms of system design. A brief introduction to film transfer and characterization techniques for 2D materials is also presented.

Published work from Chapter 2:

Briggs, N., Subramanian, S., Lin, Z., Li, X., **Zhang, X.**, Zhang, K., Xiao, K., Geohegan, D.B., Wallace, R., Chen, L., Terrones, M., Ebrahimi, A., Das, S., Redwing, J.M., Hinkle, C., Momeni, K., van Duin, A., Crespi, V., Kar, S., Robinson, J.A. "A Roadmap for Electronic Grade 2-Dimensional Materials" *2D Materials* **2019** 6 (2), 022001

Zhang, F., Erb, C., Runkle, L., **Zhang, X.**, Alem, N., “Etchant-free transfer of 2D nanostructures” *Nanotechnology* **2017**, 29 (2), 025602

Chubarov, M., Choudhury, T.H., **Zhang, X.**, Redwing, J.M. “In-plane x-ray diffraction for characterization of monolayer and few-layer transition metal dichalcogenide films” *Nanotechnology* **2018** 29 (5), 055706

Chapter 3 discusses the unintentional carbon incorporation in 2D films when using metalorganic chalcogen precursor. The chapter also presents the benefit of using hydride chalcogen precursor in terms of removing carbon contamination and achieving coalesced films.

Published work from Chapter 3:

Zhang, X., Balushi, Z.Y., Zhang, F., Choudhury, T.H., Eichfeld, S.M., Alem, N., Jackson, T. N., Robinson, J.A., Redwing, J.M. “Influence of Carbon in Metalorganic Chemical Vapor Deposition of Few-Layer WSe₂ Thin Films” *Journal of Electronic Materials* **2016** 45 (12), 6273-6279

Chapter 4 demonstrates A multi-step diffusion-mediated process was developed to control the nucleation density, size and lateral growth rate of WSe₂ domains on c-plane sapphire for the epitaxial growth of large area monolayer films by gas source chemical vapor deposition. This chapter also provides fundamental insights into the 2D growth mechanism including an estimate of the tungsten-species surface diffusivity in a 2D ripening process; a mass transport limited process over the range of 700-900 °C; and the evolution of domain shape due to local variations in the Se:W adatom ratio. The results provide an important step toward atomic level control of the epitaxial growth of WSe₂ monolayers in a scalable process that is suitable for large area device fabrication.

Published work from Chapter 4:

Zhang, X., Choudhury, T.H., Chubarov, M., Xiang, Y., Jariwala, B., Zhang, F., Alem, N., Wang, G.C., Robinson, J.A., Redwing, J.M. “Diffusion-Controlled Epitaxy of Large Area Coalesced WSe₂ Monolayers on Sapphire” *Nano letters* **2018** 18 (2), 1049-1056

Lin, Y.C., Jariwala, B., Bersch, B.M. Xu, K., Nie, Y., Wang, B., Eichfeld, S.M., **Zhang, X.**, Choudhury, T.H., Pan, Y., Addou, Rafik., Smyth, C.M., Li, J., Zhang, K., Haque, A., Fölsch, S., Feenstra, R.M., Wallace, R.M., Cho, K., Fullerton-Shirey, S.K., Redwing, J.M., Robinson, J.A. “Realizing Large-Scale, Electronic-Grade Two-Dimensional Semiconductors” *ACS Nano* **2018** 12 (2), 965-975

Chapter 5 demonstrates A defect-controlled approach for the nucleation and epitaxial growth of WSe₂ on hBN. The WSe₂ domains exhibit a preferred orientation of over 95% leading to a reduced density of inversion domain boundaries upon coalescence. This chapter presents both first-principles calculations and experimental studies including comprehensive transmission electron microscopy analysis that confirm WSe₂ nucleation density and orientation are controlled by the hBN surface single-atom vacancies on the hBN surface which trap W atoms and break surface symmetry leading to a reduced formation energy for one orientation of WSe₂ domains. Both low temperature photoluminescence (PL) measurements and transport measurements of backgated field effect transistor (FET) devices fabricated on fully coalesced WSe₂ monolayer films on hBN show improved optical and electrical properties. The whole chapter reveals an important nucleation mechanism for epitaxial growth of van der Waals (vdW) heterostructures and demonstrates hBN as a superior substrate for single crystal transition metal dichalcogenide (TMD) films.

Published work from Chapter 5:

Zhang, X., Zhang, F., Wang, Y., Schulman, D.S., Zhang, T., Bansal, A., Alem, N., Das, S., Crespi, V.H., Terrones, M., Redwing, J.M. “Defect-Controlled Nucleation and Orientation of WSe₂ on hBN – A Route to Single Crystal Epitaxial Monolayers” *ACS Nano* **2019**, 13 (3), pp 3341–3352.

Chapter 6 discusses the low temperature growth of transition metal dichalcogenide WSe₂ and group III metal chalcogenide β -In₂Se₃ by metalorganic chemical vapor deposition. The thin film transistors using the low-temperature WSe₂ thin films shows limited transport properties due to the nanocrystallinity of the film. In comparison, the β -In₂Se₃ films grown on both c-plane sapphire and Si (111) present good crystallinity and epitaxial relation with substrates. The thin film transistors based on β -In₂Se₃ films demonstrates reasonable transport properties and potential applications in optoelectronics and ferroelectronics.

Published work from Chapter 6:

Gong, Y., **Zhang, X.**, Redwing, J.M., Jackson, T.N. “Thin Film Transistors Using Wafer-Scale Low-Temperature MOCVD WSe₂” *Journal of Electronic Materials* **2016**, 45 (12), 6280-6284

1.4 References

- (1) Mak, K. F.; Lee, C.; Hone, J.; Shan, J.; Heinz, T. F. Atomically Thin MoS₂: A New Direct-Gap Semiconductor. *Phys. Rev. Lett.* **2010**, *105* (13), 136805.
- (2) Hanbicki, A. T.; Currie, M.; Kioseoglou, G.; Friedman, A. L.; Jonker, B. T. Measurement of High Exciton Binding Energy in the Monolayer Transition-Metal Dichalcogenides WS₂ and WSe₂. *Solid State Commun.* **2015**, *203*, 16–20.
- (3) Li, Z.; Xiao, Y.; Gong, Y.; Wang, Z.; Kang, Y.; Zu, S.; Ajayan, P. M.; Nordlander, P.; Fang, Z. Active Light Control of the MoS₂ Monolayer Exciton Binding Energy. *ACS Nano* **2015**, *9* (10), 10158–10164.
- (4) Fang, H.; Battaglia, C.; Carraro, C.; Nemsak, S.; Ozdol, B.; Kang, J. S.; Bechtel, H. A.; Desai, S. B.; Kronast, F.; Unal, A. A.; Conti, G.; Conlon, C.; Palsson, G. K.; Martin, M. C.; Minor, A. M.; Fadley, C. S.; Yablonovitch, E.; Maboudian, R.; Javey, A. Strong Interlayer Coupling in van Der Waals Heterostructures Built from Single-Layer Chalcogenides. *Proc. Natl. Acad. Sci. U. S. A.* **2014**, *111* (17), 6198–6202.
- (5) Yan, J.; Ma, C.; Huang, Y.; Yang, G. Tunable Control of Interlayer Excitons in WS₂/MoS₂ Heterostructures via Strong Coupling with Enhanced Mie Resonances. *Adv. Sci.* **2019**, 1802092.
- (6) Rivera, P.; Schaibley, J. R.; Jones, A. M.; Ross, J. S.; Wu, S.; Aivazian, G.; Klement, P.; Seyler, K.; Clark, G.; Ghimire, N. J.; Yan, J.; Mandrus, D. G.; Yao, W.; Xu, & X. ARTICLE Observation of Long-Lived Interlayer Excitons in

- Monolayer MoSe 2-WSe 2 Heterostructures. *Nat. Commun.* **2015**, 6.
- (7) Schaibley, J. R.; Rivera, P.; Yu, H.; Seyler, K. L.; Yan, J.; Mandrus, D. G.; Taniguchi, T.; Watanabe, K.; Yao, W.; Xu, X. Directional Interlayer Spin-Valley Transfer in Two-Dimensional Heterostructures. *Nat. Commun.* **2016**, 7, 13747.
 - (8) Schwarz, S.; Kozikov, A.; Withers, F.; Maguire, J. K.; Foster, A. P.; Dufferwiel, S.; Hague, L.; Makhonin, M. N.; Wilson, L. R.; Geim, A. K.; Novoselov, K. S.; Tartakovskii, A. I. Electrically Pumped Single-Defect Light Emitters in WSe₂. *2D Mater.* **2016**, 3 (2), 025038.
 - (9) Ye, Y.; Dou, X.; Ding, K.; Chen, Y.; Jiang, D.; Yang, F.; Sun, B. Single Photon Emission from Deep-Level Defects in Monolayer WSe₂. *Phys. Rev. B* **2017**, 95 (24), 245313.
 - (10) Baugher, B. W. H.; Churchill, H. O. H.; Yang, Y.; Jarillo-Herrero, P. Optoelectronics with Electrically Tunable PN Diodes in a Monolayer Dichalcogenide. *Nat. Nanotechnol.* **2013**, 9 (4), 262–267.
 - (11) Wang, Q. H.; Kalantar-Zadeh, K.; Kis, A.; Coleman, J. N.; Strano, M. S. Electronics and Optoelectronics of Two-Dimensional Transition Metal Dichalcogenides. *Nat. Nanotechnol.* **2012**, 7 (11), 699–712.
 - (12) Ghiasi, T. S.; Ingla-Aynés, J.; Kaverzin, A. A.; van Wees, B. J. Large Proximity-Induced Spin Lifetime Anisotropy in Transition-Metal Dichalcogenide/Graphene Heterostructures. *Nano Lett.* **2017**, 17 (12), 7528–7532.
 - (13) Zhong, D.; Seyler, K. L.; Linpeng, X.; Cheng, R.; Sivadas, N.; Huang, B.;

- Schmidgall, E.; Taniguchi, T.; Watanabe, K.; McGuire, M. A.; Yao, W.; Xiao, D.; Fu, K.-M. C.; Xu, X. Van Der Waals Engineering of Ferromagnetic Semiconductor Heterostructures for Spin and Valleytronics. *Sci. Adv.* **2017**, *3* (5), e1603113.
- (14) Palacios-Berraquero, C.; Kara, D. M.; Montblanch, A. R.-P.; Barbone, M.; Latawiec, P.; Yoon, D.; Ott, A. K.; Loncar, M.; Ferrari, A. C.; Atatüre, M. Large-Scale Quantum-Emitter Arrays in Atomically Thin Semiconductors. *Nat. Commun.* **2017**, *8*, 15093.
- (15) Gong, C.; Zhang, Y.; Chen, W.; Chu, J.; Lei, T.; Pu, J.; Dai, L.; Wu, C.; Cheng, Y.; Zhai, T.; Li, L.; Xiong, J. Electronic and Optoelectronic Applications Based on 2D Novel Anisotropic Transition Metal Dichalcogenides. *Adv. Sci.* **2017**, *4* (12), 1700231.
- (16) Edvinsson, T. Optical Quantum Confinement and Photocatalytic Properties in Two-, One- and Zero-Dimensional Nanostructures. *R. Soc. Open Sci.* **2018**, *5* (9), 180387.
- (17) Stanford, M. G.; Rack, P. D.; Jariwala, D. Emerging Nanofabrication and Quantum Confinement Techniques for 2D Materials beyond Graphene. *npj 2D Mater. Appl.* **2018**, *2*, 20.
- (18) Koperski, M.; Nogajewski, K.; Arora, A.; Cherkez, V.; Mallet, P.; Veuillen, J.-Y.; Marcus, J.; Kossacki, P.; Potemski, M. Single Photon Emitters in Exfoliated WSe₂ Structures. *Nat. Nanotechnol.* **2015**, *10* (6), 503–506.

- (19) Chakraborty, C.; Goodfellow, K. M.; Nick Vamivakas, A.; Mak, K. F.; Lee, C.; Hone, J.; Shan, J.; Heinz, T. F.; Zeng, H.; Dai, J.; Yao, W.; Xiao, D.; Cui, X.; Jones, A. M.; Yu, H.; Ghimire, N. J.; Wu, S.; Aivazian, G.; Ross, J. S.; Zhao, B.; Yan, J.; Mandrus, D. G.; Xu, X.; Li, Y.; Ludwig, J.; Low, T.; Chernikov, A.; Arefe, G.; Kim, Y. D. et al. Direct On-Chip Optical Plasmon Detection with an Atomically Thin Semiconductor. *Phys. Rev. Lett* **2010**, *105* (2), 1474.
- (20) Aharonovich, I.; Englund, D.; Toth, M. Solid-State Single-Photon Emitters. *Nat. Photonics* **2016**, *10* (10), 631–641.
- (21) Xiao, D.; Liu, G.-B.; Feng, W.; Xu, X.; Yao, W. Coupled Spin and Valley Physics in Monolayers of MoS_2 and Other Group-VI Dichalcogenides. *Phys. Rev. Lett.* **2012**, *108* (19), 196802.
- (22) Xu, X.; Yao, W.; Xiao, D.; Heinz, T. F. Spin and Pseudospins in Layered Transition Metal Dichalcogenides. *Nat. Phys.* **2014**, *10* (5), 343–350.
- (23) Xiao, D.; Chang, M.-C.; Niu, Q. Berry Phase Effects on Electronic Properties. *Rev. Mod. Phys.* **2010**, *82* (3), 1959–2007.
- (24) Srivastava, A.; Sidler, M.; Allain, A. V.; Lembke, D. S.; Kis, A.; Imamoğlu, A. Valley Zeeman Effect in Elementary Optical Excitations of Monolayer WSe_2 . *Nat. Phys.* **2015**, *11* (2), 141–147.
- (25) Price, H. M.; Ozawa, T.; Cooper, N. R.; Carusotto, I. Artificial Magnetic Fields in Momentum Space in Spin-Orbit-Coupled Systems. *Phys. Rev. A* **2015**, *91* (3), 033606.

- (26) Price, H. M.; Ozawa, T.; Carusotto, I. Quantum Mechanics with a Momentum-Space Artificial Magnetic Field. *Phys. Rev. Lett.* **2014**, *113* (19), 190403.
- (27) Cao, Y.; Fatemi, V.; Fang, S.; Watanabe, K.; Taniguchi, T.; Kaxiras, E.; Jarillo-Herrero, P. Unconventional Superconductivity in Magic-Angle Graphene Superlattices. *Nature* **2018**, *556* (7699), 43–50.
- (28) Cao, Y.; Fatemi, V.; Demir, A.; Fang, S.; Tomarken, S. L.; Luo, J. Y.; Sanchez-Yamagishi, J. D.; Watanabe, K.; Taniguchi, T.; Kaxiras, E.; Ashoori, R. C.; Jarillo-Herrero, P. Correlated Insulator Behaviour at Half-Filling in Magic-Angle Graphene Superlattices. *Nature* **2018**, *556* (7699), 80–84.
- (29) Manzeli, S.; Ovchinnikov, D.; Pasquier, D.; Yazyev, O. V.; Kis, A. 2D Transition Metal Dichalcogenides. *Nat. Rev. Mater.* **2017**, *2* (8), 17033.
- (30) Shi, Y.; Li, H.; Li, L.-J. Recent Advances in Controlled Synthesis of Two-Dimensional Transition Metal Dichalcogenides via Vapour Deposition Techniques. *Chem. Soc. Rev.* **2015**, *44* (9), 2744–2756.
- (31) Zhang, F.; Momeni, K.; AlSaud, M. A.; Azizi, A.; Hainey, M. F.; Redwing, J. M.; Chen, L.-Q.; Alem, N. Controlled Synthesis of 2D Transition Metal Dichalcogenides: From Vertical to Planar MoS₂. *2D Mater.* **2017**, *4* (2), 025029.
- (32) Chen, M.-W.; Kim, H.; Ovchinnikov, D.; Kuc, A.; Heine, T.; Renault, O.; Kis, A. Large-Grain MBE-Grown GaSe on GaAs with a Mexican Hat-like Valence Band Dispersion. *npj 2D Mater. Appl.* **2018**, *2* (1), 2.
- (33) Budiman, M.; Yamada, A.; Konagai, M. Heteroepitaxy of Layered Compound

- InSe and InSe/GaSe onto GaAs Substrates. *Jpn. J. Appl. Phys.* **1998**, *37* (Part 1, No. 7A), 4092–4098.
- (34) Vishwanath, S.; Liu, X.; Rouvimov, S.; Mende, P. C.; Azcatl, A.; McDonnell, S.; Wallace, R. M.; Feenstra, R. M.; Furdyna, J. K.; Jena, D.; Grace Xing, H. Comprehensive Structural and Optical Characterization of MBE Grown MoSe₂ on Graphite, CaF₂ and Graphene. *2D Mater.* **2015**, *2* (2), 024007.
- (35) Yue, R.; Nie, Y.; Walsh, L. A.; Addou, R.; Liang, C.; Lu, N.; Barton, A. T.; Zhu, H.; Che, Z.; Barrera, D.; Cheng, L.; Cha, P.-R.; Chabal, Y. J.; Hsu, J. W. P.; Kim, J.; Kim, M. J.; Colombo, L.; Wallace, R. M.; Cho, K.; Hinkle, C. L. Nucleation and Growth of WSe₂: Enabling Large Grain Transition Metal Dichalcogenides. *2D Mater.* **2017**, *4* (4), 045019.
- (36) Nakano, M.; Wang, Y.; Kashiwabara, Y.; Matsuoka, H.; Iwasa, Y. Layer-by-Layer Epitaxial Growth of Scalable WSe₂ on Sapphire by Molecular Beam Epitaxy. *Nano Lett.* **2017**, *17* (9), 5595–5599.
- (37) Liu, H. J.; Jiao, L.; Xie, L.; Yang, F.; Chen, J. L.; Ho, W. K.; Gao, C. L.; Jia, J. F.; Cui, X. D.; Xie, M. H. Molecular-Beam Epitaxy of Monolayer and Bilayer WSe₂: A Scanning Tunneling Microscopy/Spectroscopy Study and Deduction of Exciton Binding Energy. *2D Mater.* **2015**, *2* (3), 034004.
- (38) Zhang, Y.; Chang, T.-R.; Zhou, B.; Cui, Y.-T.; Yan, H.; Liu, Z.; Schmitt, F.; Lee, J.; Moore, R.; Chen, Y.; Lin, H.; Jeng, H.-T.; Mo, S.-K.; Hussain, Z.; Bansil, A.; Shen, Z.-X. Direct Observation of the Transition from Indirect to Direct Bandgap

- in Atomically Thin Epitaxial MoSe₂. *Nat. Nanotechnol.* **2013**, 9 (2), 111–115.
- (39) Liu, H.; Chen, J.; Yu, H.; Yang, F.; Jiao, L.; Liu, G.-B.; Ho, W.; Gao, C.; Jia, J.; Yao, W.; Xie, M. Observation of Intervalley Quantum Interference in Epitaxial Monolayer Tungsten Diselenide. *Nat. Commun.* **2015**, 6, 8180.
- (40) Kang, K.; Xie, S.; Huang, L.; Han, Y.; Huang, P. Y.; Mak, K. F.; Kim, C.-J.; Muller, D.; Park, J. High-Mobility Three-Atom-Thick Semiconducting Films with Wafer-Scale Homogeneity. *Nature* **2015**, 520 (7549), 656–660.
- (41) Eichfeld, S. M.; Hossain, L.; Lin, Y.; Piasecki, A. F.; Kupp, B.; Birdwell, a G.; Burke, R. a; Lu, N.; Peng, X.; Li, J.; Azcatl, A.; McDonnell, S.; Wallace, R. M.; Kim, M. J.; Mayer, T. S.; Redwing, J. M.; Robinson, J. a. Highly Scalable, Atomically Thin WSe₂ Grown via Metal–Organic Chemical Vapor Deposition. *ACS Nano* **2015**, 9 (2), 2080–2087.
- (42) Boscher, N. D.; Blackman, C. S.; Carmalt, C. J.; Parkin, I. P.; Prieto, A. G. Atmospheric Pressure Chemical Vapour Deposition of Vanadium Diselenide Thin Films. *Appl. Surf. Sci.* **2007**, 253 (14), 6041–6046.
- (43) Chung, J.-W.; Dai, Z. R.; Ohuchi, F. S. WS₂ Thin Films by Metal Organic Chemical Vapor Deposition. *J. Cryst. Growth* **1998**, 186 (1–2), 137–150.
- (44) Boscher, N. D.; Carmalt, C. J.; Palgrave, R. G.; Gil-Tomas, J. J.; Parkin, I. P. Atmospheric Pressure CVD of Molybdenum Diselenide Films on Glass. *Chem. Vap. Depos.* **2006**, 12 (11), 692–698.
- (45) Hofmann, W. Thin Films of Molybdenum and Tungsten Disulphides by Metal

- Organic Chemical Vapour Deposition. *J. Mater. Sci.* **1988**, 23 (11), 3981–3986.
- (46) Carmalt, C. J.; Parkin, I. P.; Peters, E. S. Atmospheric Pressure Chemical Vapour Deposition of WS₂ Thin Films on Glass. *Polyhedron* **2003**, 22 (11), 1499–1505.
- (47) Kranthi Kumar, V.; Dhar, S.; Choudhury, T. H.; Shivashankar, S. A.; Raghavan, S. A Predictive Approach to CVD of Crystalline Layers of TMDs: The Case of MoS₂. *Nanoscale* **2015**, 7 (17), 7802–7810.
- (48) Kim, T.; Mun, J.; Park, H.; Joung, D.; Diware, M.; Won, C.; Park, J.; Jeong, S.-H.; Kang, S.-W. Wafer-Scale Production of Highly Uniform Two-Dimensional MoS₂ by Metal-Organic Chemical Vapor Deposition. *Nanotechnology* **2017**, 28 (18), 18LT01.
- (49) Kalanyan, B.; Kimes, W. A.; Beams, R.; Stranick, S. J.; Garratt, E.; Kalish, I.; Davydov, A. V.; Kanjolia, R. K.; Maslar, J. E. Rapid Wafer-Scale Growth of Polycrystalline 2H-MoS₂ by Pulsed Metal–Organic Chemical Vapor Deposition. *Chem. Mater.* **2017**, 29 (15), 6279–6288.
- (50) Chiu, M.-H.; Zhang, C.; Shiu, H.-W.; Chuu, C.-P.; Chen, C.-H.; Chang, C.-Y. S.; Chen, C.-H.; Chou, M.-Y.; Shih, C.-K.; Li, L.-J. Determination of Band Alignment in the Single-Layer MoS₂/WSe₂ Heterojunction. *Nat. Commun.* **2015**, 6, 7666.
- (51) Lin, M.; Wu, D.; Zhou, Y.; Huang, W.; Jiang, W.; Zheng, W.; Zhao, S.; Jin, C.; Guo, Y.; Peng, H.; Liu, Z. Controlled Growth of Atomically Thin In₂Se₃ Flakes by van Der Waals Epitaxy. *J. Am. Chem. Soc.* **2013**, 135 (36), 13274–13277.
- (52) Shi, Y.; Zhou, W.; Lu, A.-Y.; Fang, W.; Lee, Y.-H.; Hsu, A. L.; Kim, S. M.; Kim,

- K. K.; Yang, H. Y.; Li, L.-J.; Idrobo, J.-C.; Kong, J. Van Der Waals Epitaxy of MoS₂ Layers Using Graphene As Growth Templates. *Nano Lett.* **2012**, *12* (6), 2784–2791.
- (53) Bianco, G. V.; Losurdo, M.; Giangregorio, M. M.; Sacchetti, A.; Prete, P.; Lovergine, N.; Capezzuto, P.; Bruno, G. Direct Epitaxial CVD Synthesis of Tungsten Disulfide on Epitaxial and CVD Graphene. *RSC Adv.* **2015**, *5* (119), 98700–98708.
- (54) Yan, A.; Velasco, J.; Kahn, S.; Watanabe, K.; Taniguchi, T.; Wang, F.; Crommie, M. F.; Zettl, A. Direct Growth of Single- and Few-Layer MoS₂ on h-BN with Preferred Relative Rotation Angles. *Nano Lett.* **2015**, *15* (10), 6324–6331.
- (55) Yu, H.; Yang, Z.; Du, L.; Zhang, J.; Shi, J.; Chen, W.; Chen, P.; Liao, M.; Zhao, J.; Meng, J.; Wang, G.; Zhu, J.; Yang, R.; Shi, D.; Gu, L.; Zhang, G. Precisely Aligned Monolayer MoS₂ Epitaxially Grown on h-BN Basal Plane. *Small* **2017**, *13* (7), 1603005.
- (56) Balakrishnan, N.; Steer, E. D.; Smith, E. F.; Kudrynskyi, Z. R.; Kovalyuk, Z. D.; Eaves, L.; Patané, A.; Beton, P. H. Epitaxial Growth of γ -InSe and α , β , and γ -In₂Se₃ on ϵ -GaSe. *2D Mater.* **2018**, *5* (3), 035026.
- (57) Dumcenco, D.; Ovchinnikov, D.; Marinov, K.; Lazić, P.; Gibertini, M.; Marzari, N.; Sanchez, O. L.; Kung, Y.-C.; Krasnozhan, D.; Chen, M.-W.; Bertolazzi, S.; Gillet, P.; Fontcuberta i Morral, A.; Radenovic, A.; Kis, A. Large-Area Epitaxial Monolayer MoS₂. *ACS Nano* **2015**, *9* (4), 4611–4620.

- (58) Zhang, X.; Choudhury, T. H.; Chubarov, M.; Xiang, Y.; Jariwala, B.; Zhang, F.; Alem, N.; Wang, G.-C.; Robinson, J. A.; Redwing, J. M. Diffusion-Controlled Epitaxy of Large Area Coalesced WSe₂ Monolayers on Sapphire. *Nano Lett.* **2018**, *18* (2), 1049–1056.
- (59) van der Zande, A. M.; Huang, P. Y.; Chenet, D. A.; Berkelbach, T. C.; You, Y.; Lee, G.-H.; Heinz, T. F.; Reichman, D. R.; Muller, D. A.; Hone, J. C. Grains and Grain Boundaries in Highly Crystalline Monolayer Molybdenum Disulphide. *Nat. Mater.* **2013**, *12* (6), 554–561.
- (60) Zou, X.; Liu, Y.; Yakobson, B. I. Predicting Dislocations and Grain Boundaries in Two-Dimensional Metal-Disulfides from the First Principles. *Nano Lett.* **2013**, *13* (1), 253–258.
- (61) Ly, T. H.; Perello, D. J.; Zhao, J.; Deng, Q.; Kim, H.; Han, G. H.; Chae, S. H.; Jeong, H. Y.; Lee, Y. H. Misorientation-Angle-Dependent Electrical Transport across Molybdenum Disulfide Grain Boundaries. *Nat. Commun.* **2016**, *7* (1), 10426.
- (62) Du, L.; Yu, H.; Xie, L.; Wu, S.; Wang, S.; Lu, X.; Liao, M.; Meng, J.; Zhao, J.; Zhang, J.; Zhu, J.; Chen, P.; Wang, G.; Yang, R.; Shi, D.; Zhang, G. The Effect of Twin Grain Boundary Tuned by Temperature on the Electrical Transport Properties of Monolayer MoS₂. *Crystals* **2016**, *6* (9), 115.
- (63) Zhou, S.; Wang, S.; Shi, Z.; Sawada, H.; Kirkland, A. I.; Li, J.; Warner, J. H. Atomically Sharp Interlayer Stacking Shifts at Anti-Phase Grain Boundaries in

Overlapping MoS₂ Secondary Layers. *Nanoscale* **2018**, *10* (35), 16692–16702.

- (64) Man, M. K. L.; Deckoff-Jones, S.; Winchester, A.; Shi, G.; Gupta, G.; Mohite, A. D.; Kar, S.; Kioupakis, E.; Talapatra, S.; Dani, K. M. Protecting the Properties of Monolayer MoS₂ on Silicon Based Substrates with an Atomically Thin Buffer. *Sci. Rep.* **2016**, *6* (1), 20890.
- (65) Lin, Y.-C.; Jariwala, B.; Bersch, B. M.; Xu, K.; Nie, Y.; Wang, B.; Eichfeld, S. M.; Zhang, X.; Choudhury, T. H.; Pan, Y.; Addou, R.; Smyth, C. M.; Li, J.; Zhang, K.; Haque, M. A.; Fölsch, S.; Feenstra, R. M.; Wallace, R. M.; Cho, K.; Fullerton-Shirey, S. K.; Redwing, J. M.; Robinson, J. A. Realizing Large-Scale, Electronic-Grade Two-Dimensional Semiconductors. *ACS Nano* **2018**, *12* (2), 965–975.
- (66) Zhang, F.; Wang, Y.; Erb, C.; Wang, K.; Moradifar, P.; Crespi, V. H.; Alem, N. Full orientation control of epitaxial MoS₂ on hBN assisted by substrate defects, *Phys. Rev. B* **2019**, *99*, 155430.

Chapter 2

CVD System Setup and Characterization Techniques

In this chapter, we introduce the detailed setup of the gas source chemical vapor deposition system that are used for all the growth experiments in this dissertation. This chapter also discusses some computational fluid dynamic modelling regarding the system on the consideration of gas flow rate, reactor pressure, and substrate temperature. In the end of this chapter, film transfer and characterization techniques that are mainly utilized in this dissertation are also briefly introduced.

2.1 Introduction

Chemical vapor deposition (CVD) is the process of chemical reactions of gaseous precursors including volatile compounds of solid and liquid materials, to deposit a nonvolatile material on suitably selected substrate.¹ As mentioned in Chapter 1, although powder vapor transport or powder source CVD system offers an easy and quick method to access monolayer transition metal dichalcogenides (TMDs), this kind of setup typically is lack of controllability on powder source precursors regarding flow rate, vapor pressure, and uniform distribution across the substrate. Due to these disadvantages, it is hard to systematically study the growth mechanism of 2D materials using PVT, plus, it is also difficult to develop films with doping, alloy, or even heterostructure over large substrate sizes since typical PVT systems are lack of ability to switch on/off the vaporization of powders. In comparison, gas source CVD/MOCVD, where both the metal and chalcogen

precursors are located outside of the deposition chamber, enables independent control of precursor partial pressures and ratios for scalable growth of 2D TMDs, and most importantly, studies fundamental insights into the 2D growth mechanism. In this dissertation the growth of WSe₂ (Chapter 3-6) and β -In₂Se₃ (Chapter 6) films was carried out in a custom assembled gas source CVD/MOCVD system. This system is enclosed in a cabinet including a gas panel for metering gas delivery, pressure system for pressure measurement and control, a reactor (reaction chamber) for film growth, a vacuum pump, and a scrubber.

2.2 System Configuration

2.2.1 Gas panel

The gas panel consists of pneumatic valves and mass flow controllers (MFCs) to regulate and direct the flow of gases into the reactor. The flows of gaseous sources are directly controlled by the MFCs and MFCs are calibrated to their main flowing gases. In terms of liquid and solid precursors, there are also pressure controllers (PCs) to regulate the pressure of them in the bubblers before flowing into the reactor. In addition to precursors, both ultra-high purity (UHP) of N₂ and H₂ are used in the experiment. UHP N₂ is generally used as a purge gas and UHP H₂ is used as the main carrier gas for both carrying precursors from bubblers to reactor and manipulating the total flow rate of gases in the reactor. The supply of hydrogen selenide (H₂Se, 99.998% purity) is provided by *Mathson* in a high-pressure gas cylinder and located on the exterior of the cabinet, while

N₂ and H₂ come from each N₂ and H₂ individual generator, respectively. In addition, H₂ goes through a gas purifier provided by *SAES Pure Gas, Inc* to further reduce the amount of oxygen contamination into the reactor and increase gas purity up to 99.9999%. The gas panel is equipped with solid precursor tungsten hexacarbonyl (W(CO)₆, 99.99% purity) from *Sigma-Aldrich* stored in a 150mL stainless steel bubbler purchased from *Strem Chemical, Inc*, and metalorganic solid precursor, trimethylindium with its bubbler ((CH₃)₃In or TMIIn, 99.99% purity), from *SAFC Inc*. The gas panel is also equipped with a liquid metalorganic precursor in its own bubbler, dimethylselenide ((CH₃)₂Se or DMSe, 99.99% purity), purchased from *NOVA-KEM*. A schematic diagram of the gas panel layout is shown in Figure 2-1 which includes the pneumatic valves, MFCs, pressure controller and all the precursors and gaseous source. The gas panel is controlled using a set of electronic equipment. The MFCs are controlled by MKS type 247 controllers and readouts. The throttle valve is controlled with an MKS type 651 throttle valve controller and readout. The pneumatic valves are driven by compressed air and actuated from a lab-constructed switch panel. The gas lines were constructed of ¼" diameter electropolished stainless steel tubing. VCR (face-seal, metal gasket) fittings were used to connect the valves, tubing, and MFCs together. A Pascal 2015 C2 two-stage rotary vane pump from *Pfeiffer Vacuum Inc* which is specifically designed for toxic and corrosive gases is used. Fomblin oil of grade 25/6 is used in the pump. An oil mist eliminator from *Pfeiffer Vacuum Inc* is connected to the downstream of the pump to collect any oil mist that occasionally pump out with the exhaust.

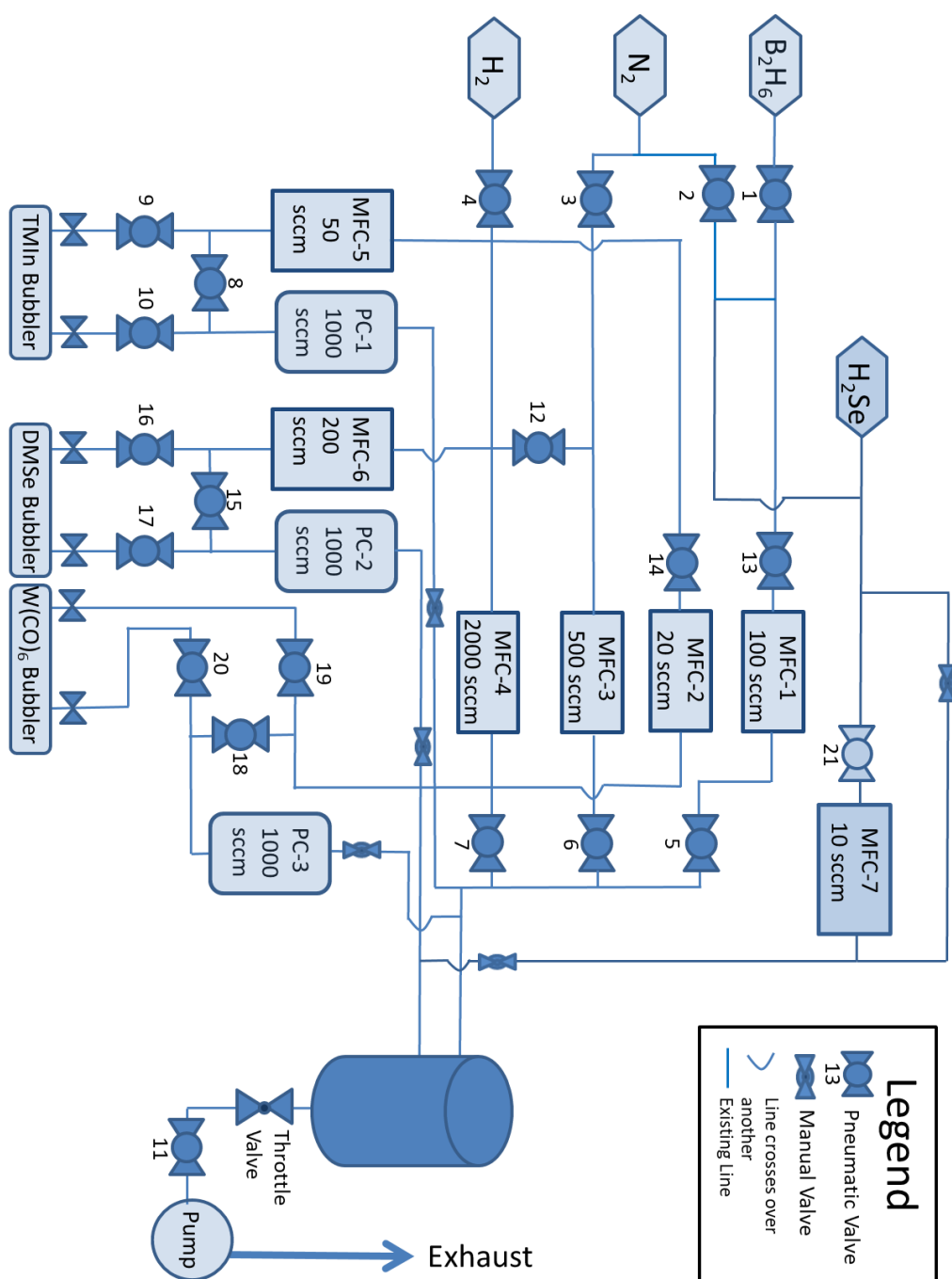


Figure 2-1. Schematic diagram of the gas panel of the CVD system

2.2.2 Reactor design

The schematic plot in Figure 2-2a depicts the design of the CVD reactor. The reactor is designed in a vertical direction with a cold-wall chamber made of quartz. The quartz has a double-wall jacket used for water flow to cool the reactor wall. The chilling water flows from the top side of the quartz jacket to the bottom side of the jacket which guarantee enough and uniform cooling through the whole body. Inside the water jacket, there is an additional quartz linear tube with a bit exceeded length of the quartz jacket to prevent direct coating on the quartz jacket during the growth process. The quartz linear tube is held with a QF-50 fitting which makes it easy for replacement and cleaning. The reactor uses a single three turn copper induction coil as the inductively heating source for the susceptor. The induction power supply is an *Ameritherm Novastar 3* with a maximum of 3 kW output. Note that the induction power supply requires chilling water supply for the cooling of the power. The copper coil is designed with a hollow center where chilling water also flows through to maintain the cool temperature of the coil itself. In the center of the coil, a SiC coated graphite susceptor is placed on a quartz shaft, with one end closed, and mounted in the reactor chamber. As the mere conductive material in the center of the coil, Figure 2-2b shows only the susceptor is heated up by the coil during the growth. The susceptor has a 1 cm \times 1 cm cutout on the surface to hold the substrate. The temperature of the susceptor is measured with a k-type thermocouple that is fed through the quartz shaft and is in contact with the closed end of the shaft. The temperature readout is a *Eurotherm 2408* PID controller. The temperature of the

susceptor is adjusted by increasing the voltage and current in coil. The *Novastar 3* is capable of both manual control and PID control through an external PID controller.

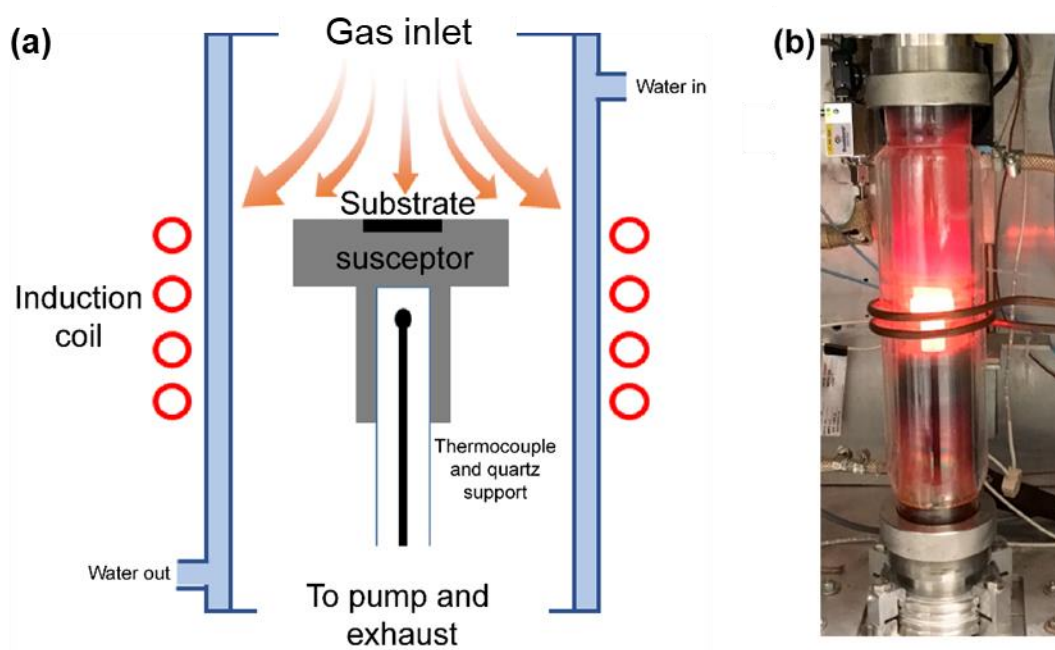


Figure 2-2. (a) Schematic plot of the cold-wall CVD reactor with inductive heater and (b) photo of the reactor when susceptor heated to 900 °C.

2.2.3 Reactor pressure

The pressure in the system is monitored with two separate pressure gauges. A baratron gauge of MKS model 246 is used as the main pressure gauge to measure the pressure during gas flow and during depositions. The baratron gauge is connected to an MKS type 651 pressure controller as indicated in Figure 3-4. The MKS 651 pressure

controller is also attached to an MKS 253 throttle valve to control the system pressure. The other pressure gauge is a pirani vacuum gauge of series 9100 from *Kurt J. Lesker*. This vacuum gauge is used to measure the base pressure of the system during the pumping and leak testing process. This is done periodically throughout the deposition procedure to ensure vacuum integrity, minimize the chance of exposure to toxic gases and to determine the effectiveness of oxygen removal during gas purging. This gauge is attached to a stand-alone readout that is not attached to any other system equipment.

2.2.4 Vapor pressure and flow rate from a bubbler

One of the main advantages of gas source CVD/MOCVD system is that it can precisely control the flow rate of precursors into the reactor. The flow rate of a gaseous precursor can be precisely and directly controlled by an MFC. In contrast, the flow rate of solid and liquid precursors are controlled by the carrier gas flow rate through the bubblers where the precursors are stored, and both bubbler pressure and bubbler temperature can also affect the final flow rate of the precursors so additional calculation is required and discussed as follow.

The vapor pressures of precursors are calculated based on the literature and the set temperature. The vapor pressure equation for $\text{W}(\text{CO})_6$ is^{2,3}

$$\log P = 12.094 - 4077/T$$

for DMSe is⁴

$$\log P = 7.968 - 1665.9/T$$

and for TMI_n is⁵

$$\log P = 10.98 - 3204/T$$

Where pressure P is in unit *Torr* and temperature T is in unit *K*.

Then, the flow rate of precursor out of the bubbler is calculated from a mass balance considering the vapor pressure the precursor at the bubbler temperature and the bubbler pressure controlled by the pressure controller based on Amagat's law

$$v_{solid\ or\ liquid} = \frac{n_{solid\ or\ liquid} v_{carrier\ gas}}{1 - n_{solid\ or\ liquid}}$$

And Dalton's law

$$n_{solid\ or\ liquid} = \frac{P_{solid\ or\ liquid}}{P_{bubbler}}$$

where v is the flow rate and n is the mole fraction.

2.3 Computational Modelling

Computational fluid dynamics simulations of the thermal-fluid environment of the gas source CVD/MOCVD system used in this work were performed to understand how the gas fluid dynamic is influenced by the inductively heated susceptor under different growth conditions. The commercial software COMSOL Multiphysics 5.3 was used to perform the computational simulations. The transport model is based on the solution of the coupled partial differential equations for the conservation of momentum, energy, and mass using the modules “Non-Isothermal Flow” built into the software. The inductive

heating of the graphite susceptor utilizes the module “Magnetic Fields” in the software that couples the transport model in terms of temperature based on the Ampere’s law. A 2D-axisymmetric model was used due to the axial symmetry of the reactor to reduce the computational complexity of the simulations.

The transport model used “Non-Isothermal Flow” to couple both gas laminar flow and heat transfer in fluids in the reactor tube. A compressible form of Navier-Stokes and continuity equations were applied to maintain mass and momentum conservation in the simulations. In the “Magnetic Fields” module, a single coil with three turns was considered with ~3 kW power input based on the experimental data. The boundary of the electromagnetic heat source includes the entire system including the air between coil and reactor while in fact only the graphite susceptor is heated up due to low conductivity of other materials. Conduction, convection and radiation were considered in the heat transfer model. The properties of the mixture gases were calculated using the ideal gas law and relevant thermodynamic properties.

Due to the high volatilization of the chalcogen resulting in high desorption rate during the growth, current CVD/MOCVD process for TMD monolayer films involve high reactor pressure and low gas flow velocity to maintain a high partial pressure of chalcogen species above substrates. However, these may also lead to several problems that reduces the controllability of a CVD system. Figure 2-3b shows some circulate gas streamline right above the substrate at high reactor pressure and low gas velocity (Figure 2-3c) due to the buoyancy effect in the vertical reactor chamber at high growth temperature. This results in the backflow of the precursors and significant upstream

deposition and depletion. In addition, the high reactor pressure reduces the mean free path length and the low gas velocity increase the gas residue time, both of which are likely to increase the possibility of gas phase pre-reaction of the precursors before they reach the substrate. Although this might not affect the CVD processes using precursors such as Mo(CO)_6 and W(CO)_6 as they will not lose all the CO ligands before reaching the substrate surface or have strong gas phase reactions at low temperature, other precursors such as TMIn and H_2Se for In_2Se_3 films can have significant gas phase pre-reaction due to the Lewis acid and base properties of the two precursors (see Chapter 6). In contrast, high gas flow rate and low reactor pressure can reduce the gas recirculation (Figure 2-3e) by further increasing gas velocity (Figure 2-3f) and thus reduce the precursor pre-reaction, however, this will also lead to change in temperature profile (Figure 2-3d and 2-3g) and reduction in precursor partial pressure.

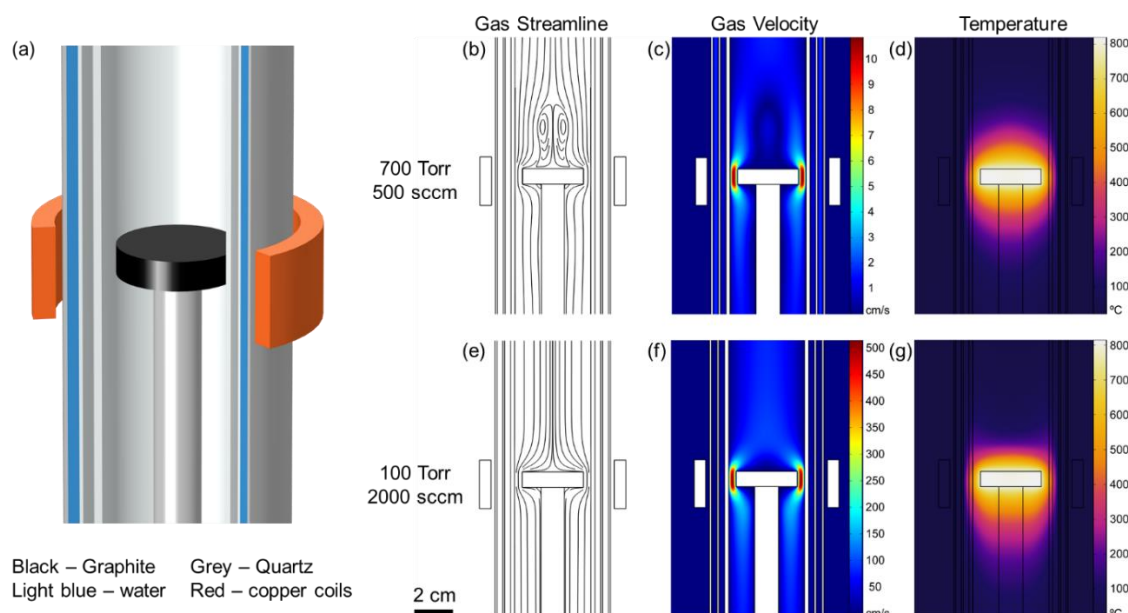


Figure 2-3. (a) Schematic plot of the simplified CVD geometry and materials regarding the susceptor, growth chamber, and surrounding RF heating coils. (b)–(d) simulations of the cold-wall CVD reactor at 700 Torr and 500 sccm of H₂, where (b) and (c) show the gas streamlines and velocity profile and (d) shows the temperature profile for the susceptor and growth chamber. (e) – (g) Gas streamlines, gas velocity, and temperature profile at 100 Torr and 2000 sccm of H₂.

2.4 Substrate Preparation

Most of substrates used in this dissertation work are c-plane double-side polished sapphire. Thermal oxide silicon (100) and silicon (111) were also used in some of the experiments. All substrates were diced into 1 cm × 1cm square piece in an automatic commercial dicing saw system *ADT 7100*. All substrates underwent a standard cleaning procedure after dicing including: (1) Sonicating the substrates in Acetone for 10 min to

dissolve most of contamination; (2) Sonicating the substrates in Isopropyl alcohol for 10 min to remove Acetone; (3) Rinsing the substrates with deionized water for 5 times to remove Isopropyl alcohol; (4) Drying the substrates with high-pressure nitrogen gun; (5) immersing the substrates into commercial Piranha solution (Nano-Strip, KMG Electronic Chemicals) under 85-100 for 20 minutes to get rid of any stubborn residue; (6) rinsing the substrates again with deionized water for 5 times to remove the Piranha solution; (7) Drying the substrates with high-pressure nitrogen gun and placing them into containers.

To remove the native oxide layer on silicon (111) substrate, additional treatment was applied after the standard cleaning procedure: (1) Immersing the substrates into 10% diluted hydrogen fluoride solution for 10 minutes to remove all the native oxide; (2) Rinsing the substrates again with deionized water for 5 times to remove the hydrogen fluoride solution; (3) Drying the substrates with high-pressure nitrogen gun and placing them into containers. Note that hydrogen fluoride solution is not compatible with glass beakers so Teflon beakers were used in this process. The silicon (111) substrate surface should be terminated with H and F and the substrate was rapidly placed into the growth reactor in case of any further oxidation.

2.5 Etch-free Transfer of 2D TMD films

Current study and development of 2D materials including heterostructure, device fabrication, and characterization require an easy and clean way to transfer the films onto arbitrary substrates. The etch-free transfer method presented in this section (designed by Fu Zhang, Penn State) introduce a simple and etchant free process to transfer wafer-scale

monolayer films from sapphire to other substrates only involving PMMA and H₂O.

Instead of deep etching of the sample in hot base solutions, such as HF and KOH,⁶⁻⁸ the PMMA-coated film can be directly delaminated and separated from sapphire substrate by simply dipping the sample in water. The process also helps to keep the film in its pristine structure and free from degradation of the crystal due to ultrasonication⁹ or exposure to chemicals from pre-etching in NaOH or other strong solutions.¹⁰

The transfer process is schematically illustrated in Figure 2-4 with five main steps: (1) PMMA is first spin-coated on the substrate with the nanostructures and the assembly is kept at room temperature overnight (Figure 2-4a and 2-4b); (2) Using blade, small gaps are created along the edge contours of the sapphire substrate (Figure 2-4c); (3) The assembly is immersed in hot water (~80 °C) for 5-10 minutes. Due to the hydrophobic nature of the 2D materials (such as graphene¹¹ and TMDs¹²) and PMMA compared with the hydrophilic character of the sapphire substrate,^{13,14} the water can easily penetrate to the interface from the created gap due to the capillary forces and further lift off the PMMA/film from the sapphire substrate while in water (Figure 2-4d). In this step, both the substrate feeding angle (~ 45°) with respect to the water surface and delamination rate (~ 1mm/s) need to be controlled to minimize the mechanical force and damage and to maintain the integrity of the transferred film. Since no chemical etchants are used in this process, sapphire substrate remains intact and can be reused for further growth. (4) The detached PMMA/film assembly can further be picked up from water with any other target substrate and placed on the hot plate (~70 °C) for 10 minutes to improve the film/substrate attachment. (5) PMMA is removed with acetone and IPA/methanol to

further eliminate any remaining organic residuals. This PMMA-assisted water transfer method significantly reduces the possible damage and chemical attacks during the transfer process. In addition, since no chemical etchants are involved in the process, PMMA/nanostructure assembly can be directly picked up by any water-compatible substrate. All the film transfers mentioned in this dissertation adopted this method.

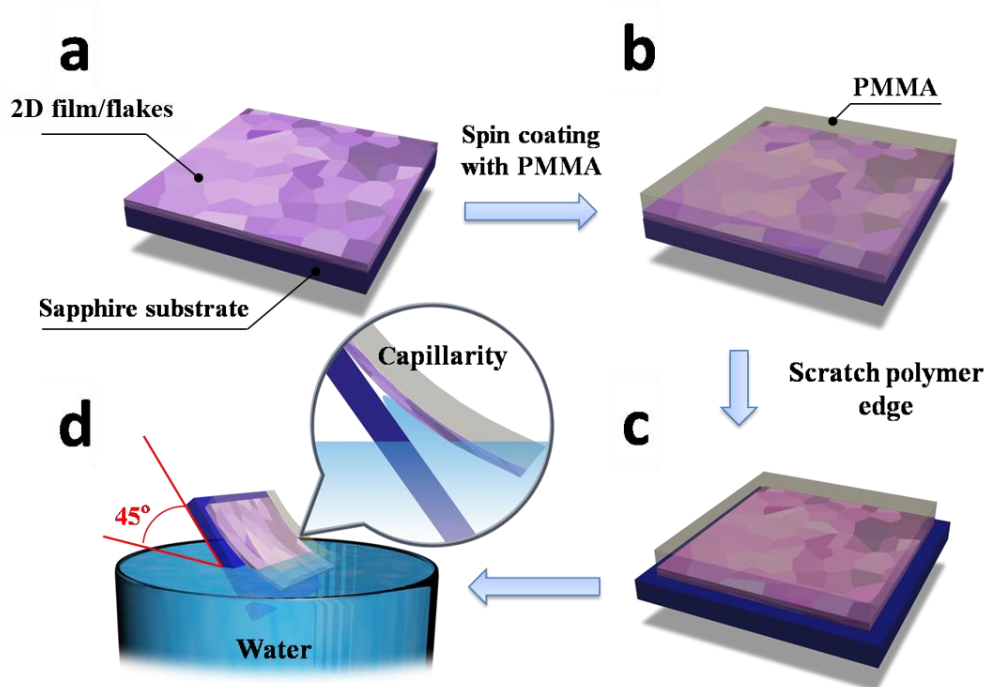


Figure 2-4. The schematic illustration of the etchant-free transfer method. (a) A 2D material film is grown on sapphire; (b) PMMA is Spin-coated on the film; (c) the film is scratched along the edge contours of the sapphire substrate using a blade; (d) The whole assembly is immersed into hot water ($\sim 80\text{ }^{\circ}\text{C}$) by a feeding angle $\sim 45^{\circ}$ for 5 to 10 minutes before the hydrophobic PMMA/2D film is delaminated from the sapphire substrate and floats on the water surface.

2.6 Characterization Techniques of 2D TMD films

2.6.1 Atomic force microscopy

Atomic Force Microscopy (AFM) is known as one of the techniques to capture topographic morphology of sample surfaces. Nowadays, the latest AFM can achieve atomic resolution in the z-direction while maintain swift scanning rate in the xy-plane. This provides the opportunity to identify the variation of monoatomic step height on the sample surface over a micron-level area, which matches perfectly with the requirement of characterizing the morphology of 2D materials with only a few-atom thickness in z-direction. In addition, AFM also allows atomic resolution in xy-plane which offers additional ways to identify surface defects and moiré pattern between monolayer materials and substrates. In addition to traditional contact (Figure 2-5a) and tapping modes (Figure 2-5b), novel modes such as PeakForce Tapping mode in Figure 2-5c (which is used in this dissertation work) have been developed to stably control ultralow imaging force to preserve both the AFM tip and fragile samples.¹⁵ This allows AFM acquiring information of surface for modulus, adhesion, deformation, conductivity, surface potential, and so on in addition to the topography and local force knowledge from conventional modes. Therefore, modern AFM can also allow studies for mechanical, electrical, and piezoelectrical properties. While AFM tip does get in contact with sample surface during the scan (in PeakForce Tapping mode), the weak force between tip and surface (typical around piconewton to nanonewton) can limit the damage on sample to minimal. On the other hand, AFM can work under variant unaggressive environments including liquid, varied temperature, glove box, and vacuum, which enable

multidisciplinary research on 2D materials such as studying black phosphorus in the inert gas glove box where oxidation can be significantly reduced. Therefore, AFM stands out as one of the most common characterization techniques for 2D materials.

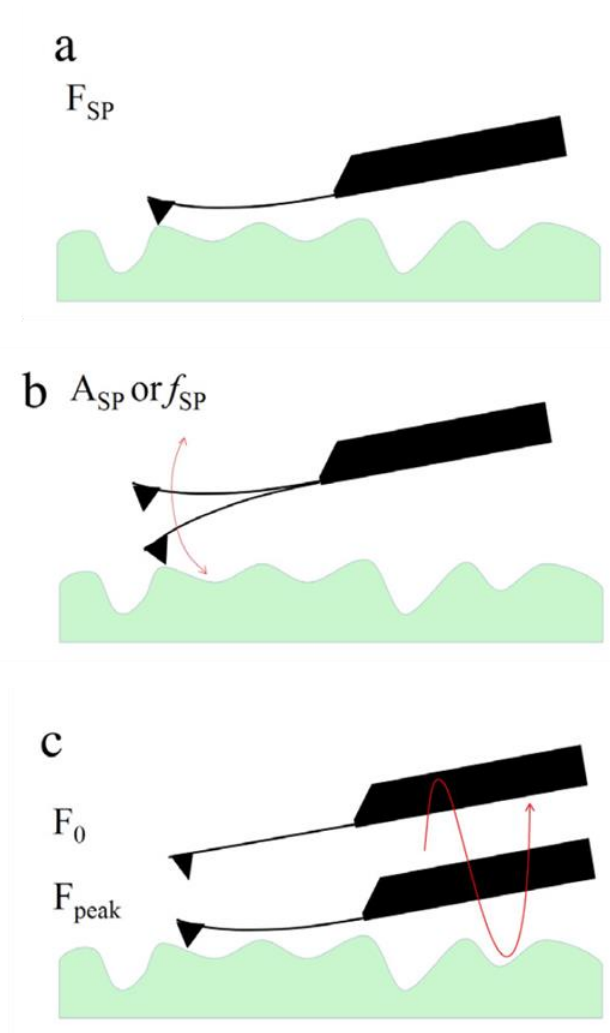


Figure 2-5. Schematic representation of basic AFM modes: **(a)** Contact mode with tip-sample force as a feedback setpoint (F_{sp}); **(b)** Tapping or AC mode where the setpoint is oscillation amplitude (A_{sp}) or frequency (f_{sp}); **(c)** PeakForce Tapping mode where the tip is modulated at an off-resonance frequency and the feedback setpoint is the maximum force, or peak force, of each tapping cycle.¹⁵

2.6.2 Raman and photoluminescence spectroscopy

Raman spectroscopy provides a quick and nondestructive method for characterizing the 2D materials.^{16–18} Typical measurements can be made at varied temperature from 4K to elevated temperature and pressure from vacuum to high pressure without complicated sample preparation processes. Raman scattering involves the inelastic scattering of the incident light in a material, where the energy of the scattered light either decreases by exciting an elementary excitation of a phonon or increases by absorbing a phonon. Raman spectra give the intensity of the scattered light as a function of the energy shift from the incident light which is called as Raman shift. Since the discovery of graphene and development of other atomic layer materials including TMDs, Raman spectroscopy has rapidly become a standard characterization technique for the characterization of low dimensional materials due to several advantages. The strong interaction between incident photon and phonon from the layer gives clear characteristic phonon frequency peaks in Raman spectra even down to monolayer level. The sensitive photon-phonon interaction can not only distinguish the materials but also obtain additional information including strain, doping level, alloy component, etc. In addition, by focusing the laser light in a confocal optical microscope, we can measure a high spatially resolved Raman signal within a few hundred nanometers. Therefore, Raman maps can also be achieved by scanning the focused laser light across the sample surface, in which information regarding the distribution of strain, defects, doping, and so on can be told over a relatively large area.

Photoluminescence (PL) spectroscopy describes the radiative emission of materials after excitation of photons. Similar to Raman spectroscopy, it is also a nondestructive characterization technique and in many cases it can be done in the same instrumental system of Raman spectroscopy (as long as the laser and spectrometer provides the suitable energy range). Unlike the Raman spectroscopy which measure the inelastic Raman shift from incident light, PL response comes from the direction emission from conduction band to valence band of material and is intrinsic to material itself and therefore has no correlation with incident laser light. PL also becomes a standard and significant technique for 2D materials, especially TMDs, due to their unique PL emission and potential optical and optoelectronic applications. Typical monolayer TMDs have direct band gap and thus have strong PL emission.^{19,20} While in addition to this. Monolayer TMDs often show strong exciton binding energy because of the strong Coulomb interaction between the electrons and holes due to the quantum confinement effect,^{19–21} which makes the PL emission peak away from the direct bandgap energy (typically a few hundred meV). Moreover, there are other quasiparticles in the monolayer TMDs such as trion that raise a lot of interest. A trion can be formed by exciton-electron pair under high carrier density, however, they are unstable and rarely observed in conventional semiconductors.^{22,23} In comparison, trions are reported stable in monolayer TMDs,^{24,25} and can be controlled by optical, electronic^{26,27} or chemical²⁸ methods. In this way, the emission of trions can be modified intentionally in monolayer TMDs for potential tunable photonic devices.

2.6.3 In-plane X-ray diffraction

For the determination of the epitaxial relation in classical thin films, the technique of choice is X-ray diffraction (XRD) pole figure measurements. This technique is also nondestructive and usually does not require sample preparation and is fast. In this technique, an $\{hkl\}$ plane family with h and/or k and l not equal to zero is probed for both film and substrate to determine crystallographic orientation. However, 2D monolayers and few-layer films that is often assumed to be impossible for conventional XRD due to the lack of periodicity in the third dimension. While there is no crystal periodicity out-of-plane, the in-plane component is present and has been probed by implementing XRD θ - 2θ and ϕ measurements in the in-plane geometry, to observe the presence of the reciprocal space points and their distribution, respectively. Thus, for the transition metal dichalcogenides where both constituents have high electron density, lab scale X-ray diffraction performed with the X-ray incidence plane nearly coinciding with the sample surface plane (an offset angle that is higher than the X-ray total external reflection angle) should be able to determine the in-plane epitaxial relation between the film and the substrate. “Nearly” in this case is determined by the X-ray total external reflection angle which is materials dependent and usually below 1° from the surface to the beam. This technique is so-called in-plane XRD since it can determine the in-plane epitaxial relation between films and substrates. It can also tell presence of different crystal phases as well as alloy formation and its composition similar to conventional XRD.

Figure 2-6 shows illustrations of the Bragg-Brentano measurement geometry (Figure 2-6a) where the X-ray scattering vector \mathbf{Q} ($\mathbf{Q} = \mathbf{k}_1 - \mathbf{k}_0$) is normal to the sample

surface (parallel to surface normal \mathbf{n}) and in-plane measurement geometry illustrations from two sides (Figure 2-6b and 2-6c).²⁹ In this illustration, \mathbf{k}_0 and \mathbf{k}_1 are the incident and diffracted beams, respectively. Angle ω is an angle between incident beam \mathbf{k}_0 and \mathbf{a} vector that defines the intersection line between the sample surface and the X-ray incidence planes. In Bragg-Brentano geometry, this angle is well defined while in in-plane diffraction this angle coincides with the angle ϕ that defines the rotation of the sample around its surface normal \mathbf{n} . Angle χ is defined as an angle between the surface normal \mathbf{n} and the X-ray incidence plane. 2θ angle is an angle between incident \mathbf{k}_0 and diffracted \mathbf{k}_1 beams.

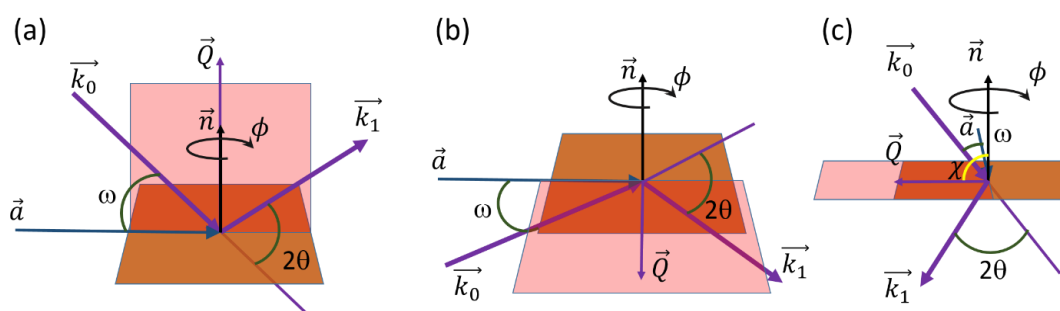


Figure 2-6. (a) Bragg-Brentano measurement geometry. (b) and (c) In-plane measurement geometry from two perspectives. (Mikhail Chubarov, Penn State)²⁹

2.6.4 Transmission electron microscopy

Characterization of atomic and chemical structure of materials is the key to understand the physic and chemistry properties at nanoscale and to further tune the properties.³⁰ The nature of the atomic bonding structure gives direct information regarding both electronic and mechanical properties. The nanoscale structure change

(such as defects, substitutional doping, grain boundary) in 2D materials can be even more crucial considering they have limited expansion in z-direction. In order to achieve high spatial resolution studies, aberration-corrected high-resolution transmission electron microscopy (AC-HRTEM) and scanning transmission electron microscopy (S/TEM) are commonly used for 2D materials. The atomically thin and transferrable properties of 2D materials advance the imaging the materials under TEM as film/flake can be suspended on the TEM grid easily. In addition, large area imaging and diffraction can be performed to gain information regarding the crystallinity of the films and moiré pattern of stacking and twisted stacking 2D materials can also be identified and studied under TEM, which has been recently reported to probe new physic properties.³¹⁻³³

Additionally, several advances have been critical in the field of electron microscopy which have allowed for atomic resolution imaging of 2D materials. Hardware aberration corrector electron optics dramatically minimizes the effect of intrinsic spherical aberrations of electron lenses and chromatic aberration correctors or monochromators can reduce the energy spread of the electron beam illumination for sub-ångstrom imaging.³⁴ The other important perspective is the low accelerating voltages (~60-80 kV) has been developed for imaging of 2D materials. The dramatically reduces the possible damage to the sample as well as the increasing electron scattering cross-section at low voltage, which produces more contract for a given illumination dose.^{35,36}

2.7 References

- (1) Ohring, M. *Materials Science of Thin Films : Deposition and Structure*; Academic Press, 2002.
- (2) Lai, K. K.; Lamb, H. H. Tungsten Chemical Vapor Deposition Using Tungsten Hexacarbonyl: Microstructure of as-Deposited and Annealed Films. *Thin Solid Films* **2000**, *370* (1), 114–121.
- (3) Lander, J. J.; Germer, L. H. Plating Molybdenum, Tungsten, and Chromium by Thermal Decomposition of Their Carbonyls. *Trans. Am. Inst. Min. Metall. Eng.* **1948**, *175*, 648–692.
- (4) Karlson, U.; Frankenberger, W. T.; Spencer, W. F. Physicochemical Properties of Dimethyl Selenide and Dimethyl Diselenide. *J. Chem. Eng. Data* **1994**, *39* (3), 608–610.
- (5) Shenai-Khatkhate, D. V.; DiCarlo, R. L.; Ware, R. A. Accurate Vapor Pressure Equation for Trimethylindium in OMVPE. *J. Cryst. Growth* **2008**, *310* (7–9), 2395–2398.
- (6) Zhang, Y.; Zhang, Y.; Ji, Q.; Ju, J.; Yuan, H.; Shi, J.; Gao, T.; Ma, D.; Liu, M.; Chen, Y.; Song, X.; Hwang, H. Y.; Cui, Y.; Liu, Z. Controlled Growth of High-Quality Monolayer WS₂ Layers on Sapphire and Imaging Its Grain Boundary. *ACS Nano* **2013**, *7* (10), 8963–8971.
- (7) Lin, Y.-C.; Zhang, W.; Huang, J.-K.; Liu, K.-K.; Lee, Y.-H.; Liang, C.-T.; Chu, C.-W.; Li, L.-J. Wafer-Scale MoS₂ Thin Layers Prepared by MoO₃ Sulfurization. *Nanoscale* **2012**, *4* (20), 6637.
- (8) Elías, A. L.; Perea-López, N.; Castro-Beltrán, A.; Berkdemir, A.; Lv, R.; Feng, S.;

- Long, A. D.; Hayashi, T.; Kim, Y. A.; Endo, M.; Gutiérrez, H. R.; Pradhan, N. R.; Balicas, L.; Mallouk, T. E.; López-Urías, F.; Terrones, H.; Terrones, M. Controlled Synthesis and Transfer of Large-Area WS₂ Sheets: From Single Layer to Few Layers. *ACS Nano* **2013**, 7 (6), 5235–5242.
- (9) Ma, D.; Shi, J.; Ji, Q.; Chen, K.; Yin, J.; Lin, Y.; Zhang, Y.; Liu, M.; Feng, Q.; Song, X.; Guo, X.; Zhang, J.; Zhang, Y.; Liu, Z. A Universal Etching-Free Transfer of MoS₂ Films for Applications in Photodetectors. *Nano Res.* **2015**, 8 (11), 3662–3672.
- (10) Xu, Z.-Q.; Zhang, Y.; Lin, S.; Zheng, C.; Zhong, Y. L.; Xia, X.; Li, Z.; Sophia, P. J.; Fuhrer, M. S.; Cheng, Y.-B.; Bao, Q. Synthesis and Transfer of Large-Area Monolayer WS₂ Crystals: Moving Toward the Recyclable Use of Sapphire Substrates. *ACS Nano* **2015**, 9 (6), 6178–6187.
- (11) Qi, J. L.; Wang, X.; Lin, J. H.; Zhang, F.; Feng, J. C.; Fei, W.-D. A High-Performance Supercapacitor of Vertically-Oriented Few-Layered Graphene with High-Density Defects. *Nanoscale* **2015**, 7 (8), 3675–3682.
- (12) Chow, P. K.; Singh, E.; Viana, B. C.; Gao, J.; Luo, J.; Li, J.; Lin, Z.; Elías, A. L.; Shi, Y.; Wang, Z.; Terrones, M.; Koratkar, N. Wetting of Mono and Few-Layered WS₂ and MoS₂ Films Supported on Si/SiO₂ Substrates. *ACS Nano* **2015**, 9 (3), 3023–3031.
- (13) Azimi, G.; Dhiman, R.; Kwon, H.-M.; Paxson, A. T.; Varanasi, K. K. Hydrophobicity of Rare-Earth Oxide Ceramics. *Nat. Mater.* **2013**, 12 (4), 315–320.
- (14) Gurarlan, A.; Yu, Y.; Su, L.; Yu, Y.; Suarez, F.; Yao, S.; Zhu, Y.; Ozturk, M.; Zhang, Y.; Cao, L. Surface-Energy-Assisted Perfect Transfer of Centimeter-Scale

Monolayer and Few-Layer MoS₂ Films onto Arbitrary Substrates. *ACS Nano* **2014**, *8* (11), 11522–11528.

(15) Zhang, H.; Huang, J.; Wang, Y.; Liu, R.; Huai, X.; Jiang, J.; Anfuso, C. Atomic Force Microscopy for Two-Dimensional Materials: A Tutorial Review. *Opt. Commun.* **2018**, *406*, 3–17.

(16) Dresselhaus, M. S.; Jorio, A.; Saito, R. Characterizing Graphene, Graphite, and Carbon Nanotubes by Raman Spectroscopy. *Annu. Rev. Condens. Matter Phys.* **2010**, *1* (1), 89–108.

(17) Saito, R.; Hofmann, M.; Dresselhaus, G.; Jorio, A.; Dresselhaus, M. S. Raman Spectroscopy of Graphene and Carbon Nanotubes. *Adv. Phys.* **2011**, *60* (3), 413–550.

(18) Zhang, X.; Qiao, X.-F.; Shi, W.; Wu, J.-B.; Jiang, D.-S.; Tan, P.-H. Phonon and Raman Scattering of Two-Dimensional Transition Metal Dichalcogenides from Monolayer, Multilayer to Bulk Material. *Chem. Soc. Rev.* **2015**, *44* (9), 2757–2785.

(19) Cheiwchanchamnangij, T.; Lambrecht, W. R. L. Quasiparticle Band Structure Calculation of Monolayer, Bilayer, and Bulk MoS₂. *Phys. Rev. B* **2012**, *85* (20), 205302.

(20) Mak, K. F.; Lee, C.; Hone, J.; Shan, J.; Heinz, T. F. Atomically Thin MoS₂: A New Direct-Gap Semiconductor. *Phys. Rev. Lett.* **2010**, *105* (13), 136805.

(21) Li, T.; Galli, G. Electronic Properties of MoS₂ Nanoparticles. *J. Phys. Chem. C* **2007**, *111* (44), 16192–16196.

(22) Tripathi, G. S. Itinerant Electrons in Strong Magnetic Fields: Onset of a Metamagnetic Transition. *Phys. Rev. B* **1995**, *52* (9), 6522–6529.

- (23) Finkelstein, G.; Shtrikman, H.; Bar-Joseph, I. Optical Spectroscopy of a Two-Dimensional Electron Gas near the Metal-Insulator Transition. *Phys. Rev. Lett.* **1995**, *74* (6), 976–979.
- (24) Stébé, B.; Ainane, A. Ground State Energy and Optical Absorption of Excitonic Trions in Two Dimensional Semiconductors. *Superlattices Microstruct.* **1989**, *5* (4), 545–548.
- (25) Tongay, S.; Zhou, J.; Ataca, C.; Liu, J.; Kang, J. S.; Matthews, T. S.; You, L.; Li, J.; Grossman, J. C.; Wu, J. Broad-Range Modulation of Light Emission in Two-Dimensional Semiconductors by Molecular Physisorption Gating. *Nano Lett.* **2013**, *13* (6), 2831–2836.
- (26) Mak, K. F.; He, K.; Lee, C.; Lee, G. H.; Hone, J.; Heinz, T. F.; Shan, J. Tightly Bound Trions in Monolayer MoS₂. *Nat. Mater.* **2013**, *12* (3), 207–211.
- (27) Ross, J. S.; Wu, S.; Yu, H.; Ghimire, N. J.; Jones, A. M.; Aivazian, G.; Yan, J.; Mandrus, D. G.; Xiao, D.; Yao, W.; Xu, X. Electrical Control of Neutral and Charged Excitons in a Monolayer Semiconductor. *Nat. Commun.* **2013**, *4* (1), 1474.
- (28) Mouri, S.; Miyauchi, Y.; Matsuda, K. Tunable Photoluminescence of Monolayer MoS₂ via Chemical Doping. *Nano Lett.* **2013**, *13* (12), 5944–5948.
- (29) Chubarov, M.; Choudhury, T. H.; Zhang, X.; Redwing, J. M. In-Plane x-Ray Diffraction for Characterization of Monolayer and Few-Layer Transition Metal Dichalcogenide Films. *Nanotechnology* **2018**, *29* (5), 055706.
- (30) Rasool, H. I.; Ophus, C.; Zettl, A. Atomic Defects in Two Dimensional Materials.

Adv. Mater. **2015**, 27 (38), 5771–5777.

(31) Cao, Y.; Fatemi, V.; Demir, A.; Fang, S.; Tomarken, S. L.; Luo, J. Y.; Sanchez-Yamagishi, J. D.; Watanabe, K.; Taniguchi, T.; Kaxiras, E.; Ashoori, R. C.; Jarillo-Herrero, P. Correlated Insulator Behaviour at Half-Filling in Magic-Angle Graphene Superlattices. *Nature* **2018**, 556 (7699), 80–84.

(32) Cao, Y.; Fatemi, V.; Fang, S.; Watanabe, K.; Taniguchi, T.; Kaxiras, E.; Jarillo-Herrero, P. Unconventional Superconductivity in Magic-Angle Graphene Superlattices. *Nature* **2018**, 556 (7699), 43–50.

(33) Yoo, H.; Engelke, R.; Carr, S.; Fang, S.; Zhang, K.; Cazeaux, P.; Sung, S. H.; Hovden, R.; Tsen, A. W.; Taniguchi, T.; Watanabe, K.; Yi, G.-C.; Kim, M.; Luskin, M.; Tadmor, E. B.; Kaxiras, E.; Kim, P. Atomic and Electronic Reconstruction at the van Der Waals Interface in Twisted Bilayer Graphene. *Nat. Mater.* **2019**, 18 (5), 448–453.

(34) Warner, J. H.; Margine, E. R.; Mukai, M.; Robertson, A. W.; Giustino, F.; Kirkland, A. I. Dislocation-Driven Deformations in Graphene. *Science*. **2012**, 337 (6091), 209–212.

(35) Suenaga, K.; Koshino, M. Atom-by-Atom Spectroscopy at Graphene Edge. *Nature* **2010**, 468 (7327), 1088–1090.

(36) Urban, K. W.; Meyer, J. C.; Erni, R.; Rossell, M. D.; Kisielowski, C.; Yang, L.; Park, C.-H.; Crommie, M. F.; Cohen, M. L.; Louie, S. G.; Zettl, A. Studying Atomic Structures by Aberration-Corrected Transmission Electron Microscopy. *Science*. **2008**, 321 (5888), 506–510.

Chapter 3

Influence of Carbon and Precursor Consideration in the Growth of WSe₂

This chapter discusses initial development of a metalorganic chemical vapor deposition (MOCVD) of monolayer or few-layer WSe₂ thin films and the influence of unintentional carbon incorporation when using metalorganic chalcogen precursor. The results demonstrate the presence of a defective graphene layer that forms simultaneously during MOCVD growth of WSe₂ on sapphire at high growth temperature and high Se:W ratio when using dimethyl selenide as chalcogen precursors. The formation of the defective graphene layer on sapphire competes with the nucleation and lateral growth of WSe₂ ultimately suppressing lateral growth and increasing the vertical growth rate of the domains. The alternative use of hydride chalcogen precursor such as hydrogen selenide eliminates the main carbon source during the growth process and thus prevents the formation of defective graphene layer enables coalesced monolayer and few-layer WSe₂ films.

3.1 Introduction

Unintentional carbon incorporation has been a persistent problem in metalorganic chemical vapor deposition (MOCVD) processes due to the use of precursor molecules with organic ligands. In the conventional MOCVD growth of III-V compound semiconductor thin films, carbon concentrations are typically lower than 10^{15} cm^{-3} .¹ However, even low levels of carbon can impact device performance and therefore carbon

as both an unintentional impurity and intentional dopant in MOCVD has been thoroughly investigated over the years. Compared to conventional MOCVD-grown semiconductor layers which may be hundreds of nanometers or more in thickness, two-dimensional (2D) transition metal dichalcogenide (TMD) monolayers are atomically thin with highly reactive edge surfaces and are bound to the substrate by van der Waals forces. Therefore, the presence of even small amounts of carbon in TMD growth may impact the nucleation and lateral growth of TMD layers and the resulting structural, optical and electrical properties of the films.

In the case of WSe₂, previous studies have demonstrated that MOCVD growth conditions, particularly substrate temperature and selenium-to-tungsten (Se:W) ratio, play a significant role in the nucleation and lateral growth of the films.² The high melting temperature/low vapor pressure of transition metals such as W in this case results in reduced surface adatom mobility which necessitates the use of high substrate temperatures (>600 °C) to enhance surface diffusion and achieve large domain sizes. On the other hand, the low melting temperature/high vapor pressure of Se and other chalcogens reduces the sticking coefficient of Se on the growth surface which makes it necessary to use very high Se:W ratios in order to achieve large and stoichiometric domains.² While high Se:W can be obtained using metalorganic precursors through manipulating the bubbler temperatures for intentional vapor pressure and controlling the carrier gas through the bubblers, the extreme high flow rate of metalorganic precursor and high growth temperature raises the concern of carbon contamination. Although the presence of residual carbon was noted in TMD monolayer and few-layer thin films grown

using MOCVD precursors,^{2,3} the reason for the formation of the carbon in the films has not been understood and the influence of the carbon has not been investigated in detail.

In this chapter, we examined the growth of WSe₂ thin films on (0001) sapphire (α -Al₂O₃) substrates by MOCVD in a vertical cold-wall reactor chamber using tungsten hexacarbonyl (W(CO)₆), dimethyl selenide (DMSe) and hydrogen selenide (H₂Se) as precursors. The results reveal the formation of a defective graphene layer on the sapphire substrate at high substrate temperature (~800 °C) and Se/W ratios over 3200 when DMSe is used as the Se precursor which competes with the nucleation and growth of WSe₂ on the sapphire surface and impacts the lateral growth as well as the epitaxy of the triangular WSe₂ islands. In comparison, carbon contamination does not occur when H₂Se is used in place of DMSe indicating that the methyl radicals from DMSe are the primary source of carbon. Without the competition from carbon contamination, a high nucleation rate and a coalesced WSe₂ film can be achieved when selecting H₂Se as chalcogen precursor. These results identify the influence of carbon in the MOCVD growth of 2D TMD films and suggest a carbon-free hydride chalcogen as a better choice in precursor selection, which establish the foundation of further study in Chapter 4 and 5.

3.2 Experimental Details

3.2.1 MOCVD growth conditions

Tungsten diselenide films were synthesized using W(CO)₆ (Sigma-Aldrich, 99.99% purity), DMSe (NOVA-KEM, 99.99% purity) and H₂Se (Matheson, 99.998%

purity) in the cold-wall vertical quartz tube reactor with an inductively heated SiC-coated graphite susceptor. Ultra high purity hydrogen was used as the carrier gas through the bubblers and reactor to maintain a total flow rate at 450 sccm. The W(CO)_6 powder was contained inside a stainless steel bubbler which was held at 30 °C and 730 Torr.

Hydrogen carrier gas was passed through the bubbler at a flow rate of 15 sccm which resulted in a W(CO)_6 flow rate of 9×10^{-4} sccm out of the bubbler. DMSe liquid was also contained inside a stainless steel bubbler which was held at room temperature and 760 Torr. Hydrogen carrier gas was passed through the bubbler at a flow rate in the range of 2.5-25 sccm which resulted in a DMSe flow rate of 0.75-7.5 sccm out of the bubbler. Growth was carried out at a total reactor pressure of 700 Torr, a growth time of 30 min and a substrate temperature of 800 °C for all experiments. As-received c-plane (0001) double-side polished sapphire were used as substrates.

3.2.2 Post-growth characterization setup

To analyze the composition of the atomically thin films, surface elemental compositions of different regions on the sample were analyzed by high resolution Auger electron spectroscopy (AES) in a PHI 720 Scanning Auger Nanoprobe using 10keV electron beam energy. Raman spectroscopy was carried out in a HORIBA LabRAM HR Evolution high spectral resolution analytical Raman microscope with a laser wavelength of 532 nm. To measure the film thickness and domain heights, a step edge was formed on the as-grown WSe_2 film via using a plastic tweezer to scratch the sample surface and the step height was profiled using a Digital Instruments Multimode Atomic Force

Microscope (AFM). Compared the AFM, larger range of surface morphology of the samples were shown in field emission scanning electron microscopy (FESEM) images obtained in a Zeiss Merlin instrument. Transmission electron microscopy (TEM) was used to examine the cross-sectional morphology and obtain structural information on the WSe₂ samples. Cross-sectional TEM samples were fabricated by the focused ion beam (FIB) method on a HELIOS Nanolab 660. A thin layer of gold was sputtered on top of the substrate to enhance the conductivity and a layer of platinum was deposited to protect and mark the cut region. A FEI Tecnai G2 TEM operating at 80 kV was used to study the atomic structure of the WSe₂ samples produced in this study.

3.3 Chalcogen Precursor: DMSe

3.3.1 Effect of Se:W ratio and high DMSe flow rate

The effect of Se:W ratio on the nucleation and lateral growth of WSe₂ on sapphire was initially investigated by maintaining a constant W(CO)₆ partial pressure of 1.4×10^{-3} Torr in the reactor chamber and varying the flow rate of DMSe to change the Se:W ratio from approximately 800 to 8000. The WSe₂ domain size increased and the nucleation density decreased as the Se:W ratio was increased from 800 to 4800 as shown in Figure 3-1. This follows the expectation as the increased Se:W ratio results in the surface species moving towards to stoichiometric ratio due to the large vapor pressure difference between Se and W. Therefore the growth rate of domains increases and the nucleation density decreases in compensation for surface species participating into the growth of existing

domains. In addition, AFM results in Figure 3-2 shows the domain thickness increases with increasing Se:W ratio. This indicates the surface energy changed on the substrates since the WSe₂ domains prefer to wet the whole sapphire surface at low Se:W ratio while they prefer to stay on top of themselves at high Se:W ratio.

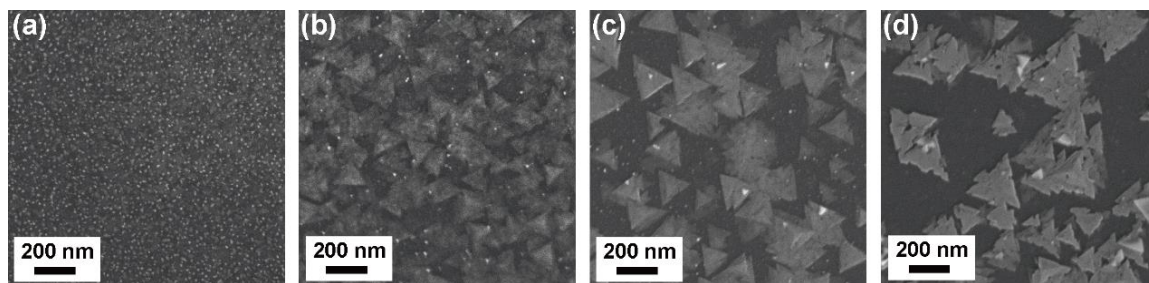


Figure 3-1. FESEM images of WSe₂ domains grown on sapphire substrate using DMSe and W(CO)₆ as precursors with Se:W ratios of (a) 800, (b) 1600, (c) 3200, (d) 4800. The (e) average domain size, (f) surface coverage and (g) domain thickness of the as-grown WSe₂ at Se:W ratios from 800 to 8000.

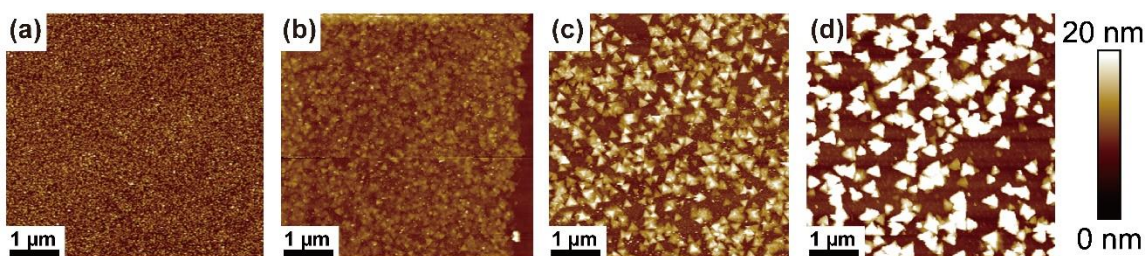


Figure 3-2. AFM images of WSe₂ domains grown on sapphire substrate using DMSe and W(CO)₆ as precursors with Se:W ratios of (a) 800, (b) 1600, (c) 3200, (d) 4800.

Further increases in the Se:W ratio up to 8000 did not result in a significant increase in the domain size or a reduction in both nucleation density and surface coverage as shown in Figure 3-3a and 3-3b. Interestingly, while the surface coverage of WSe₂ domains was reduced at high Se:W ratios above 3200, the height of the domains increased significantly from < 10 nm at Se:W=3200 to 20-30 nm for Se:W ratios ranging from 4800 to 8000

(Figure 3-3c). In addition, as the Se:W ratio was increased above 3200, the edges of the triangular domains become jagged and pits appear in the islands and near the domain edges (Figure 3-1d). Prior studies have reported changes in the shape and edge structure of TMD domains as a function of the chalcogen-to-metal ratio⁴ and growth rate⁵ and in the presence of impurities and oxidation⁶ and intentional dopants⁷.

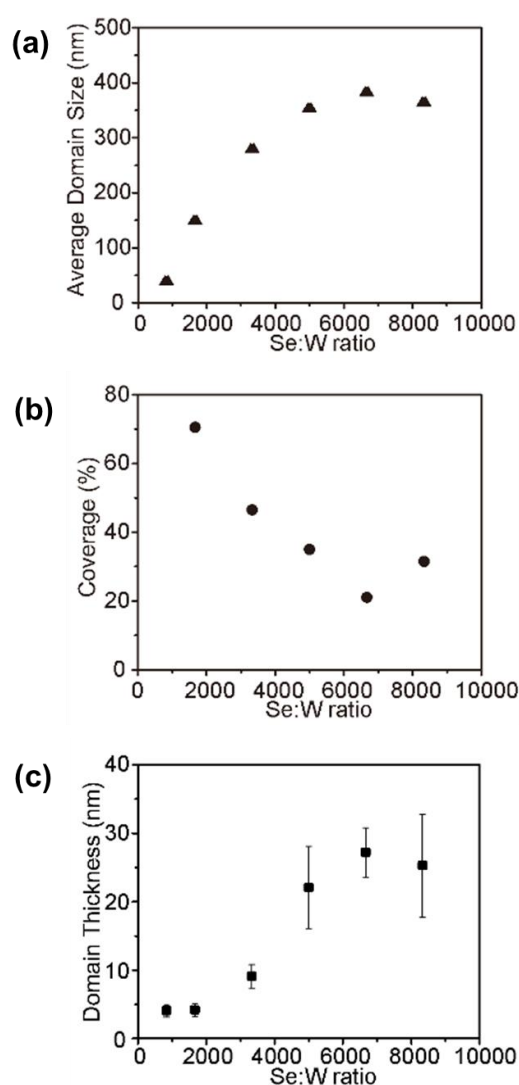


Figure 3-3. The (a) average domain size, (b) surface coverage and (c) domain thickness of the as-grown WSe₂ at Se:W ratios from 800 to 8000.

3.3.2 Discovery of defective graphene layer

The change in the lateral versus vertical growth rate at high Se:W ratios as well as the deformed edge shape in the previous section suggests changes in surface energy which make it more energetically favorable for the WSe₂ to grow vertically on existing domains instead of laterally on the substrate surface. When examining the scratched sample surface that was used to obtain a step height for domain thickness measurements by FESEM (Figure 3-4a), a region of darker contrast (region 3) was observed between the WSe₂ triangle domains (region 2) and the sapphire surface (region 1) at the scratched boundary, which suggested the presence of a thin layer of different conductivity on the surface. This layer was determined to be ~1.5 nm thick from AFM measurements in the scanned region (Figure 3-4b). The combining FESEM and AFM results confirm an additional coalesced layer formed between WSe₂ domains and sapphire substrate surface during the growth. In order to identify the composition of this layer, AES was used to analyze the elemental composition of the three regions with different FESEM contrasts, and the results are shown in Figure 3-4c (done by Zakaria Al Balushi, Penn State). Note that AES is merely sensitive to compositional surface element and thus should not be affected by the impurity in the deep of sapphire substrates. Only Al and O were detected on the sapphire surface region (region 1). As expected, W and Se elements were detected in the triangular domain regions (region 2) consistent with the formation of WSe₂ along with a small carbon signal. In the region between the WSe₂ domains (region 3), however, a strong carbon signal was observed but no W or Se signals indicating that the thin layer on the sapphire surface contains mostly carbon.

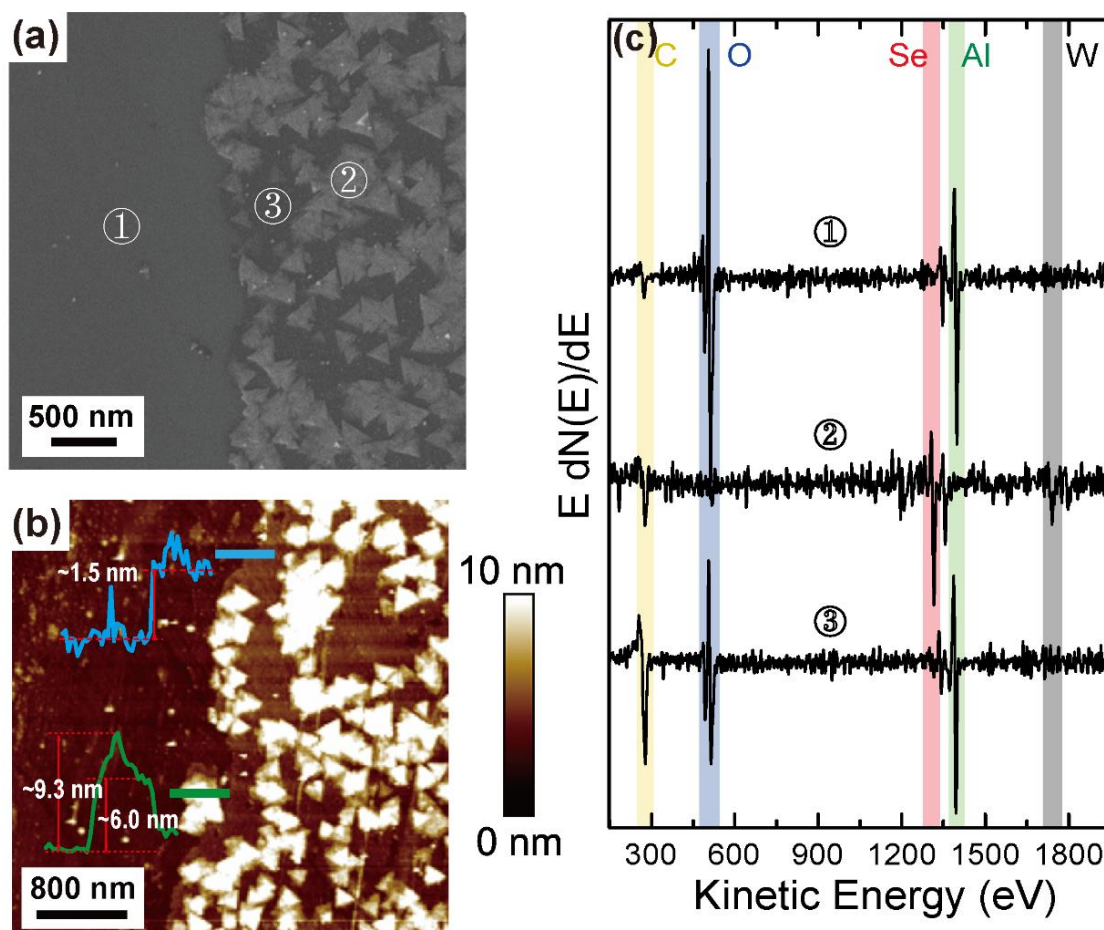


Figure 3-4. (a) FESEM image of the WSe₂ sample grown at 800 °C with Se:W=3200 showing three regions: 1) sapphire surface; 2) WSe₂ triangular domains; 3) region of darker contrast between WSe₂ islands. (b) AFM image revealing a continuous layer ~1.5 nm thick and WSe₂ triangular domains ~6-9 nm thick on the sapphire surface. (c) AES spectra indicating the presence of Al and O in region 1, W, Se and C in region 2, and Al, O, and C in region 3.

Now that the additional layer was identified as carbon layer, cross-sectional TEM was applied to acquire further structural information of this carbon layer (done by Fu Zhang, Penn State). A cross-sectional TEM image of the sample grown using DMSe at

800 °C and Se:W=3200, shown in Figure 3-5, obtained in an area similar to that of region 2 above, revealed a carbon layer beneath the WSe₂ domains. The thickness of this carbon layer is ~2 nm, which is consistent with the AFM thickness measurement in Figure 3-4b. Additional cross-sectional TEM images obtained from different regions across the sample in Figure 3-6 show that the thickness of the carbon layer varies from ~1.2 to ~5.5 nm. The WSe₂ layer is ~6 nm thick and shows a layered structure with spacing between layers of ~0.67 nm which is consistent with WSe₂. Some regions of the carbon layer exhibit a layered structure indicating the formation of graphene.

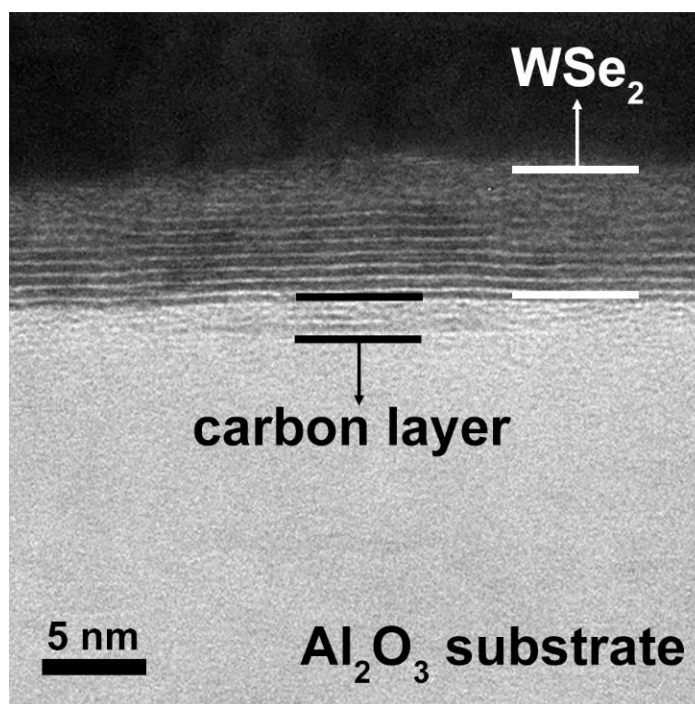


Figure 3-5. Cross-sectional TEM image of WSe₂ sample grown using DMSe at 800 °C and Se:W=3200 revealing a carbon layer beneath the WSe₂. Some regions of the carbon layer exhibit a layered structure typical of defective graphene.

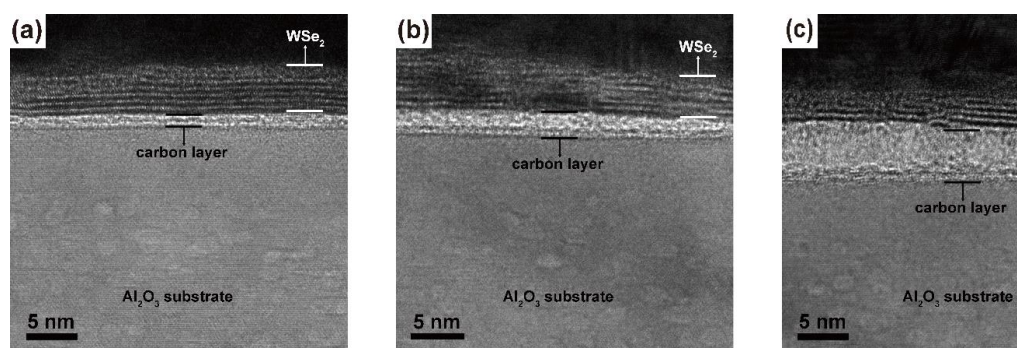


Figure 3-6. Cross-sectional TEM images of different regions on the WSe₂ sample grown using DMSe at 800 °C and Se:W=3200 showing different carbon layer thickness (a) ~1.2nm; (b) ~2.7nm; (c) ~5.5nm.

3.3.3 Origin of defective graphene layer

The carbon layer present in the WSe₂ sample shown in Figures 2 and 3 likely results from the high concentration of carbon-containing ligands present in the MOCVD growth environment. Prior studies have demonstrated that methane (CH₄) can be used as a precursor to deposit graphene on sapphire at temperatures as low as 950°C.^{8,9} Graphene produced by this process is typically defective as demonstrated by the presence of a strong D peak at ~1350 cm⁻¹ in the Raman spectra.^{8,10,11} The methyl radicals produced by the decomposition of the DMSe precursor are likely responsible for the formation of the carbon layer on sapphire in the WSe₂ MOCVD process. Methyl radicals (CH₃*) are more chemically reactive than CH₄, consequently, this could lead to defective graphene formation at the lower temperatures (800°C) used in this study. Furthermore, the high Se:W ratios utilized in the growth result in an inlet C:W ratio which is two times higher than the Se:W ratio creating a carbon-rich growth environment. To investigate this

further, a growth run was carried out at 800°C under identical conditions to that used for WSe₂ growth but with only DMSe and H₂ flowing through the reactor. A high density of nanoscale nuclei were observed on the sapphire substrate through FESEM as shown in Figure 3-7a. The Raman spectrum of this sample in Figure 3-7b revealed the presence of

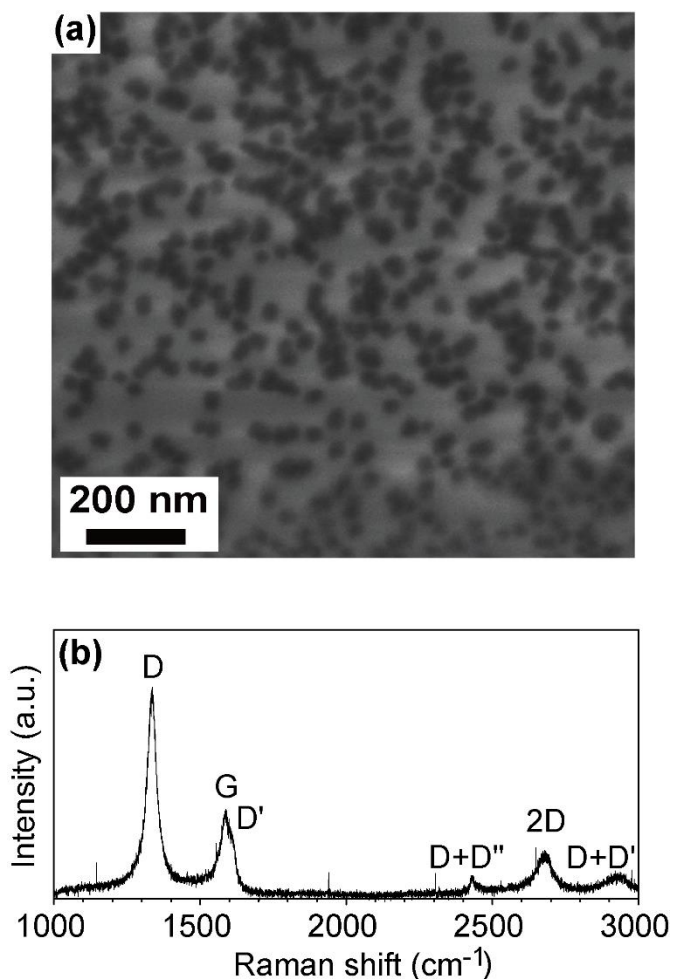


Figure 3-7. Sapphire surface after flowing only DMSe and H₂ at 800 °C under identical condition for WSe₂ growth: **(a)** FESEM image showing the presence of defective graphene domains; **(b)** Raman spectrum of sapphire surface showing G and 2D peaks associated with graphene and the family of D peaks indicating defects in the graphene.

peaks associated with defective graphene. The presence of carbon G peak at $\sim 1580\text{ cm}^{-1}$ and 2D peak at $\sim 2680\text{ cm}^{-1}$ indicates a graphene-like structure^{10,12} while the high intensity of the carbon D peaks indicates that the graphene is highly defective.^{10,11} The size of the defective graphene domains is small, less than 50 nm, possibly due to the low carbon adatom surface diffusion lengths and growth rate at 800°C and the relatively short 30-min growth time. In contrast, the carbon layer in between the WSe₂ domains is continuous with a thickness of 1.5 nm suggesting that the deposition rate of carbon is higher in the presence of W(CO)₆. One interpretation is that the tungsten adatoms on the surface act as a catalyst to adsorb carbon and promote graphene formation as previously reported.¹³

3.4 Chalcogen Precursor: H₂Se

3.4.1 Elimination of carbon

Hydride precursors are typically utilized in III-V MOCVD to reduce carbon incorporation due to their lack of carbon-containing ligands and the atomic hydrogen produced from hydride decomposition which reacts with methyl groups on the surface to form methane that can readily desorb from substrate surface.^{14,15} To investigate the effect of the chalcogen precursor chemistry, WSe₂ films were grown on sapphire using W(CO)₆ and H₂Se or DMSe using the same Se:W ratio of 3200 and substrate temperature of 800°C. Compared to the growth with DMSe (Figure 3-8a), the Raman spectrum of the

sample grown with H_2Se (Figure 3-8b) shows negligible carbon D and G peaks, which indicates a significant reduction of carbon deposition on the sample.

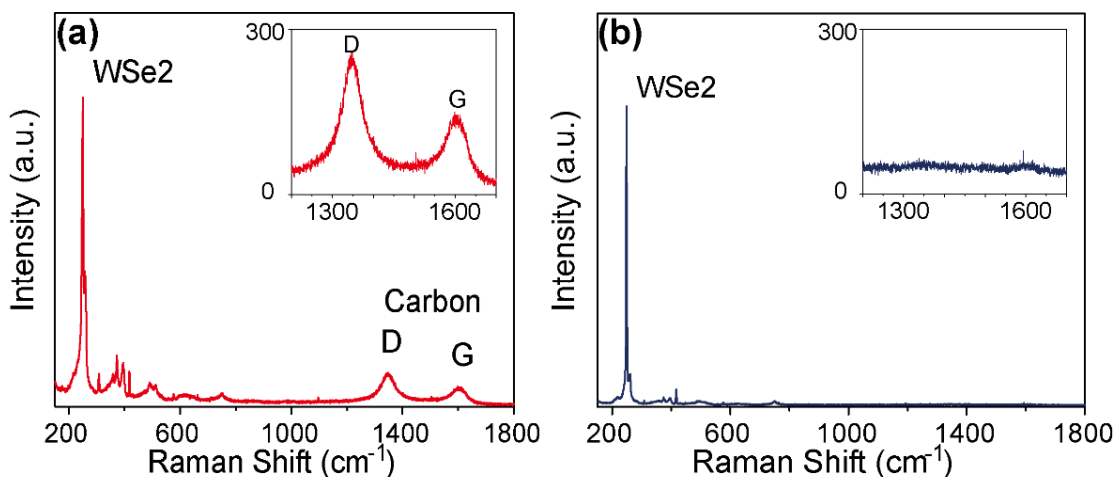


Figure 3-8. Raman spectra of WSe_2 grown using (a) DMSe and (b) H_2Se at 800°C and $\text{Se}:\text{W}$ ratio of 3200. The insets are zoom-in regions showing the carbon D and G peaks in WSe_2 grown with DMSe but no carbon characteristic peaks in WSe_2 grown with H_2Se .

3.4.2 Fully coalesced WSe_2 film

The AFM results also show significantly different nucleation density and lateral growth of WSe_2 with H_2Se versus DMSe . Unlike WSe_2 growth with DMSe in Figure 3-9a where the surface coverage is reduced and the WSe_2 tends to grow vertically on top of existing WSe_2 islands instead of nucleating on the carbon-covered sapphire surface resulting in multi-layer domains ~ 10 nm in height, the density of WSe_2 domains is significantly increased with H_2Se resulting in a fully coalesced film, approximately 3 nm in thickness (Figure 3-9b).

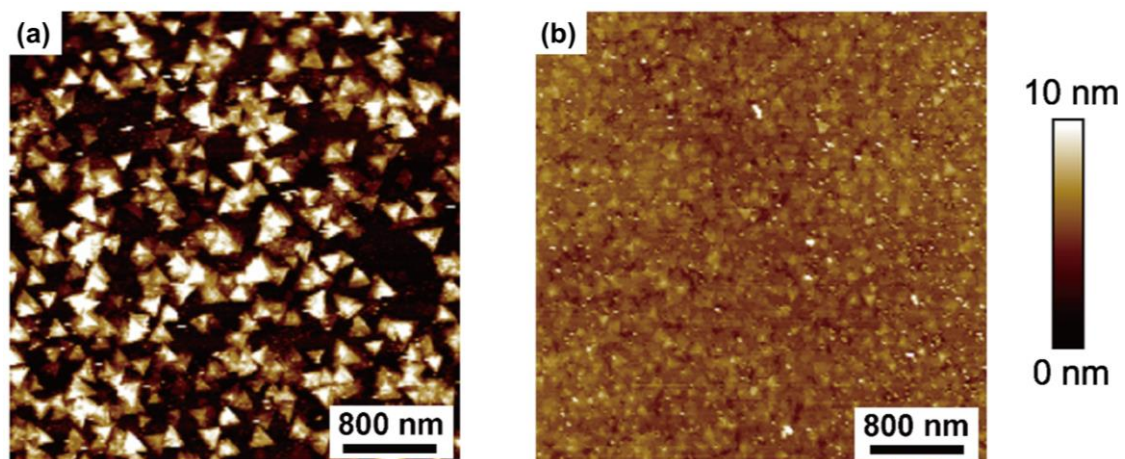


Figure 3-9. AFM images of WSe₂ grown using (a) DMSe and (b) H₂Se at 800 °C and Se:W ratio of 3200.

The defective graphene layer can also be viewed as a competitor to WSe₂ on the substrate surface and thus limits the nucleation as well as the lateral growth of WSe₂. As shown Figure 3-1c and 3-1d, the WSe₂ nucleation density decreases but the domain size does not increase as the Se:W ratio is further increased from 3200 to 4800 and beyond. Increasing the Se:W results in a higher concentration of methyl radicals in the gas phase, therefore, more carbon atoms adsorb on the sapphire surface and occupy sites that would otherwise be available for nucleation and lateral growth of WSe₂. As a result, the W and Se atoms prefer to nucleate and grow on existing WSe₂ domains due possibly to site competition of W, Se and C on the defective graphene surface and/or the reduced surface energy of the defective graphene compared to WSe₂. In either case, the presence of defective graphene on the sapphire surface increases the vertical-to-lateral growth of the WSe₂ domains. In addition, the WSe₂ domains start losing their epitaxy at high Se:W ratio. It can be interpreted that the defective graphene layer cannot guide the WSe₂ domains on top due to its own random orientation, or/and the competition between WSe₂

and C limits the rotation of initial WSe₂ nucleation thus resulting in distorted orientation. In comparison, the results obtained for WSe₂ films grown with H₂Se which contain negligible amounts of carbon support this interpretation. Figure 3-10 shows the TEM image of the WSe₂ film grown with H₂Se (done by Fu Zhang, Penn State). The absence of competing carbon adsorption, diffusion and graphene growth on the sapphire surface results in a higher nucleation density of WSe₂ and nearly complete coalescence of the films. The inset selected area electron diffraction (SAED) pattern shows a clearly discernible hexagonal symmetry of the WSe₂ film and two main orientations with 30°

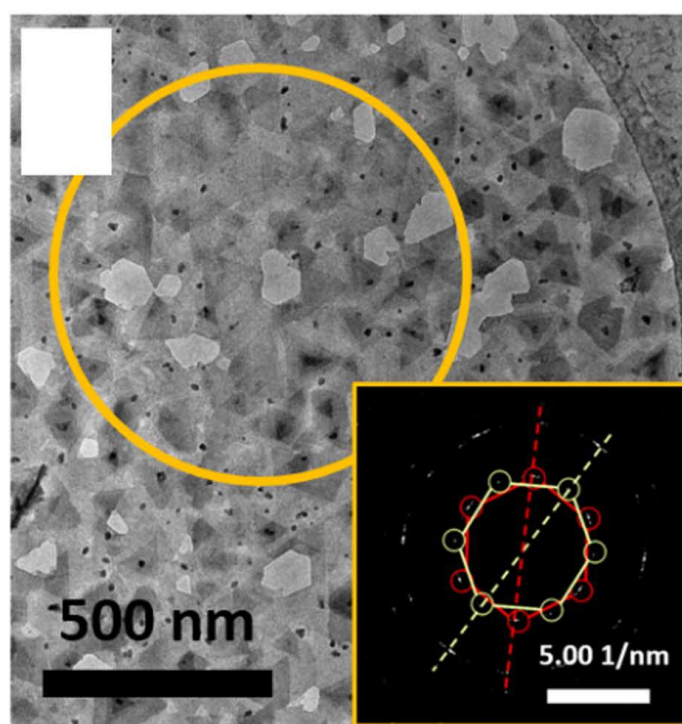


Figure 3-10. TEM image of the WSe₂ film grown using H₂Se at 800 °C and Se:W ratio of 3200, inset SAED pattern of the yellow circle showing two hexagonal diffraction patterns with 30° misorientation indicating epitaxial growth of WSe₂ on sapphire.

misorientation. This is consistent with previous simulation results for MoS₂ grown on sapphire suggesting the two lowest energy configurations of the epitaxy.¹⁶

3.4.3 Toxicity and safety

Hydrogen Selenide (H₂Se) is a colorless inorganic acid gas at room temperature. It is also a flammable and highly toxic gas that requires extra caution when handling.¹⁷ It can attack the eyes and mucus membranes.¹⁷ The permissible exposure limit (threshold limit value) for H₂Se is 50 ppb and irritation becomes intolerable at 2 ppm.¹⁸ Safe laboratory use of H₂Se requires ventilated enclosures for the gas cylinder, gas handling manifold, CVD reactor, exhaust pump, etc. Gas lines were welded stainless steel with metal gasket-seal fittings that were helium leak tested under vacuum. In order to prevent H₂Se exposure to air, all exhaust from the system is run through a chemical scrubber. A NaOH neutralization system (CVD Equipment Inc. EasyExhaust™) was used to treat the exhaust gases and a toxic gas detection system (Honeywell Chemcassette®) was in place for H₂Se detection during system operation which can switch off all pneumatic valves to shut off all gas flow in case of detecting overlimit amount of H₂Se or an emergency.

3.5 Conclusions

The results of this study demonstrate the potential problems that may be encountered in using organic chalcogen precursors in MOCVD growth of very thin TMDs films.

MOCVD provides opportunities for scalability to large wafer sizes, improved thickness

and composition uniformity and the ability for in-situ heterostructure growth, however, carbon deposition as found in our experiments significantly reduces the ability of MOCVD to produce coalesced WSe₂ films with large domain sizes on sapphire substrates. It is also possible that carbon is incorporated substitutionally within the WSe₂ domains or is attached at the domain edge which could further impact the optical and electrical properties of the films but additional studies are required to determine this. Also, carbon deposition is expected to be strongly dependent on the particular substrate used for MOCVD growth and may be less of a problem on amorphous surfaces such as SiO₂/Si which do not typically promote graphene formation. In any event, hydride chalcogen precursors such as H₂Se are good candidates to replace organic chalcogen precursors used in growth although care must be taken when handling these sources due to their high toxicity.

3.6 References

- (1) Kuech, T. F.; Redwing, J. M. Carbon Doping in Metalorganic Vapor Phase Epitaxy. *J. Cryst. Growth* **1994**, *145* (1–4), 382–389.
- (2) Eichfeld, S. M.; Hossain, L.; Lin, Y.; Piasecki, A. F.; Kupp, B.; Birdwell, a G.; Burke, R. a; Lu, N.; Peng, X.; Li, J.; Azcatl, A.; McDonnell, S.; Wallace, R. M.; Kim, M. J.; Mayer, T. S.; Redwing, J. M.; Robinson, J. a. Highly Scalable, Atomically Thin WSe₂ Grown via Metal–Organic Chemical Vapor Deposition. *ACS Nano* **2015**, *9* (2), 2080–2087.
- (3) Kang, K.; Xie, S.; Huang, L.; Han, Y.; Huang, P. Y.; Mak, K. F.; Kim, C.-J.; Muller, D.; Park, J. High-Mobility Three-Atom-Thick Semiconducting Films with Wafer-Scale Homogeneity. *Nature* **2015**, *520* (7549), 656–660.
- (4) Wang, S.; Rong, Y.; Fan, Y.; Pacios, M.; Bhaskaran, H.; He, K.; Warner, J. H. Shape Evolution of Monolayer MoS₂ Crystals Grown by Chemical Vapor Deposition. *Chem. Mater.* **2014**, *26* (22), 6371–6379.
- (5) Xie, S.; Xu, M.; Liang, T.; Huang, G.; Wang, S.; Xue, G.; Meng, N.; Xu, Y.; Chen, H.; Ma, X.; Yang, D. High-Quality Round-Shaped Monolayer MoS₂ Domain and Its Transformation. *Nanoscale* **2015**, *8*, 219–225.
- (6) Ionescu, R.; George, A.; Ruiz, I.; Favors, Z.; Mutlu, Z.; Liu, C.; Ahmed, K.; Wu, R.; Jeong, J. S.; Zavala, L.; Mkhoyan, K. A.; Ozkan, M.; Ozkan, C. S. Oxygen Etching of Thick MoS₂ Films. *Chem. Commun.* **2014**, *50* (76), 11226.
- (7) Zhang, K.; Feng, S.; Wang, J.; Azcatl, A.; Lu, N.; Addou, R.; Wang, N.; Zhou,

C.; Lerach, J.; Bojan, V.; Kim, M. J.; Chen, L. Q.; Wallace, R. M.; Terrones, M.; Zhu, J.; Robinson, J. A. Manganese Doping of Monolayer MoS₂: The Substrate Is Critical. *Nano Lett.* **2015**, *15* (10), 6586–6591.

(8) Song, H. J.; Son, M.; Park, C.; Lim, H.; Levendorf, M. P.; Tsen, A. W.; Park, J.; Choi, H. C. Large Scale Metal-Free Synthesis of Graphene on Sapphire and Transfer-Free Device Fabrication. *Nanoscale* **2012**, *4* (10), 3050.

(9) Hwang, J.; Kim, M.; Campbell, D.; Alsalman, H. A.; Kwak, J. Y.; Shivaraman, S.; Woll, A. R.; Singh, A. K.; Hennig, R. G.; Gorantla, S.; Rummeli, M. H.; Spencer, M. G. Van Der Waals Epitaxial Growth of Graphene on Sapphire by Chemical Vapor Deposition without a Metal Catalyst. *ACS Nano* **2012**, *7* (1), 385–395.

(10) Ferrari, A. C.; Basko, D. M. Raman Spectroscopy as a Versatile Tool for Studying the Properties of Graphene. *Nat. Nanotechnol.* **2013**, *8* (4), 235–246.

(11) Fanton, M. A.; Robinson, J. A.; Puls, C.; Liu, Y.; Hollander, M. J.; Weiland, B. E.; Labella, M.; Trumbull, K.; Kasarda, R.; Howsare, C.; Stitt, J.; Snyder, D. W. Characterization of Graphene Films and Transistors Grown on Sapphire by Metal-Free Chemical Vapor Deposition. *ACS Nano* **2011**, *5* (10), 8062–8069.

(12) Ferrari, A. C.; Meyer, J. C.; Scardaci, V.; Casiraghi, C.; Lazzeri, M.; Mauri, F.; Piscanec, S.; Jiang, D.; Novoselov, K. S.; Roth, S.; Geim, A. K. The Raman Fingerprint of Graphene. *Phys. Rev. Lett.* **2006**, *97* (18), 41–47.

(13) Fang, W.; Hsu, A.; Shin, Y. C.; Liao, A.; Huang, S.; Song, Y.; Ling, X.; Dresselhaus, M. S.; Palacios, T.; Kong, J. Application of Tungsten as a Carbon Sink for

Synthesis of Large-Domain Uniform Monolayer Graphene Free of Bilayers/Multilayers.

Nanoscale **2015**, 7 (11), 4929–4934.

(14) Fornari, R. Epitaxy for Energy Materials. In *Handbook of Crystal Growth: Thin Films and Epitaxy: Second Edition*; 2014; Vol. 3, pp 1–49.

(15) Malik, M. A.; O'Brien, P. Precursors Basic Chemistry of CVD and ALD Precursors. In *Chemical Vapour Deposition: Precursors, Processes and Applications*; Royal Society of Chemistry: Cambridge, 2005; pp 207–271.

(16) Dumcenco, D.; Ovchinnikov, D.; Marinov, K.; Lazić, P.; Gibertini, M.; Marzari, N.; Sanchez, O. L.; Kung, Y.-C.; Krasnozhan, D.; Chen, M.-W.; Bertolazzi, S.; Gillet, P.; Fontcuberta i Morral, A.; Radenovic, A.; Kis, A. Large-Area Epitaxial Monolayer MoS₂. *ACS Nano* **2015**, 9 (4), 4611–4620.

(17) HYDROGEN SELENIDE MATERIAL SAFETY DATA SHEET

<https://www.mathesongas.com/pdfs/msds/MAT11200.pdf> (accessed Mar 17, 2019).

(18) The National Institute for Occupational Safety and Health , Occupational Health Guideline for Hydrogen Selenide <https://www.cdc.gov/niosh/docs/81-123/pdfs/0336.pdf> (accessed Mar 17, 2019).

Chapter 4

Diffusion-Controlled Epitaxial Growth of WSe₂ on Sapphire

In the previous chapter, we discuss how the unintentional carbon incorporation from using metalorganic chalcogen precursor can significantly influence the growth of monolayer or few-layer WSe₂ films, and a coalesced film can eventually be achieved through elimination of carbon contamination via hydride chalcogen precursor. Although coalesced WSe₂ film is achievable, the lack of controllability on both nucleation and lateral growth makes it extremely hard to approach monolayer growth of WSe₂. Meanwhile, the high nucleation rate of WSe₂ nucleation shown in previous chapter results in two major orientations with 30° rotation and thus the films are far from single crystal. In this chapter, we demonstrate a multi-step growth process in the same gas source CVD process for the epitaxial growth of large area, single crystal WSe₂ monolayer and few layer thin films. This multi-step growth process enables independent control of nucleation, domain ripening, lateral growth and film coalescence and provides fundamental insights into the 2D growth mechanism. The results in this chapter provide an important step toward atomic level control of the epitaxial growth of WSe₂ monolayers in a scalable process that is suitable for large area device fabrication.

4.1 Introduction

Current development of device technologies based on transition metal dichalcogenides (TMDs) requires the ability to synthesize large area single crystal

monolayer and few layer films. Although powder vapor transport (PVT) has been widely used to prepare TMD crystal domains and films,^{1,2} it is difficult to control and modulate the source supply in this process and uniform deposition over large substrate areas is challenging. In comparison, gas source chemical vapor deposition (CVD) has both the metal and chalcogen precursors located outside of the deposition chamber which enables independent control of precursor partial pressures and ratios. The realization of large area single crystal TMDC monolayer films, however, requires the ability to precisely control the density and orientation of nuclei on the substrate surface and the lateral growth rate of the domains to achieve fully-coalesced 2D monolayer films with minimal 3D growth.

In this chapter, we demonstrate a diffusion-controlled gas source CVD process for the epitaxial growth of large area, single crystal WSe₂ monolayer and few layer films on c-plane sapphire. A multi-step growth process was developed which employs modulation of the metal precursor partial pressure to independently control nucleation, domain ripening, lateral growth and film coalescence via surface diffusion processes. By separating out the nucleation and lateral growth stages, the effects of process conditions on surface diffusion and lateral growth can be clearly discerned, providing insights into the fundamental processes that control WSe₂ domain growth.

4.2 Experimental Details

4.2.1 Gas source CVD growth conditions

WSe₂ films were synthesized in the same cold wall vertical quartz tube reactor with an inductively heated SiC-coated graphite susceptor. Tungsten hexacarbonyl (W(CO)₆) and hydrogen selenide (H₂Se) were used as precursors with ultra-high purity H₂ as the carrier gas. 1 cm×1 cm square C-plane sapphire ((0001) α -Al₂O₃) were used as substrates. In a typical growth run, the substrate was heated to the growth temperature (800 °C) under 700 Torr of H₂ at a total flow rate of 450 sccm. A multi-step W(CO)₆ flow process was then used to control nucleation and lateral growth. The precursors (H₂Se and W(CO)₆) were simultaneously introduced into the gas stream when the substrate reached the growth temperature. The H₂Se flow rate was held constant at 7 sccm throughout the entire growth process. The W(CO)₆ source powder was contained inside a stainless steel bubbler which was held at 30 °C and 730 Torr. Initially, H₂ carrier gas was passed through the bubbler at a flow rate of 20 sccm which resulted in a W(CO)₆ flow rate of 1.8×10^{-3} sccm out of the bubbler for 0.5-5 min for the nucleation step. The flow rate of W(CO)₆ out of the bubbler was calculated from a mass balance considering the vapor pressure of the W(CO)₆ precursor at 30 °C^{3,4} and the bubbler pressure at 730 Torr. The W(CO)₆ was then removed from the inlet gas stream and the sample was held in H₂Se and H₂ at 800 °C for 0-50 min to allow ripening to occur. Subsequently, for the lateral growth step, W(CO)₆ was re-introduced into the inlet gas stream using a H₂ carrier gas flow rate of 4.5 sccm which resulted in a W(CO)₆ flow rate of 4.2×10^{-4} sccm. In additional experiments, the substrate temperature was held constant at 800 °C during the

nucleation and ripening steps and was varied from 600 °C to 900 °C during lateral growth. Studies were also carried out using H₂Se flow rates ranging from 4 sccm to 10 sccm during lateral growth to investigate the effect of Se:W ratio.

4.2.2 Film characterization setup

The surface morphology of the samples was analyzed by atomic force microscopy (AFM) using a Bruker Dimension Icon Atomic Force Microscope system and field emission scanning electron microscopy (FESEM) using a Zeiss Merlin instrument. Raman and photoluminescence spectroscopy were carried out using a HORIBA LabRAM HR Evolution high spectral resolution analytical Raman microscope with a laser wavelength of 532nm. The composition of the films was investigated by X-ray photoelectron spectroscopy (XPS) (Phi Versa Probe II) with monochromatic Al K α x-ray excitation at 20 kV, equipped with dual beam charge neutralization. Charging offsets were corrected by calibrating the XPS spectrum based on the C 1s peak position (284.8 eV). Peak fitting was done to confirm the stoichiometry and extent of oxidation of the films. Reflection high-energy electron diffraction (RHEED) measurement was carried out using a model RDA-003G electron gun which generates an electron beam of 20 keV and emission current of 48 μ A which was incident on the sample surface at a glancing angle of $\sim 1^\circ$. The RHEED pattern was projected on a phosphor screen mounted on a 6-in flange which was about 20 cm away from the sample and opposite to the electron gun flange in a vacuum chamber. The RHEED pattern was captured by a digital camera positioned outside the chamber facing the phosphor screen. The sample was rotated

azimuthally with a 1.8° step size increment from 0° to 180° in 100 steps and the corresponding RHEED pattern was recorded at each azimuthal angle.⁵ In-plane X-ray diffraction (XRD) measurements were conducted using a Panalytical MRD diffractometer with 5 axis cradle employing Cu K_α radiation and filtering K_β radiation employing Ni filter. For transmission electron microscopy (TEM) characterization, the WSe₂ film were transferred from sapphire substrate onto Quantifoil Au TEM grid by a PMMA-assisted water transfer method. An FEI Titan 3 (60-300) at 80 kV was used to examine and study the atomic structure of the WSe₂ film.

4.3 Single-Step Growth

In chapter 3, we have demonstrated how to achieve a coalesced WSe₂ film via removing carbon contamination and using hydride precursor. It is worth noting that even the film is fully-coalesced, the small domain sizes and lack of controllability on both film epitaxy and thickness limit its usage in 2D applications. The coalesced film was grown in a single-step process where both precursors W(CO)₆ and H₂Se were maintain at constant flow rate once the substrate reaches target temperature, and high W(CO)₆ flow rate ($\sim 9.0 \times 10^{-4}$ sccm) was adopted to provide enough nucleation for coalesced film (Note: here “high” is in terms of flow rate used in monolayer TMDs fabrication). The disadvantage of using high W(CO)₆ flow rate is the high growth rate, which results in both additional nucleation and growth for multilayers and not enough time for domains to rotate and form single epitaxy. So the question becomes “why don’t we use low W(CO)₆ flow rate and long growth time?” Figure 4-1 demonstrate the FESEM image of the

sample using very low $W(CO)_6$ flow rate (3.0×10^{-4} sccm) and long growth time (90 min). Indeed, the triangular domains under this condition depict larger domains with $\sim 2 \mu m$ in edge length and more epitaxy with fewer 30° rotation. However, the domains fail to fully coalesce with each other due to limited number of nucleation at low $W(CO)_6$ flow rate, and the contrast on those domains in FESEM indicate “pyramid” structure formed where multilayer WSe_2 starts to grow on the monolayer. Although WSe_2 domains tend to grow laterally at low $W(CO)_6$ flow rate, the limited surface diffusion length at the growth temperature is not long enough and the reactant species that fails to diffuse to the edge either nucleate as second layer or leave the surface. Higher growth temperature should help but the elevated vapor pressure of Se at higher temperature will result in even higher flow rate of H_2Se . The exceeded Se will condense downstream during the growth and higher flow rate means a more frequent clean is needed. Further reduction of flow rate of $W(CO)_6$ should also work and has been demonstrated in previous report,⁶ however, the extremely long 24-hour growth time makes the whole process not that feasible.

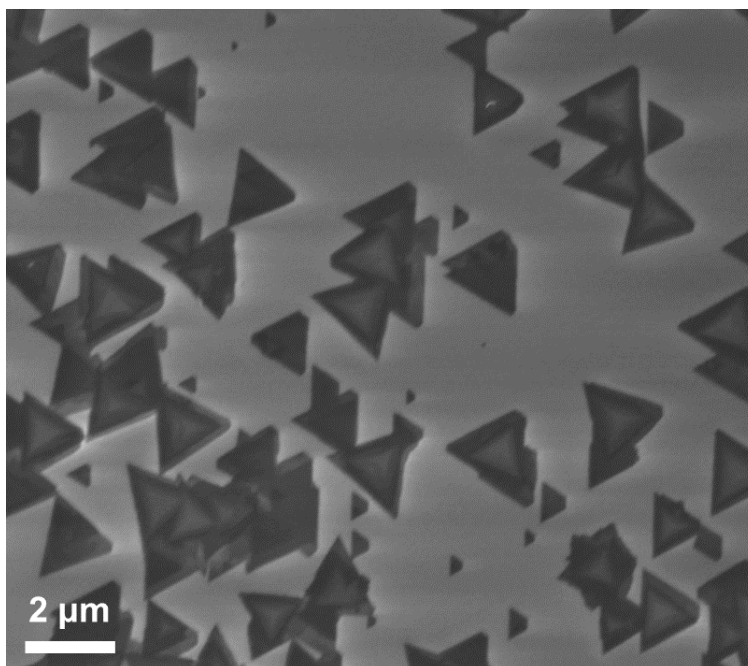


Figure 4-1. FESEM image of WSe₂ domains grown at W(CO)₆ flow rate of 3.0×10^{-4} sccm, H₂Se flow rate of 7 sccm, 800 °C substrate temperature, and growth time of 90 min.

4.4 Multi-Step Growth

A schematic of the multi-step process employed in this work is shown in Figure 4-2a along with representative AFM images of the sample surface throughout the process. Tungsten hexacarbonyl (W(CO)₆) was initially introduced into the reactor at a higher flow rate ($\sim 1.2 \times 10^{-3}$ sccm) for 30 sec to drive nucleation on the sapphire surface. Immediately after this short nucleation step, a high density of W-containing nanoscale clusters (~ 5 nm in size) are present on the stepped sapphire surface along with a few larger particles (Figure 4-2b). The W(CO)₆ flow was then removed from the inlet gas

stream and the sample was annealed in H_2Se for 15 min. During this annealing period, the density of nanoscale clusters decreased significantly and oriented triangular WSe_2 islands with uniform size formed in a process that resembles two-dimensional ripening (Figure 4-2c). The $\text{W}(\text{CO})_6$ was then re-introduced into the inlet gas at a lower flow rate than the nucleation step ($\sim 4.2 \times 10^{-4}$ sccm) to limit further nucleation and promote lateral growth of the domains (Figure 4-2d).

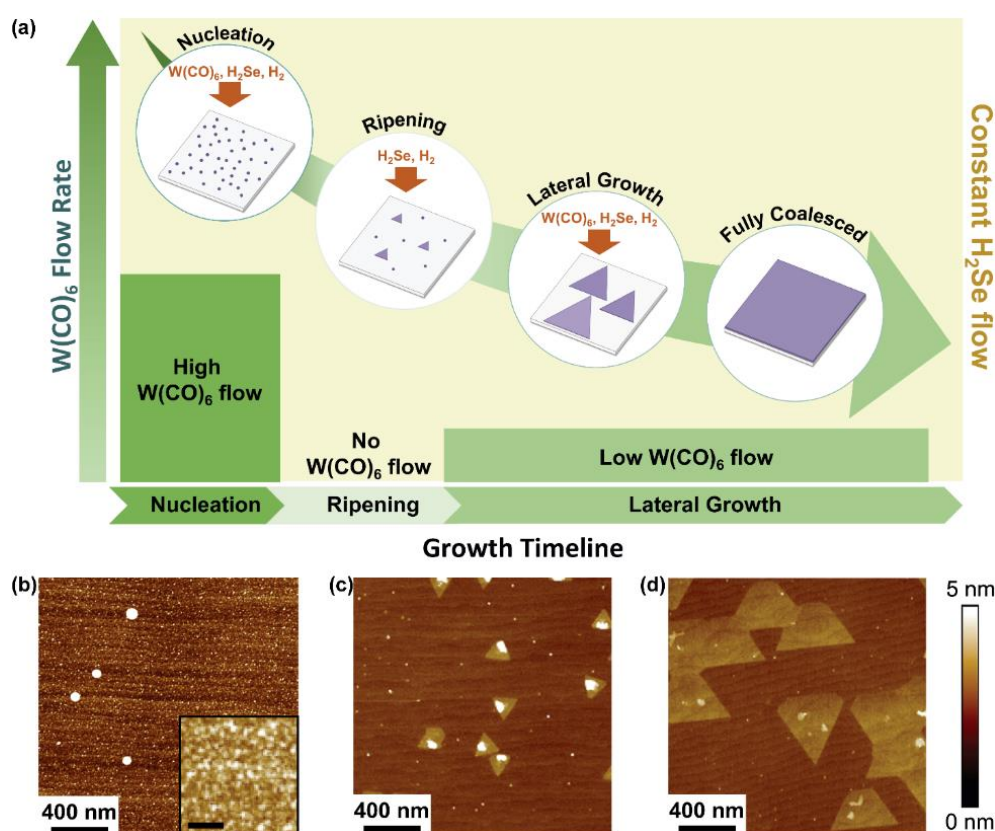


Figure 4-2. (a) Schematic diagram of the multi-step process showing variation in $\text{W}(\text{CO})_6$ flow rate that was used to control nucleation, ripening and lateral growth. AFM images of WSe_2 grown on sapphire substrate (surface steps aligned horizontally) after (b) nucleation stage (inset shows the 5 times magnification of the surface, scale bar: 50 nm), (c) ripening stage, and (d) lateral growth stage.

4.5 Nucleation

4.5.1 Initial nucleation clusters

In the initial short nucleation step, a high density of nanoscale clusters revealed on the substrate surface after cooldown. XPS was carried out to verify the chemical composition of the W-Se compound formed during the initial nucleation and lateral growth steps (done by Tanushree Choudhury, Penn State). Figure 4-4 shows high-resolution scans for Se 3d and W 4f obtained on two samples immediately after the nucleation step when nanoscale clusters are present on the surface and after the lateral growth step when the WSe₂ monolayer is coalesced. In the case of the coalesced film, the peak positions for W 4f and Se 3d correspond to WSe₂ and the stoichiometry obtained from the area under the peaks indicates the W to Se ratio to be 1:2. In comparison, immediately after the nucleation stage, the XPS spectra contains predominant W 4f peaks and a smaller peak associated with Se 3d indicating that the clusters are W-rich WSe_x particles. This is consistent with results from prior cross-section TEM analysis.⁷ Note that the W 4f peaks are also shifted to higher binding energy indicating the formation of a tungsten oxide.³ In this case, the oxide likely forms rapidly when the sample is exposed to air after removal from the reactor chamber due to the small nanoparticle size and non-stoichiometric composition.

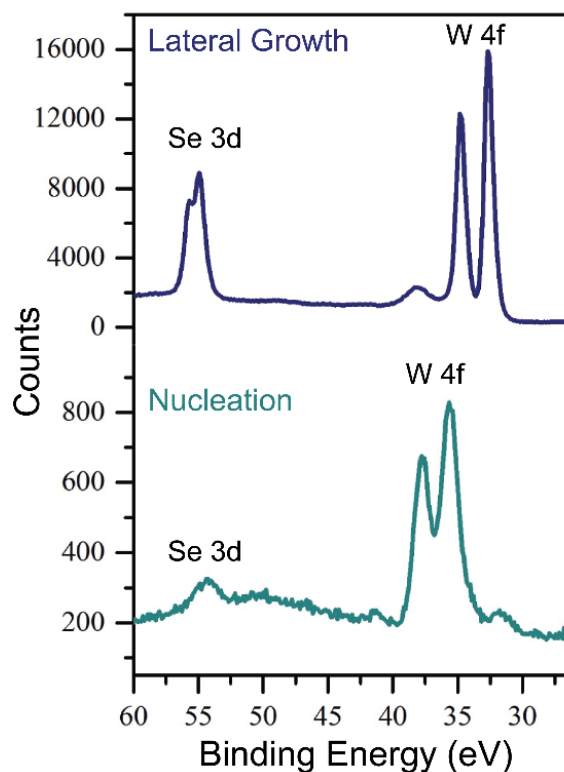


Figure 4-3. High-resolution XPS spectra of Se 3d and W 4f for samples (top) after the lateral growth to form a coalesced WSe₂ film and (bottom) immediately after the nucleation step when nanoscale clusters are present on the surface.

4.5.2 Density of initial WSe₂ islands

The nucleation and ripening steps provide a means to control the density, size and orientation of WSe₂ islands which is essential for achieving coalesced monolayer films.

The size and density of WSe₂ islands after the nucleation and ripening stages was controlled by varying the nucleation time. Figure 4-4a shows the surface morphology under 30 sec, 1 min and 2 min nucleation time respectively and 10 min ripening time.

Figure 4-4b demonstrates the coverage of WSe₂ islands on the sapphire surface after 10

mins ripening was found to increase approximately linearly from 9 to 40 percentage as the nucleation time was increased from 30 sec to 5 min. Similarly, Figure 4-4c depicts the density of WSe₂ islands increase linearly from 4 to 60 μm^{-2} at the same time with a slope of approximately $12/(\mu\text{m}^2 \cdot \text{min})$. It is also apparent from the AFM images in Figure S3a that the small cluster density on the substrate surface decreases with increasing nucleation time. This is attributed to the reduced spacing between WSe₂ islands at larger nucleation densities which decreases the length the clusters must diffuse on the surface before incorporating in an island.

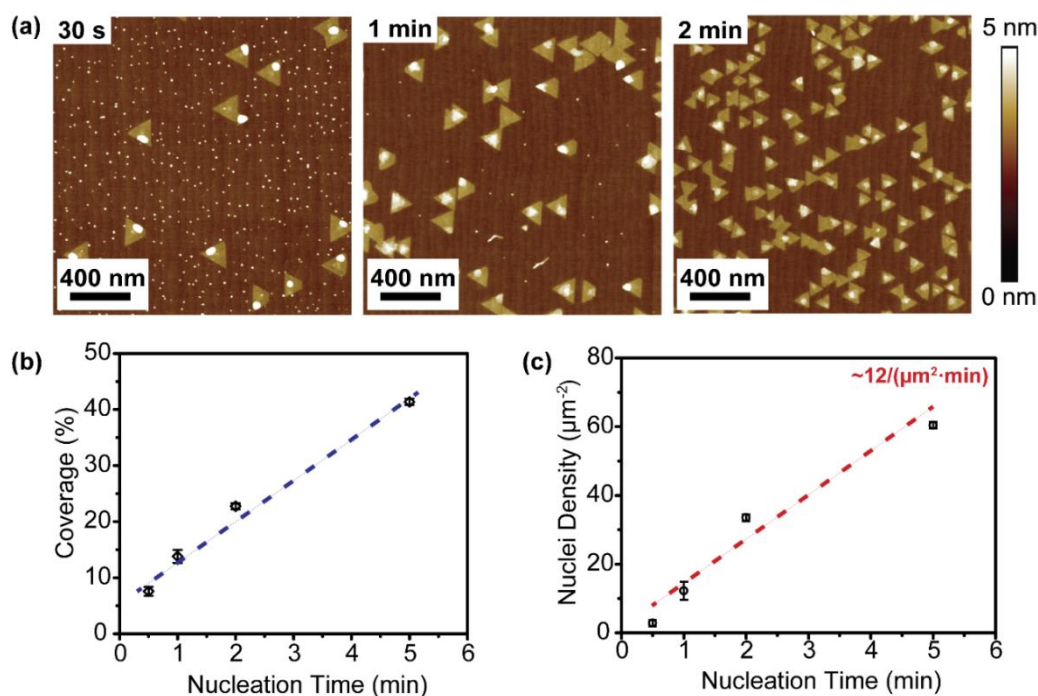


Figure 4-4. (a) AFM images of WSe₂ grown on sapphire substrate under varied nucleation times of 30 sec, 1 min, and, 2 min, and ripening time of 10 min. (b) Sample surface coverage as a function of nucleation time. (c) WSe₂ domain density as a function of nucleation time showing an $\sim 12/(\mu\text{m}^2 \cdot \text{min})$ nucleation rate.

4.6 Ripening

4.6.1 Post-growth characterization

A detailed study of the ripening stage provides insights into surface diffusion which is the key mechanism responsible for lateral growth of 2D monolayer domains. Figure 4-5a shows the WSe₂ surface morphology grown using a constant nucleation time of 30 sec and increasing ripening times ranging from 7.5 min to 30 min. As ripening proceeds, triangular domains start to appear with increasing density and size while the

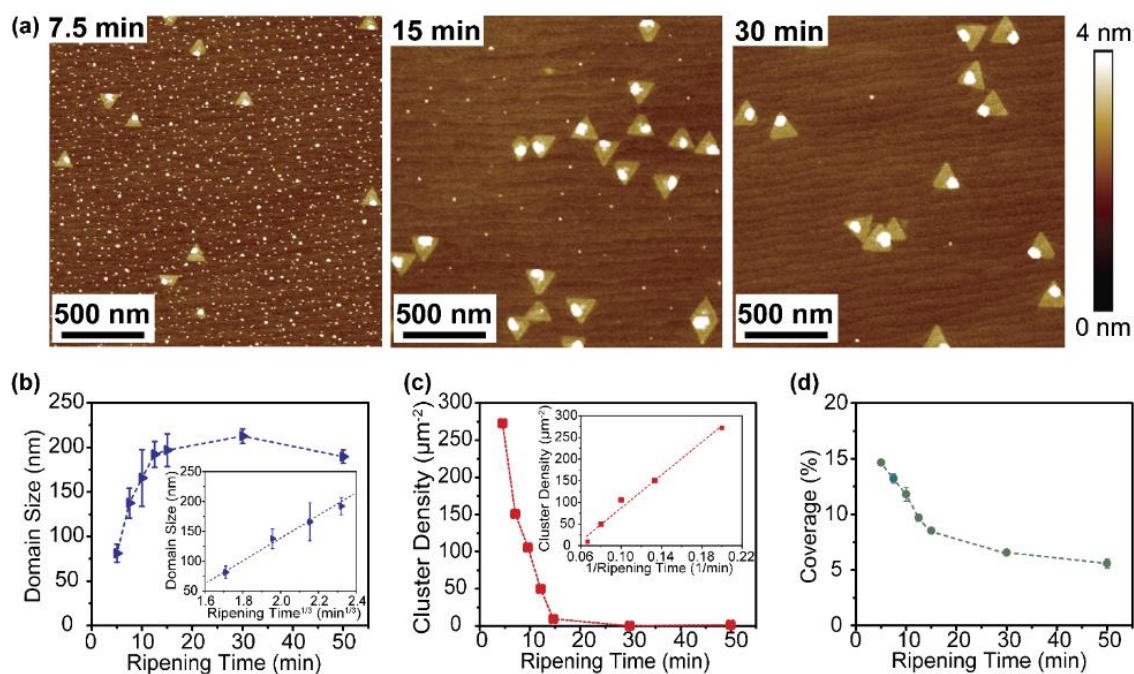


Figure 4-5. (a) AFM images of WSe₂ grown on sapphire substrate under 30 sec nucleation time and varied ripening time for 7.5, 15, and 30 min. (b) WSe₂ domain size as a function of ripening time and cubic root of ripening time (inset). (c) Cluster density as a function of ripening time and reciprocal of ripening time (inset). (d) Substrate surface coverage as a function of ripening time.

small clusters between the triangles decrease in number. The size of the triangular domains (measured by the edge length of the triangle) increases rapidly up to ~200 nm within the first 15 min of ripening (Figure 4-5b) with a corresponding decrease in cluster density (Figure 4-5c). During this same time period, the total surface coverage decreases from 15% to 8.5% (Figure 4-5d) mainly due to differences in the projected areas of clusters versus triangular WSe₂ domains. Beyond 15 min, the domain size, cluster density and coverage remain relatively constant or decrease only slightly with further annealing time.

4.6.2 Ripening and surface diffusion

The time dependencies of the domain size and cluster density within the first 15 min are consistent with classical models of 2D ripening⁸⁻¹¹ whereby large particles increase in size as $t^{1/3}$ (Figure 4-5b inset) and small particles decrease in density as $1/t$ (Figure 4-5c inset). The exact mechanism by which ripening occurs is not known although it is believed to be associated with surface diffusion of W adatoms or migration of W-rich WSe_x clusters. A simplified comparison of the vapor pressures of W (<10⁻⁶ Torr)¹² and Se (~2750 Torr)¹³ at 800 °C suggests that there should be negligible desorption of W-containing species from the surface and hence are likely the species involved in the ripening process. Tungsten-containing adatoms may diffuse from small to large clusters driven by the concentration gradient resulting from the Gibbs-Thompson effect (known as Ostwald ripening),¹⁰ or the clusters themselves may migrate on the

surface and coalesce into larger domains (known as Smoluchowski ripening),^{11,14} or a combination of both processes may occur.

4.6.3 Derivation of surface diffusion coefficient

In the case of 2D Smoluchowski ripening, the derivation of surface diffusion coefficient is based on the following assumptions: the WSe₂ cluster size is negligible compared to the distance between clusters; clusters coalesce into one larger cluster once they reach each other. The surface diffusion coefficient (D) of the clusters can be estimated based on Brownian motion and the Einstein equation $L_D = 2\sqrt{Dt}$ where L_D is the mean cluster displacement and t is the ripening time.¹⁴ The mean cluster displacement can be approximated as $L_D \approx 1/2L_{av}$ where L_{av} is the average distance between clusters. The schematic plot in Figure 4-6a shows the relationship between L_D and L_{av} . Since all clusters participate in the coalescence event, any cluster distance smaller than $2L_D$ should coalesce. Along with the assumption that WSe₂ cluster size is negligible, the L_{av} should be approximately equal to $2L_D$, where $L_{av} = \sqrt{(1/N)}$. In this way, the cluster density is then related to the ripening time as $1/N = 16Dt$. A plot of $(1/N)$ as a function of t (Figure 4-6b) shows a linear dependence in the first 10 minutes of ripening from which the cluster surface diffusion coefficient can be estimated as $1.2 \times 10^{-14} \text{ cm}^2/\text{s}$. This value which we associate with the diffusivity of the W-rich WSe_x particles is comparable to the diffusivities of $\sim 5 \text{ nm}$ Pt particles on alumina ($1.5 \times 10^{-14} \text{ cm}^2/\text{s}$ at 600°C)¹¹ and $\sim 6 \text{ nm}$ Au particles on sapphire ($2.0 \times 10^{-14} \text{ cm}^2/\text{s}$ at 500°C).¹⁵ Note that small clusters are also present on the top surface of the WSe₂ islands after ripening, typically near the edge of a

domain (Figure 4-5a). These small clusters have been reported as W-rich WSe_x particles,⁷ which are similar to those present on the sapphire surface that are unable to migrate over the domain edge due to an Ehrlich-Schwoebel diffusion barrier.^{16,17}

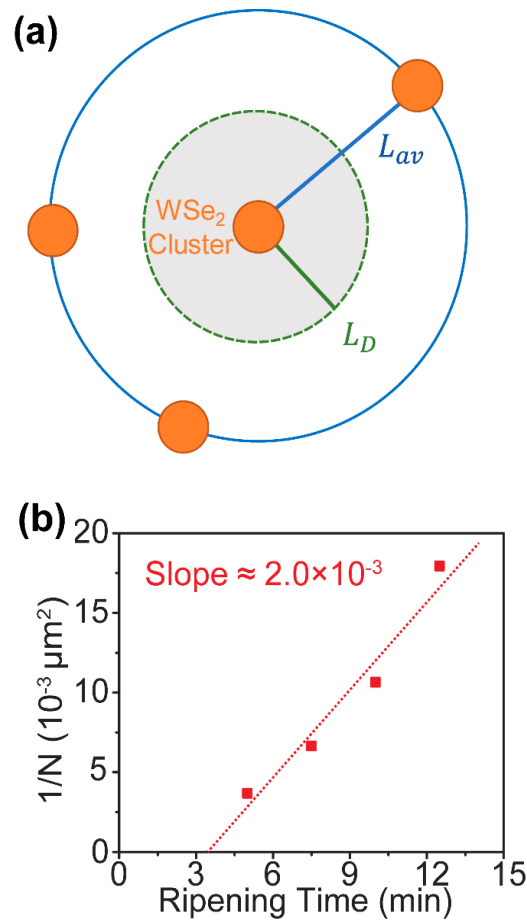


Figure 4-6. (a) Schematic plot showing the method to estimate diffusivity. The average distance between clusters $L_{av} = \sqrt{(1/N)}$, where N is the cluster density. Assume the size of the cluster is small to be neglected, the estimated mean cluster displacement $L_D \approx 1/2L_{av}$. (b) The reciprocal of cluster density as a function of ripening time showing a linear relationship in the first 10 min with a slope of $2 \times 10^{-3} \mu\text{m}^2/\text{min}$, from which the diffusivity can be derived as $1.2 \times 10^{-14} \text{ cm}^2/\text{s}$.

4.7 Lateral Growth

4.7.1 Coalesced monolayer film

To achieve a coalesced monolayer of WSe₂, continued nucleation between or on top of the initial WSe₂ islands needs to be suppressed in order to promote lateral growth of existing domains. Therefore, following the nucleation and ripening steps, the W(CO)₆ precursor was reintroduced into the inlet gas stream at a lower flow rate of 4.2×10^{-4} sccm in order to reduce the gas phase supersaturation which is the driving force for crystal nucleation and growth.¹⁸ Figure 4-7a shows scanning electron microscope (SEM) images of samples grown using 30 sec nucleation time, 15 min ripening time and varied lateral growth time of 5 min, 20 min, 30 min, and 45 min. Immediately after ripening, the domains are approximately 120 nm in size and cover 8% of the sapphire surface (t=0 of Figure 4-7b). As the lateral growth time is increased, the density of triangular domains remains relatively constant and the domain size and surface coverage increase nearly linearly with lateral growth time from 5-15 mins (Figure 4-7b). It should be noted that the lateral growth rate in first 5 min appears to be reduced which is likely due to a short time lag for the W(CO)₆ precursor to reach the substrate after it is re-introduced into the inlet gas stream. As the surface coverage increases above ~50% (15 mins), however, the lateral growth rate of the monolayer decreases likely due to precursor adsorption occurring more frequently on existing WSe₂ monolayers rather than on the sapphire surface. As the WSe₂ monolayer domains increase in size, the adatoms must diffuse a longer distance to reach the domain edges, therefore, it becomes more likely that they will contribute to bilayer growth instead rather than fill in the initial monolayer. Indeed,

the lateral growth rate and coverage of bilayers increases after 15 mins when the monolayer lateral growth rate decreases (Figure 4-7b). A fully coalesced monolayer with ~36% bilayer coverage across the entire 1 cm×1 cm sapphire substrate can be achieved in ~45 min.

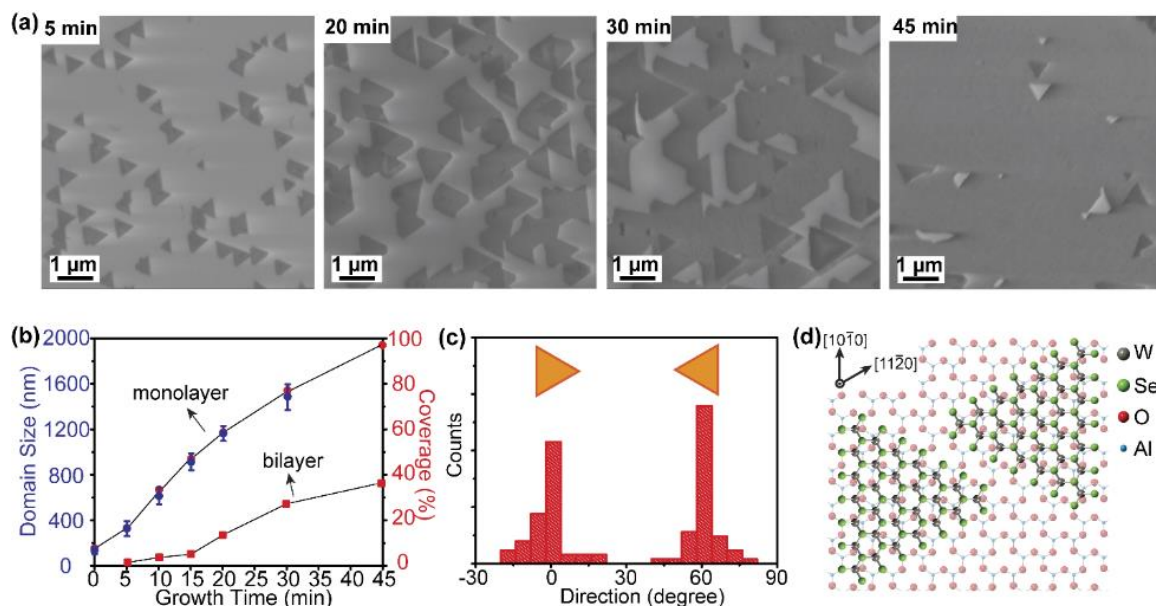


Figure 4-7. (a) SEM images of WSe₂ grown on sapphire substrate under 30 sec nucleation time, 15 min ripening time and varied lateral growth time for 5 min, 20 min, 30 min, and 45 min. (b) WSe₂ monolayer domain size and surface coverage as a function of lateral growth time and bilayer surface coverage as a function of lateral growth time. A fully coalesced monolayer WSe₂ film is achieved in ~45 min lateral growth. (c) Orientation histogram from 10 min and 20 min samples confirms that WSe₂ domain edges are primarily oriented at 0° and 60° with respect to steps on sapphire. (d) Schematic illustrating 0° and 60° oriented WSe₂ domains on sapphire (0001) surface.

4.7.2 Preferential orientation

The WSe₂ domains clearly exhibit preferred orientations on the (0001) sapphire surface which begins during the ripening stage (Figure 4-5) and is maintained throughout the lateral growth stage. A histogram (Figure 4-7c) of domain orientations measured after 5 min, 10 min and 20 min of lateral growth when the domains are still isolated from each other shows two preferred orientations of 0° and 60° with respect to the step edge direction which corresponds to the $[11\bar{2}0]$ direction of sapphire, similar to that reported for epitaxial growth of MoS₂ domains on (0001) sapphire substrate by oxide powder vaporization.¹⁹ The preferred orientation results from the commensurability between WSe₂ and sapphire (0001). Although there is large lattice mismatch between WSe₂ ($a=3.282 \text{ \AA}$)²⁰ and sapphire (001) ($a=4.760 \text{ \AA}$),²¹ it is reduced to ~3.4% mismatch for 3×3 WSe₂ unit cells on a 2×2 (0001) sapphire surface (Figure 3d). Raman and room temperature photoluminescence (PL) spectroscopy confirm the existence of monolayer WSe₂ due to the absence of a breathing mode at ~310 cm⁻¹ WSe₂ (Figure 4-8a)²²⁻²⁵ and a strong PL peak that varies from 1.60 to 1.64 eV (Figure 4-8b)²² across the sample surface. Raman mapping (Figure 4-8c) indicates that film is largely monolayer across the 5 μm×5 μm scan area, however, smaller scale lateral variations are evident from changes in the Raman peak intensity (Figure 4-8c) and PL peak position (Figure 4-8d). The lateral non-uniformity may arise from localized Fermi level modulations in the WSe₂ due to surface reconstruction of sapphire at the step edges,²⁶ and/or local variations in strain in the WSe₂ film due to tensile stress that is induced in the film upon cooldown from the growth temperature due to differences in the coefficients of thermal expansion of WSe₂

($\alpha_a=11.08\times10^{-6}/^{\circ}\text{C}$)²⁷ and sapphire ($\alpha_a=8.1\times10^{-6}/^{\circ}\text{C}$)²⁸ as has been reported for CVD-grown MoSe₂ on SiO₂.²⁹

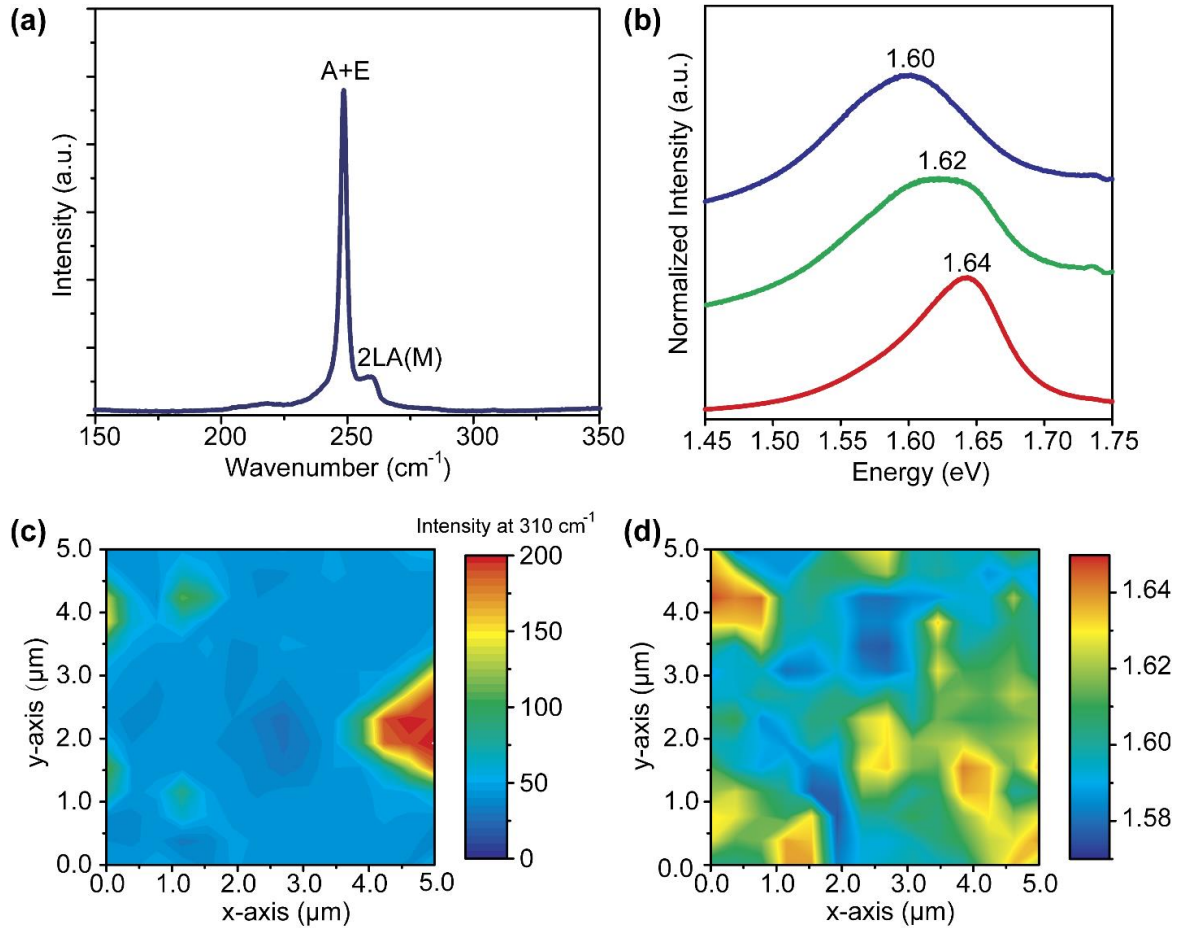


Figure 4-8. (a) Raman spectrum of coalesced monolayer WSe₂ film. (b) PL spectra of different regions on monolayer WSe₂ film showing the optical band gap energy varies 1.60-1.64 eV. (c) 5 μm×5 μm Raman intensity map at 310 cm⁻¹ showing most of region across the film is monolayer. (d) 5 μm×5 μm PL peak position map illustrating the uniformity of PL spectra across the film.

4.7.3 Substrate temperature effect

The multi-step process also provides a pathway to study the effects of growth conditions on the domain shape and lateral growth rate independent of their impact on the nucleation process. For example, Figure 4-9a shows the WSe₂ domain morphology after 10 min of lateral growth at 600 °C, 700 °C, 800 °C, and 900 °C with the nucleation and ripening conditions held constant (30 sec of nucleation and 15 min of ripening at 800 °C) to maintain a constant initial WSe₂ domain density and size. Over the temperature range from 700 °C to 900 °C, the domain size and density are only weakly dependent on the growth temperature (Figure 4-9b) suggesting that the growth is limited by mass transport of precursors to the growth surface as is commonly observed for MOCVD growth of III-V epilayers.³⁰ This is reasonable considering that both W(CO)₆ and H₂Se are expected to decompose in the gas phase at temperatures as low as 375°C,^{31–33} consequently, WSe₂ growth is unlikely to be limited by kinetics at the growth conditions used in this study. At a lower temperature of 600 °C, however, a bimodal distribution of domain sizes was observed. The larger domains can be attributed to the initial islands formed during the nucleation and ripening stages while the smaller domains likely arise from additional nucleation occurring during the lateral growth step due to reduced surface diffusion at the lower substrate temperature. In this case, surface adatoms are likely to form new nucleation sites rather than diffuse to one of the existing WSe₂ islands and contribute to lateral growth.

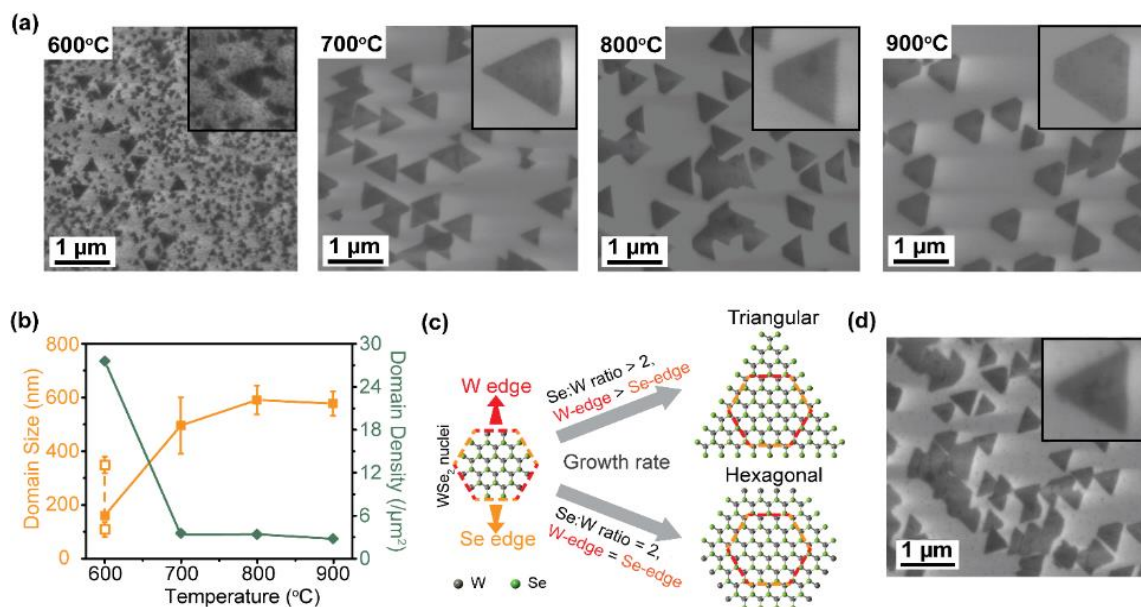


Figure 4-9. (a) SEM images of WSe₂ grown on sapphire substrate under 30 sec of nucleation, 15 min of ripening, and 10 min of lateral growth at varied substrate temperatures of 600 °C, 700 °C, 800 °C, and 900 °C. H₂Se flow rate was held constant at 7 sccm and Se:W ratio was ~26000 during the lateral growth stage. Inset SEM images show the shape of the WSe₂ domains. (b) WSe₂ domain size and domain density as a function of substrate temperature. (c) Schematic diagram showing the variation of WSe₂ domain shape under different surface Se:W ratios. (d) SEM image of WSe₂ grown under 30 sec of nucleation, 15 min of ripening, and 10 min of lateral growth at substrate temperature of 900 °C. H₂Se flow rate was increased to 10 sccm and Se:W ratio was ~37000 during the lateral growth stage. Inset SEM image shows the shape of WSe₂ domain.

The change in substrate temperature also alters the shape of the WSe₂ domains which evolves from triangular at 700 °C to truncated triangular at 900 °C (Figure 4-9a insets). Previous reports have demonstrated a similar shape evolution of individual MoS₂ and WSe₂ domains in PVT with respect to the source evaporation temperature,³⁴ substrate location relative to the source,³⁵ and growth temperature.³⁶ Based on these prior studies, the triangular domains shape can be attributed to the faster growth rate of W-terminated edges relative to the Se-terminated edges due to excess Se at the growth front which is expected given the high Se:W inlet gas ratio (~26,000) used in the growth process. As the growth temperature is increased, however, the W-terminated edge growth rate decreases relative to that of the Se-terminated edge resulting in truncated triangular domains which are expected to transition to a hexagonal shape when the local Se:W ratio is ~2 (Figure 4-9c).³⁵ While the Se:W inlet gas ratio remained constant in these experiments, the local Se:W ratio at the growth front is expected to be strongly temperature dependent due to the large differences in vapor pressure between Se and W which will impact surface adatom concentrations. As previously discussed, the vapor pressure of selenium is ~2750 Torr at 800 °C and increases exponentially with temperature³⁷ while the vapor pressure of W remains negligibly low throughout this temperature range.¹² Consequently, the sticking coefficient of Se on the sapphire surface should decrease significantly with temperature relative to that of W resulting in a reduction in the local Se:W ratio on the surface as the temperature is increased. To test this hypothesis, the Se:W inlet gas ratio was raised from 26,000 to 37,000 for growth at 900 °C which resulted in a transition back from truncated triangular to triangular shaped domains (Figure 4-9d) confirming the local Se:W dependence of the domain shape.

4.8 Structural Characterization

4.8.1 RHEED

4.8.1.1 In-plane lattice constant of WSe₂ layer

The RHEED in this chapter was carried out by Yu Xiang at Rensselaer Polytechnic Institute. For RHEED analysis, the sample was aligned with the sapphire $\langle 10\bar{1}0 \rangle$ parallel to the incident electron beam at the initial position (azimuthal angle $\varphi = 0^\circ$). Figures 4-10a and 4-10b show the RHEED patterns from two azimuthal angles about 30° apart, $\varphi = 239.0^\circ$ and $\varphi = 269.6^\circ$, respectively. Figures 4-10c and 4-10d show the integrated intensity from the yellow dashed box plotted in parallel momentum transfer k_{\parallel} direction (parallel to the shadowing edge of the sample) assuming the intensity along streaks (perpendicular momentum transfer k_{\perp} direction) is featureless. These peaks are symmetric with respect to the central streak. From the peaks in Figures 4-10c and 4-10d, the average adjacent reciprocal spacing between the streaks are measured to be $2.2 \pm 0.1 \text{ \AA}^{-1}$ and $4.0 \pm 0.1 \text{ \AA}^{-1}$, respectively. 2H phase WSe₂ has a hexagonal lattice with a bulk lattice constant $a = b = 3.2820 \text{ \AA}$, $c = 12.9600 \text{ \AA}$, $\alpha = \beta = 90^\circ$, $\gamma = 120^\circ$. If we choose the angle between the reciprocal base vectors of WSe₂ to be 60° , then $|\vec{G}(hk)| = \frac{4\pi}{\sqrt{3}a} \sqrt{h^2 + hk + k^2}$. Theoretically, $|\vec{G}(10)| = 2.2106 \text{ \AA}^{-1}$, $|\vec{G}(11)| = 3.8289 \text{ \AA}^{-1}$. The measured numbers $2.2 \pm 0.1 \text{ \AA}^{-1}$ and $4.0 \pm 0.1 \text{ \AA}^{-1}$ agree very well with the theoretical calculation for $|\vec{G}(10)|$ and $|\vec{G}(11)|$ of WSe₂. From the experimentally measured values

of $|\vec{G}(hk)|$, the lattice constant of WSe₂ is determined to be $a = 3.2 \pm 0.1 \text{ \AA}$, which agrees very well with the bulk value.

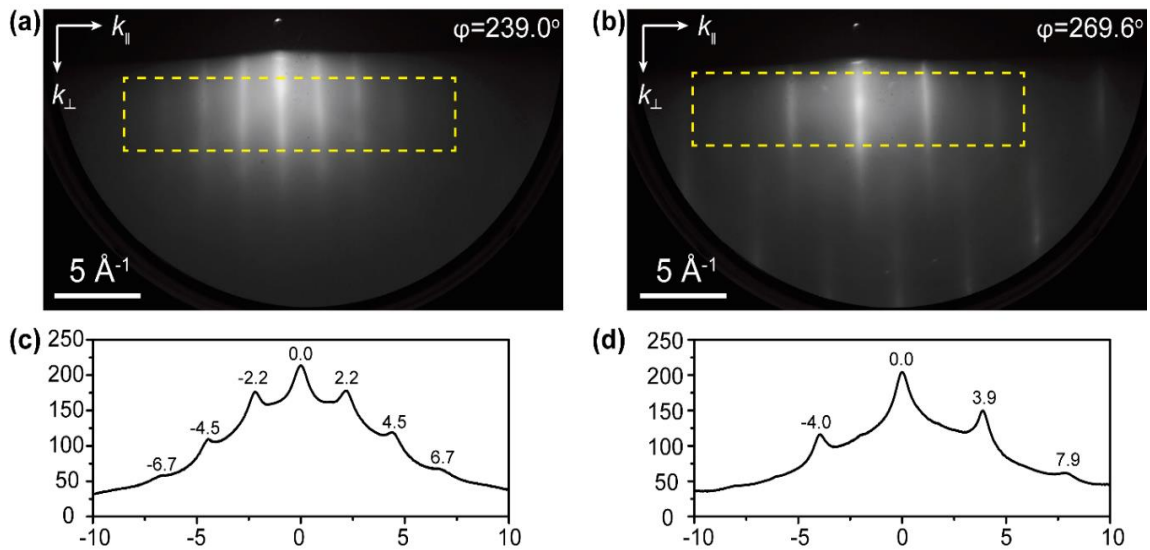


Figure 4-10. RHEED patterns of WSe₂ collected from 20 keV incident electrons scattered from two azimuthal angles about 30° apart, **(a)** $\varphi = 239.0^\circ$ and **(b)** $\varphi = 269.6^\circ$. **(c)** Integrated intensity from the yellow dashed box plotted in parallel momentum transfer k_{\parallel} direction in (a). **(d)** Integrated intensity from the yellow dashed box plotted in parallel momentum transfer k_{\parallel} direction in (b).

4.8.1.2 Reciprocal space structure of WSe₂ and its epitaxial relationship with sapphire

The regular orientation of WSe₂ domains on the surface of the non-coalesced samples suggests that the film is epitaxially oriented with respect to the sapphire. This was confirmed and quantified through RHEED analysis which was carried out on 1 cm×1 cm fully-coalesced monolayer films. Figure 4-11a shows the experimentally measured

RHEED 2D reciprocal space structure of the WSe₂ monolayer plotted as the intensity k_{\parallel} (the momentum transfer parallel to the surface) vs. 360° azimuthal directions constructed from 100 RHEED patterns recorded when the sample was rotated azimuthally with a 1.8° step size from 0° to 180° in 100 steps as previously demonstrated.^{38,39} In order to enhance the signal to noise ratio the intensity at each k_{\parallel} is averaged within the range $2.8 \text{ \AA}^{-1} < k_{\perp} < 3.1 \text{ \AA}^{-1}$. The averaged intensity is then normalized to one. The experimental RHEED 2D reciprocal space structure shows six-fold symmetry. It also implies if not all or at least the majority of the WSe₂ flakes have the same orientation on $\alpha\text{-Al}_2\text{O}_3$ (0001) substrate.

Figure 4-11b shows the theoretical simulation of 2D reciprocal space structure of WSe₂ when the out-of-plane direction is the [0001] direction. The good agreement between constructed 2D reciprocal space structure of WSe₂ and simulated one indicates that the WSe₂ monolayer is nominally single crystal with an epitaxial relation of $[10\bar{1}0] \text{ WSe}_2 \parallel [10\bar{1}0] \alpha\text{-Al}_2\text{O}_3$.

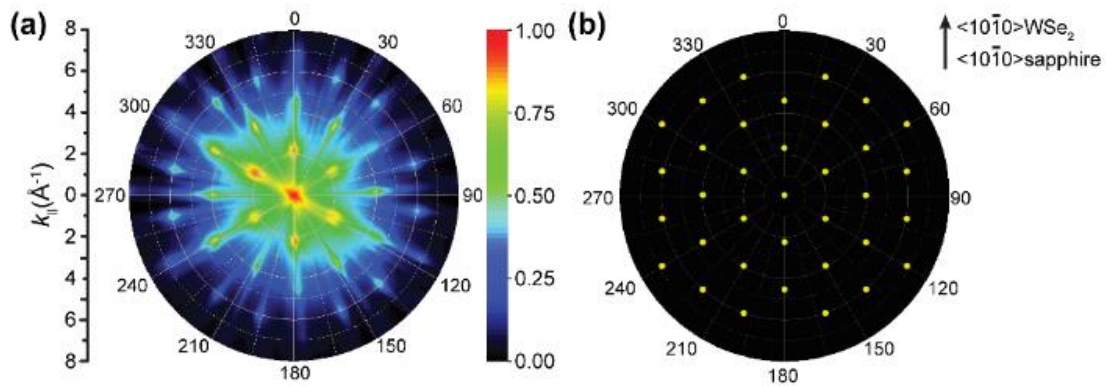


Figure 4-11. (a) Experimentally constructed RHEED 2D reciprocal space structure of WSe₂ plotted as the intensity (k_{\parallel}) vs. 360° azimuthal directions from 100 RHEED patterns recorded when the sample was rotated azimuthally with a 1.8° step size from 0° to 180° in 100 steps. (b) Theoretical simulation of 2D reciprocal space structure of WSe₂

looking along the out-of-plane $[0001]$ direction which matches the experimental result in (a), showing $[10\bar{1}0]$ $\text{WSe}_2 \parallel [10\bar{1}0]$ $\alpha\text{-Al}_2\text{O}_3$.

4.8.2 In-plane XRD

The in-plane XRD in this chapter was carried out by Mikhail Chubarov at Penn State. The epitaxial relation was also confirmed by in-plane XRD measurements⁴⁰ which were carried out across the entire $1\text{cm} \times 1\text{cm}$ sample area. The X-ray θ – 2θ scan recorded using in-plane diffraction geometry at a ϕ angle where the $11\bar{2}0$ peak of $\alpha\text{-Al}_2\text{O}_3$ was observed, revealed the presence of both WSe_2 and substrate $11\bar{2}0$ peaks (Figure 4-12a). Rotation around the surface normal fixing the 2θ angle at the $11\bar{2}0$ peaks of WSe_2 and $\alpha\text{-Al}_2\text{O}_3$ (Figure 4-12b) shows epitaxial growth with an in-plane epitaxial relation of $[11\bar{2}0]$ $\text{WSe}_2 \parallel [11\bar{2}0]$ $\alpha\text{-Al}_2\text{O}_3$ which is consistent with RHEED measurement based on the crystal symmetry of WSe_2 . The measured full width at half maximum (FWHM) of $(11\bar{2}0)$ peaks of WSe_2 in Figure 4-12b show a narrow value of 0.28° indicating the film is highly oriented.

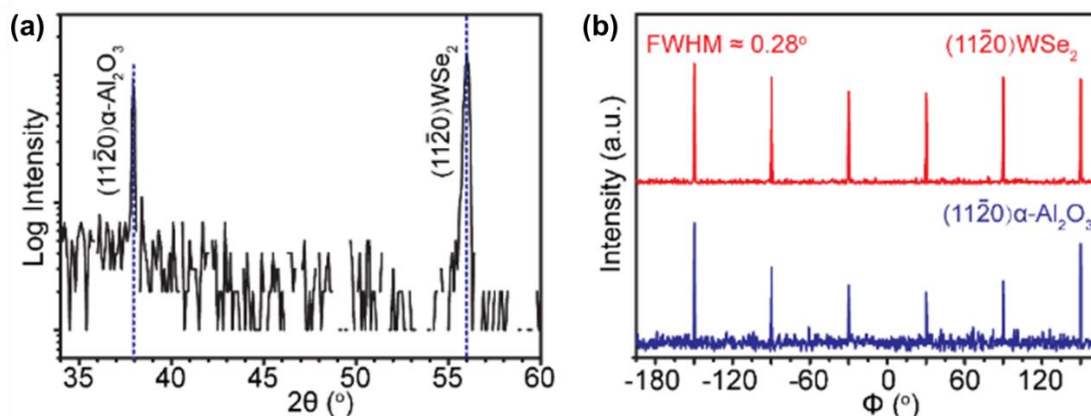


Figure 4-12. (a) θ - 2θ X-ray diffractogram recorded at $\phi=30^\circ$ showing reflections which correspond to $(11\bar{2}0)$ of WSe_2 and $\alpha\text{-Al}_2\text{O}_3$. (b) ϕ -scan recorded at $2\theta = 37.91^\circ$ showing $[11\bar{2}0] \text{WSe}_2 \parallel [11\bar{2}0] \alpha\text{-Al}_2\text{O}_3$.

4.8.3 High Resolution STEM

High resolution scanning transmission electron microscopy (STEM) was done by Fu Zhang at Penn State and used to further study crystallinity and identify defects and grain boundaries in WSe_2 films removed from the sapphire substrate by a water transfer process.⁴¹ The STEM image (Figure 4-13a) under low magnification and the corresponding selected area electron diffraction (SAED) pattern (Figure 4-13a inset) shows that the film consists of a single crystal coalesced monolayer of WSe_2 with some additional bilayer and trilayer growth. High angle annular dark field scanning TEM (HAADF-STEM) images (Figure 4-13b and 4-13c) display the atomic structure of the WSe_2 film where W and Se atoms can be identified by analyzing the intensity profile due to the Z-contrast (atomic number) characteristics in the monolayer region of WSe_2 . A 60°

grain boundary (GB) (inversion domain boundary) is evident in the monolayer region of WSe_2 (marked by red dashed line in Figure 4-13b). Figure 4-13c shows a higher resolution HAADF-STEM image of the 60° GB that is parallel to the zigzag geometry of the WSe_2 lattice and is stitched together by 4-fold (marked in yellow) and 8-fold (marked in green) (4|8) rings via point sharing at common Se_2 sites. This indicates the formation of inversion domain boundaries that result from coalescence of 0° and 60° WSe_2 domains.^{42,43}

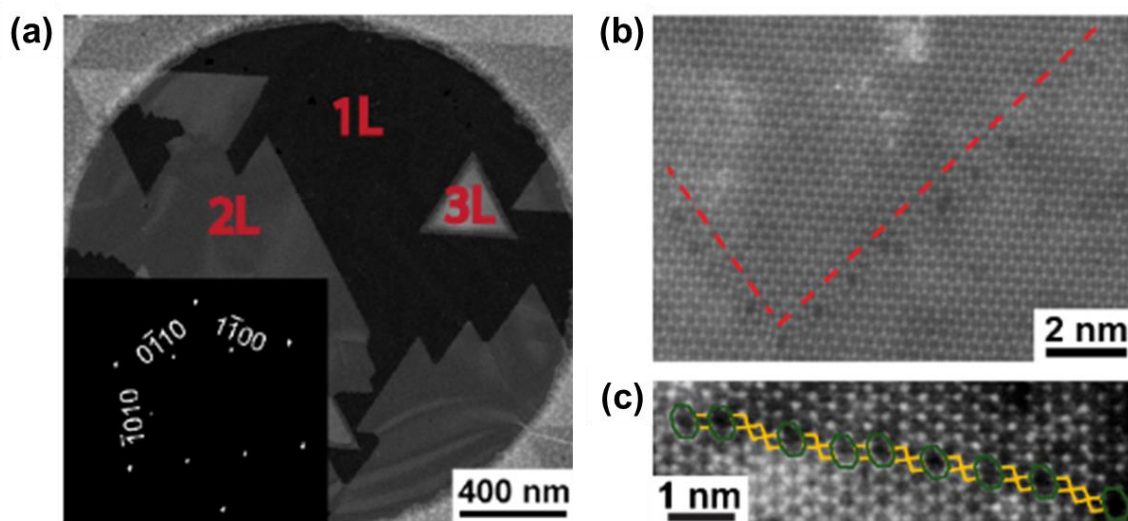


Figure 4-13. (a) Low-magnification TEM image of coalesced WSe_2 showing single layer structure and sequent layers and the corresponding SAED pattern (inset). (b) Atomic resolution HAADF-STEM image showing the existence of anti-phase grain boundaries in the film. (c) Higher resolution HAADF-STEM image showing 4|8 rings attributed to the coalescence of 0° and 60° WSe_2 domains.

4.9 Conclusions

In summary, this chapter demonstrates a diffusion-controlled gas source CVD process for the epitaxial growth of large area, fully-coalesced single crystal WSe₂ monolayer and few layer films on c-plane sapphire. A multi-step growth process was developed which employs modulation of the metal precursor partial pressure to independently control nucleation, domain ripening, lateral growth and film coalescence via surface diffusion processes. By separating out the nucleation and lateral growth stages, the effects of process conditions on nucleation density, lateral growth rate and domain shape can be clearly distinguished, providing experimental insights into the fundamental mechanisms that control 2D domain growth. The results of this study are an important step in the development of a reproducible epitaxial growth technology for large area monolayer TMDC films and 2D heterostructures.

4.10 References

- (1) Manzeli, S.; Ovchinnikov, D.; Pasquier, D.; Yazyev, O. V.; Kis, A. 2D Transition Metal Dichalcogenides. *Nat. Rev. Mater.* **2017**, 2 (8), 17033.
- (2) Shi, Y.; Li, H.; Li, L.-J. Recent Advances in Controlled Synthesis of Two-Dimensional Transition Metal Dichalcogenides via Vapour Deposition Techniques. *Chem. Soc. Rev.* **2015**, 44 (9), 2744–2756.
- (3) Lai, K. K.; Lamb, H. H. Tungsten Chemical Vapor Deposition Using Tungsten Hexacarbonyl: Microstructure of as-Deposited and Annealed Films. *Thin Solid Films* **2000**, 370 (1), 114–121.
- (4) Lander, J. J.; Germer, L. H. Plating Molybdenum, Tungsten, and Chromium by Thermal Decomposition of Their Carbonyls. *Trans. Am. Inst. Min. Metall. Eng.* **1948**, 175, 648–692.
- (5) Tang, F.; Parker, T.; Wang, G.-C.; Lu, T.-M. Surface Texture Evolution of Polycrystalline and Nanostructured Films: RHEED Surface Pole Figure Analysis. *J. Phys. D. Appl. Phys.* **2007**, 40 (23), R427–R439.
- (6) Kang, K.; Xie, S.; Huang, L.; Han, Y.; Huang, P. Y.; Mak, K. F.; Kim, C.-J.; Muller, D.; Park, J. High-Mobility Three-Atom-Thick Semiconducting Films with Wafer-Scale Homogeneity. *Nature* **2015**, 520 (7549), 656–660.
- (7) Eichfeld, S. M.; Hossain, L.; Lin, Y.; Piasecki, A. F.; Kupp, B.; Birdwell, a G.; Burke, R. a; Lu, N.; Peng, X.; Li, J.; Azcatl, A.; McDonnell, S.; Wallace, R. M.; Kim, M. J.; Mayer, T. S.; Redwing, J. M.; Robinson, J. a. Highly Scalable, Atomically Thin WSe₂

Grown via Metal–Organic Chemical Vapor Deposition. *ACS Nano* **2015**, 9 (2), 2080–2087.

(8) Baldan, A. Review Progress in Ostwald Ripening Theories and Their Applications to Nickel-Base Superalloys Part I: Ostwald Ripening Theories. *J. Mater. Sci.* **2002**, 37 (11), 2171–2202.

(9) Lifshitz, I. M.; Slyozov, V. V. The Kinetics of Precipitation from Supersaturated Solid Solutions. *J. Phys. Chem. Solids* **1961**, 19 (1–2), 35–50.

(10) Zinke-Allmang, M.; Feldman, L. C.; Grabow, M. H. Clustering on Surfaces. *Surf. Sci. Rep.* **1992**, 16 (8), 377–463.

(11) Wynblatt, P.; Gjostein, N. A. Supported Metal Crystallites. *Prog. Solid State Chem.* **1975**, 9 (C), 21–58.

(12) Szwarc, R.; Plante, E. R.; Diamond, J. J. Vapor Pressure and Heat of Sublimation of Tungsten. *J. Res. Natl. Bur. Stand. Sect. A Phys. Chem.* **1965**, 69A (5), 417.

(13) Brooks, L. S. The Vapor Pressures of Tellurium and Selenium. *J. Am. Chem. Soc.* **1952**, 74 (1), 227–229.

(14) Stoldt, C. R.; Jenks, C. J.; Thiel, P. a.; Cadilhe, a. M.; Evans, J. W. Smoluchowski Ripening of Ag Islands on Ag(100). *J. Chem. Phys.* **1999**, 111 (11), 5157–5166.

(15) Beszeda, I.; Gontier-Moya, E. G.; Imre, Á. W. Surface Ostwald-Ripening and Evaporation of Gold Beaded Films on Sapphire. *Appl. Phys. A* **2005**, 81 (4), 673–677.

- (16) Ehrlich, G.; Hudda, F. G. Atomic View of Surface Self-Diffusion: Tungsten on Tungsten. *J. Chem. Phys.* **1966**, *44* (3), 1039–1049.
- (17) Schwoebel, R. L.; Shipsey, E. J. Step Motion on Crystal Surfaces. *J. Appl. Phys.* **1966**, *37* (10), 3682–3686.
- (18) Cubillas, P.; Anderson, M. W. Synthesis Mechanism: Crystal Growth and Nucleation. In *Zeolites and Catalysis: Synthesis, Reactions and Applications*; Wiley-VCH Verlag GmbH & Co. KGaA: Weinheim, Germany, 2010; Vol. 1, pp 1–55.
- (19) Dumcenco, D.; Ovchinnikov, D.; Marinov, K.; Lazić, P.; Gibertini, M.; Marzari, N.; Sanchez, O. L.; Kung, Y.-C.; Krasnozhan, D.; Chen, M.-W.; Bertolazzi, S.; Gillet, P.; Fontcuberta i Morral, A.; Radenovic, A.; Kis, A. Large-Area Epitaxial Monolayer MoS₂. *ACS Nano* **2015**, *9* (4), 4611–4620.
- (20) Schutte, W. J.; De Boer, J. L.; Jellinek, F. Crystal Structures of Tungsten Disulfide and Diselenide. *J. Solid State Chem.* **1987**, *70* (2), 207–209.
- (21) Tsirelson, V. G.; Yu. Antipin, M.; Gerr, R. G.; Ozerov, R. P.; Struchkov, Y. T. Ruby Structure Peculiarities Derived from X-Ray Diffraction Data Localization of Chromium Atoms and Electron Deformation Density. *Phys. status solidi* **1985**, *87* (2), 425–433.
- (22) Tonndorf, P.; Schmidt, R.; Böttger, P.; Zhang, X.; Börner, J.; Liebig, A.; Albrecht, M.; Kloc, C.; Gordan, O.; Zahn, D. R. T.; Michaelis de Vasconcellos, S.; Bratschitsch, R. Photoluminescence Emission and Raman Response of Monolayer MoS₂, MoSe₂, and WSe₂. *Opt. Express* **2013**, *21* (4), 4908.

- (23) Zhao, Y.; Luo, X.; Li, H.; Zhang, J.; Araujo, P. T.; Gan, C. K.; Wu, J.; Zhang, H.; Quek, S. Y.; Dresselhaus, M. S.; Xiong, Q. Interlayer Breathing and Shear Modes in Few-Trilayer MoS₂ and WSe₂. *Nano Lett.* **2013**, *13* (3), 1007–1015.
- (24) Del Corro, E.; Terrones, H.; Elias, A.; Fantini, C.; Feng, S.; Nguyen, M. A.; Mallouk, T. E.; Terrones, M.; Pimenta, M. A. Excited Excitonic States in 1L, 2L, 3L, and Bulk WSe₂ Observed by Resonant Raman Spectroscopy. *ACS Nano* **2014**, *8* (9), 9629–9635.
- (25) Zhao, W.; Ghorannevis, Z.; Amara, K. K.; Pang, J. R.; Toh, M.; Zhang, X.; Kloc, C.; Tan, P. H.; Eda, G. Lattice Dynamics in Mono- and Few-Layer Sheets of WS₂ and WSe₂. *Nanoscale* **2013**, *5* (20), 9677.
- (26) Lin, Y.-C.; Jariwala, B.; Bersch, B. M.; Xu, K.; Nie, Y.; Wang, B.; Eichfeld, S. M.; Zhang, X.; Choudhury, T. H.; Pan, Y.; Addou, R.; Smyth, C. M.; Li, J.; Zhang, K.; Haque, M. A.; Fölsch, S.; Feenstra, R. M.; Wallace, R. M.; Cho, K.; Fullerton-Shirey, S. K.; Redwing, J. M.; Robinson, J. A. Realizing Large-Scale, Electronic-Grade Two-Dimensional Semiconductors. *ACS Nano* **2018**, *12* (2), 965–975.
- (27) El-Mahalawy, S. H.; Evans, B. L. The Thermal Expansion of 2 H -MoS₂, 2 H -MoSe₂ and 2 H -WSe₂ between 20 and 800°C. *J. Appl. Crystallogr.* **1976**, *9* (5), 403–406.
- (28) Yim, W. M.; Paff, R. J. Thermal Expansion of AlN, Sapphire, and Silicon. *J. Appl. Phys.* **1974**, *45* (3), 1456–1457.
- (29) Krustok, J.; Kaupmees, R.; Jaaniso, R.; Kiisk, V.; Sildos, I.; Li, B.; Gong, Y.

Local Strain-Induced Band Gap Fluctuations and Exciton Localization in Aged WS₂ Monolayers. *AIP Adv.* **2017**, 7 (6), 065005.

(30) Biefeld, R. M.; Koleske, D. D.; Cederberg, J. G. The Science and Practice of Metal-Organic Vapor Phase Epitaxy (MOVPE). In *Handbook of Crystal Growth, 2nd Ed. Thin Films and Epitaxy: Basic Techniques, Vol. IIIA*; Kuech, T. F., Ed.; Elsevier, 2015; p 95.

(31) Haigh, J.; Burkhardt, G.; Blake, K. Thermal Decomposition of Tungsten Hexacarbonyl in Hydrogen, the Production of Thin Tungsten-Rich Layers, and Their Modification by Plasma Treatment. *J. Cryst. Growth* **1995**, 155 (3–4), 266–271.

(32) PEARSON, R.; HAUGEN, G. Kinetics of the Thermal Decomposition of H₂Se. *Int. J. Hydrogen Energy* **1981**, 6 (5), 509–519.

(33) Lewis, K. E.; Golden, D. M.; Smith, G. P. Organometallic Bond Dissociation Energies: Laser Pyrolysis of Iron Pentacarbonyl, Chromium Hexacarbonyl, Molybdenum Hexacarbonyl, and Tungsten Hexacarbonyl. *J. Am. Chem. Soc.* **1984**, 106 (14), 3905–3912.

(34) Xie, S.; Xu, M.; Liang, T.; Huang, G.; Wang, S.; Xue, G.; Meng, N.; Xu, Y.; Chen, H.; Ma, X.; Yang, D. A High-Quality Round-Shaped Monolayer MoS₂ Domain and Its Transformation. *Nanoscale* **2016**, 8 (1), 219–225.

(35) Wang, S.; Rong, Y.; Fan, Y.; Pacios, M.; Bhaskaran, H.; He, K.; Warner, J. H. Shape Evolution of Monolayer MoS₂ Crystals Grown by Chemical Vapor Deposition. *Chem. Mater.* **2014**, 26 (22), 6371–6379.

- (36) Liu, B.; Fathi, M.; Chen, L.; Abbas, A.; Ma, Y.; Zhou, C. Chemical Vapor Deposition Growth of Monolayer WSe₂ with Tunable Device Characteristics and Growth Mechanism Study. *ACS Nano* **2015**, 9 (6), 6119–6127.
- (37) Brebrick, R. F. Partial Pressure of Se 2 (g) in Selenium Vapor. *J. Chem. Phys.* **1968**, 48 (12), 5741–5743.
- (38) Xiang, Y.; Guo, F.-W.; Lu, T.-M.; Wang, G.-C. Reflection High-Energy Electron Diffraction Measurements of Reciprocal Space Structure of 2D Materials. *Nanotechnology* **2016**, 27 (48), 485703.
- (39) Tang, F.; Parker, T.; Wang, G.-C.; Lu, T.-M. Surface Texture Evolution of Polycrystalline and Nanostructured Films: RHEED Surface Pole Figure Analysis. *J. Phys. D: Appl. Phys.* **2007**, 40 (23), R427–R439.
- (40) Chubarov, M.; Choudhury, T. H.; Zhang, X.; Redwing, J. M. In-Plane x-Ray Diffraction for Characterization of Monolayer and Few-Layer Transition Metal Dichalcogenide Films. *Nanotechnology* **2018**, 29 (5), 055706.
- (41) Zhang, F.; Erb, C.; Runkle, L.; Zhang, X.; Alem, N. Etchant-Free Transfer of 2D Nanostructures. *Nanotechnology* **2018**, 29 (2), 025602.
- (42) van der Zande, A. M.; Huang, P. Y.; Chenet, D. A.; Berkelbach, T. C.; You, Y.; Lee, G.-H.; Heinz, T. F.; Reichman, D. R.; Muller, D. A.; Hone, J. C. Grains and Grain Boundaries in Highly Crystalline Monolayer Molybdenum Disulphide. *Nat. Mater.* **2013**, 12 (6), 554–561.
- (43) Zou, X.; Liu, Y.; Yakobson, B. I. Predicting Dislocations and Grain Boundaries in

Two-Dimensional Metal-Disulfides from the First Principles. *Nano Lett.* **2013**, *13* (1), 253–258.

Chapter 5

Defect-Controlled Nucleation and Orientation of WSe₂ on hBN

This chapter further developed a defect-controlled approach for the nucleation and epitaxial growth of WSe₂ on hBN in a gas source chemical vapor deposition process and explored the role of single-atom vacancies on the hBN surface in controlling orientation of WSe₂ domains. In previous chapter, inversion domain boundaries become an unsolved issue in the coalesced monolayer film grown on sapphire substrate. The results in this chapter reveal an important nucleation mechanism for epitaxial growth of van der Waals heterostructures and demonstrate hBN as a superior substrate for single crystal transition metal dichalcogenide films, resulting in a reduced density of inversion domain boundaries and improved properties. The results motivate further efforts focused on the development of single crystal hBN substrates and epilayers for synthesis of wafer-scale single crystal transition metal dichalcogenide films.

5.1 Introduction

The rapid development of device technologies based on 2D transition metal dichalcogenides (TMDs) and their heterostructures presents increasing demand for synthesis of wafer-scale high quality single crystal monolayer and few layer films. Wafer-scale coalesced polycrystalline TMD films on amorphous substrates have been demonstrated via a hot-wall metalorganic chemical vapor deposition (MOCVD) process.¹⁻³ To reduce the prevalence of random orientations and high-angle grain

boundaries, epitaxial growth of TMD domains or films has been further investigated on various single crystal substrates such as epitaxial graphene,^{4–6} hexagonal boron nitride (hBN),^{7,8} Au (111),⁹ and c-plane sapphire.¹⁰ The epitaxial growth of TMDs has been further developed into a wafer-scale process via controlled nucleation and coalescence of a high density of islands into a continuous film on c-plane sapphire.¹¹ However, inversion domain boundaries (IDBs) (also referred to as mirror twin grain boundaries) were still observed in these films resulting from a merging of a mixture of 0° and 180° oriented domains.^{5,8,11,12} IDBs have been predicted and experimentally demonstrated to exhibit metallic character and consequently can serve as conducting channels within the monolayer that negatively impact both electrical and optical properties.^{13–16} In addition, non-uniformities in the optical and transport properties of these TMD films arise from steps and surface dangling bonds at the interface between the 2D film and 3D substrate.^{11,17,18} All of these factors negatively impact the properties of coalesced monolayer films and also promote undesirable multilayer growth.

In contrast to conventional single crystal substrates (e.g. sapphire), an hBN substrate offers many potential benefits for the epitaxial growth of large TMD domains. The basal plane of hBN, in its pristine form, can be considered free of steps and dangling bonds and is expected to enable reduced nucleation density and high adatom surface diffusivity. The hexagonal crystal structure of hBN makes it compatible for epitaxial growth of most 2D TMDs.^{8,19} In addition, the high dielectric constant and chemically inert surface of hBN suppresses scattering from charged impurities and substrate phonons, yielding higher mobilities^{20–22} and increased exciton densities^{23,24} in adjacent

TMD monolayers. Okada et al. first presented the 0° and 180° oriented domains for WS_2 grown on hBN via powder vapor transport (PVT),³² followed by Yu et al. who demonstrated the epitaxial growth of MoS_2 on hBN via PVT showing these two oriented domains in approximately equal number similar to that obtained for growth on sapphire.⁸ However, Fu et al. observed up to 98% preferred orientation for monolayer MoS_2 domains grown on hBN by molecular beam epitaxy (MBE).²⁵ Subsequent first-principles calculations reported by Zhang et al. proposed that the orientation selectivity originates from single-atom vacancies on the hBN surface that act as nucleation sites and break the nearly degenerate $0/180^\circ$ domain orientations.²⁶ Achieving a single preferred orientation of TMD domains on hBN is highly desired to reduce the density of IDBs in coalesced epitaxial films, however, little is known about the origin and nature of the single atom vacancies in hBN responsible for this behavior. In addition, the ability to harness these defects to control both the nucleation density and orientation of TMD monolayer domains is highly desired as a pathway to achieve high quality single crystal monolayers over large areas via coalescence of individual domains.

In this study, we investigate the mechanism of defect-controlled domain alignment of 2D TMDs on hBN using a combination of experimental studies and first-principles calculations. The results provide experimental evidence that single-atom vacancies in hBN trap W atoms and thereby act as nucleation sites that break the symmetry and selectively stabilize a single preferred WSe_2 domain orientation. Subsequent coalescence of the WSe_2 domains leads to monolayer films with reduced

IDBs and enhanced photoluminescence and transport properties thereby demonstrating the significant benefits of hBN as a substrate or template layer for TMD epitaxy.

5.2 Experimental Setup

5.2.1 Substrate preparation

The hBN flakes were mechanically exfoliated (ME) from powder (grade PT 110, Momentive Performance Materials) and placed on a c-plane sapphire substrate. Both freestanding ME-hBN transferred onto TEM grid and ME-hBN placed on sapphire substrate were used as templates to fabricate WSe₂/hBN heterostructures by gas source CVD process.

5.2.2 WSe₂ multi-step growth process

The multi-step gas source CVD process developed in chapter 4 was also employed in this study. Substrate was placed onto a SiC-coated graphite susceptor which was inductively heated up to 800 °C under H₂ in a cold wall vertical quartz tube reactor. W(CO)₆ was first introduced into the reactor at a high flow rate of 1.2×10^{-3} sccm to drive nucleation. The W(CO)₆ flow was then removed for 10 min which allows surface species to diffuse and form oriented WSe₂ domains. Afterward, the W(CO)₆ flow was re-introduced into the reactor at a lower flow rate of 6.1×10^{-4} sccm to promote lateral growth of the domains. The H₂Se flow rate was maintained at 7 sccm during the whole growth process.

5.2.3 Plasma treatment

The hBN flakes on sapphire substrate were exposed to reactive ion etching treatment. 50 sccm of He gas was introduced into a Tepla M4L Plasma Etch system at a regulated pressure of 180 mTorr, with a radio frequency (13.56 MHz) power of 50W to generate He plasma. Different etching times were applied to hBN surfaces while fixing other plasma generation parameters.

5.2.4 NH₃ Annealing

The hBN flakes on sapphire substrate were annealed in a group III-nitride MOCVD system under NH₃/H₂ environment for 30 minutes at a temperature of 1100 °C. An NH₃ flow rate of 1 slm was used and ultra high purity H₂ was used as an additional carrier gas with a total flow rate of 7 slm and reactor pressure of 50 Torr.

5.2.5 Morphology characterization

The surface morphology of the samples was analyzed by atomic force microscopy (AFM) using a Bruker Dimension Icon Atomic Force Microscope system and field emission scanning electron microscopy (FESEM) using a Zeiss Merlin instrument.

5.2.6 TEM characterization

Scanning transmission electron microscopy (STEM) imaging were carried out on a FEI Titan³ 60-300 microscope operating at 80kV with a monochromated gun and spherical aberration corrected lenses, providing sub-angstrom resolution. A HAADF detector was used for the ADF-STEM imaging with a collection angle of 51-300 mrad, a beam current of 45 pA, and beam convergence angle of 30 mrad (C2 aperture of 70 μm) for STEM image acquisition. The HREM imaging condition for hBN surface defects was tuned to a negative Cs to provide white atom contrast at a slight over focus. Imaging of surface defects on BN carried out at the electron dose of $\sim 5000 \text{ e}^-/\text{\AA}^2 \cdot \text{s}$ to minimize structural damage.²⁷

5.2.7 Photoluminescence measurement

A Renishaw inVia microscope with a Coherent Innova 70C argon-krypton laser with 488 nm excitation wavelength was used for acquiring the Raman and photoluminescence (PL) spectra using a backscattering configuration with a 1800 lines/mm grating. PL mapping of both WSe₂/hBN and WSe₂/sapphire were carried out using a HORIBA LabRAM HR Evolution high spectral resolution analytical Raman microscope with a laser wavelength of 532 nm. Temperature-dependent PL spectra were measured using a Linkam THMS600 optical stage as the sample holder. All the low-temperature PL spectra were acquired in nitrogen environment.

5.2.8 Electrical measurement

The films were transferred onto a 100 nm SiO₂ on p⁺⁺ Si substrate using a PMMA assisted transfer process (see 2.5 Etch-free Transfer of 2D TMD films).²⁸ The 5 μ m channel regions for the WSe₂ on SiO₂ and WSe₂ on hBN on SiO₂ devices were defined using electron beam lithography (Raith EBPG-5200) and ZEP520A photoresist. The WSe₂ was etched using a SF₆/O₂ based etch in a Plasma-Therm Versalock etch tool. The resist was then removed by submersing in 85 °C JT Baker PRS3000 for 30 minutes followed by an IPA rise. The source drain contacts were patterned using a MMA/PMMA resist process and the 40 nm Ni/ 30 nm Au metal contacts were deposited via electron beam evaporation (Kurt J. Lesker Lab-18). Measurements were taken in vacuum (<10⁻⁵ Torr) using a Lakeshore CRX-VF probe station and a Keysight B1500A. The hBN thickness was measured by AFM.

5.2.9 First principles calculations

All first-principles calculations were performed within density functional theory, using the Perdew-Burke-Ernzerhof parametrization of the generalized gradient approximation (GGA-PBE) exchange-correlation functional.^{29,30} Electron-ion interactions were modeled by projector augmented wave (PAW)^{31,32} pseudopotentials, as implemented in the Vienna Ab initio Simulation Package (VASP).³³ A semi-empirical pairwise Van der Waals correction were included using the DFT-D3 method by Grimme.³⁴ Structural relaxations were performed until forces were smaller than 0.01

eV/Å. For the migration barrier of a W adatom on top of WSe₂, the nudged elastic band calculation³⁵ were performed using the climbing image method.³⁶

5.3 Preferential Domain Orientation

WSe₂ monolayer films were grown by a multi-step process in a gas source CVD reactor at 800 °C using W(CO)₆ and H₂Se in a H₂ carrier gas.²³ Single crystal hBN flakes exfoliated from bulk crystals onto c-plane sapphire ((0001) α-Al₂O₃) were used as substrates. In this case, a short 20 min growth time was used to achieve separated WSe₂ domains. The WSe₂ triangular domains grow epitaxially on the mechanically exfoliated hBN surface with only two orientations (Figure 5-1a), with the majority of the domains (~84%) exhibiting a single orientation, and the remainder inversely oriented (Figure 5-1b). This is different than previous growth outcomes of TMD monolayers on c-plane sapphire where the epitaxial domains show 0° and 180° oriented domains with nearly equal proportion.^{10,11} To directly inspect the structure of laterally stitched regions, a partially-coalesced WSe₂ monolayer on an hBN flake was transferred onto a transmission electron microscopy (TEM) grid and an area with two types of merging domains – between the same (region A in Figure 5-1c) and inverse (region B) orientations – was identified by scanning TEM (STEM) (done by Fu Zhang, Penn State). Figure 5-1d shows the high angle annular dark field (HAADF-) STEM image (top) and corresponding inverse fast Fourier transform (FFT) image (after selecting only the WSe₂ FFT spots, bottom) of region A, demonstrating a continuous WSe₂ lattice on hBN stitched seamlessly between the two domains with the same orientation. In contrast, the HAADF-

STEM image (top) and corresponding inverse FFT image (bottom) of region B in Figure 1e clearly shows the formation of an IDB between two domains with 0° and 180° orientation. An atomic resolution HAADF-STEM image along the IDB shows 4|8 ring motifs (Figure 5-2), consistent with a previous report.¹² This demonstrates that the density of IDBs can be minimized by maximizing the orientational uniformity of WSe₂ on hBN, in which case stitching across same-orientation domains would not be troubled by translationally offset grain boundaries and would not leave an unclosed gap inaccessible to incoming source molecules.

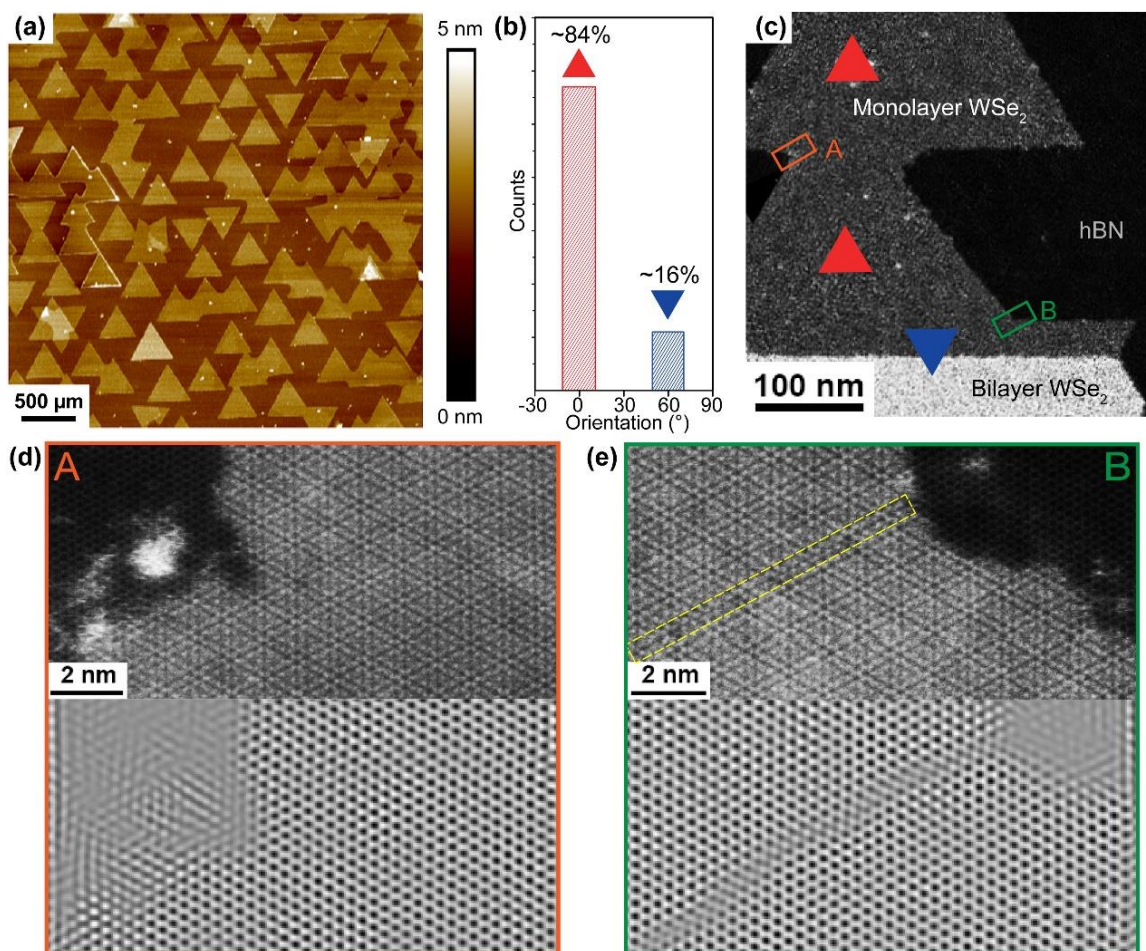


Figure 5-1. (a) AFM image of epitaxial WSe₂ domains on hBN. (b) Orientation histogram of 0° and 180° oriented WSe₂ domains on hBN. (c) ADF-STEM image of region with two types of merging domains. (d) HAADF-STEM image (top) and corresponding inverse FFT image (bottom) of region A in (c) showing no grain boundary formed between two domains with same orientation. (e) HAADF-STEM image (top) and corresponding inverse FFT image (bottom) of region B in (c) showing inversion domain boundary formed between two domains with 0° and 180° orientation.

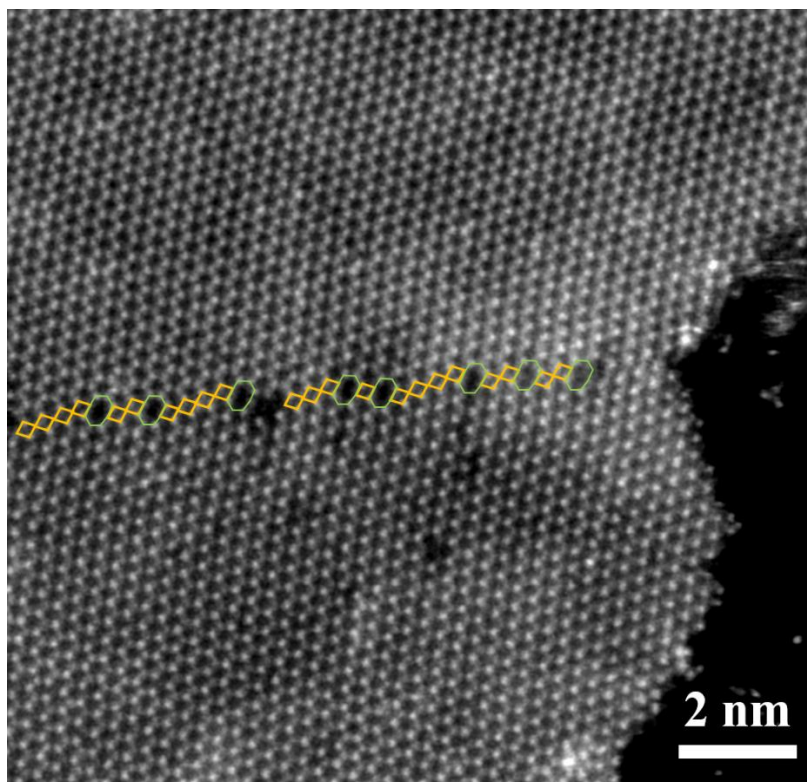


Figure 5-2. HAADF-STEM image of WSe₂ on BN, the anti-phase grain boundary between the 0° and 60° domains contains 4|8 rings highlighted in the image. It is noted that a slight sample tilt and high contrast are applied in the imaging condition to blur the information of underlying BN and the corresponding Moiré patterns between WSe₂ and BN, which help identify the WSe₂ lattice.

5.4 Defect-Controlled Nucleation

First-principle calculations previously carried out for MoS₂ growth on hBN suggest the preferred orientation arises from single-atom vacancies on the hBN surface that lift the 0/180° degeneracy and stabilize one orientation against its inverse.²⁶ In addition, this mechanism also offers a pathway to control the nucleation density of TMD

domains on the surface. To investigate this further, the multi-step growth process from chapter 4 was adopted for WSe₂ growth on hBN which employs modulation of the W(CO)₆ partial pressure to independently control nucleation, domain ripening, and lateral growth of domains.¹¹ By isolating the nucleation step from the subsequent growth of domains, insights into the fundamental mechanisms that control WSe₂ growth on hBN can be gleaned. Figure 5-3a shows a series of SEM images of WSe₂ grown on hBN and sapphire surfaces under varied nucleation times of 30 s, 1 min, and 2 min while holding the times for ripening (10 min) and lateral growth (10 min) constant. For growth on sapphire, a continuous increase in domain density with increasing nucleation time was observed (Figure 5-3b). In contrast, the domain of WSe₂ on the hBN surface remains relatively constant density and preferred orientation (Figure 5-4) irrespective of the nucleation time.

The results can be interpreted using classical nucleation theory,³⁷ whereby the surface nucleation density N can be expressed as

$$N = \int n_s J A \exp\left(-\frac{\Delta G^*}{k_B T}\right) dt$$

where n_s is the available surface nucleation site density, J is the impingement rate of precursor molecules, A is the area of the nucleus, ΔG^* is the energy barrier to reach a critical nucleation size, T is the growth temperature and t is the nucleation time. In the case of sapphire, WSe₂ can readily nucleate on the surface due to the relatively high surface energy (from dangling bonds, steps, etc.), which results in a reduced energy barrier ΔG^* to nucleation. In addition, the available surface nucleation site density n_s on sapphire is large and invariant due to the high concentration of steps and other defects

which act as nucleation sites. Since, for the experimental conditions employed, A , ΔG^* , J and T are constant, the nucleation density N is expected to vary linearly with the growth time t , which is consistent with the near linear relationship between domain density and nucleation time experimentally observed on sapphire in Figure 5-3b.

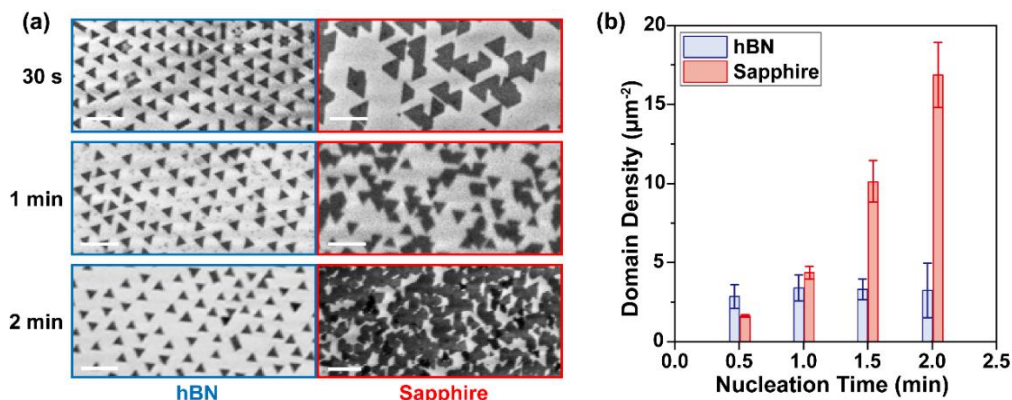


Figure 5-3. (a) SEM images of WSe₂ grown on hBN (left) and sapphire (right) respectively under varied nucleation time of 30 s, 1 min, and 2 min and same 10 min ripening and growth time. Scale bar: 1 μm. (b) Domain density histogram versus nucleation time showing the nucleation on hBN is not controlled by the amount of precursors on the surface.

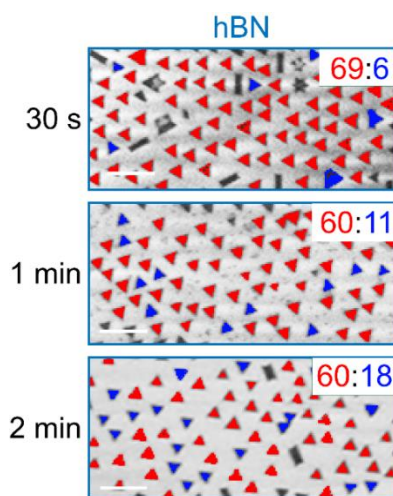


Figure 5-4. Color-marked SEM images of WSe₂ grown on hBN with a preferred orientation shown in Figure 2a. Scale bar: 1 μm.

In comparison, for pristine hBN, the low surface energy associated with the basal plane vdW surface results in a high nucleation energy barrier ΔG^* that makes WSe₂ nucleation on pristine hBN prohibitively unfavorable, limiting nucleation to hBN defects (e.g. single atom B or N vacancies), where ΔG^* is locally reduced. The available surface nucleation site density $n_s(t)$ thus starts equal to the defect density of hBN and becomes quickly depleted with increasing nucleation time due to the limited number of surface defects. Consequently, the domain density N saturates and becomes independent of nucleation time t (Figure 5-4b). Additional evidence of defect-limited nucleation comes from the non-uniform distribution of WSe₂ domains observed on one hBN flake (Figure 5-5), likely due to non-uniformities in the distribution and type of defects formed during mechanical exfoliation. All of the above observations reflect a defect-controlled nucleation mechanism for WSe₂ growth on hBN.

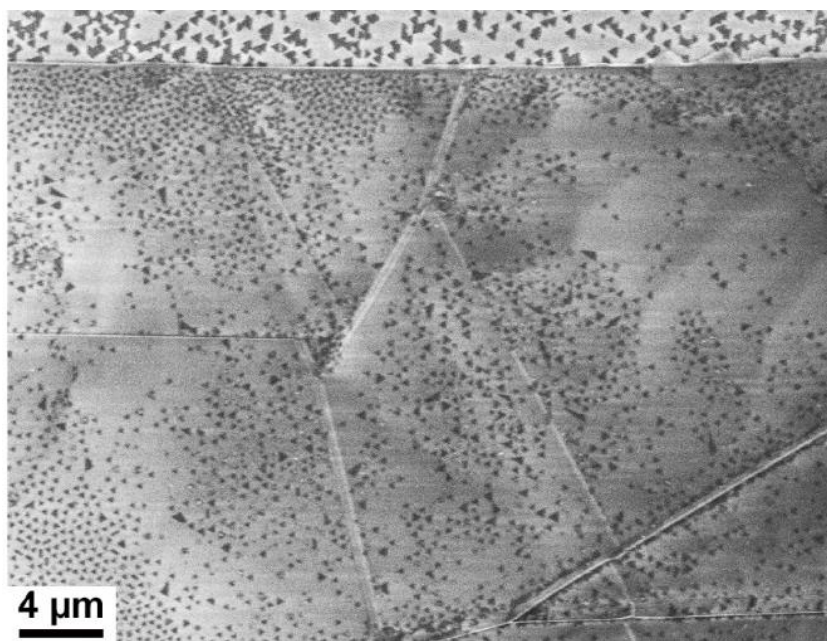


Figure 5-5. WSe₂ grown on pristine hBN surface under 30 s nucleation and 10 min ripening showing a non-uniform distribution of WSe₂ domains.

5.5 First-Principles Calculations

To further verify whether the density of hBN surface defects are on the order of μm^{-2} (thus limiting the WSe₂ domain density on hBN at the same level), first-principles density functional theory (DFT) calculations were used to predict the equilibrium hBN defect concentration as a function of temperature. The all DFT calculations in this chapter was done by Yuanxi Wang at Penn State. The experimental thermochemical condition (under which hBN defects are created) controlled by e.g. μ_{N} can be determined if we assume an initially defectless hBN reacts with H₂ to yield an equilibrium population of defects along with NH₃, and B₂H₆.³⁸ By requiring total atom conservation for B and N, the equilibrium population ratio of B to N vacancies should equal the partial pressure ratio of the corresponding products

$$\frac{e^{\frac{E_{\text{B-vac}} + \mu_{\text{B}} - E_{\text{hBN}}}{kT}}}{e^{\frac{E_{\text{N-vac}} + \mu_{\text{N}} - E_{\text{hBN}}}{kT}}} = \frac{2P_{\text{B}_2\text{H}_6}}{P_{\text{NH}_3}} = \frac{2e^{\frac{GB_2\text{H}_6 + 2\mu_{\text{N}} - 2GB_{\text{N}} - 3GH_2}{kT}}}{e^{\frac{GNH_3 + \mu_{\text{B}} - GB_{\text{N}} - 3/2GH_2}{kT}}}$$

where G terms are the standard Gibbs free energies and $E_{\text{B-vac}}$ and $E_{\text{N-vac}}$ are the total energies of boron and nitrogen vacancy systems respectively; the Gibbs energy for each gas species is given by $G = E_{\text{DFT}} + E_{\text{ZPE}} - TS$, where E_{ZPE} is the vibrational zero-point energy, and the entropy term TS is evaluated from the translational, rotational, electronic, and vibrational partition functions of the gas species at 800°C.³⁹ Together with the constraint of $\mu_{\text{B}} + \mu_{\text{N}} = E_{\text{hBN}}$, the equilibrium μ_{N} can be determined to be close to the N-poor condition, as discussed in the main text. Estimating hBN defect population if defects were created during hBN synthesis (and “frozen-in” during subsequent WSe₂ synthesis) or during hBN exfoliation is more challenging and beyond the scope of the present study.

As shown in Figure 5-6a, plotting the equilibrium defect density ($N_0 e^{-E_{\text{def}}/kT}$ where N_0 is the number of hBN unit cells per area and E_{def} the defect formation energy) with respect to temperature, a defect formation energy within the range of 1.5 to 2 eV is required to reach a defect density on the order of $\sim 1 \mu\text{m}^{-2}$ at 800 °C, as indicated by the dashed horizontal line. The defect formation energies for N and B vacancies are shown by the solid lines in Figure 5-6b, as a function of the Fermi energy relative to the valence band edge of hBN, where the two panels reflect the N-rich (N chemical potential μ_N set to the energy of N_2) and N-poor limit (B chemical potential $\mu_B = E_{\text{hBN}} - \mu_N$ set to the energy of bulk α -Boron).⁴⁰ Both simple boron and nitrogen vacancies (V_B and V_N in solid lines) and their hydrogenated complexes (dashed lines) are shown. The positive and negative slopes indicate positively and negatively charged states. Note that the entire range of Fermi energies is not realistically accessible (e.g. the conduction band edge of hBN is close to the vacuum level): it is estimated to be 1–2 eV above the valence band edge since WSe_2 exhibits p-type conductivity,⁴¹ as marked by the aligned WSe_2 bandgap in the same figure. The equilibrium μ_N can be determined to be close to the N-poor condition if we assume hBN defects are created during WSe_2 growth, with the lowest defect formation energy at ~ 3 eV. Along with additional defects formed during exfoliation, the above estimates suggest that μm^{-2} orders of defect densities are achievable by B and N vacancies in the hBN substrate before growth, leading to the same order of saturated nucleation densities during WSe_2 growth.

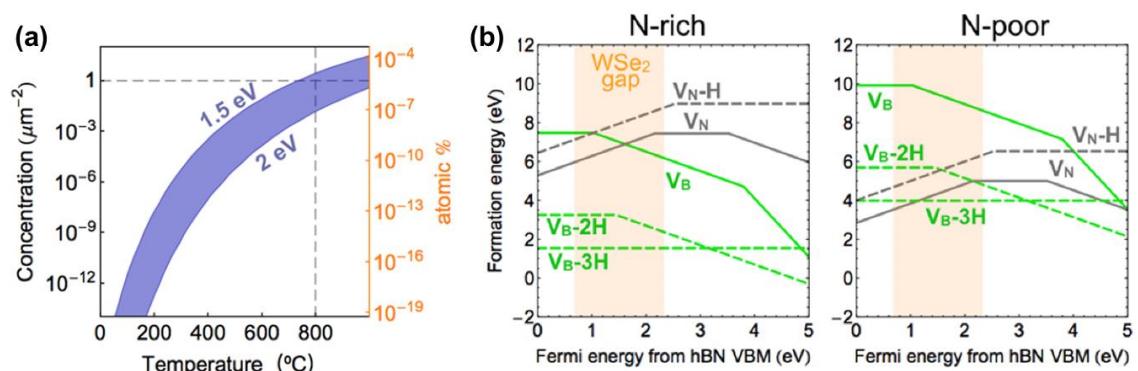


Figure 5-6. (a) Equilibrium defect concentration for a point defect with formation energies between 1.5 and 2 eV, as a function of temperature: a defect needs to have a formation energy in this range to achieve concentrations on the order of μm^{-2} at 800 $^{\circ}\text{C}$. (b) Defect formation energy for N and B vacancies under N-rich and N-poor conditions, considering bare vacancies (solid) and hydrogen-passivated ones (dashed). The orange energy range marks the calculated WSe₂ bandgap aligned with that of hBN.

5.6 TEM Investigation

To further probe the role of defects in nucleation and orientation, samples were prepared using hBN flakes transferred directly onto the TEM grid and then exposed to W species only in the gas source CVD system using a 30 s pulse of $\text{W}(\text{CO})_6$ at 800 $^{\circ}\text{C}$. The defect-assisted nucleation model described previously predicts the presence of an interstitial transition metal “glue” atom at the single atom vacancies on the hBN surface which controls the nucleation and orientation of the TMD on the point defect site.²⁶ The same defect-mediated distinction between 0/180 $^{\circ}$ stacking in WSe₂ calculated from DFT using an 8×8 hBN + 6×6 WSe₂ supercell is 0.90 eV, where the “eclipsed”

configuration²⁶ (top and side view in Figure 5-7a) is more stable; the “staggered” configuration²⁶ that would nucleate a domain with inverse orientation is unfavorable and suppressed. Compared to Figure 5-7b, which shows the bare ultra-thin hBN flake with surface defects of one kind (V_B or V_N), the HAADF-STEM image after W exposure in Figure 5-7c (done by Fu Zhang, Penn State) shows a single W atom stably trapped on the hBN surface at a single vacancy site. Furthermore, direct growth of tiny WSe₂ domains on the hBN on a TEM grid was carried out under 30 s nucleation and 5 min ripening. In the corresponding STEM image shown in Figure 5-7d (done by Fu Zhang, Penn State), a brighter imaged defect is visible which is consistent with the glue W atom between WSe₂ and the underlying hBN. The WSe₂ domain also has inevitably formed defects such as V_{Se} and V_{Se2} . In all of the WSe₂ domains examined, the glue W atoms appear within 3-5 nm of the center of the domain. This offset from the exact domain center likely arises from the fact that during the very early stages of growth, the domain may not grow at the same rate in all directions due to differences in edge stability and variations in precursor flux. To further test if the imaged glue W atoms are interstitials trapped at substrate defects instead of adatoms on top of WSe₂, we compare the energy landscape of W atoms on WSe₂ with typical knock-on energies from the imaging electron beam. Using nudged elastic band calculations at the DFT level, the migration barrier of a surface W adatom is found to be 0.4 eV (between the ground state at the metal site and the metastable state at the hollow site, as shown in Figure 5-7e) (done by Yuanxi Wang, Penn State); the migration barrier of a W adatom between WSe₂ and pristine hBN should be similar (according to similar migration barriers for metal adatoms on monolayer TMDs and inside bulk TMDs).⁴² Assuming relativistic binary collisions, the 80 keV electron beam

can transfer up to 1.0 eV kinetic energy to a W atom, sufficient for a surface adatom to hop between lattice sites. In addition, metal atom migration on TMDs has been previously reported under similar imaging conditions (80 keV).⁴³ Since hopping events were not seen over the duration of 10 min during STEM scanning, the imaged point-defects are unlikely to be mobile adatoms or interstitials and are likely trapped interstitials at vacancy sites in the hBN substrate.

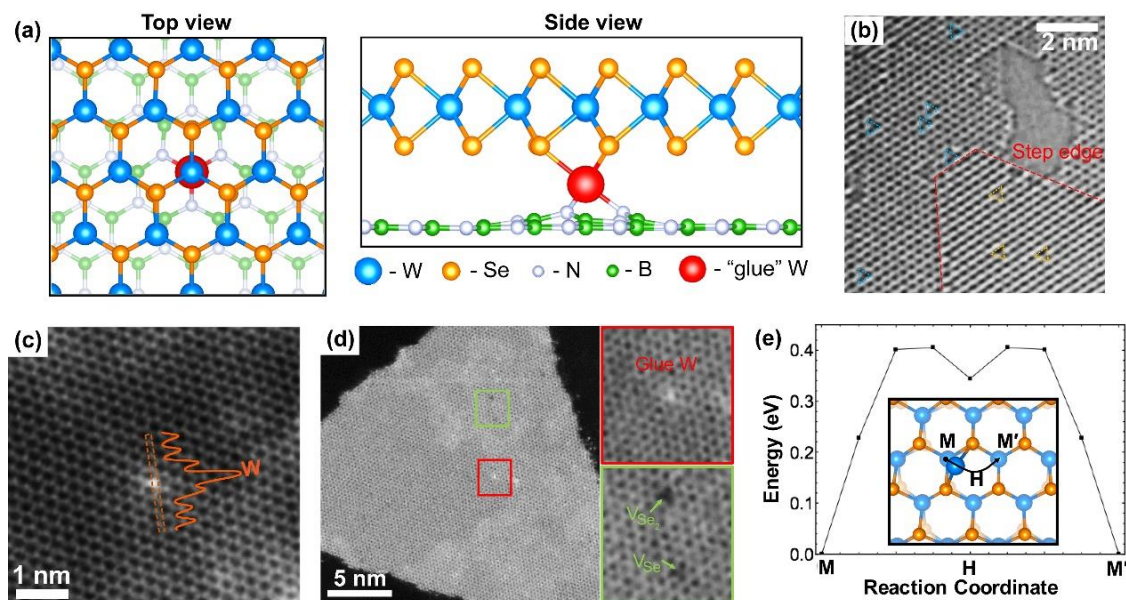


Figure 5-7. (a) Top and side view of the relaxed DFT structure of a W interstitial atom (red) sandwiched between pristine WSe₂ and a boron vacancy in hBN. (b) HRTEM images of monolayer to multilayer pristine hBN at 80 kV with a monochromated electron source; the intrinsic vacancies in BN is mostly V_N on the surface, which is also shown at the other side of the step edge. (c) HAADF-STEM image of a single W atom trapped at hBN surface after seeding process (30 s of W(CO)₆ flow at 800 °C), the overlay on the plot is the corresponding imaging intensity near the single W atom. (d) HAADF-STEM image of a brighter imaged defect indicating the glue W atom between WSe₂ and the underlying BN (red, top right). The WSe₂ domain also has inevitably formed defects such as V_{Se} and V_{Se2} (green, bottom right). (e) The migration barrier of a W adatom on a WSe₂ surface between the ground state at the (Metal) site and the metastable state at the (Hollow) site is 0.4 eV from a nudged elastic band calculation.

5.7 Controllable Nucleation via Defect Formation and Annealing

5.7.1 He plasma treatment

The fact that WSe₂ nucleation is determined by point defects on the hBN surface motivates a defect-assisted growth mechanism for vdW epitaxy whereby the nucleation density can be controlled by manipulating surface defect density. In order to test this, He direct plasma treatment at a RF power of 50 W was employed to intentionally introduce surface defects on the hBN/sapphire substrates. Figure 5-8 shows the SEM images of WSe₂ grown with 30 s nucleation and 10 min ripening on pristine hBN, hBN treated by 1 s He plasma, and hBN treated by 15 s He plasma, respectively. The short 1 s plasma treatment has already created a large number of defects on the hBN surface that significantly increases the WSe₂ domain density while still maintaining the epitaxial growth. Similarly, STEM results also show a consistently increasing density of glue atoms trapped at the defective surface which act as seeding sites (Figure 5-9 done by Fu Zhang, Penn State). Note that W atoms are always trapped at one set of BN lattices where either V_B or V_N forms, supporting the result of the single preferred orientation growth of WSe₂ domains. The distribution of WSe₂ domains on hBN becomes more uniform (Figure 5-10) at the same time indicating that the defects were created uniformly across hBN, when compared to the pristine case where additional defects could form during the mechanical exfoliation. However, the WSe₂ domains also start losing the character of single preferred orientation after the 1 s plasma treatment, possibly because both B and N single atom vacancies were created simultaneously during the plasma treatment. Longer plasma treatment can further increase the nucleation density but also heavily damages the

hBN surface and introduces other structural defects that results in island growth (multilayer domains) and loss of epitaxy in Figure 5-8.

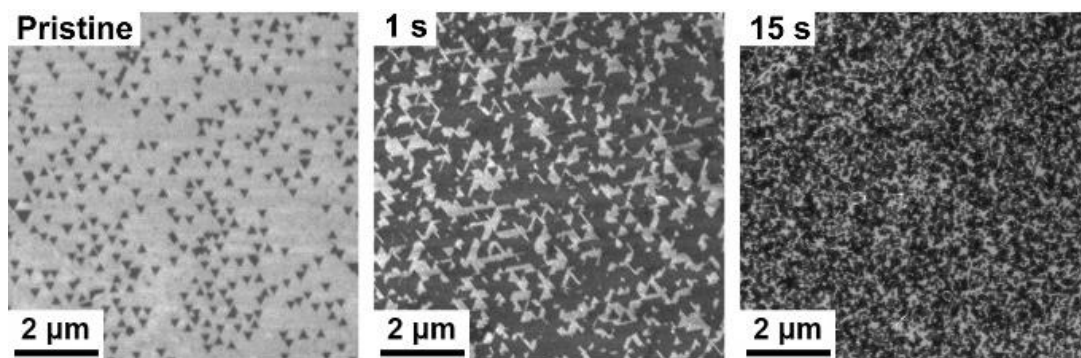


Figure 5-8. SEM images from left to right showing WSe₂ grown on pristine hBN, hBN treated by 1 s He plasma at 50 W, and hBN treated by 15 s He plasma at 50W respectively.

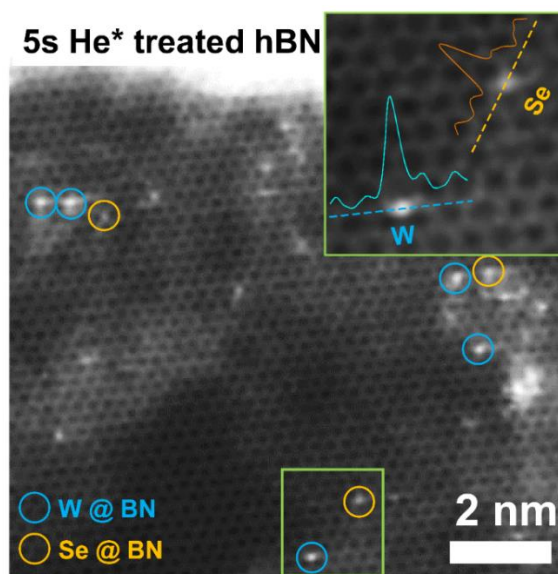


Figure 5-9. HAADF-STEM image of W and Se atoms trapped at hBN surface after growth process (with 5 s He plasma treated BN substrate), the overlay plots are the corresponding imaging intensity near the single W (blue) and Se (orange) atoms; respectively.

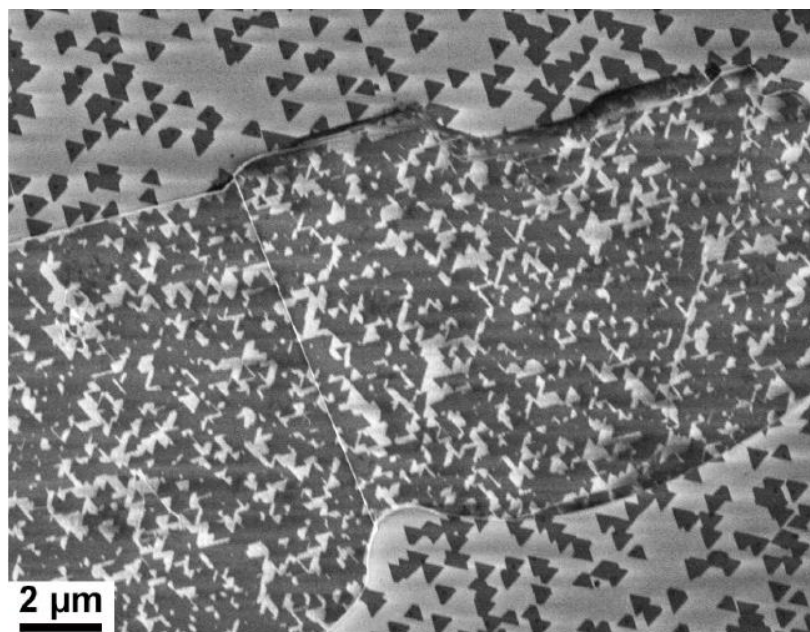


Figure 5-10. WSe₂ grown on 5 s He plasma treated hBN surface under 30 s nucleation and 10 min ripening showing that the distribution of WSe₂ domains on hBN becomes more uniform.

5.7.2 NH₃ annealing

In order to controllably create single atom vacancies of only one element, the plasma treated hBN surfaces were further annealed in NH₃ at 1100 °C for 30 min to reduce the concentration of N single atom vacancies. In this case, most of the N vacancies should be healed and B vacancies should be the majority on the hBN surface. Figure 5-11 shows SEM images of WSe₂ grown with 30 s nucleation and 10 min ripening on three types of hBN: hBN annealed in NH₃, hBN first treated by 1 s He plasma at 50 W then annealed in NH₃, and hBN first treated by 5 s He plasma at 50W then annealed in NH₃. All annealings were performed at 1100 °C for 30 min. When compared to WSe₂

grown on pristine hBN, both domain density and percentage of major domain orientation decrease for WSe₂ grown on the NH₃ annealed hBN surface (Figure 5-12a and 5-12b). Native B and N vacancies should exist on pristine hBN while N single atom vacancies are expected to be the major native defects due to their lower formation energy.^{44,45} By healing most of N vacancies during the NH₃ annealing, the total single atom vacancy density decreases, resulting in a decreased density of WSe₂ domains. However, not all N vacancies are expected to be healed and some N vacancies can even reform under the high temperature (800 °C) and H₂-rich environment during the WSe₂ growth process. In this case, the similar density of N and B vacancies results in the inverse orientations and thus decreases the percentage of major domain orientation. It is also possible that N antisite defects (N sitting on B vacancy) could form under NH₃ annealing, however we do not observe a distinctive peak at ~ 623 nm in the room temperature photoluminescence spectra (Figure 5-13) of the NH₃ annealed WSe₂/hBN sample which is associated with antisite defects.⁴⁶ Consequently, the decrease in nucleation density is likely not related to a decrease in B vacancies via formation of antisite defects during the NH₃ annealing process.

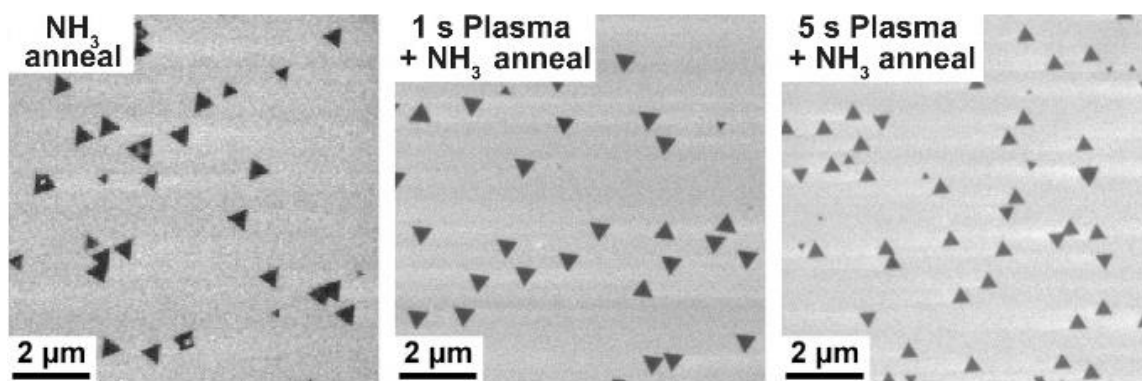


Figure 5-11. SEM images from left to right showing WSe₂ grown on hBN annealed in NH₃ at 1100 °C for 30 min, hBN first treated by 1 s He plasma at 50 W then annealed in NH₃ at 1100 °C for 30 min, and hBN first treated by 5 s He plasma at 50W then annealed in NH₃ at 1100 °C for 30 min respectively.

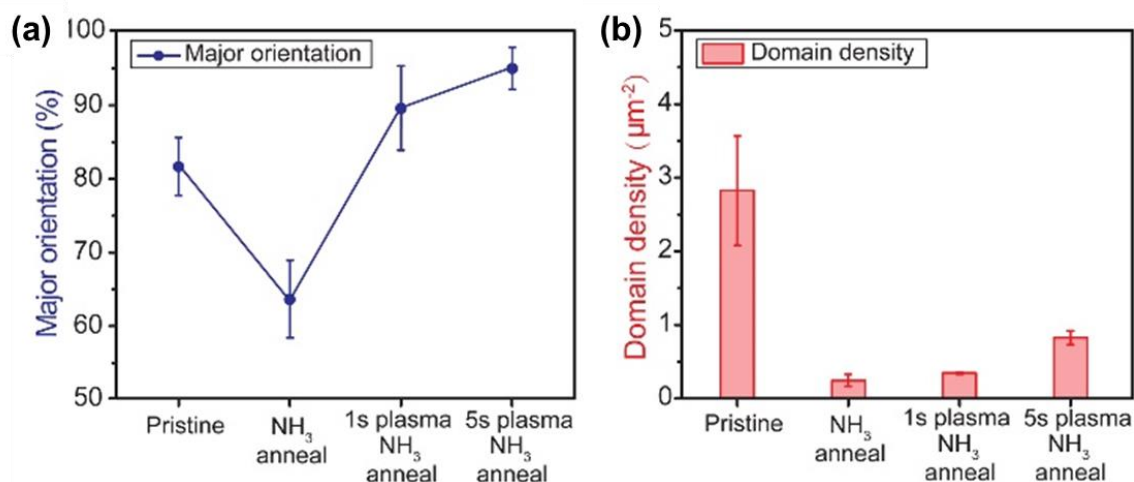


Figure 5-12. (a) Measured percentage of major domain orientation of WSe₂ domains grown on hBN surfaces under different treatment. (b) Measured nucleation density of WSe₂ domains grown on hBN surfaces under different treatment.

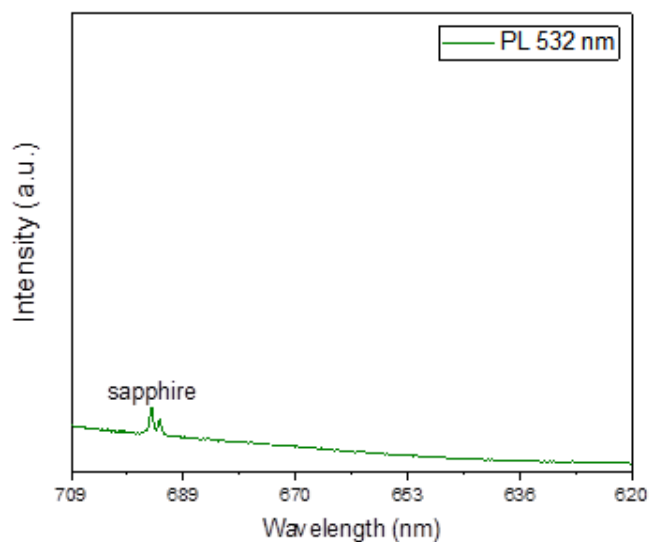


Figure 5-13. Room temperature PL spectrum of WSe₂/hBN sample annealed in NH₃ at 1100 °C for 30 min in the region where emission from N antisite defects is expected.

In comparison, on the hBN surface that was first treated by 1 s He plasma then annealed in NH₃, both domain density and the percentage of major domain orientation WSe₂ increase due to the additional B single atom vacancies formed at the hBN surface from the plasma treatment (Figure 5-12a and 5-12b). By further increasing the plasma treatment time to 5 s, a 95% major orientation (Figure 5-12a) and $\sim 0.9 \mu\text{m}^{-2}$ domain density (Figure 5-12b) can be achieved. Ideally, 100% single orientation can be approached by further removing steps, wrinkles and other defects in the hBN and suppressing N vacancy formation with in-situ NH₃ annealing. This defect-assisted nucleation introduces a useful way to control both the density and orientation of nuclei when establishing vdW epitaxial growth.

5.8 Coalesced Monolayer of WSe₂ on hBN

5.8.1 Lateral growth of WSe₂ domains

Once the nucleation density of WSe₂ on hBN has been controlled, the growth rate of the WSe₂ domains on hBN can be determined for a particular set of growth conditions by varying the lateral growth time. In this case, the hBN surface was only treated with NH₃ annealing to minimize the density of domains for better observation. The area of individual WSe₂ domains (Figure 5-14a) and the overall surface coverage of WSe₂ (Figure 5-14b) increase linearly as the lateral growth time is varied from 10, 15, 30, 60 to 90 min. This indicates that the precursors likely contribute to lateral growth of existing monolayer domains, rather than nucleating new domains, which is consistent with observations from atomic force microscopy (AFM) images (Figure 5-14d). It is worth noting that the measured growth rate for WSe₂ monolayers on hBN (~0.35 monolayers/min) is only a quarter of that observed for WSe₂ on sapphire (~1.3 monolayers/min),²³ even though a higher W(CO)₆ flow rate (6.1×10^{-4} sccm) was used during the lateral growth step when growing on hBN. This is likely due to the lower sticking coefficient and higher surface desorption rate of precursors on hBN compared to sapphire. In comparison, a similar W(CO)₆ flow rate (6.8×10^{-4} sccm) results in a high nucleation density on sapphire and a multilayer film can be achieved in 30 min.⁴⁷ This further validates the defect-controlled mechanism of WSe₂ nucleation on hBN. With appropriate nucleation density of WSe₂ achieved by plasma treatment and NH₃ annealing on hBN, continued lateral growth of the initial domains eventually leads to coalescence into a continuous monolayer film. Figure 5-14c shows a SEM image of a fully coalesced

monolayer WSe₂ film on an hBN flake. The dark triangular domains in Figure 5c are additional bilayer domains of WSe₂. These bilayer domains possibly arise from additional nucleation at intrinsic defects in the WSe₂ monolayer.

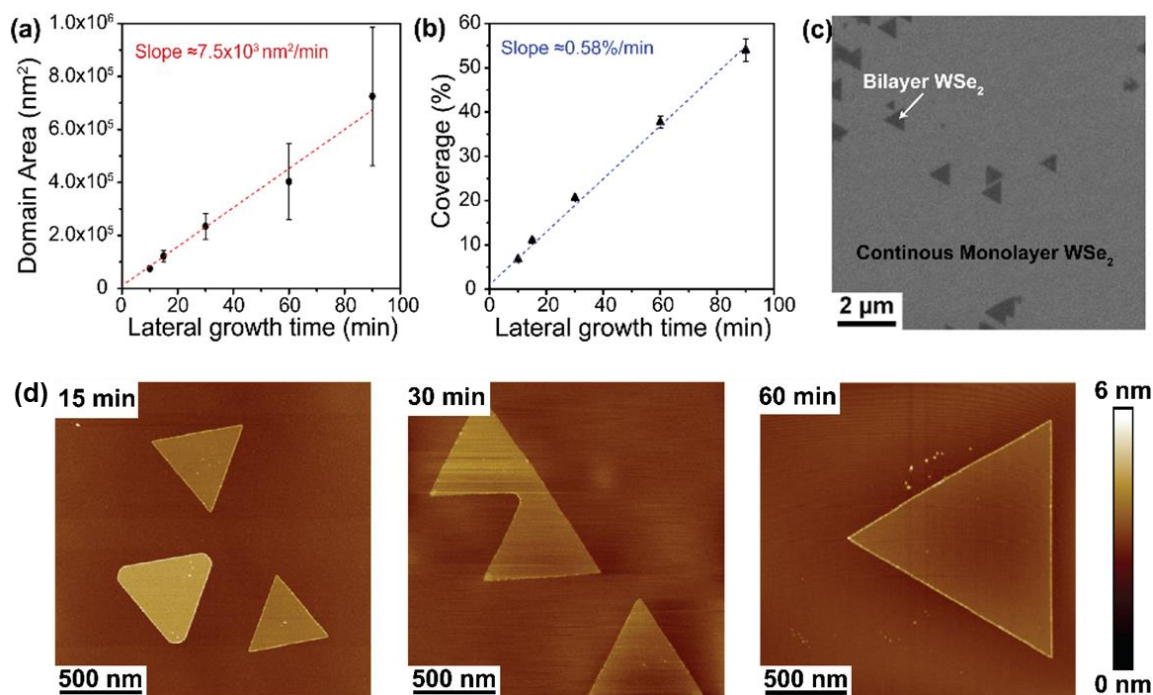


Figure 5-14. (a) WSe₂ monolayer domain area on hBN as a function of lateral growth time. The slope shows a linear growth rate of $7.5 \times 10^3 \text{ nm}^2/\text{min}$. (b) WSe₂ monolayer coverage on hBN as a function of lateral growth time. The slope shows a linear growth rate of 0.58 %/min. (c) SEM image of coalesced monolayer WSe₂ film on hBN. (d) AFM images of WSe₂ grown on NH₃ annealed hBN surfaces under 30 s nucleation time, 10 min ripening time and varied lateral growth time for 15, 30, and 60 min. The results show the increasing WSe₂ domain size with lateral growth time without any additional nucleation.

5.8.2 Epitaxial relationship between WSe₂ and hBN

To further validate and understand the epitaxial relationship between WSe₂ and hBN, a fully coalesced monolayer WSe₂ and its underneath substrate hBN flake were transferred onto a TEM grid together for STEM study (done by Fu Zhang, Penn State). Figure 5-15a shows an atomic resolution HAADF-STEM image of WSe₂ on hBN. The Moiré patterns of the WSe₂/hBN region and the hexagonal crystal structure of the hBN-only region at the edge indicate an epitaxial growth of monolayer WSe₂ on hBN. The selected area electron diffraction (SAED) pattern of the film shown in Figure 5-15b identifies the in-plane epitaxial relationship as $(1\bar{1}00)$ WSe₂ \parallel $(1\bar{1}00)$ hBN with 0° misorientation. Based on the Moiré patterns and the lattice constants of WSe₂ and hBN, the mismatch can be reduced to 1.5% for 3×3 WSe₂ unit cells on 4×4 hBN (schematic in Figure 5-15c).

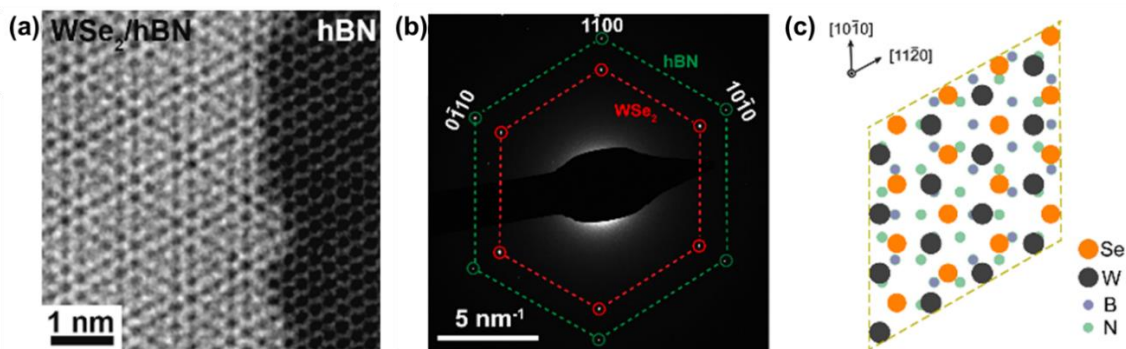


Figure 5-15. (a) Atomic resolution HAADF-STEM image showing the Moiré pattern of WSe₂ on hBN. (b) SAED pattern showing the epitaxial relationship between WSe₂ and hBN. (c) Schematic illustrating 3×3 WSe₂ unit cells on 4×4 hBN.

5.8.3 WSe₂/hBN vdW interface

Cross-sectional TEM was also performed on a coalesced WSe₂/hBN sample to further understand the interface between WSe₂ and hBN (done by Fu Zhang, Penn State). A region that contained a tri-layer domain of WSe₂ was selected to clearly distinguish the interlayer spacing. In Figure 5-16a, the regions of hBN, WSe₂, and the carbon protection layer can be distinguished by the crystal structure and interlayer distance. The first layer of WSe₂ shows the highest intensity since it is a fully coalesced monolayer that spans the entire sample thickness while the second and third layers which are from a portion of an isolated domain have lower intensity. A clear and sharp interface between WSe₂ and hBN indicates vdW epitaxy occurs with no additional passivating layer. This is different than growth of WSe₂ on sapphire where an extra Se passivating layer and strong WSe₂-substrate bonding at step edges on the sapphire surface were found.¹⁸ In addition, a variation of interlayer distance at the WSe₂/hBN interface was also observed. Figure 5-16b depicts the intensity profile of the red dot line section in Figure 5-16a. Based on the intensity profile, the interlayer spacing of hBN-hBN and WSe₂-WSe₂ were measured as 0.33 nm and 0.67 nm, respectively. The spacing between WSe₂/hBN, however, was measured as 0.49 nm, which is nearly identical to the arithmetic mean of the hBN-hBN and WSe₂-WSe₂ spacings. This is consistent with the 0.51 nm hBN-WSe₂ spacing calculated from DFT (including the DFT-D3 vdW correction, done by Yuanxi Wang, Penn State), and with the usual arithmetic mean used for the vdW radii combination rule in empirical forcefield construction, i.e. $R_{ij} = (R_i + R_j)/2$ analogous to a hard-sphere model.^{48,49}

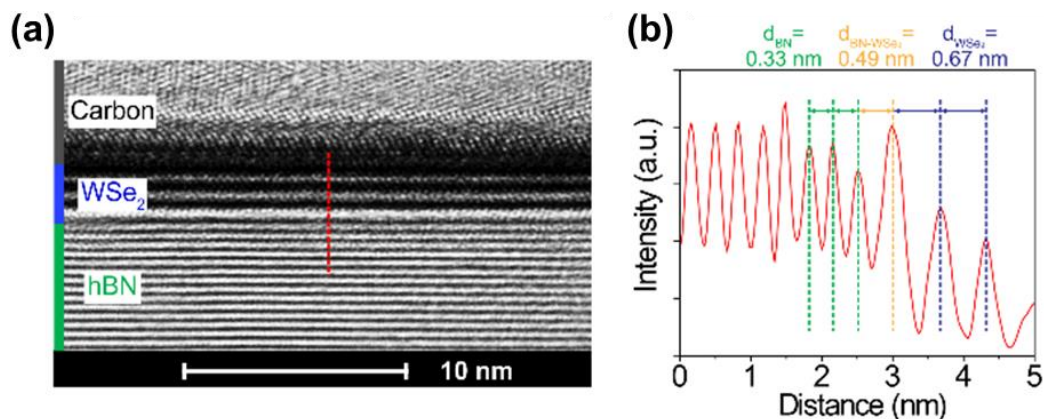


Figure 5-16. (a) Cross-sectional HRTEM image of the WSe₂ film on hBN showing a clear WSe₂ and hBN interface. (b) Intensity profile of the red dot line in (a) showing the interlayer spacing of hBN-hBN, hBN-WSe₂, and WSe₂-WSe₂ are 0.33 nm, 0.49 nm, and 0.67 nm respectively.

5.9 Enhanced Optical and Transport Properties

5.9.1 Photoluminescence properties of coalesced WSe₂

5.9.1.1 Room temperature PL and mappings

PL spectroscopy is an effective way to optically probe exciton-related emission and defect states in semiconducting TMDs.^{50,51} Figure 5-17a shows the PL spectra of coalesced WSe₂/hBN/sapphire and WSe₂/sapphire samples grown under identical conditions using the same power of 488 nm laser excitation. The results show an over 50 × enhancement in PL response for WSe₂/hBN compared to WSe₂/sapphire. In addition, the 1.65 eV PL peak position is uniform across the 5 × 5 μm measured area from the

WSe₂/hBN as shown in Figure 5-17b. In contrast, the PL peak position varied from 1.58 eV to 1.64 eV across the WSe₂/sapphire sample. This improvement can be attributed to the screening effect of the hBN substrate which suppresses the effects of charged impurities and substrate phonons thereby preserving the intrinsic properties of WSe₂.^{17,52,53} In comparison, the WSe₂ film on sapphire is affected by several factors including strain and substrate steps, which lead to non-uniformity in PL peak position and a decrease in PL intensity.

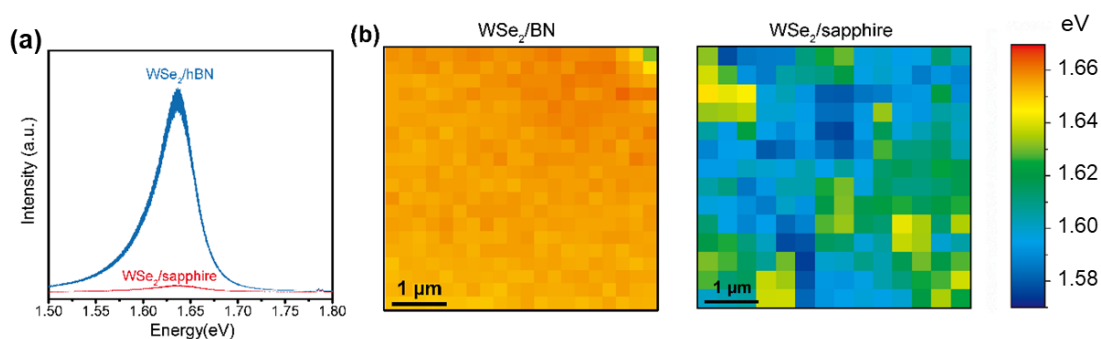


Figure 5-17. (a) PL spectra showing an over $50 \times$ enhancement in intensity for WSe₂/hBN compared to WSe₂/sapphire. (b) $5 \mu\text{m} \times 5 \mu\text{m}$ PL maps of coalesced WSe₂/hBN showing a uniform PL peak position at 1.65 eV (top) compared to varied peak positions ranging from 1.58-1.64 eV for coalesced WSe₂/sapphire (bottom).

5.9.1.2 Low temperature PL

To further investigate and compare the optical properties of monolayer WSe₂/hBN and WSe₂/sapphire, we acquired a series of temperature-dependent PL spectra from 300 K to 80 K (Figure 6c and 6d, respectively). All the low temperature PL in this chapter was carried out by Tianyi Zhang in Mauricio Terrones's lab at Penn State. At

higher temperature (above 200 K for WSe₂/hBN, and above 240 K for WSe₂/sapphire), the PL spectra exhibit a symmetrical single-peak, indicating the dominance of neutral exciton (X^0) emission in the higher temperature regime.⁵⁴ With the decrease of temperature, a low-energy shoulder emerges in the PL spectra for both samples, which can be assigned as negative trion (X^-) emission with a trion binding energy (E_{X^-}) \sim 30 meV. Remarkably, in the case of WSe₂/hBN, the X^0 and X^- peaks significantly sharpen and enhance at low temperatures, resulting in clearly resolved exciton emission (FWHM = 18.6 meV) and trion emission (FWHM = 38.5 meV) at 80 K (Figure S7). The FWHM values of both the exciton and trion emission are comparable to the emission spectra at 77 K⁵¹ and 4 K⁵⁵ reported for WSe₂/hBN heterostructures formed by exfoliation from bulk single crystals. This indicates that the optical properties of monolayer WSe₂ grown by gas source CVD on hBN in this work are comparable to that of single crystal flakes, especially considering that the reported samples either consisted of WSe₂ encapsulated in between two hBN flakes (removing the impact of the environment)⁵¹ or were characterized at lower temperature (further reducing linewidth broadening by reducing phonon scattering).^{55,56} In addition, no obvious defect-bound exciton (X^B) emission was observed in the monolayer WSe₂/hBN sample, indicating that the crystalline quality of WSe₂ was high when compared to other CVD processes.⁵⁰

In contrast, the WSe₂ film grown on sapphire exhibits broader PL emission at temperatures ranging from 80 K to 300 K. A broad X^B peak emerges in WSe₂/sapphire at temperatures below 160 K, causing the asymmetrical lineshape of PL emission. The fitting results of temperature-dependent PL emission peak position for both samples are plotted in Figure 6e and 6f, which also indicate the consistent X^0 and X^- emissions of

WSe₂ on hBN at different temperatures, and the emergence of X^B emissions from WSe₂ on sapphire at low temperature.

The narrower PL linewidths and negligible X^B emission for WSe₂/hBN compared to WSe₂/sapphire may be attributed to two factors: (1) The direct synthesis on the atomically-flat hBN surface which leads to a higher crystal quality monolayer WSe₂ film that contains less defects and IDBs, thus decreasing emission from optically-active defect states; and (2) WSe₂ grown on sapphire suffers from the substrate-induced charge doping,⁵⁶ which leads to the inhomogeneous broadening of excitonic emissions. By in-situ synthesizing WSe₂ on hBN, the interaction between charged sapphire and WSe₂ can be isolated by the hBN flake, allowing access to the intrinsic optical quality of as-grown WSe₂ films.^{57,58}

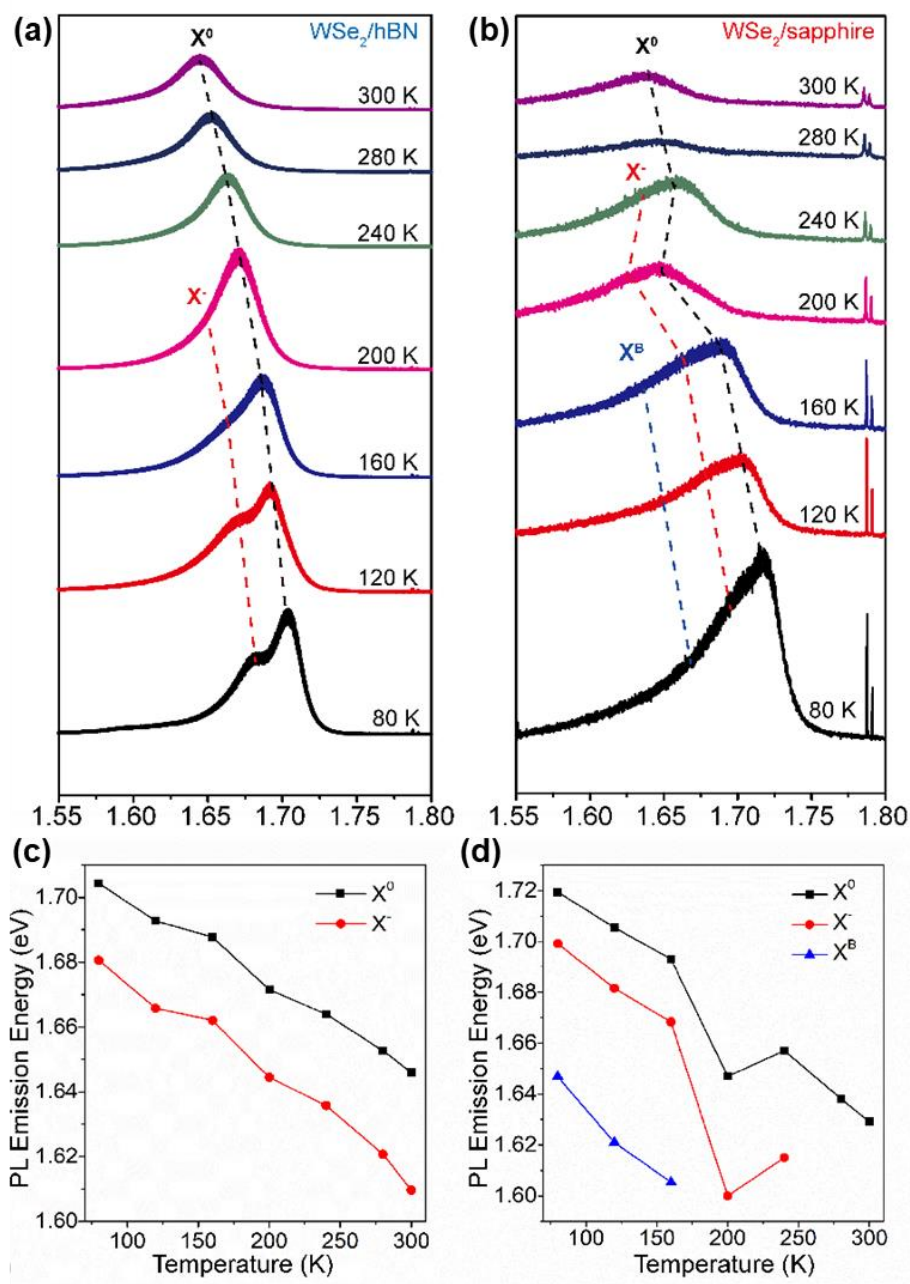


Figure 5-18. (a)-(b) Temperature-dependent PL spectra of WSe₂/hBN and WSe₂/sapphire under 488 nm laser excitation, respectively. The measured temperature ranges for both samples are from 80 K to 300 K. (c)-(d) Plots of fitted PL emission peak energy of WSe₂/hBN and WSe₂/sapphire versus temperature, respectively.

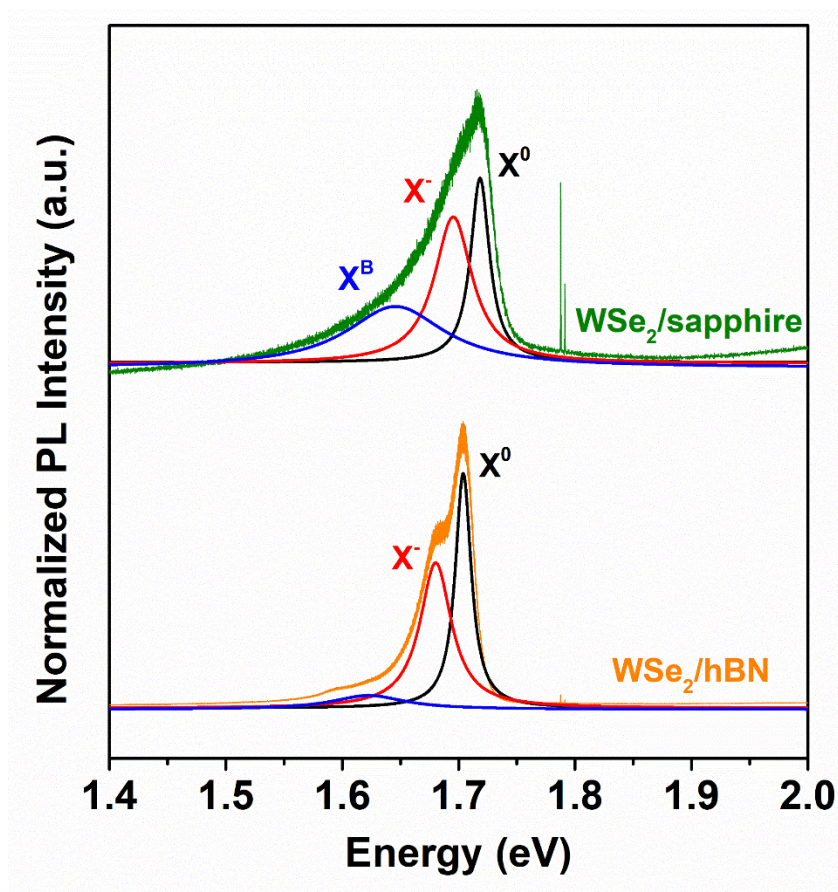


Figure 5-19. Deconvoluted PL spectra of WSe₂/hBN and WSe₂/sapphire at 80 K. The deconvoluted spectra were acquired by performing multipeak Lorentzian fitting using three peak components: neutral exciton (X^0), trion (X^-) and defect-bound exciton (X^B).

5.9.2 Transport properties of coalesced WSe₂

To characterize the electrical properties of both the WSe₂ grown on sapphire and on hBN, the films were removed from the sapphire substrates and transferred onto 100 nm SiO₂ on p⁺⁺ Si substrates. All the device fabrications in this chapter were carried out by Daniel Schulman at Penn State. Back gated FETs (BGFETs) with a channel length

(L_{CH}) of 1 μm and width (W) of 5 μm were fabricated as shown schematically in Figure 5-20a and 5-20d, respectively. Note that for the growth on hBN, the entire WSe_2/hBN stack was subsequently transferred. In this case, the hBN thickness has been verified as ~ 10 nm by AFM. Figure 5-20b and 5-20e, show the transfer characteristics i.e. drain current (I_{DS}) versus back gate voltage (V_{BG}) for different drain voltages (V_{DS}) and Figure 5-20c and 5-20f show the output characteristics i.e. I_{DS} versus V_{DS} for different V_{BG} for BGFETs based on WSe_2 grown on sapphire and hBN, respectively. Clearly, ambipolar transport i.e. the presence of a prominent electron branch current for $V_{BG} > 0$ V and hole branch current for $V_{BG} < 0$ V are observed for BGFETs based on WSe_2 grown on sapphire as seen in Figure 5-20b. This ambipolar transport is a result of the contact metal (in this case Ni) Fermi level being pinned near the center of the WSe_2 bandgap allowing injection of electrons and holes into the conduction and the valence band, respectively, through the corresponding Schottky barriers.⁵⁹ However, since carriers must tunnel through relatively large Schottky barrier heights which are almost half the bandgap energy of WSe_2 , the corresponding contact resistances for both electron and hole injections are large, limiting the ON state current as seen in the rectifying type behavior in Figure 7b. The field effect mobility extracted in the ON state from the peak transconductance, $\mu_{FE} = \frac{\partial I_{DS}}{\partial V_{GS}} \frac{L_{CH}}{C_G W V_{DS}}$, is severely underestimated in devices with Schottky barrier contacts.⁶⁰ For WSe_2 grown on sapphire, a contact limited electron μ_{FE} of $\sim 0.3 \text{ cm}^2/\text{Vs}$ was extracted (Figure 5-21a).⁶⁰ The devices are slightly n-type with an electron to hole current ratio of $\sim 100:1$ indicative of Ni Fermi level pinning closer to the conduction band. Note that although in the literature there are reports of WSe_2 FETs with

higher ON state currents and larger electron and hole μ_{FE} , these tend to use contact strategies engineered towards achieving primarily n-type or p-type devices at the expense of ambipolar characteristics which is achieved with the Ni contacts used in this work.^{61–63}

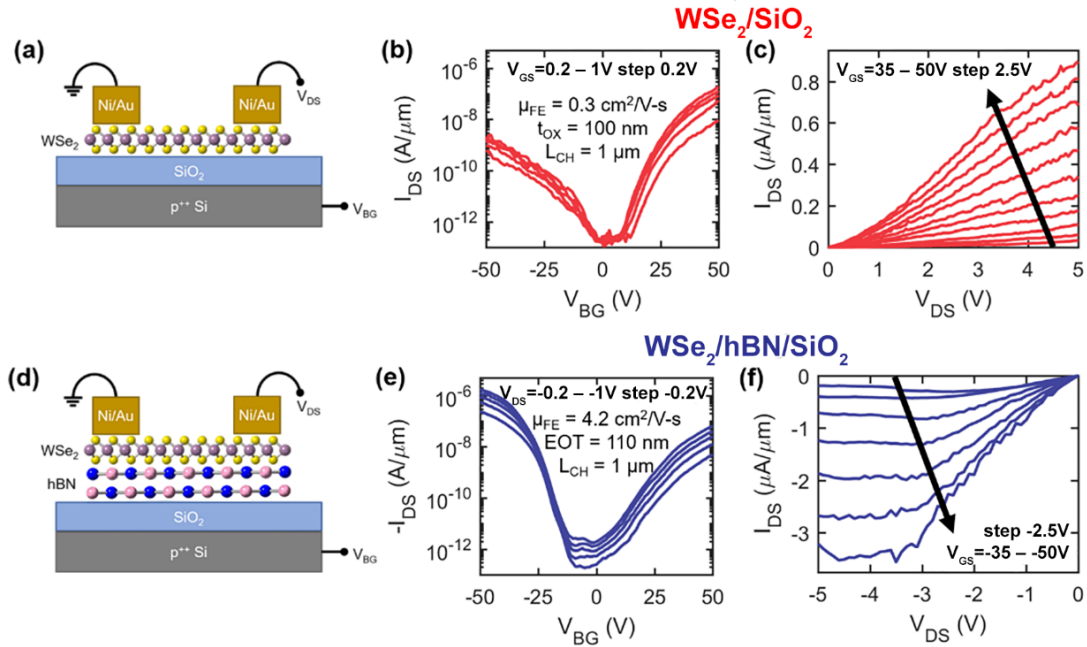


Figure 5-20. Electrical FET characterization of transferred WSe₂ and transferred WSe₂/hBN on SiO₂/p⁺⁺ Si. Schematic showing a back gated WSe₂ FETs (a) directly on 100 nm SiO₂ and (d) on 10 nm hBN on 100 nm SiO₂ on p⁺⁺ Si with Ni contacts. (b,e) Drain current (I_{DS}) versus back gate voltage (V_{BG}) at various drain voltages (V_{DS}) with step of 0.2 V and (c,f) I_{DS} versus V_{DS} at various V_{BG} with step of 2.5 V for WSe₂ on SiO₂ and on hBN/SiO₂, respectively.

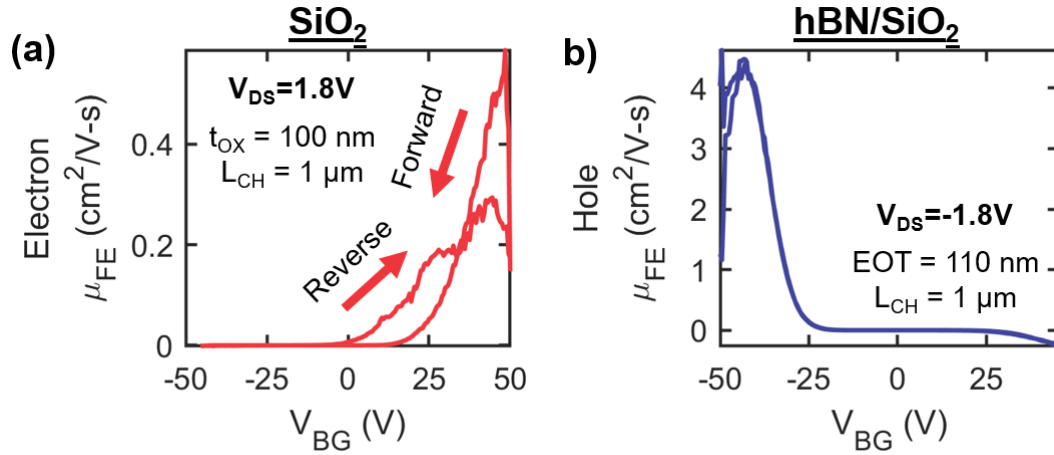


Figure 5-21. Mobility extraction for WSe₂ on SiO₂ and hBN/SiO₂. (a,b) The field effect mobility (μ_{FE}) versus V_{BG} at $V_{DS} = 1.8$ V and $V_{DS} = -1.8$ V for WSe₂ on SiO₂ and on hBN/SiO₂, respectively. The mobility is derived from the peak transconductance method where $\mu_{FE} = \frac{\partial I_{DS}}{\partial V_{GS}} \frac{L_{CH}}{C_G W V_{DS}}$. For WSe₂ on SiO₂, the mobility ($\mu_{FE} \approx 0.2$ cm²/V-s) is extracted from the reverse sweep direction (negative to positive V_{BG}) since interface trap discharging obscures the forward sweep characteristics. For WSe₂ on hBN/SiO₂, the large contact resistance causes the extracted μ_{FE} to decrease when $V_{BG} < -43$ V. Hence, the peak mobility of 4.2 cm²/V-s is contact limited, underestimating the true hole mobility of the material.

For BGFETs based on WSe₂ grown on hBN, there is no observable threshold shift, confirming the growth on hBN has not induced any significant substrate doping effect. While the electron branch currents are similar to those on SiO₂, a dramatic 3 orders of magnitude increase in the hole branch currents is observed. This cannot be

attributed to a simple change in the Fermi level pinning since an increase in the hole branch current would be accompanied by a decrease in the electron branch current. We hypothesize this hole branch improvement is due to a combination of factors. Part of the current increase can be attributed to an increase in the hole mobility, due to both a reduction in the IDBs as well as reduced interface scattering from the hBN versus SiO₂ interface. It is well known that hBN encapsulation of 2D materials improves the mobility, often by orders of magnitude, and reduces the interface states which can cause device hysteresis and degraded subthreshold slopes.^{64–66} Second, since the WSe₂ is monolayer, the hBN substrate may influence how the WSe₂ hybridizes with the Ni contact in such a way that hole injection has been facilitated. The charge injection from the contact into the WSe₂ can occur through a combination of many mechanisms and strongly depends on interface with the metal contact.⁶⁷ We notice these results are contrary to recent reports which show devices on hBN have reduced hole branch currents compared to on SiO₂.⁶⁸ The hole μ_{FE} extracted from these devices was 4.2 cm²/V-s (Figure 5-21b); however, this is likely contact limited since the I_{DS} versus V_{DS} characteristics in Figure 5-20f show rectifying type behavior.⁶⁰ These results demonstrate that WSe₂ growth on hBN is an effective means to improve the hole transport characteristics and tune FET devices to be ambipolar or p-type.

5.10 Conclusions

This chapter demonstrates a defect-controlled nucleation and orientation process for controllable epitaxial growth of single crystal WSe₂ monolayers on single crystal hBN

flakes. By appropriate plasma treatment and NH_3 annealing, the density of single atom vacancies on the hBN surface, and consequently the nucleation density of single oriented WSe_2 , can be controlled. The mechanism of this defect-controlled 2D heterostructure growth was investigated through first principles calculations and TEM characterization. A single crystal monolayer film was eventually achieved via coalescence of the initial domains with extended growth time. PL and electrical measurements show enhanced optical and transport properties, respectively, for the monolayer WSe_2 film grown on hBN compared to sapphire. Considering that wafer-scale single crystalline hBN has recently been demonstrated through a CVD method employing a liquid gold substrate,⁶⁹ this research clearly shows the potential of hBN as a substrate or template layer for epitaxial growth of high quality single crystal monolayer TMD films.

5.11 References

- (1) Chiu, M.-H.; Zhang, C.; Shiu, H.-W.; Chuu, C.-P.; Chen, C.-H.; Chang, C.-Y. S.; Chen, C.-H.; Chou, M.-Y.; Shih, C.-K.; Li, L.-J. Determination of Band Alignment in the Single-Layer MoS₂/WSe₂ Heterojunction. *Nat. Commun.* **2015**, *6*, 7666.
- (2) Kim, T.; Mun, J.; Park, H.; Joung, D.; Diware, M.; Won, C.; Park, J.; Jeong, S.-H.; Kang, S.-W. Wafer-Scale Production of Highly Uniform Two-Dimensional MoS₂ by Metal-Organic Chemical Vapor Deposition. *Nanotechnology* **2017**, *28* (18), 18LT01.
- (3) Kalanyan, B.; Kimes, W. A.; Beams, R.; Stranick, S. J.; Garratt, E.; Kalish, I.; Davydov, A. V.; Kanjolia, R. K.; Maslar, J. E. Rapid Wafer-Scale Growth of Polycrystalline 2H-MoS₂ by Pulsed Metal–Organic Chemical Vapor Deposition. *Chem. Mater.* **2017**, *29* (15), 6279–6288.
- (4) Shi, Y.; Zhou, W.; Lu, A.-Y.; Fang, W.; Lee, Y.-H.; Hsu, A. L.; Kim, S. M.; Kim, K. K.; Yang, H. Y.; Li, L.-J.; Idrobo, J.-C.; Kong, J. Van Der Waals Epitaxy of MoS₂ Layers Using Graphene As Growth Templates. *Nano Lett.* **2012**, *12* (6), 2784–2791.
- (5) Bianco, G. V.; Losurdo, M.; Giangregorio, M. M.; Sacchetti, A.; Prete, P.; Lovergine, N.; Capezzuto, P.; Bruno, G. Direct Epitaxial CVD Synthesis of Tungsten Disulfide on Epitaxial and CVD Graphene. *RSC Adv.* **2015**, *5* (119), 98700–98708.
- (6) Eichfeld, S. M.; Hossain, L.; Lin, Y.; Piasecki, A. F.; Kupp, B.; Birdwell, a G.;

- Burke, R. a; Lu, N.; Peng, X.; Li, J.; Azcatl, A.; McDonnell, S.; Wallace, R. M.; Kim, M. J.; Mayer, T. S.; Redwing, J. M.; Robinson, J. a. Highly Scalable, Atomically Thin WSe₂ Grown via Metal–Organic Chemical Vapor Deposition. *ACS Nano* **2015**, *9* (2), 2080–2087.
- (7) Yan, A.; Velasco, J.; Kahn, S.; Watanabe, K.; Taniguchi, T.; Wang, F.; Crommie, M. F.; Zettl, A. Direct Growth of Single- and Few-Layer MoS₂ on h-BN with Preferred Relative Rotation Angles. *Nano Lett.* **2015**, *15* (10), 6324–6331.
- (8) Yu, H.; Yang, Z.; Du, L.; Zhang, J.; Shi, J.; Chen, W.; Chen, P.; Liao, M.; Zhao, J.; Meng, J.; Wang, G.; Zhu, J.; Yang, R.; Shi, D.; Gu, L.; Zhang, G. Precisely Aligned Monolayer MoS₂ Epitaxially Grown on h-BN Basal Plane. *Small* **2017**, *13* (7), 1603005.
- (9) Zhang, F.; Momeni, K.; AlSaud, M. A.; Azizi, A.; Hainey, M. F.; Redwing, J. M.; Chen, L.-Q.; Alem, N. Controlled Synthesis of 2D Transition Metal Dichalcogenides: From Vertical to Planar MoS₂. *2D Mater.* **2017**, *4* (2), 025029.
- (10) Dumcenco, D.; Ovchinnikov, D.; Marinov, K.; Lazić, P.; Gibertini, M.; Marzari, N.; Sanchez, O. L.; Kung, Y.-C.; Krasnozhon, D.; Chen, M.-W.; Bertolazzi, S.; Gillet, P.; Fontcuberta i Morral, A.; Radenovic, A.; Kis, A. Large-Area Epitaxial Monolayer MoS₂. *ACS Nano* **2015**, *9* (4), 4611–4620.
- (11) Zhang, X.; Choudhury, T. H.; Chubarov, M.; Xiang, Y.; Jariwala, B.; Zhang, F.; Alem, N.; Wang, G.-C.; Robinson, J. A.; Redwing, J. M. Diffusion-Controlled Epitaxy of Large Area Coalesced WSe₂ Monolayers on Sapphire. *Nano Lett.* **2018**,

18 (2), 1049–1056.

- (12) van der Zande, A. M.; Huang, P. Y.; Chenet, D. A.; Berkelbach, T. C.; You, Y.; Lee, G.-H.; Heinz, T. F.; Reichman, D. R.; Muller, D. A.; Hone, J. C. Grains and Grain Boundaries in Highly Crystalline Monolayer Molybdenum Disulphide. *Nat. Mater.* **2013**, 12 (6), 554–561.
- (13) Zou, X.; Liu, Y.; Yakobson, B. I. Predicting Dislocations and Grain Boundaries in Two-Dimensional Metal-Disulfides from the First Principles. *Nano Lett.* **2013**, 13 (1), 253–258.
- (14) Ly, T. H.; Perello, D. J.; Zhao, J.; Deng, Q.; Kim, H.; Han, G. H.; Chae, S. H.; Jeong, H. Y.; Lee, Y. H. Misorientation-Angle-Dependent Electrical Transport across Molybdenum Disulfide Grain Boundaries. *Nat. Commun.* **2016**, 7 (1), 10426.
- (15) Du, L.; Yu, H.; Xie, L.; Wu, S.; Wang, S.; Lu, X.; Liao, M.; Meng, J.; Zhao, J.; Zhang, J.; Zhu, J.; Chen, P.; Wang, G.; Yang, R.; Shi, D.; Zhang, G. The Effect of Twin Grain Boundary Tuned by Temperature on the Electrical Transport Properties of Monolayer MoS₂. *Crystals* **2016**, 6 (9), 115.
- (16) Zhou, S.; Wang, S.; Shi, Z.; Sawada, H.; Kirkland, A. I.; Li, J.; Warner, J. H. Atomically Sharp Interlayer Stacking Shifts at Anti-Phase Grain Boundaries in Overlapping MoS₂ Secondary Layers. *Nanoscale* **2018**, 10 (35), 16692–16702.
- (17) Man, M. K. L.; Deckoff-Jones, S.; Winchester, A.; Shi, G.; Gupta, G.; Mohite, A. D.; Kar, S.; Kioupakis, E.; Talapatra, S.; Dani, K. M. Protecting the Properties of

Monolayer MoS₂ on Silicon Based Substrates with an Atomically Thin Buffer. *Sci. Rep.* **2016**, *6* (1), 20890.

- (18) Lin, Y.-C.; Jariwala, B.; Bersch, B. M.; Xu, K.; Nie, Y.; Wang, B.; Eichfeld, S. M.; Zhang, X.; Choudhury, T. H.; Pan, Y.; Addou, R.; Smyth, C. M.; Li, J.; Zhang, K.; Haque, M. A.; Fölsch, S.; Feenstra, R. M.; Wallace, R. M.; Cho, K.; Fullerton-Shirey, S. K.; Redwing, J. M.; Robinson, J. A. Realizing Large-Scale, Electronic-Grade Two-Dimensional Semiconductors. *ACS Nano* **2018**, *12* (2), 965–975.
- (19) Okada, M.; Sawazaki, T.; Watanabe, K.; Taniguchi, T.; Hibino, H.; Shinohara, H.; Kitaura, R. Direct Chemical Vapor Deposition Growth of WS₂ Atomic Layers on Hexagonal Boron Nitride. *ACS Nano* **2014**, *8* (8), 8273–8277.
- (20) Kretinin, A. V.; Cao, Y.; Tu, J. S.; Yu, G. L.; Jalil, R.; Novoselov, K. S.; Haigh, S. J.; Gholinia, A.; Mishchenko, A.; Lozada, M.; Georgiou, T.; Woods, C. R.; Withers, F.; Blake, P.; Eda, G.; Wirsig, A.; Hucho, C.; Watanabe, K.; Taniguchi, T.; Geim, A. K.; Gorbachev, R. V. Electronic Properties of Graphene Encapsulated with Different Two-Dimensional Atomic Crystals. *Nano Lett.* **2014**, *14* (6), 3270–3276.
- (21) Mayorov, A. S.; Gorbachev, R. V.; Morozov, S. V.; Britnell, L.; Jalil, R.; Ponomarenko, L. A.; Blake, P.; Novoselov, K. S.; Watanabe, K.; Taniguchi, T.; Geim, A. K. Micrometer-Scale Ballistic Transport in Encapsulated Graphene at Room Temperature. *Nano Lett.* **2011**, *11* (6), 2396–2399.
- (22) Ma, N.; Jena, D. Charge Scattering and Mobility in Atomically Thin

- Semiconductors. *Phys. Rev. X* **2014**, 4 (1), 1–9.
- (23) Wierzbowski, J.; Klein, J.; Sigger, F.; Straubinger, C.; Kremser, M.; Taniguchi, T.; Watanabe, K.; Wurstbauer, U.; Holleitner, A. W.; Kaniber, M.; Müller, K.; Finley, J. J. Direct Exciton Emission from Atomically Thin Transition Metal Dichalcogenide Heterostructures near the Lifetime Limit. *Sci. Rep.* **2017**, 7 (1), 12383.
- (24) Hoshi, Y.; Kuroda, T.; Okada, M.; Moriya, R.; Masubuchi, S.; Watanabe, K.; Taniguchi, T.; Kitaura, R.; Machida, T. Suppression of Exciton-Exciton Annihilation in Tungsten Disulfide Monolayers Encapsulated by Hexagonal Boron Nitrides. *Phys. Rev. B* **2017**, 95 (24), 241403.
- (25) Fu, D.; Zhao, X.; Zhang, Y.; Li, L.; Xu, H.; Jang, A.; Yoon, S. I.; Song, P.; Poh, S. M.; Ren, T.; Ding, Z.; Fu, W.; Shin, T. J.; Shin, H. S.; Pantelides, S. T.; Zhou, W.; Loh, K. P. Molecular Beam Epitaxy of Highly Crystalline Monolayer Molybdenum Disulfide on Hexagonal Boron Nitride. *J. Am. Chem. Soc.* **2017**, 139 (27), 9392–9400.
- (26) Zhang, F.; Wang, Y.; Erb, C.; Wang, K.; Moradifar, P.; Crespi, V.; Alem, N. Full Orientation Control of Epitaxial MoS₂ on HBN Assisted by Substrate Defects. **2018**.
- (27) Meyer, J. C.; Chuvilin, A.; Algara-Siller, G.; Biskupek, J.; Kaiser, U. Selective Sputtering and Atomic Resolution Imaging of Atomically Thin Boron Nitride Membranes. *Nano Lett.* **2009**, 9 (7), 2683–2689.

- (28) Zhang, F.; Erb, C.; Runkle, L.; Zhang, X.; Alem, N. Etchant-Free Transfer of 2D Nanostructures. *Nanotechnology* **2018**, 29 (2), 025602.
- (29) Perdew, J. P.; Burke, K.; Ernzerhof, M. Generalized Gradient Approximation Made Simple. *Phys. Rev. Lett.* **1996**, 77 (18), 3865–3868.
- (30) Perdew, J. P.; Burke, K.; Ernzerhof, M. Erratum: Generalized Gradient Approximation Made Simple (Physical Review Letters (1996) 77 (3865)). *Phys. Rev. Lett.* **1997**, 78 (8), 1396.
- (31) Joubert, D. From Ultrasoft Pseudopotentials to the Projector Augmented-Wave Method. *Phys. Rev. B - Condens. Matter Mater. Phys.* **1999**, 59 (3), 1758–1775.
- (32) Blöchl, P. E. Projector Augmented-Wave Method. *Phys. Rev. B* **1994**, 50 (24), 17953–17979.
- (33) Kresse, G.; Furthmüller, J. Efficient Iterative Schemes for Ab Initio Total-Energy Calculations Using a Plane-Wave Basis Set. *Phys. Rev. B - Condens. Matter Mater. Phys.* **1996**, 54 (16), 11169–11186.
- (34) Grimme, S.; Antony, J.; Ehrlich, S.; Krieg, H. A Consistent and Accurate Ab Initio Parametrization of Density Functional Dispersion Correction (DFT-D) for the 94 Elements H-Pu. *J. Chem. Phys.* **2010**, 132 (15), 154104.
- (35) JÓNSSON, H.; MILLS, G.; JACOBSEN, K. W. Nudged Elastic Band Method for Finding Minimum Energy Paths of Transitions. In *Classical and Quantum Dynamics in Condensed Phase Simulations*; WORLD SCIENTIFIC, 1998; pp 385–404.

- (36) Henkelman, G.; Uberuaga, B. P.; Jónsson, H. A Climbing Image Nudged Elastic Band Method for Finding Saddle Points and Minimum Energy Paths. *J. Chem. Phys.* **2000**, *113* (22), 9901–9904.
- (37) Ohring, M. A Review of Materials Science. In *Materials Science of Thin Films*; Elsevier, 2002; pp 1–56.
- (38) Ansary, A.; Nasser, M.; Boland, M. J.; Strachan, D. R. Parallel Boron Nitride Nanoribbons and Etch Tracks Formed through Catalytic Etching. *Nano Res.* **2018**, *11* (9), 4874–4882.
- (39) Cramer, C. J. *Essentials of Computational Chemistry: Theories and Models*, 2nd Edition; John Wiley & Sons, 2004.
- (40) Weston, L.; Wickramaratne, D.; Macko, M.; Alkauskas, A.; Van de Walle, C. G. Native Point Defects and Impurities in Hexagonal Boron Nitride. *Phys. Rev. B* **2018**, *97* (21), 214104.
- (41) Wang, J. I.-J.; Yang, Y.; Chen, Y.-A.; Watanabe, K.; Taniguchi, T.; Churchill, H. O. H.; Jarillo-Herrero, P. Electronic Transport of Encapsulated Graphene and WSe₂ Devices Fabricated by Pick-up of Prepatterned HBN. *Nano Lett.* **2015**, *15* (3), 1898–1903.
- (42) Komsa, H.-P.; Krasheninnikov, A. V. Native Defects in Bulk and Monolayer MoS₂ from First Principles. *Phys. Rev. B* **2015**, *91* (12), 125304.
- (43) Lin, Y.-C.; Dumcenco, D. O.; Komsa, H.-P.; Niimi, Y.; Krasheninnikov, A. V.; Huang, Y.-S.; Suenaga, K. Properties of Individual Dopant Atoms in Single-Layer

- MoS₂ : Atomic Structure, Migration, and Enhanced Reactivity. *Adv. Mater.* **2014**, 26 (18), 2857–2861.
- (44) Zobelli, A.; Ewels, C. P.; Gloter, A.; Seifert, G. Vacancy Migration in Hexagonal Boron Nitride. *Phys. Rev. B* **2007**, 75 (9), 094104.
- (45) Wong, D.; Velasco, J.; Ju, L.; Lee, J.; Kahn, S.; Tsai, H.-Z.; Germany, C.; Taniguchi, T.; Watanabe, K.; Zettl, A.; Wang, F.; Crommie, M. F. Characterization and Manipulation of Individual Defects in Insulating Hexagonal Boron Nitride Using Scanning Tunnelling Microscopy. *Nat. Nanotechnol.* **2015**, 10 (11), 949–953.
- (46) Tran, T. T.; Bray, K.; Ford, M. J.; Toth, M.; Aharonovich, I. Quantum Emission from Hexagonal Boron Nitride Monolayers. *Nat. Nanotechnol.* **2016**, 11 (1), 37–41.
- (47) Zhang, X.; Al Balushi, Z. Y.; Zhang, F.; Choudhury, T. H.; Eichfeld, S. M.; Alem, N.; Jackson, T. N.; Robinson, J. A.; Redwing, J. M. Influence of Carbon in Metalorganic Chemical Vapor Deposition of Few-Layer WSe₂ Thin Films. *J. Electron. Mater.* **2016**, 45 (12), 6273–6279.
- (48) Goodisman, J. *Diatomic Interaction Potential Theory*; Elsevier, 1973.
- (49) Hünenberger, P. H.; van Gunsteren, W. F. Empirical Classical Force Fields for Molecular Systems; Springer, Berlin, Heidelberg, 1999; pp 177–214.
- (50) Carozo, V.; Wang, Y.; Fujisawa, K.; Carvalho, B. R.; McCreary, A.; Feng, S.; Lin, Z.; Zhou, C.; Perea-López, N.; Elías, A. L.; Kabius, B.; Crespi, V. H.; Terrones,

- M. Optical Identification of Sulfur Vacancies: Bound Excitons at the Edges of Monolayer Tungsten Disulfide. *Sci. Adv.* **2017**, 3 (4), e1602813.
- (51) Li, X.; Piretzky, A. A.; Sang, X.; KC, S.; Tian, M.; Ceballos, F.; Mahjouri-Samani, M.; Wang, K.; Unocic, R. R.; Zhao, H.; Duscher, G.; Cooper, V. R.; Rouleau, C. M.; Geohegan, D. B.; Xiao, K. Suppression of Defects and Deep Levels Using Isoelectronic Tungsten Substitution in Monolayer MoSe₂. *Adv. Funct. Mater.* **2017**, 27 (19), 1603850.
- (52) Wang, L.; Chen, Z.; Dean, C. R.; Taniguchi, T.; Watanabe, K.; Brus, L. E.; Hone, J. Negligible Environmental Sensitivity of Graphene in a Hexagonal Boron Nitride/Graphene/h-BN Sandwich Structure. *ACS Nano* **2012**, 6 (10), 9314–9319.
- (53) Jin, C.; Kim, J.; Suh, J.; Shi, Z.; Chen, B.; Fan, X.; Kam, M.; Watanabe, K.; Taniguchi, T.; Tongay, S.; Zettl, A.; Wu, J.; Wang, F. Interlayer Electron–phonon Coupling in WSe₂/hBN Heterostructures. *Nat. Phys.* **2017**, 13 (2), 127–131.
- (54) Huang, J.; Hoang, T. B.; Mikkelsen, M. H. Probing the Origin of Excitonic States in Monolayer WSe₂. *Sci. Rep.* **2016**, 6 (1), 22414.
- (55) Lippert, S.; Schneider, L. M.; Renaud, D.; Kang, K. N.; Ajayi, O.; Kuhnert, J.; Halbach, M.-U.; Abdulmunem, O. M.; Lin, X.; Hassoon, K.; Edalati-Boostan, S.; Kim, Y. D.; Heimbrodt, W.; Yang, E.-H.; Hone, J. C.; Rahimi-Iman, A. Influence of the Substrate Material on the Optical Properties of Tungsten Diselenide Monolayers. *2D Mater.* **2017**, 4 (2), 025045.
- (56) Dey, P.; Paul, J.; Wang, Z.; Stevens, C. E.; Liu, C.; Romero, A. H.; Shan, J.;

- Hilton, D. J.; Karauskaj, D. Optical Coherence in Atomic-Monolayer Transition-Metal Dichalcogenides Limited by Electron-Phonon Interactions. *Phys. Rev. Lett.* **2016**, *116* (12), 127402.
- (57) Yu, Y.; Yu, Y.; Xu, C.; Cai, Y. Q.; Su, L.; Zhang, Y.; Zhang, Y. W.; Gundogdu, K.; Cao, L. Engineering Substrate Interactions for High Luminescence Efficiency of Transition-Metal Dichalcogenide Monolayers. *Adv. Funct. Mater.* **2016**, *26* (26), 4733–4739.
- (58) Cadiz, F.; Courtade, E.; Robert, C.; Wang, G.; Shen, Y.; Cai, H.; Taniguchi, T.; Watanabe, K.; Carrere, H.; Lagarde, D.; Manca, M.; Amand, T.; Renucci, P.; Tongay, S.; Marie, X.; Urbaszek, B. Excitonic Linewidth Approaching the Homogeneous Limit in MoS₂-Based van Der Waals Heterostructures. *Phys. Rev. X* **2017**, *7* (2), 1–12.
- (59) Das, S.; Appenzeller, J. WSe₂ Field Effect Transistors with Enhanced Ambipolar Characteristics. *Appl. Phys. Lett.* **2013**, *103* (10), 103501.
- (60) Nasr, J. R.; Schulman, D. S.; Sebastian, A.; Horn, M. W.; Das, S. Mobility Deception in Nanoscale Transistors: An Untold Contact Story. *Adv. Mater.* **2019**, *31* (2), 1806020.
- (61) Zhou, H.; Wang, C.; Shaw, J. C.; Cheng, R.; Chen, Y.; Huang, X.; Liu, Y.; Weiss, N. O.; Lin, Z.; Huang, Y.; Duan, X. Large Area Growth and Electrical Properties of P-Type WSe₂ Atomic Layers. *Nano Lett.* **2015**, *15* (1), 709–713.
- (62) Fang, H.; Chuang, S.; Chang, T. C.; Takei, K.; Takahashi, T.; Javey, A. High-

Performance Single Layered WSe₂ p-FETs with Chemically Doped Contacts.

Nano Lett. **2012**, *12* (7), 3788–3792.

- (63) Liu, W.; Kang, J.; Sarkar, D.; Khatami, Y.; Jena, D.; Banerjee, K. Role of Metal Contacts in Designing High-Performance Monolayer n-Type WSe₂ Field Effect Transistors. *Nano Lett.* **2013**, *13* (5), 1983–1990.
- (64) Illarionov, Y. Y.; Rzepa, G.; Walzl, M.; Knobloch, T.; Grill, A.; Furchi, M. M.; Mueller, T.; Grasser, T. The Role of Charge Trapping in MoS₂/SiO₂ and MoS₂/HBN Field-Effect Transistors. *2D Mater.* **2016**, *3* (3), 035004.
- (65) Dean, C. R.; Young, A. F.; Meric, I.; Lee, C.; Wang, L.; Sorgenfrei, S.; Watanabe, K.; Taniguchi, T.; Kim, P.; Shepard, K. L.; Hone, J. Boron Nitride Substrates for High-Quality Graphene Electronics. *Nat. Nanotechnol.* **2010**, *5* (10), 722–726.
- (66) Wang, J. I.-J.; Yang, Y.; Chen, Y.-A.; Watanabe, K.; Taniguchi, T.; Churchill, H. O. H.; Jarillo-Herrero, P. Electronic Transport of Encapsulated Graphene and WSe₂ Devices Fabricated by Pick-up of Prepatterned HBN. *Nano Lett.* **2015**, *15* (3), 1898–1903.
- (67) Schulman, D. S.; Arnold, A. J.; Das, S. Contact Engineering for 2D Materials and Devices. *Chem. Soc. Rev.* **2018**, *47* (9), 3037–3058.
- (68) Wang, F.; Tu, B.; He, P.; Wang, Z.; Yin, L.; Cheng, R.; Wang, J.; Fang, Q.; He, J. Uncovering the Conduction Behavior of van Der Waals Ambipolar Semiconductors. *Adv. Mater.* **2018**, 1805317.
- (69) Lee, J. S.; Choi, S. H.; Yun, S. J.; Kim, Y. I.; Boandoh, S.; Park, J.-H.; Shin, B. G.;

Ko, H.; Lee, S. H.; Kim, Y.-M.; Lee, Y. H.; Kim, K. K.; Kim, S. M. Wafer-Scale Single-Crystal Hexagonal Boron Nitride Film via Self-Collimated Grain Formation. *Science* **2018**, *362* (6416), 817–821.

Chapter 6

Low Temperature Growth of Layered Metal Chalcogenides via Metalorganic Chemical Vapor Deposition

6.1 Motivation

2D materials and especially two-dimensional transition metal dichalcogenides (2D-TMDs) have attracted wide interest because of their potential performance and diversity of function as electronic materials. The majority of these efforts have focused on TMDs such as MoS₂ and WSe₂, which offer the prospect of ultra-thin channel regions, high on/off ratios and moderate carrier mobilities. However, growth of transition metal dichalcogenides (TMDs) typically requires high temperatures (>700°C) for large domain size and epitaxy. This restricts the applications of these materials, especially considering the growing interest in 2D materials integration with silicon in back-end-of-line (BEOL) applications and 3D fabrication and integration in flexible electronics that require processing temperature < 450°C. Although low-temperature (400 °C) large area WSe₂ film can be obtained via metalorganic chemical vapor deposition (MOCVD) as discussed in the first part of this chapter, the nanocrystallinity of the films and lack of epitaxy result in limited performance in transport properties with field effect mobility of ~0.01 cm²/Vs.¹ Consequently, TMDs which are “high temperature” materials are not ideal candidates for 2D materials integration using direct deposition approaches.

Instead, there are rising interest in other 2D layered materials, especially in group IIIA and group IVA metal layered chalcogenides, which also offer intriguing physical and electronic properties in addition to their typically low melting temperature under

900 °C (Table 6-1). Recent reports have already shown promising results regarding this sort of 2D metal chalcogenides. For example, room temperature carrier mobilities $\sim 1000 \text{ cm}^2/\text{Vs}$ for FETs fabricated using exfoliated flakes γ -InSe with hBN-encapsulation.^{2,3} Fast photoresponsivity within the millisecond level has been demonstrated in both α -In₂Se₃ flakes and β -In₂Se₃ single domains.^{4,5} In addition, room temperature in-plane and out-of-plane ferroelectricity has been explored in α - and β -In₂Se₃.⁶⁻⁹ Considering the low melting temperatures of all these materials, depositing crystalline and high quality films are more feasible at lower temperature which is suitable for BEOL or flexible electronic applications. In the second part of this chapter, a scalable metalorganic chemical vapor deposition (MOCVD) growth of epitaxial β -In₂Se₃ film on both c-plane sapphire and Si (111) substrate under 400 °C with thickness control down to 5 nm is demonstrated. The relatively high crystalline film grown at low temperature should enable the development future phase-change memory and photoelectronic application.

Material	T _{melt} (°C)	E _g (eV)
Bi ₂ Te ₃	580	0.13
Bi ₂ Se ₃	710	0.30
γ -InSe	618	1.26
β -In ₂ Se ₃	888	2.1
GaSe	937	2.1
2H-SnSe ₂	656	1.01
2H-SnS ₂	870	2.17
2H-MoS ₂	1185	1.23 (bulk)
2H-WSe ₂	1500	1.3 (bulk)

Table 6-1. Melting temperatures and bulk bandgap energies of selected layered chalcogenides.

6.2 Low Temperature Growth of WSe₂ Films

6.2.1 Growth condition

The WSe₂ thin films were grown on thermally oxidized silicon substrates with 50 nm SiO₂ using gas source MOCVD system with precursors tungsten hexacarbonyl (W(CO)₆) and dimethyl selenium (DMSe). The substrate was heated to 300 °C in H₂ for 10 mins as a pre-cleaning step. Then the substrate temperature was increased to 400 °C. After the temperature was stabilized, 10 sccm of H₂ passed through tungsten hexacarbonyl (W(CO)₆) bubbler held at 30 °C and 730 Torr which resulted in 6×10⁻⁴ sccm of W(CO)₆ out of the bubbler and 12 sccm of H₂ passed through dimethyl selenium (DMSe) bubbler held at room temperature and 760 Torr which resulted in 3.6 sccm of DMSe out of the bubbler. This also leads to a large Se:W ratio of 6300:1. A total flow rate

of 450 sccm of H_2 was used and the reactor pressure was maintained at 700 Torr during the growth.

6.2.2 Device Fabrication

The plasma etching and the device fabrication of low-temperature WSe_2 was done by Yiyang Gong at Penn State.¹⁰ Plasma etching with O_2 was used to pattern WSe_2 device areas and to modify film thickness. 100 sccm O_2 gas flow was used with the pressure and dc self-bias maintained at 100 mTorr and -100 V, respectively. No volatile species are formed and the etching is mainly attributed to the physical bombardment of oxygen ions, so the etch rate is as low. For the conditions reported here the etch rate for WSe_2 is ~ 0.25 nm/min.

Arrays of thin film transistors (TFTs) with bottom gate or top gate structures were fabricated using WSe_2 films grown on oxidized silicon wafers. To fabricate bottom gate TFTs, the WSe_2 film was patterned using photolithography and CF_4/Ar plasma etching. For some samples, the patterned WSe_2 channels were further thinned using O_2 plasma etching. Next, 50 nm thick Au source and drain contacts were deposited by evaporation and patterned by photolithography and lift-off. A layer of 50 nm Al_2O_3 was then deposited at 200 °C by plasma enhanced atomic layer deposition (PEALD) using trimethyl aluminum and carbon dioxide as precursors. To reduce the contact resistivity, the completed devices were annealed in vacuum at 150°C for 10 hours before measurement. For the top gate TFTs, 100 nm Ti was deposited and patterned by

photolithography and lift-off to form gate electrodes on top of the encapsulation layer of the bottom gate TFTs. For these devices the Al_2O_3 layer is used as the top gate dielectric.

6.2.3 Film morphology

Under the low temperature regime, MOCVD growth is typically limited by reaction kinetics and therefore the growth is sensitive to substrate temperature. We have tested the growth of WSe_2 using $\text{W}(\text{CO})_6$ and DMSe as precursors starting from 300 °C. Below that temperature, no growth happens possibly due to the thermodynamic limit of precursor decomposition, in this case, most likely to be the DMSe . Figure 6-1a shows an SEM image of the continuous WSe_2 film grown on the oxidized silicon wafer under 400 °C. At this growth condition, no triangular domains are observed and only numerous particle-like domains with typical size < 20 nm are covering the whole surface without any epitaxial signature. This is expected as surface diffusion is significantly limited at low temperature and only nanocrystalline WSe_2 can be formed. Figure 6-1b shows the Raman spectrum of the WSe_2 film measured using the 532 nm wavelength laser source. The existence of WSe_2 in the 2H phase is confirmed by the observation of a single peak around 250 cm^{-1} , which consists of the degenerate E_{2g} and A_{1g} peaks standing for the in-plane and out-of-plane modes.^{11–14} Atomic force microscopy was used to characterize the thickness and surface roughness of the WSe_2 films. Figure 6-1c shows an AFM image taken at a scratched boundary (by plastic tweezer) of a ~ 3 nm WSe_2 film. The thickness of the film is estimated as the height of the step using the cross-section profile. Note that even though the film presents as nanocrystalline, the film RMS roughness is relatively

low as ~ 1.0 nm. In addition, a steady linear relationship between film thickness and growth time is achieved under this condition as shown in Figure 6-1d. In the first stage, from 0 to 10 mins, the growth shows a delay in the first 10 min possibly due to the initial nucleation of WSe_2 on the oxidized silicon wafer. From 10 to 30 mins, the growth rate is linearly around 0.3 nm/min.

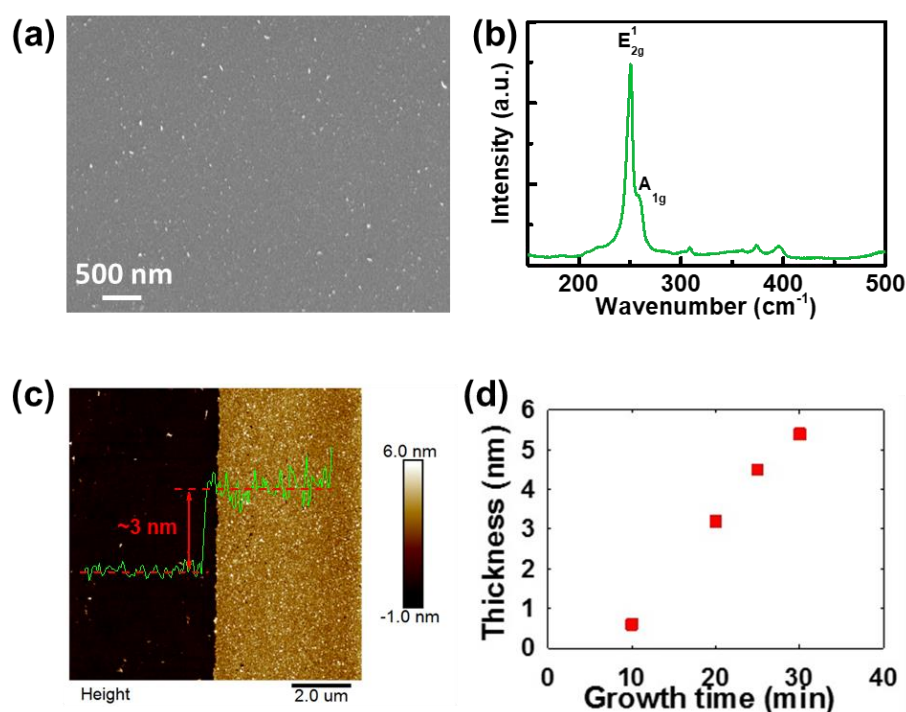


Figure 6-1. (a) SEM image of continuous WSe_2 thin film on SiO_2/Si substrate. (b) Raman spectrum of ~ 3 nm WSe_2 thin film. (c) AFM image of 3 nm thick WSe_2 thin film. (d) WSe_2 film thickness as function of growth time.

6.2.4 Device characterization

To investigate the electrical properties of the low-temperature MOCVD WSe₂ films, arrays of TFTs were fabricated using 6 nm and 3 nm thick as-grown WSe₂ films. Figure 6-2 shows schematic and optical images of double gate WSe₂ TFTs (these devices have both top and bottom gates). The WSe₂ TFT channel width varies from 10 μm to 200 μm and the channel length varies from 2 μm to 50 μm . Figure 6-3a shows the I_D - V_{DS} characteristics of a TFT with 6 nm thick WSe₂ and 20/10 μm channel width/length. In the measurement, the drain-to-source voltage is swept from 0 V to -30 V, and the top gate voltage varied from 10 V to -30 V in steps of -10 V. P-channel behavior and well-defined drain current saturation can be observed. The on-off current ratio is ~ 100 . The high off state current ($\sim 1.1 \times 10^{-8}$ A when $V_{DS} = -10$ V) indicates that the conductivity of the 6 nm WSe₂ film is high and that thinner films should be used for lower off state current and higher on-off ratio. Figure 6-3b shows the I_D - V_{DS} characteristics of a TFT with 3 nm thick WSe₂ film and 200/5 μm channel width/length. In this measurement, the drain-to-source voltage is swept from 0 V to 15 V, and the bottom gate voltage is varied from -10 V to 30 V in steps of 10 V. The device has high resistance and only weak n-channel behavior, with maximum drain current lower than 10^{-9} A.

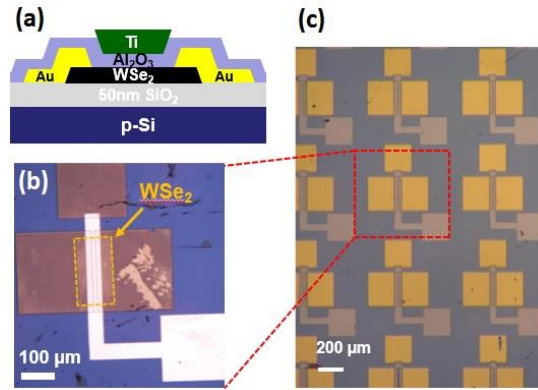


Figure 6-2. (a) Cross-section and (b) optical microscopic image of a double gate WSe₂ TFT. (c) Array of WSe₂ TFTs.

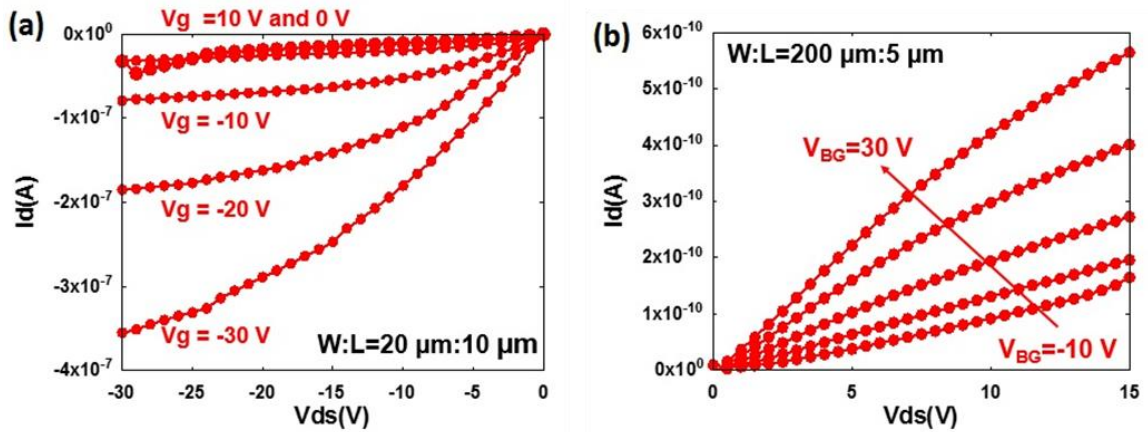


Figure 6-3. I_D - V_{DS} characteristics of WSe₂ TFTs using as-grown film. (a) Top gate TFT with 6 nm thick channel and (b) bottom gate TFT with 3 nm thick channel.

To further understand the thickness dependent electrical properties of the MOCVD WSe₂ thin films, TFTs were fabricated with a 6 nm thick WSe₂ film thinned to 3 nm using oxygen plasma etching. Figure 6-4a shows the I_D - V_{DS} characteristics of TFTs with channel length/width = 2/200 μm and 50/200 μm , respectively. The on-off ratio of the device is improved to greater than 10^4 while the off state current is limited to below

10^{-11} A. Figure 6-4b shows the I_D - V_{DS} characteristics for $V_{DS} = -3V$ and $-20V$. The linear region differential field effect mobility is extracted using

$$\mu_{linear} = \frac{dI_d}{dV_g} \frac{L}{W} \frac{1}{C} \frac{1}{V_D},$$

where L and W are the length and the width of the channel, C is the unit area capacitance of the gate dielectric, and V_D is the drain-to-source voltage. When $V_G = -35$ V and $V_{DS} = -20$ V, the extracted field effect mobility is ~ 0.01 cm^2/Vs . The turn-on voltages for $V_{DS} = -3$ V and $V_{DS} = -20$ V are ~ 5 V and ~ 0 V, respectively. The devices have significant hysteresis, possibly due to a high trap density in the WSe_2 film or at the WSe_2 /dielectric interface. Though further investigation is needed to understand the significant difference in device performance between as-grown 3 nm thick WSe_2 and plasma thinned 3 nm thick WSe_2 , our results demonstrate that plasma etching provides an additional degree of freedom to modulate the electrical properties of CVD WSe_2 thin films.

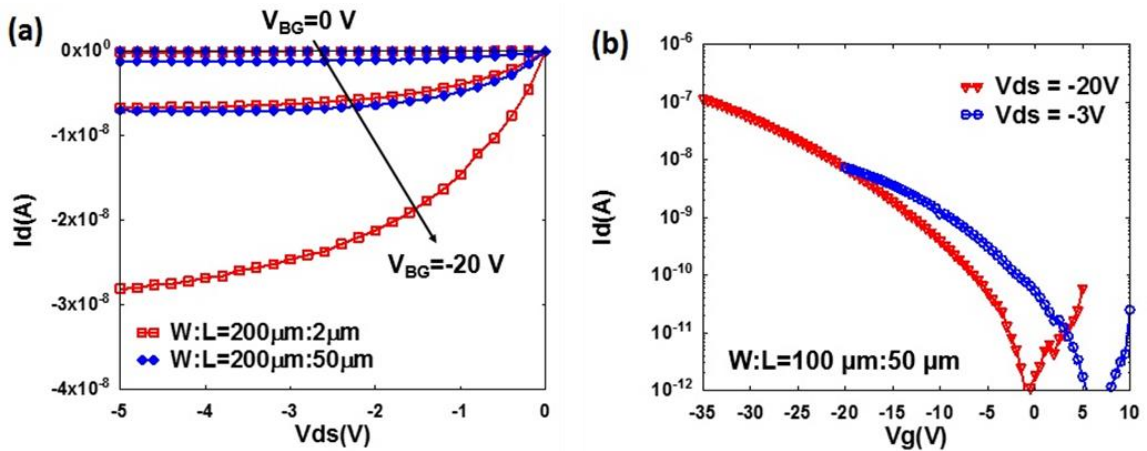


Figure 6-4. (a) I_D - V_{DS} and (b) I_D - V_G characteristics of WSe_2 TFTs using 3 nm thick RIE thinned film.

To estimate the impact of contacts on the device, the resistance of TFTs was extracted from linear region ($V_{DS} = 0.4$ V) I_D - V_{DS} characteristics. Figure 6-5a shows the total resistance, $R_{TOT} = R_{CH} + 2 R_C$, for TFTs with different channel lengths and for two gate voltages, where R_{CH} and R_C represent the channel resistance and contact resistance, respectively. The resistance of contact and channel for $V_G = -10$ V and -20 V are shown in Figure 6-5b. The contact resistance is gate voltage dependent as expected for Schottky barrier contacts. While both channel resistance and contact resistance decrease as gate voltage increases from -10 V to -20 V, the contact resistance dominates for $V_G = -20$ V. For example, for a TFT with $5\text{ }\mu\text{m}$ channel length, the contact resistance is 68% and 94% of the total channel resistance when $V_G = -10$ V and -20 V, respectively. This large contact resistance significantly limits the performance of these WSe_2 TFTs.^{15,16}

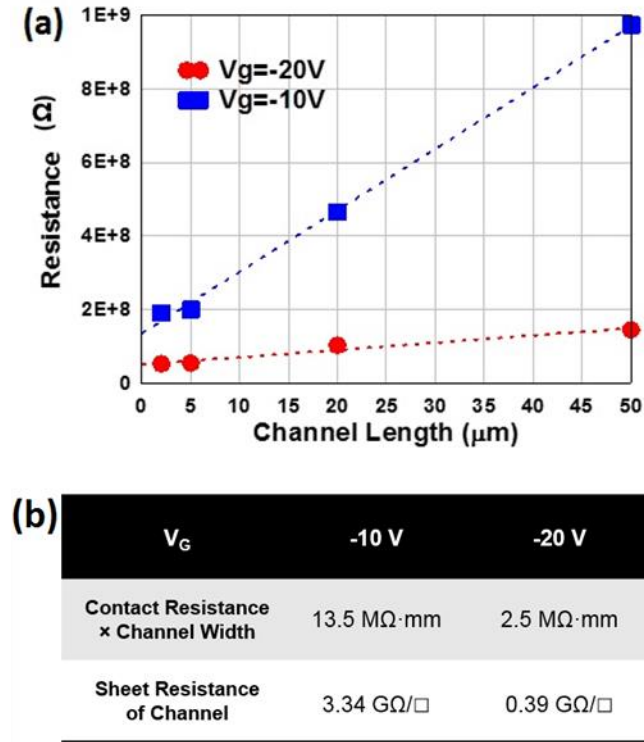


Figure 6-5. (a) Total resistance extracted from I_D - V_{DS} characteristics of TFTs with RIE etched 3 nm thick WSe_2 channel for different channel length (with channel width fixed at 200 μm) and gate voltage ($V_{DS} = 0.4$ V). (b) Contact resistance and sheet resistance of channel for $V_G = -10$ V and -20 V.

6.2.5 Summary

This work demonstrates the fabrication of top gate and bottom gate WSe_2 TFTs with hole mobility of ~ 0.01 cm^2/Vs and on-off current ratio $> 10^4$. The mobility of the films is significantly limited by the contact resistance as well as the nanocrystallinity and non-epitaxy of the film due to low growing temperature which results in high density of grain boundaries. Although the performance of the film is not competitive in terms of mobility,

it still shows the high feasibility of using gas source CVD technique to deposit uniform large-area films for future large-scale production. It also offers the potential opportunity for low-temperature growth of TMDs in specific 3D device structure and integration in flexible electronics.

6.3 Epitaxial Growth of Layered β - In_2Se_3 Thin Films

6.3.1 Introduction

Beyond 2D TMDs, group IIIA-VA metal dichalcogenides are currently being studied as next generation of 2D materials, especially for their fast and ultrasensitive photoresponse and their potential in fabrication of new optoelectronic devices.^{17–23} Aside from other metal dichalcogenides, In_2Se_3 (both α and β phases) have also demonstrated in-plane and/or out-of-plane ferroelectricity at room temperature in addition to their intrigue optical properties,^{6–9} which enables further size reduction of ferroelectric devices and new prospects for nonvolatile switching and manipulation of electrical and optical properties in a vdW heterostructure.^{17,21}

To date, most of studies on layered In_2Se_3 have been achieved using mechanically exfoliated from bulk crystals. Growth by powder vapor transport (PVT) has also been explored recently, with some success in producing large single crystal flakes of α - and β - In_2Se_3 on amorphous substrates.^{5,9} Although these results are encouraging, the scalable synthesis of uniform layers and heterostructures remain to be developed and the stoichiometry and polymorph of In_2Se_3 on specific substrates are still hard to predict and

control. In addition, epitaxial growth of β -In₂Se₃ has been successfully demonstrated on single crystal GaSe⁴ and graphene¹⁷ substrate, though these materials from the lab still have limited availability and a commercial substrate for epitaxial growth of β -In₂Se₃ is desired. On the other hand, large area and epitaxial growth of 2D TMDs by gas source CVD/MOCVD has been successfully demonstrated for both high scalability and precise precursor control.^{24–29} Besides, group III metal precursors (e.g. trimethyl indium, (CH₃)₃In, TMIIn) are also available and have been widely used and studied in previous MOCVD growth of III-V semiconducting materials. In this case, the large area epitaxial growth of layered group III metal chalcogenides by gas source CVD/MOCVD is potentially feasible.

In this section, we report a large area epitaxial growth of layered β -In₂Se₃ thin films by MOCVD. Gas phase reaction between the TMIIn and H₂Se precursors was found to occur due to their Lewis acid and base properties, which can potentially affect the growth. Epitaxial growth has been found on both c-plane sapphire and Si (111), however different growth modes are observed with island growth on sapphire and step flow growth on Si (111), respectively. The epitaxial film of β -In₂Se₃ has been further thinned down to 5 nm by flowing precursor in a pulsed way to minimize the effect of gas phase reaction. In the end, scalable fabrication of top gate TFTs on centimeter-scale β -In₂Se₃ thin film has been demonstrated with electron mobility of ~ 1 cm²/Vs and on-off current ratio $> 10^6$. The research shows an important step towards the scalable production of high-quality β -In₂Se₃ films and functional devices.

6.3.2 Experimental setup

6.3.2.1 MOCVD growth conditions

β -In₂Se₃ films were synthesized in the same cold wall vertical quartz tube reactor used for WSe₂ growth that includes an inductively heated SiC-coated graphite susceptor. Trimethylindium (TMIn) and hydrogen selenide (H₂Se) were used as precursors with ultra-high purity H₂ as the carrier gas. The TMIn was contained inside a stainless steel bubbler which was held at 20 °C and 730 Torr. H₂ carrier gas was passed through the bubbler at a flow rate of 10-50 sccm which resulted in a TMIn flow rate of $1.5-7.7 \times 10^{-2}$ sccm out of the bubbler.³⁰ H₂Se flow rate was controlled ranging from 1 to 10 sccm. The total flow rate of H₂ through the reactor was maintained at 2000 sccm. 1 cm×1 cm square c-plane sapphire ((0001) α -Al₂O₃) and Si (111) were used as substrates. All substrates underwent cleaning process prior to the growth to remove possible contamination and surface oxide for Si (details in Chapter 2.4). Growth was carried out at a total reactor pressure of 100 Torr, a growth time of 30 min.

6.3.2.2 Film characterization setup

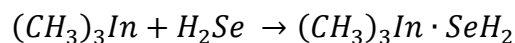
The surface morphology of the samples was analyzed by atomic force microscopy (AFM) using a Bruker Dimension Icon Atomic Force Microscope system and field emission scanning electron microscopy (FESEM) using a Zeiss Merlin instrument. The thickness of the films was measured by AFM through creating a step with film and substrate via a soft scratch. Raman and photoluminescence spectroscopy were carried out

using a HORIBA LabRAM HR Evolution high spectral resolution analytical Raman microscope with a laser wavelength of 532 nm. A PANalytical MRD diffractometer was used for high resolution X-ray diffraction (HRXRD) in a triple-axis geometry to identify the phase of In_2Se_3 and determine the crystalline quality of the films using θ - 2θ and ω scans respectively. Also, pole figures were used to determine the epitaxial relationship between the film and the substrate. In-plane XRD measurements were conducted in the same PANalytical MRD diffractometer with 5 axis cradle employing $\text{Cu K}\alpha$ radiation and filtering $\text{K}\beta$ radiation employing Ni filter. The cross-section transmission electron microscopy (TEM) samples were prepared using a focused ion beam (FIB) technique in FEI SEM Helios Nanolab 660. High resolution TEM (HRTEM) and scanning TEM/electron dispersive spectroscopy (STEM-EDS) of the cross-section sample was performed by FEI Talos F200X microscope with a SuperX EDS detector, operating at 200kV.

6.3.3 Gas phase reaction

In the growth of 2D TMDs, a high chalcogen to metal ratio is typically employed due to the high volatility of chalcogen at elevated temperature resulting in loss of chalcogen at the substrate surface if the overpressure is not high enough. In this case, most growth of 2D TMDs prefers high reactor pressure with high flow rate of chalcogen precursors to guarantee high partial pressure of chalcogen. Although the desorption of Se reduces at low temperature, high chalcogen to metal ratio condition is still applicable to In_2Se_3 growth, considering a significant number of phases with different stoichiometric

ratios in In-Se phase diagram (Figure 6-6) and high Se ratio is needed in order to achieve pure 2:3 ratio of In_2Se_3 compound. However, when using TMIIn and H_2Se as precursors, a strong gas phase reaction as shown happens,



This is possibly due to the Lewis acid (for H_2Se) and base (for TMIIn) properties of the two precursors and similar reaction has been reported for TMGa and H_2Se .³¹ This reaction leads to significant coating on the reactor wall with more runs (Figure 6-7). Consequently, it also affects the growth rate of the films and ultimately even the phase of the films. In order to minimize the impact from this gas phase reaction, a low reactor pressure and high gas velocity were selected to reduce the gas molecule collision and time before reaching the substrate surface. Fortunately, the relatively low growth temperature of In_2Se_3 also reduces the possibility of Se loss at the surface, enabling the use of lower H_2Se partial pressure and thus further reducing the impact from the gas phase reaction.

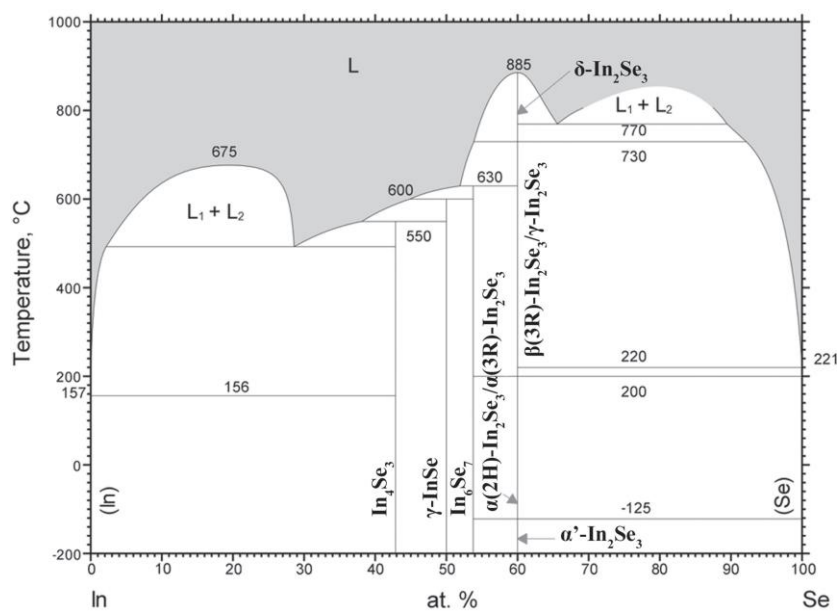


Figure 6-6. In-Se phase diagram³²



Figure 6-7. Significant coating on the reactor wall after a few runs at high pressure and low gas velocity due to the strong gas phase reaction between precursors.

6.3.4 Temperature study

As indicated from the phase diagram, In_2Se_3 compound can also have few polymorphs under varied temperatures. Among them, only α - and β - In_2Se_3 possess the layered structures.³² Therefore, a temperature study was first carried out at high TMI flow rate (7.7×10^{-2} sccm) to identify the growth temperature window for β - In_2Se_3 . As shown in Figure 6-8a, the film started forming at 350 °C, with only a few nucleation particles on the surface. We noticed no growth happen below 350 °C due to the thermodynamic limit of decomposition of two precursors. In Figure 6-8b, a coalesced film was achieved at 400 °C and the three major peaks in its Raman spectrum match well with the E and A peaks of β - In_2Se_3 from literature, confirming the film is the β phase of In_2Se_3 .^{5,23,33} Further increasing temperature resulted in less coalescence in the film growth (Figure 6-8c and 6-8d), and only individual domains were found at 500 °C, which is believed to correlate to high evaporation rate and depletion of the precursors that results in this significant reduction in growth rate. In this case, we identify the optimal temperature window for β - In_2Se_3 is between 400 °C to 450 °C and 400 °C was selected as the growth temperature for the following studies.

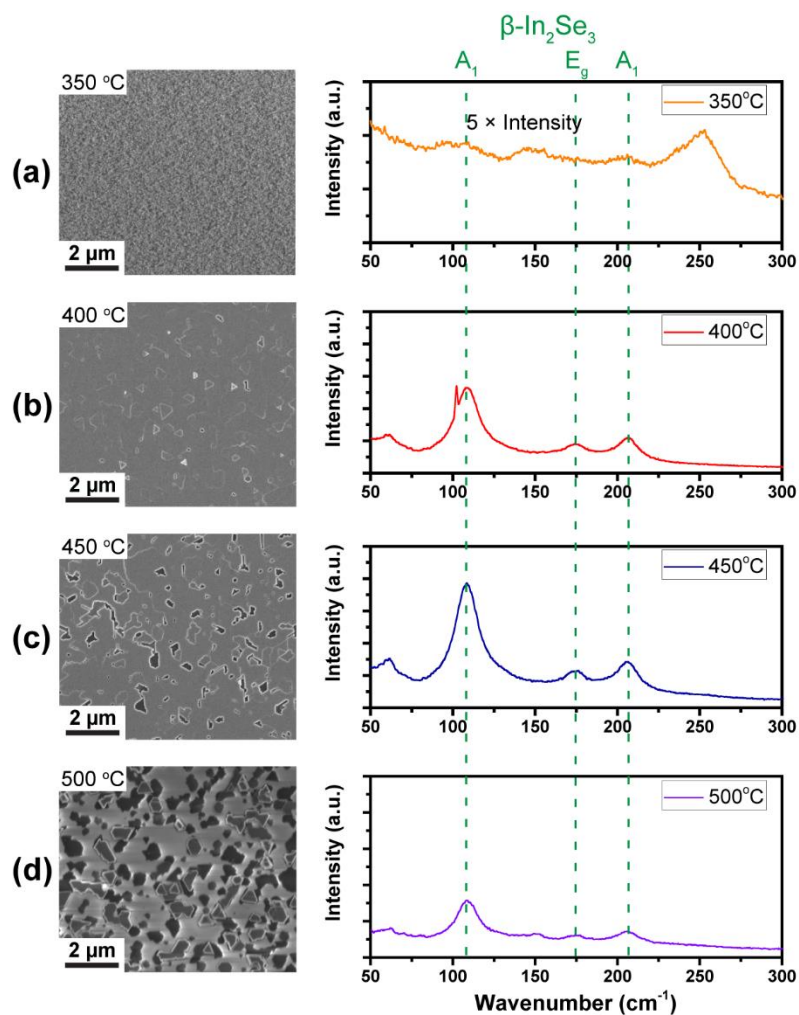


Figure 6-8. FESEM images (left) and Raman spectra (right) of $\beta\text{-In}_2\text{Se}_3$ films grown on c-plane sapphire at (a) 350 °C; (b) 400 °C; (c) 450 °C; (d) 500 °C. The flow rate for TMIn is 7.7×10^{-2} sccm; for H_2Se is 7 sccm.

6.3.5 Se:In ratio study

The effect of Se:In ratio on the film growth rate and morphology was investigated by two ways: maintaining a constant TMIn flow rate and varying the H_2Se flow rate, and vice versa. By increasing the H_2Se flow rate from 1 to 10 sccm at constant TMIn flow

rate at 7.7×10^{-2} sccm and thus increasing the Se:In ratio from 13 to 130 in Figure 6-9a, all the films growing on c-plane sapphire were made of triangular pyramid-like domains that coalesce into each other. This follows the description of island growth model where surface diffusion is limited compared to fast growth rate. We also noticed the film roughness reduced by adding more H_2Se at low Se:In ratio. This indicates the rich Se environment assists the diffusion of adatoms at the surface as well as the formation of pure $\beta\text{-In}_2\text{Se}_3$. However, the film became less coalesced at high Se:In ratio, likely due to two reasons: 1) excess Se may occupy surface sites and prevent the growth of $\beta\text{-In}_2\text{Se}_3$; 2) the extreme high flow rate of H_2Se results in significant gas phase reaction and wall deposition and thus depletes some of the TMIn from the gas phase. In either case, the results indicate the overflow of H_2Se will hinder the growth of coalesced $\beta\text{-In}_2\text{Se}_3$ films.

On the other hand, by decreasing the TMIn flow rate from 7.7×10^{-2} to 1.5×10^{-2} sccm at constant H_2Se flow rate of 7 sccm (increasing Se:In ratio from 91 to 450) in Figure 6-9b, the thickness of the films significantly decreased. This follows the expectation as the amount of metal introduced typically controls the thickness due to their less-volatile properties. However, the thickness decreased much faster than the flow rate dropped. The film thickness reduced more than half when the TMIn flow rate dropped in half, and there was almost no film when the Se:In ratio reached 450. Combined with the previous observation when increasing H_2Se flow, the superlinear decrease in film thickness is likely due to the gas phase reaction at extreme high Se:In ratio. Therefore, once the ratio reduced from 450 to 90 by decreasing the H_2Se flow rate simultaneously, a

coalesced film returned with thickness ~ 10 nm as shown in Figure 6-9c, consistent with the drop in TMIn flow rate.

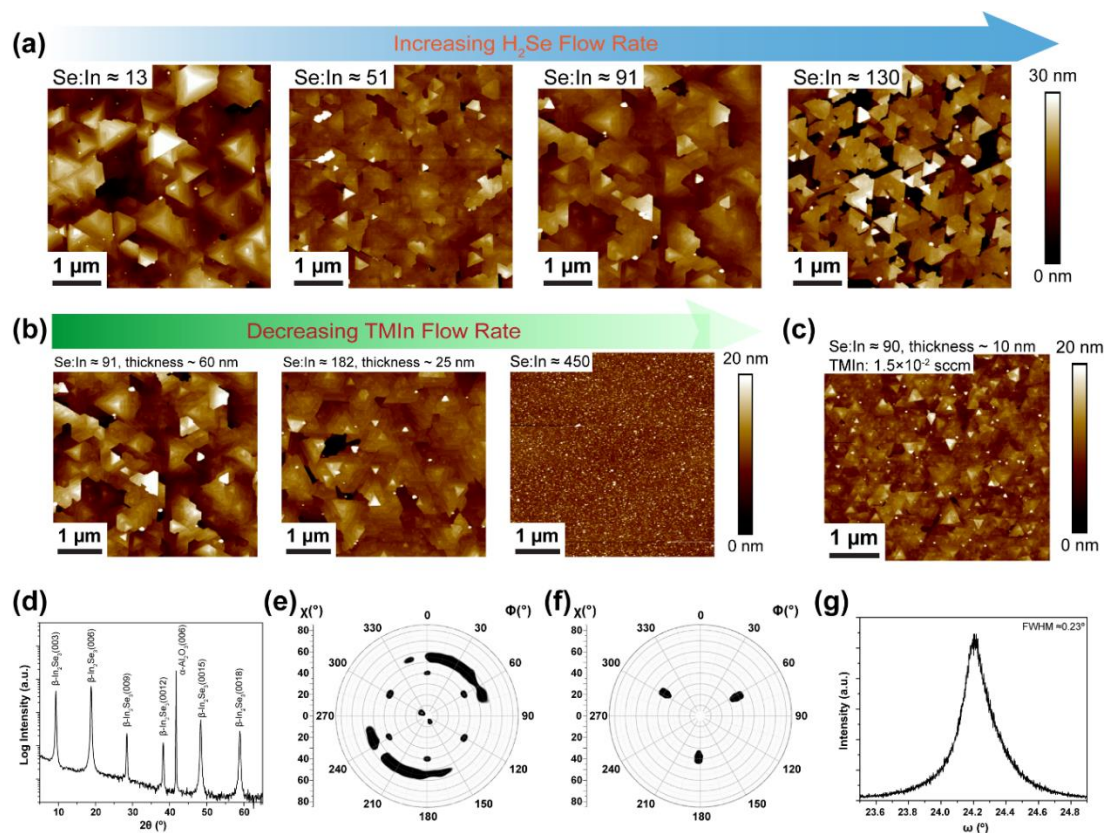


Figure 6-9. AFM images of β - In_2Se_3 films grown at different H_2Se flow rate (a) 2 sccm and (b) 4 sccm with a pulse flow of TMIn flow rate at 1.5×10^{-2} sccm every 30 s on/off for 30 min at 400 $^\circ\text{C}$. (c) ϕ -scan recorded at $2\theta = 37.91^\circ$ of sample in (b) showing $[11\bar{2}0]$ β - $\text{In}_2\text{Se}_3 \parallel [11\bar{2}0]$ α - Al_2O_3 . (d) Cross-sectional TEM image of β - In_2Se_3 sample in (b) showing layered structure of the film and clean interface with sapphire substrate. EDS spectra of (e) In and (f) Se in corresponding region in (d) showing a Se:In ratio of 3:2.

The oriented triangular domains in all the AFM images of Figure 6-9 already indicate the existence of an epitaxial relationship between the coalesced β - In_2Se_3 film and c-plane sapphire. XRD of β - In_2Se_3 films on sapphire was carried out (by Anushka

Bansal, Penn State) to further verify this epitaxial relationship. The θ - 2θ X-ray diffractogram of In_2Se_3 on c-plane sapphire in Figure 6-9d shows diffraction peaks associated with only the β phase of In_2Se_3 family of planes and the (0 0 6) reflection of α - Al_2O_3 indicating that the In_2Se_3 grows with its c-axis perpendicular to the basal plane of sapphire. The X-ray pole figures obtained on this sample in Figure 6-9e and 6-9f in (1 0 10) plane shows that the In_2Se_3 film exhibits epitaxial relationship with the substrate. The six-fold pattern is from well-oriented β - In_2Se_3 (Figure 6-9e), while the three-fold-symmetric spots are attributed to the sapphire substrate (Figure 6-9f). In addition, a partial ring-like texture was also observed in the film, which is likely due to the slight tilt and rotation in the film (such as screw dislocation).³⁴ This is consistent with the observed asymmetric peak in the ω scan in Figure 6-9f, which is also due to the slight misalignment of the domains.

6.3.6 Pulse growth

To achieve better control over film thickness, pulse growth was investigated where precursors are introduced in a pulsed way to reduce the mixture time of precursors and therefore can further limit the impact of gas phase reaction. In this study, a TMIn flow rate of 1.5×10^{-2} sccm was repeatedly introduced into reactor for 30 s and then removed from reactor for another 30 s during the growth period of 30 min. Figure 6-10a shows the morphology of the film using 2 sccm of H_2Se during the growth. The film thickness was measured as ~ 5 nm, exactly half of the thickness in Figure 6-9c, which indicates the growth is not limited by the gas phase reaction considering the total amount

of TMIn was cut down to half of the amount used in Figure 6-9c. Additionally, the domain shapes in Figure 6-10a evolve into hexagonal, which is attributed to the same growth rate of In-terminated edges relative to the Se-terminated edges, similar to previous observation in TMDs growth.^{28,35} This also indicates local Se:In ratio at the growth front is close to 3:2, even though the flow rate ratio (~90) is beyond this value. By increasing H₂Se flow to 4 sccm, the domain shape changes back to triangular in Figure 6-10b indicates the growth condition was under local Se-rich environment and further validates the local Se:In dependence of the domain shape. The epitaxial relation was still maintained in the pulsed growth and confirmed by in-plane XRD measurement in Figure 6-10c (done by Anushka Bansal, Penn State).³⁶ The presence of periodic $11\bar{2}0$ peaks for both In₂Se₃ and sapphire substrate demonstrates epitaxial growth with an in-plane epitaxial relation of $[11\bar{2}0] \text{ In}_2\text{Se}_3 \parallel [11\bar{2}0] \alpha\text{-Al}_2\text{O}_3$. Cross-sectional TEM was also performed on the coalesced $\beta\text{-In}_2\text{Se}_3$ films (by Fu Zhang, Penn State) to understand the film composition and the interface between film and substrate. The regions of sapphire, In₂Se₃, and the carbon protection layer can be distinguished by the crystal structure and contrast in Figure 6-10d. The In₂Se₃ shows a layered structure with a sharp interface with sapphire indicates with no additional passivating layer. The corresponding EDS mappings in Figure 6-10e and 6-10f (done by Fu Zhang, Penn State) reveal only Se and In are in the In₂Se₃ layer with a consistent measured stoichiometric ratio of ~3:2 (31%:21%).

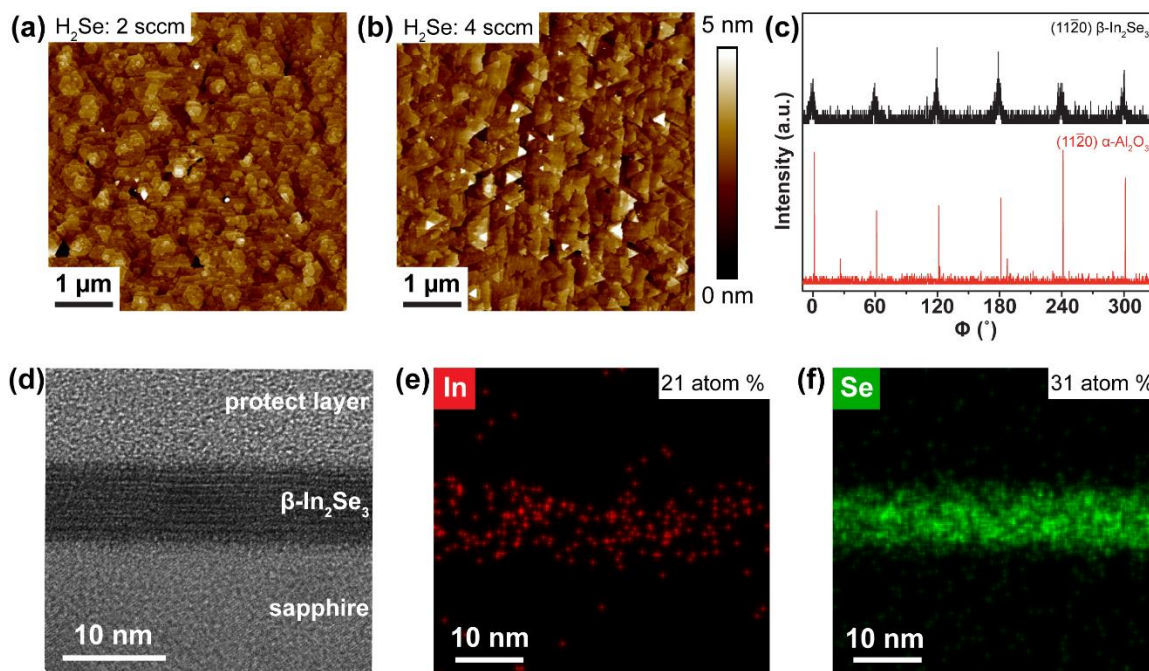


Figure 6-10. AFM images of β - In_2Se_3 films grown at different H_2Se flow rate (a) 2 sccm and (b) 4 sccm with a pulse flow of TMIn flow rate at 1.5×10^{-2} sccm every 30 s on/off for 30 min at 400°C . (c) ϕ -scan recorded at $2\theta = 37.91^\circ$ of sample in (b) showing $[11\bar{2}0]$ β - $\text{In}_2\text{Se}_3 \parallel [11\bar{2}0]$ α - Al_2O_3 . (d) Cross-sectional TEM image of β - In_2Se_3 sample in (b) showing clear layered structure of the film and clean interface with sapphire substrate. EDS spectra of (e) In and (f) Se in corresponding region in (d) showing a Se:In ratio of 3:2.

6.3.7 Substrate impact

The selection of substrate also plays a significant role in determining the growth mode and the phase of the In_2Se_3 films, in addition to epitaxy. Figure 6-11a and 6-11b show the AFM and FESEM images of In_2Se_3 film grown on Si (111) substrate under the

condition with TMIn flow rate of 1.5×10^{-2} sccm and H_2Se flow rate of 7 sccm. The (111) plane of Si was chosen as the surface due to its trigonal symmetry and small lattice mismatch ($<4\%$) with $\beta\text{-In}_2\text{Se}_3$. Although the film is fully coalesced and ~ 25 nm in thickness, the morphology of the film on Si (111) show distinctive steps compared to the island domains on sapphire. The oriented steps indicate a step flow growth mode happens on the Si (111) substrate, in which surface species diffuse faster in certain direction resulting in faster growth rate and formation of steps. Regardless of different growth modes and morphology, the In_2Se_3 films grown on Si (111) were still confirmed as β phase. The films also possess high crystallinity and both in plane and out of plane epitaxial relation with substrate, based on the XRD measurement of θ - 2θ X-ray diffractogram (by Anushka Bansal, Penn State) in Figure 6-11d and pole figures of $\beta\text{-In}_2\text{Se}_3$ (Figure 6-11e) and Si substrate (Figure 6-11f). While $\beta\text{-In}_2\text{Se}_3$ films can be grown on single crystal substrates with proper surface symmetry, using amorphous substrate can lead to phase transition in the film. The FESEM image in Figure 6-12a shows the morphology of the In_2Se_3 film grown on 300 nm amorphous SiO_2/Si substrate under the same growth condition. The cubic 3D structure with no triangular shape indicates the phase changed in the film and the morphology is very similar to $\gamma\text{-In}_2\text{Se}_3$ reported in prior literature.³⁷ Further Raman spectrum in Figure 6-1b confirmed the pure existence of $\gamma\text{-In}_2\text{Se}_3$ with no evidence for other phases.^{4,38} It is possible that the formation of $\gamma\text{-In}_2\text{Se}_3$ is more favorable due to the dangling bonds on the surface and lack of symmetric guidance from the amorphous SiO_2/Si substrate.

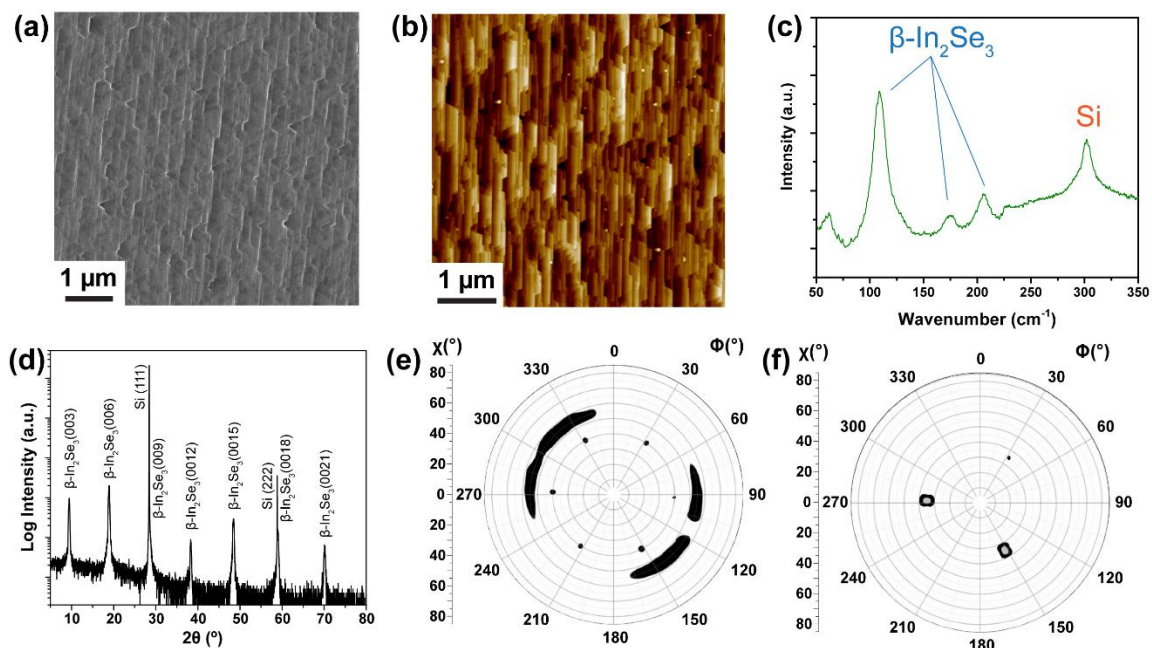


Figure 6-11. (a) FESEM image and (b) AFM image of β -In₂Se₃ film grown on Si (111) substrate. (c) Raman spectrum of β -In₂Se₃ film grown on Si (111) confirming the only existence of β phase. (d) θ -2 θ X-ray diffractogram showing the β -In₂Se₃ film is epitaxial with Si (111) in c-axis. Pole figures of (e) β -In₂Se₃ film along (1 0 10) and (f) Si substrate along (2 0 2) showing the in-plane epitaxy between film and substrate.

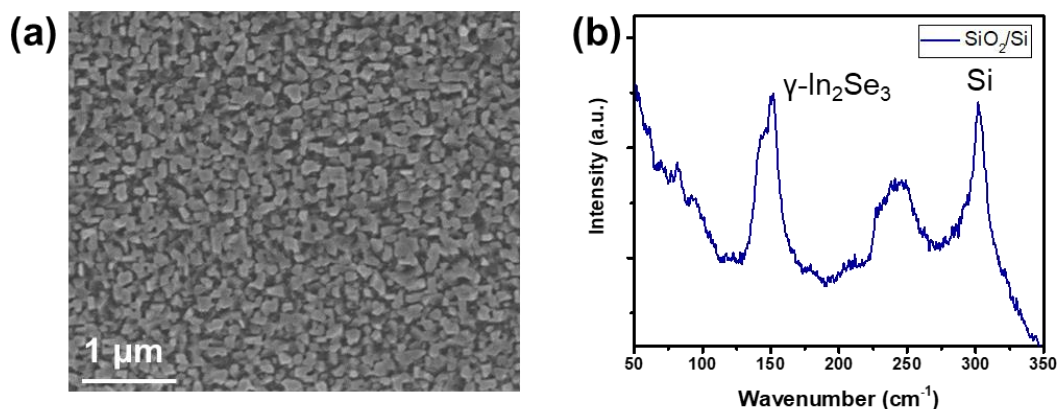


Figure 6-12. (a) FESEM image and (b) Raman spectrum of γ -In₂Se₃ film grown on 300 nm amorphous SiO₂/Si substrate.

6.3.8 Electrical characterization

Top-gate β - In_2Se_3 TFTs were fabricated on 25 nm thick In_2Se_3 grown on c-plane sapphire by Sora Lee at Penn State. Figure 6-13a shows the cross-section of a β - In_2Se_3 TFT. Source and drain contacts were patterned on the as-grown β - In_2Se_3 film with 15 nm thick chromium and 75 nm thick gold, both deposited by thermal evaporation. The β - In_2Se_3 channel region was patterned by photolithography and wet-etching in dilute hydrochloric acid at room temperature. A 31 nm thick aluminum oxide gate dielectric layer was deposited by plasma-enhanced atomic layer deposition at 200 °C. Finally, 100 nm thick titanium was deposited by sputtering and patterned by lift-off as the top gates. Figure 6-13b and 6-13c show the log scale of the drain current (I_D) versus gate voltage (V_{GS}) and the drain current (I_D) versus drain voltage (V_{DS}) for several gate voltages, respectively. The results show the top gate β - In_2Se_3 TFT has n-channel behavior with the threshold voltage ~ -1 V and a high current on/off ratio greater than 10^6 . The gate leakage was negligible (< 0.1 nA) for all measurements. We also notice a strong hysteresis behavior in Figure 6-13b, possibly due to the in-plane ferroelectricity that was induced by both voltage and strain in the film.⁸ The linear region differential field effect mobility was derived and plotted in the linear scale I_D - V_{GS} , as shown in Figure 6-13d. The extracted mobility was near $1 \text{ cm}^2/\text{V}\cdot\text{s}$.

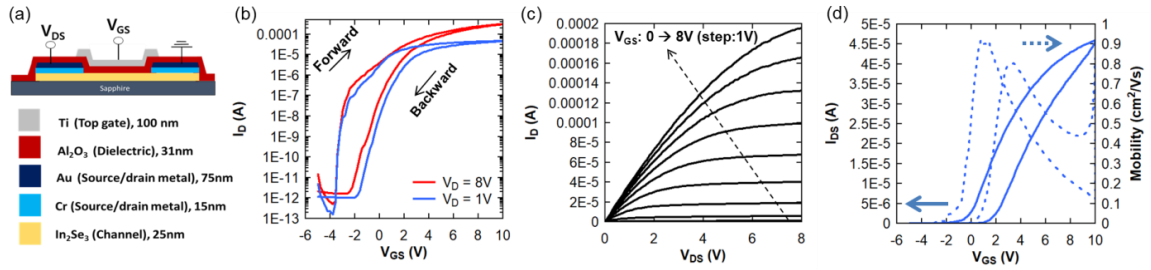


Figure 6-13. (a) schematic of top gate beta-phase In_2Se_3 thin film transistors (TFTs), (b) $\log(I_D)$ - V_{GS} for $V_{DS} = 1$ and 8 V, (c) I_D - V_{DS} characteristics for V_{GS} from 0 to 8 V (step: 1 V), (d) linear (I_D)- V_{GS} with linear field effect mobility for $V_{DS} = 1$ V ($W:L = 200 \mu\text{m}: 5 \mu\text{m}$).

6.3.9 Summary

We demonstrate a scalable production of high-quality $\beta\text{-In}_2\text{Se}_3$ films at low temperature by MOCVD. Both c-plane sapphire and Si (111) are good substrate candidates for epitaxial growth of $\beta\text{-In}_2\text{Se}_3$ films, though different growth models are found with island growth on sapphire and step flow growth on Si (111). A precise control of the growth rate of $\beta\text{-In}_2\text{Se}_3$ film has been demonstrated in this work and a 5 nm coalesced film is achieved via a pulse flow of In precursor. Top gate WSe_2 TFTs on centimeter-scale $\beta\text{-In}_2\text{Se}_3$ thin film reasonable carrier mobility and high on-off ratio, with electron mobility of $\sim 1 \text{ cm}^2/\text{Vs}$ and on-off current ratio $> 10^6$, extending the potential of the films in integrated and flexible electronic, optoelectronic, and ferroelectric applications.

6.4 References

- (1) Gong, Y.; Zhang, X.; Redwing, J. M.; Jackson, T. N. Thin Film Transistors Using Wafer-Scale Low-Temperature MOCVD WSe₂. *J. Electron. Mater.* **2016**, *45* (12), 6280–6284.
- (2) Bandurin, D. A.; Tyurnina, A. V.; Yu, G. L.; Mishchenko, A.; Zólyomi, V.; Morozov, S. V.; Kumar, R. K.; Gorbachev, R. V.; Kudrynskyi, Z. R.; Pezzini, S.; Kovalyuk, Z. D.; Zeitler, U.; Novoselov, K. S.; Patanè, A.; Eaves, L.; Grigorieva, I. V.; Fal'ko, V. I.; Geim, A. K.; Cao, Y. High Electron Mobility, Quantum Hall Effect and Anomalous Optical Response in Atomically Thin InSe. *Nat. Nanotechnol.* **2017**, *12* (3), 223–227.
- (3) Kudrynskyi, Z. R.; Bhuiyan, M. A.; Makarovskiy, O.; Greener, J. D. G.; Vdovin, E. E.; Kovalyuk, Z. D.; Cao, Y.; Mishchenko, A.; Novoselov, K. S.; Beton, P. H.; Eaves, L.; Patanè, A. Giant Quantum Hall Plateau in Graphene Coupled to an InSe van Der Waals Crystal. **2017**.
- (4) Balakrishnan, N.; Steer, E. D.; Smith, E. F.; Kudrynskyi, Z. R.; Kovalyuk, Z. D.; Eaves, L.; Patanè, A.; Beton, P. H. Epitaxial Growth of γ -InSe and α , β , and γ -In₂Se₃ on ϵ -GaSe. *2D Mater.* **2018**, *5* (3), 035026.
- (5) Balakrishnan, N.; Staddon, C. R.; Smith, E. F.; Stec, J.; Gay, D.; Mudd, G. W.; Makarovskiy, O.; Kudrynskyi, Z. R.; Kovalyuk, Z. D.; Eaves, L.; Patanè, A.; Beton, P. H. Quantum Confinement and Photoresponsivity of β -In₂Se₃ Nanosheets Grown by Physical Vapour Transport. *2D Mater.* **2016**, *3* (2), 025030.

- (6) Ding, W.; Zhu, J.; Wang, Z.; Gao, Y.; Xiao, D.; Gu, Y.; Zhang, Z.; Zhu, W.
Prediction of Intrinsic Two-Dimensional Ferroelectrics in In₂Se₃ and Other III₂-VI₃ van Der Waals Materials. *Nat. Commun.* **2017**, 8, 1–8.
- (7) Xue, F.; Hu, W.; Lee, K. C.; Lu, L. S.; Zhang, J.; Tang, H. L.; Han, A.; Hsu, W. T.; Tu, S.; Chang, W. H.; Lien, C. H.; He, J. H.; Zhang, Z.; Li, L. J.; Zhang, X.
Room-Temperature Ferroelectricity in Hexagonally Layered α -In₂Se₃ Nanoflakes down to the Monolayer Limit. *Adv. Funct. Mater.* **2018**, 28 (50), 1–7.
- (8) Li, S.; Liu, J. Z.; Edmonds, M. T.; Yu, L.; Collins, J. L.; Lou, Y.; Xu, C.; Zheng, C.; Wei, Z.; Fuhrer, M. S.; Kim, D.; Seidel, J.; Zhang, Y.; Tang, W.-X.; Zhu, Y.; Li, M.; Zhu, L. Room Temperature In-Plane Ferroelectricity in van Der Waals In₂Se₃. *Sci. Adv.* **2018**, 4 (7), eaar7720.
- (9) Cui, C.; Hu, W. J.; Yan, X.; Addiego, C.; Gao, W.; Wang, Y.; Wang, Z.; Li, L.; Cheng, Y.; Li, P.; Zhang, X.; Alshareef, H. N.; Wu, T.; Zhu, W.; Pan, X.; Li, L. J.
Intercorrelated In-Plane and Out-of-Plane Ferroelectricity in Ultrathin Two-Dimensional Layered Semiconductor In₂Se₃. *Nano Lett.* **2018**, 18 (2), 1253–1258.
- (10) Gong, Y. THIN FILM ELECTRONICS WITH NOVEL MATERIALS: ZINC OXIDE AND 2D TRANSITION METAL DICHALCOGENIDES (Doctoral dissertation). The Pennsylvania State University, 2017. Retrieved from <https://etda.libraries.psu.edu/catalog/14420ywg5045>
- (11) del Corro, E.; Terrones, H.; Elias, A.; Fantini, C.; Feng, S.; Nguyen, M. A.;

- Mallouk, T. E.; Terrones, M.; Pimenta, M. A. Excited Excitonic States in 1L, 2L, 3L, and Bulk WSe₂ Observed by Resonant Raman Spectroscopy. *ACS Nano* **2014**, *8* (9), 9629–9635.
- (12) Terrones, H.; Corro, E. Del; Feng, S.; Poumirol, J. M.; Rhodes, D.; Smirnov, D.; Pradhan, N. R.; Lin, Z.; Nguyen, M. A. T.; Elías, A. L.; Mallouk, T. E.; Balicas, L.; Pimenta, M. A.; Terrones, M. New First Order Raman-Active Modes in Few Layered Transition Metal Dichalcogenides. *Sci. Rep.* **2015**, *4* (1), 4215.
- (13) Sahin, H.; Tongay, S.; Horzum, S.; Fan, W.; Zhou, J.; Li, J.; Wu, J.; Peeters, F. M. Anomalous Raman Spectra and Thickness-Dependent Electronic Properties of WSe₂. *Phys. Rev. B* **2013**, *87* (16), 165409.
- (14) Luo, X.; Zhao, Y.; Zhang, J.; Toh, M.; Kloc, C.; Xiong, Q.; Quek, S. Y. Effects of Lower Symmetry and Dimensionality on Raman Spectra in Two-Dimensional WSe₂. *Phys. Rev. B* **2013**, *88* (19), 195313.
- (15) Ma, Y.; Liu, B.; Zhang, A.; Chen, L.; Fathi, M.; Shen, C.; Abbas, A. N.; Ge, M.; Mecklenburg, M.; Zhou, C. Reversible Semiconducting-to-Metallic Phase Transition in Chemical Vapor Deposition Grown Monolayer WSe₂ and Applications for Devices. *ACS Nano* **2015**, *9* (7), 7383–7391.
- (16) Kappera, R.; Voiry, D.; Yalcin, S. E.; Branch, B.; Gupta, G.; Mohite, A. D.; Chhowalla, M. Phase-Engineered Low-Resistance Contacts for Ultrathin MoS₂ Transistors. *Nat. Mater.* **2014**, *13* (12), 1128–1134.
- (17) Lin, M.; Wu, D.; Zhou, Y.; Huang, W.; Jiang, W.; Zheng, W.; Zhao, S.; Jin, C.;

- Guo, Y.; Peng, H.; Liu, Z. Controlled Growth of Atomically Thin In₂Se₃ Flakes by van Der Waals Epitaxy. *J. Am. Chem. Soc.* **2013**, *135* (36), 13274–13277.
- (18) Zhang, W.; Chuu, C.-P.; Huang, J.-K.; Chen, C.-H.; Tsai, M.-L.; Chang, Y.-H.; Liang, C.-T.; Chen, Y.-Z.; Chueh, Y.-L.; He, J.-H.; Chou, M.-Y.; Li, L.-J. Ultrahigh-Gain Photodetectors Based on Atomically Thin Graphene-MoS₂ Heterostructures. *Sci. Rep.* **2015**, *4* (1), 3826.
- (19) Tielrooij, K. J.; Piatkowski, L.; Massicotte, M.; Woessner, A.; Ma, Q.; Lee, Y.; Myhro, K. S.; Lau, C. N.; Jarillo-Herrero, P.; van Hulst, N. F.; Koppens, F. H. L. Generation of Photovoltage in Graphene on a Femtosecond Timescale through Efficient Carrier Heating. *Nat. Nanotechnol.* **2015**, *10* (5), 437–443.
- (20) Mudd, G. W.; Svatek, S. A.; Hague, L.; Makarovskiy, O.; Kudrynskiy, Z. R.; Mellor, C. J.; Beton, P. H.; Eaves, L.; Novoselov, K. S.; Kovalyuk, Z. D.; Vdovin, E. E.; Marsden, A. J.; Wilson, N. R.; Patanè, A. High Broad-Band Photoresponsivity of Mechanically Formed InSe-Graphene van Der Waals Heterostructures. *Adv. Mater.* **2015**, *27* (25), 3760–3766.
- (21) Li, X.; Basile, L.; Huang, B.; Ma, C.; Lee, J.; Vlassiouk, I. V.; Puzos, A. A.; Lin, M.-W.; Yoon, M.; Chi, M.; Idrobo, J. C.; Rouleau, C. M.; Sumpter, B. G.; Geohegan, D. B.; Xiao, K. Van Der Waals Epitaxial Growth of Two-Dimensional Single-Crystalline GaSe Domains on Graphene. *ACS Nano* **2015**, *9* (8), 8078–8088.
- (22) Avsar, A.; Vera-Marun, I. J.; Tan, J. Y.; Watanabe, K.; Taniguchi, T.; Castro Neto,

- A. H.; Özyilmaz, B. Air-Stable Transport in Graphene-Contacted, Fully Encapsulated Ultrathin Black Phosphorus-Based Field-Effect Transistors. *ACS Nano* **2015**, 9 (4), 4138–4145.
- (23) Almeida, G.; Dogan, S.; Bertoni, G.; Giannini, C.; Gaspari, R.; Perissinotto, S.; Krahne, R.; Ghosh, S.; Manna, L. Colloidal Monolayer β -In₂Se₃ Nanosheets with High Photoresponsivity. *J. Am. Chem. Soc.* **2017**, 139 (8), 3005–3011.
- (24) Chiu, M.-H.; Zhang, C.; Shiu, H.-W.; Chuu, C.-P.; Chen, C.-H.; Chang, C.-Y. S.; Chen, C.-H.; Chou, M.-Y.; Shih, C.-K.; Li, L.-J. Determination of Band Alignment in the Single-Layer MoS₂/WSe₂ Heterojunction. *Nat. Commun.* **2015**, 6, 7666.
- (25) Kim, T.; Mun, J.; Park, H.; Joung, D.; Diware, M.; Won, C.; Park, J.; Jeong, S.-H.; Kang, S.-W. Wafer-Scale Production of Highly Uniform Two-Dimensional MoS₂ by Metal-Organic Chemical Vapor Deposition. *Nanotechnology* **2017**, 28 (18), 18LT01.
- (26) Kalanyan, B.; Kimes, W. A.; Beams, R.; Stranick, S. J.; Garratt, E.; Kalish, I.; Davydov, A. V.; Kanjolia, R. K.; Maslar, J. E. Rapid Wafer-Scale Growth of Polycrystalline 2H-MoS₂ by Pulsed Metal–Organic Chemical Vapor Deposition. *Chem. Mater.* **2017**, 29 (15), 6279–6288.
- (27) Dumcenco, D.; Ovchinnikov, D.; Marinov, K.; Lazić, P.; Gibertini, M.; Marzari, N.; Sanchez, O. L.; Kung, Y.-C.; Krasnozhan, D.; Chen, M.-W.; Bertolazzi, S.; Gillet, P.; Fontcuberta i Morral, A.; Radenovic, A.; Kis, A. Large-Area Epitaxial Monolayer MoS₂. *ACS Nano* **2015**, 9 (4), 4611–4620.

- (28) Zhang, X.; Choudhury, T. H.; Chubarov, M.; Xiang, Y.; Jariwala, B.; Zhang, F.; Alem, N.; Wang, G.-C.; Robinson, J. A.; Redwing, J. M. Diffusion-Controlled Epitaxy of Large Area Coalesced WSe₂ Monolayers on Sapphire. *Nano Lett.* **2018**, *18* (2), 1049–1056.
- (29) Zhang, X.; Zhang, F.; Wang, Y.; Schulman, D. S.; Zhang, T.; Bansal, A.; Alem, N.; Das, S.; Crespi, V. H.; Terrones, M.; Redwing, J. M. Defect-Controlled Nucleation and Orientation of WSe₂ on HBN: A Route to Single-Crystal Epitaxial Monolayers. *ACS Nano* **2019**.
- (30) Shenai-Khatkhate, D. V.; DiCarlo, R. L.; Ware, R. A. Accurate Vapor Pressure Equation for Trimethylindium in OMVPE. *J. Cryst. Growth* **2008**, *310* (7–9), 2395–2398.
- (31) Maung, N.; Fan, G.; Ng, T.; Williams, J. O.; Wright, A. C. A Study of the Mechanism of the Reaction of Trimethylgallium with Hydrogen Selenide. *J. Mater. Chem.* **1999**, *9* (10), 2489–2494.
- (32) Han, G.; Chen, Z. G.; Drennan, J.; Zou, J. Indium Selenides: Structural Characteristics, Synthesis and Their Thermoelectric Performances. *Small* **2014**, *10* (14), 2747–2765.
- (33) Tao, X.; Gu, Y. Crystalline–Crystalline Phase Transformation in Two-Dimensional In₂Se₃ Thin Layers. *Nano Lett.* **2013**, *13* (8), 3501–3505.
- (34) Widjonarko, N. Introduction to Advanced X-Ray Diffraction Techniques for Polymeric Thin Films. *Coatings* **2016**, *6* (4), 54.

- (35) Wang, S.; Rong, Y.; Fan, Y.; Pacios, M.; Bhaskaran, H.; He, K.; Warner, J. H. Shape Evolution of Monolayer MoS₂ Crystals Grown by Chemical Vapor Deposition. *Chem. Mater.* **2014**, 26 (22), 6371–6379.
- (36) Chubarov, M.; Choudhury, T. H.; Zhang, X.; Redwing, J. M. In-Plane x-Ray Diffraction for Characterization of Monolayer and Few-Layer Transition Metal Dichalcogenide Films. *Nanotechnology* **2018**, 29 (5), 055706.
- (37) Lyu, D. Y.; Lin, T. Y.; Lin, J. H.; Tseng, S. C.; Hwang, J. S.; Chiang, H. P.; Chiang, C. C.; Lan, S. M. Growth and Properties of Single-Phase γ -In₂Se₃ Thin Films on (1 1 1) Si Substrate by AP-MOCVD Using H₂Se Precursor. *Sol. Energy Mater. Sol. Cells* **2007**, 91 (10), 888–891.
- (38) Kambas, K.; Julien, C.; Jouanne, M.; Likforman, A.; Guittard, M. Raman Spectra of α - and γ -In₂Se₃. *Phys. status solidi* **1984**, 124 (2), K105–K108.

Chapter 7 Summary and Future Work

The modern development based on 2-dimensional (2D) layered materials relies heavily on the crystallinity of the materials. Therefore, most advanced discovery of 2D materials still utilizes exfoliated flakes of bulk single crystals. Although 2D fields show promising future and outlook, the reliance on the flakes or micron-size single-crystal domains constrains their further applications and makes the 2D concepts still far from the real life. The dissertation demonstrates the research effort towards producing high-quality and large-area WSe₂ and In₂Se₃ atomically thin films by metalorganic chemical vapor deposition (MOCVD), with detailed investigation on growth mechanism of these materials with van der Waals (vdW) structures. This is a significant process to the synthesis of 2D materials, in which case research on scalable devices and applications now are also feasible.

The dissertation started with the impact of the selenium precursors on the growth of coalesced WSe₂ films. The simultaneous formation of carbon layer during the growth at high temperature due to the methyl group in the dimethyl selenide (DMSe) prevents the coalescence of the films. By substituting the DMSe precursor with hydrogen selenide (H₂Se), the source of carbon has been removed and coalesced film can be achieved. In addition to the selenium precursors, the selection of tungsten precursors could be also an interesting topic for future study. Tungsten hexacarbonyl (W(CO)₆) has been adapted in this dissertation due to its low pyrolysis temperature and high vapor pressure. However, other tungsten precursors especially the halogen precursors such as WF₆ and WCl₆ were

also commonly used in the chemical vapor deposition (CVD) for tungsten films.¹⁻³

Although usage of halogen precursors typically introduces the formation of etching side product, the existing of halogen atoms (Cl in common cases) during the silicon nanowires (SiNWs) growth can improve the surface morphology of the SiNWs resulting in smooth sidewall surfaces and reduced tapering.^{4,5} Therefore, the presence of halogen atom in the CVD WSe₂ process may increase the low surface diffusion length of W on the substrate surface that leads to a limited WSe₂ domain size. Besides, chalcogen atoms may also be substitutionally doped in the WSe₂ monolayers or adsorbed on the WSe₂ layer surface, which may consequently change the electrical properties of the film.

One of the main success in this dissertation is the development of a multi-step growth process for balancing the nucleation and lateral growth of WSe₂ and eventually leading to the formation of completely coalesced monolayer. The multi-step process consists of an initial nucleation step which used a high W(CO)₆ flow rate along with H₂Se to promote nucleation. The W(CO)₆ was then switched out of the reactor and the sample was annealed in H₂Se to promote surface diffusion of tungsten-containing species to form oriented WSe₂ islands. The W(CO)₆ was then switched back into the reactor at a lower flow rate to suppress further nucleation and laterally grow the WSe₂ islands to form a fully coalesced monolayer film. The orientation of the domains and the epitaxial relation of the coalesced films have been identified and the growth mechanism such as the temperature for mass transport limited regime as well as the domain shape evolution correlated to the local variations in the Se:W adatom ratio has been detailed studied. Additionally, the phenomenon during the H₂Se annealed only process can be the key to

further understand the 2D growth mechanism. We noticed the evolution of domain size and cluster density with annealing time follows a 2D ripening process, and therefore estimate the tungsten-species surface diffusivity based on the post-growth results. However, there are few more points remaining unclear. The domains show more uniform size after the ripening, compared to the cluster size distribution in classical Ostwald ripening. This is an indication that the diffusion and rearrangement of the surface adatoms during the growth of WSe₂ are more complicated than typical ripening process and an interaction between domains (especially when they are closed to each other) can exist. Also, we often notice the concentrated the compact WSe₂ domains typically have the same orientation regardless of the degenerated formation energy of 0° and 60° orientations. This may further support the hypothesis of domain interaction and can be important to reduce the density of inversion domain boundaries in the films.

The last part of the WSe₂ growth study in this dissertation demonstrates the single-crystal hexagonal boron nitride (hBN) as a superior substrate for WSe₂ growth. The discovery of the WSe₂ growth driven by the single atom vacancies on hBN surface offers a desirable method to control both nucleation and orientation of the WSe₂ towards a perfect single-crystal monolayer. Moreover, hBN is well known for its atomically flat surface and the screening effect to avoid environmental impact, which significantly preserve and even improve the properties of 2D films in between. Therefore, more growth studies on wafer-scale high quality hBN films and substrates are urged. Apart from all the advantages of using hBN as substrate, we notice the negative thermal expansion coefficient of hBN often leads to the cracks in the flakes, which also results in the cracks in the WSe₂ film deposited on top. This can be a potential issue for large-scale

fabrication and strain engineering such as controlling film thickness and introducing buffer layer should be considered when investigating the growth of hBN films.

This dissertation also points out the potential interest in integrating 2D materials with silicon in back-end-of-line (BEOL) applications and 3D fabrication and in flexible electronics, which typically requires processing temperature $< 450\text{ }^{\circ}\text{C}$. The initial attempt on low-temperature growth WSe_2 at $400\text{ }^{\circ}\text{C}$ shows properties are significantly limited due to the nanocrystallinity of the films. On the other hand, the dissertation demonstrates a scalable production of high-quality layered metal chalcogenide (MC), $\beta\text{-In}_2\text{Se}_3$ films, at $400\text{ }^{\circ}\text{C}$ by MOCVD. The process shows controllable growth rate and the films exhibit epitaxial relation with both c-plane sapphire and Si (111) substrates. This low-temperature growth of epitaxial $\beta\text{-In}_2\text{Se}_3$ films extends the potential of 2D materials in integrated and flexible electronic, optoelectronic, and ferroelectric applications. It is also crucial to address the scalable growth of other 2D materials can be potentially feasible, such as phosphorene and layered perovskites, which have exhibited very interesting properties such as narrow bandgap and magnetism, but are lack of support from scalable synthesis and growth study.

Apart from what has been achieved in this dissertation, the author believes the following aspects can be crucial to next step and future development of 2D. A scalable and damage-free transfer method of 2D materials with no interface contamination is definitely needed. Although scalable transfer process of 2D materials has been developing all this time since the discovery of graphene, most transfer methods involve contact with environment (air, etchant, solution, etc.) and mechanical deformation.

Therefore, these methods typically lead to certain degree of damage on the transferred flake/film, in addition to the possible residue or oxidation on the interface between transferred flake/film and target substrates. This is crucial for one that defects and interfacial contaminations are known to heavily impact the properties of 2D materials, and two that the thermodynamic and kinetic properties of 2D materials limit the synthetic design where not all the 2D heterostructure stackings or substrates can be fulfilled. In addition, growth investigation such as doping, alloys, and heterostructures is very practical and should be pursued. Early studies have shown the possibility of these structures and more research is expected to focus on controllability on doping concentration, alloy components and heterostructure design. In addition, the synthesis in 2D materials should be associated more closely with the synthesis of conventional single-crystal thin films. For example, 2D materials are similar to the interfacial layer in III-V thin heterostructures and thus some of the growth mechanism should be inherited from the established knowledge of thin film epitaxy.

7.1 References

- (1) Carmalt, C. J.; Parkin, I. P.; Peters, E. S. Atmospheric Pressure Chemical Vapour Deposition of WS₂ Thin Films on Glass. *Polyhedron* **2003**, 22 (11), 1499–1505.
- (2) Boscher, N.; Carmalt, C.; Parkin, I. Atmospheric Pressure Chemical Vapor Deposition of WSe₂ Thin Films on Glass - Highly Hydrophobic Sticky Surfaces. **2006**, 122–127.
- (3) Gesheva, K. A.; Vlahov, E. S.; Stoyanov, G. I.; Beshkov, G. D.; Marinov, M. Deposition and Characterization of CVD-Tungsten and Tungsten Carbonitrides on (100) Si. *Ceram. Int.* **1996**, 22 (1), 87–89.
- (4) Oehler, F.; Gentile, P.; Baron, T.; Ferret, P. The Effects of HCl on Silicon Nanowire Growth: Surface Chlorination and Existence of a ‘Diffusion-Limited Minimum Diameter.’ *Nanotechnology* **2009**, 20 (47), 475307.
- (5) Gentile, P.; Solanki, a; Pauc, N.; Oehler, F.; Salem, B.; Rosaz, G.; Baron, T.; Den Hertog, M.; Calvo, V. Effect of HCl on the Doping and Shape Control of Silicon Nanowires. *Nanotechnology* **2012**, 23 (21), 215702.

VITA

Xiaotian Zhang

EDUCATION

Ph.D., Materials Science and Engineering, 2019

The Pennsylvania State University, University Park, PA

Dissertation: “*Metalorganic Chemical Vapor Deposition of Two-Dimensional Layered Chalcogenides*”

B.S., Materials Science and Engineering, 2014

The Pennsylvania State University, University Park, PA

SELECTED PUBLICATIONS

Zhang, X., Zhang, F., Wang, Y., Schulman, D.S., Zhang, T., Bansal, A., Alem, N., Das, S., Crespi, V.H., Terrones, M., Redwing, J.M. “Defect-Controlled Nucleation and Orientation of WSe₂ on hBN – A Route to Single Crystal Epitaxial Monolayers” *ACS Nano* **2019** 12 (2), 965-975

Zhang, X., Choudhury, T.H., Chubarov, M., Xiang, Y., Jariwala, B., Zhang, F., Alem, N., Wang, G.C., Robinson, J.A., Redwing, J.M. “Diffusion-Controlled Epitaxy of Large Area Coalesced WSe₂ Monolayers on Sapphire” *Nano letters* **2018** 18 (2), 1049-1056

Zhang, X., Balushi, Z.Y., Zhang, F., Choudhury, T.H., Eichfeld, S.M., Alem, N., Jackson, T. N., Robinson, J.A., Redwing, J.M. “Influence of Carbon in Metalorganic Chemical Vapor Deposition of Few-Layer WSe₂ Thin Films” *Journal of Electronic Materials* **2016** 45 (12), 6273-6279

Hainey, F.M., Jr, **Zhang, X.**, Wang, K., Redwing, J.M. “Aluminum-Catalyzed Growth of Silicon Nanowires in High-Energy Growth Directions” *ACS Appl. Nano Mater.* **2018** 1 (10), 5493-5499

Gong, Y., **Zhang, X.**, Redwing, J.M., Jackson, T.N. “Thin Film Transistors Using Wafer-Scale Low-Temperature MOCVD WSe₂” *Journal of Electronic Materials* **2016**, 45 (12), 6280-6284

Chubarov, M., Choudhury, T.H., **Zhang, X.**, Redwing, J.M. “In-plane x-ray diffraction for characterization of monolayer and few-layer transition metal dichalcogenide films” *Nanotechnology* **2018** 29 (5), 055706

Walter, T.N., Lee, S., **Zhang, X.**, Chubarov, M., Redwing, J.M., Jackson, T.N., Mohny, S.E. “Atomic layer deposition of ZnO on MoS₂ and WSe₂” *Appl Surf Sci.* **2019** 480, 43-51

Zhang, F., Erb, C., Runkle, L., **Zhang, X.**, Alem, N., “Etchant-free transfer of 2D nanostructures” *Nanotechnology* **2017**, 29 (2), 025602

Lin, Y.C., Jariwala, B., Bersch, B.M. Xu, K., Nie, Y., Wang, B., Eichfeld, S.M., **Zhang, X.**, Choudhury, T.H., Pan, Y., Addou, Rafik., Smyth, C.M., Li, J., Zhang, K., Haque, A., Fölsch, S., Feenstra, R.M., Wallace, R.M., Cho, K., Fullerton-Shirey, S.K., Redwing, J.M., Robinson, J.A. “Realizing Large-Scale, Electronic-Grade Two-Dimensional Semiconductors” *ACS Nano* **2018** 12 (2), 965-975

AWARDS

Young Scientist Award at 46th Conference on the Physics & Chemistry of Surface & Interfaces (PCSI-46), 2019

Robert E. Newnham award for research excellence, 2018